

University of New Hampshire

University of New Hampshire Scholars' Repository

Doctoral Dissertations

Student Scholarship

Winter 1995

A system model for multipath interference on terrestrial line-of-sight QAM digital radio

Charles Henry Bianchi
University of New Hampshire, Durham

Follow this and additional works at: <https://scholars.unh.edu/dissertation>

Recommended Citation

Bianchi, Charles Henry, "A system model for multipath interference on terrestrial line-of-sight QAM digital radio" (1995). *Doctoral Dissertations*. 1867.
<https://scholars.unh.edu/dissertation/1867>

This Dissertation is brought to you for free and open access by the Student Scholarship at University of New Hampshire Scholars' Repository. It has been accepted for inclusion in Doctoral Dissertations by an authorized administrator of University of New Hampshire Scholars' Repository. For more information, please contact Scholarly.Communication@unh.edu.

INFORMATION TO USERS

This manuscript has been reproduced from the microfilm master. UMI films the text directly from the original or copy submitted. Thus, some thesis and dissertation copies are in typewriter face, while others may be from any type of computer printer.

The quality of this reproduction is dependent upon the quality of the copy submitted. Broken or indistinct print, colored or poor quality illustrations and photographs, print bleedthrough, substandard margins, and improper alignment can adversely affect reproduction.

In the unlikely event that the author did not send UMI a complete manuscript and there are missing pages, these will be noted. Also, if unauthorized copyright material had to be removed, a note will indicate the deletion.

Oversize materials (e.g., maps, drawings, charts) are reproduced by sectioning the original, beginning at the upper left-hand corner and continuing from left to right in equal sections with small overlaps. Each original is also photographed in one exposure and is included in reduced form at the back of the book.

Photographs included in the original manuscript have been reproduced xerographically in this copy. Higher quality 6" x 9" black and white photographic prints are available for any photographs or illustrations appearing in this copy for an additional charge. Contact UMI directly to order.

UMI

A Bell & Howell Information Company
300 North Zeeb Road, Ann Arbor MI 48106-1346 USA
313/761-4700 800/521-0600

**A SYSTEM MODEL FOR MULTIPATH INTERFERENCE
ON TERRESTRIAL LINE-OF-SIGHT QAM DIGITAL RADIO**

BY

CHARLES HENRY BIANCHI

B.S., University of New Hampshire, May, 1983

M.S., University of New Hampshire, December, 1985

DISSERTATION

**Submitted to the University of New Hampshire
in Partial Fulfillment of
the Requirements for the Degree of**

Doctor of Philosophy

in

Engineering

December, 1995


UMI Number: 9617066

UMI Microform 9617066
Copyright 1996, by UMI Company. All rights reserved.


**This microform edition is protected against unauthorized
copying under Title 17, United States Code.**

UMI
300 North Zeeb Road
Ann Arbor, MI 48103

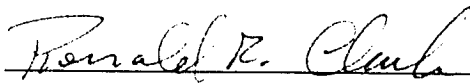
This dissertation has been examined and approved.



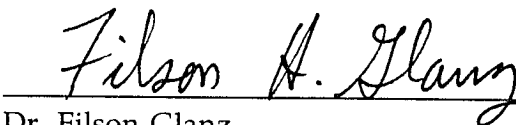
Dr. Kondagunta Sivaprasad,
Professor of Electrical and Computer Engineering



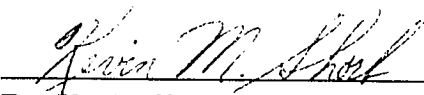
Dr. Kent Chamberlin,
Professor of Electrical and Computer Engineering



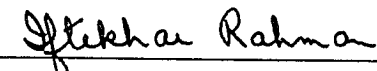
Dr. Ronald Clark,
Professor of Electrical and Computer Engineering



Dr. Filson Glanz,
Professor of Electrical and Computer Engineering



Dr. Kevin Short,
Professor of Mathematics



Dr. Iftekhar Rahman,
Member of Technical Staff, AT&T Bell Laboratories

11/15/95
Date

DEDICATION

Quest'opera e' dedicata a mia figlia Marisa Angelia Bianchi. Se lei non fosse portata via, avrebbe passato questo tempo con noi. Ho completato quest'opera aspettandola. Adesso solo l'opera e' rimasta. L'ho scritta per lei. Addio, mio caro angelo.

ACKNOWLEDGEMENTS

Many friends, relatives, colleagues, and advisors have been instrumental in guiding and assisting me through this project. Without their support, I do not feel that I could have completed such an endeavor.

I would like to thank the members of my graduate committee at the University of New Hampshire. I am grateful for the time and effort involved in critically examining the theory and results, and in proofreading the manuscript. I would also like to thank the faculty of the Department of Electrical and Computer Engineering for providing me with the guidance, preparation, resources, and will to pursue graduate study in electrical engineering. Without their encouragement and assistance over the years, I would have given up long ago.

In addition, I would like to thank my colleagues at AT&T Bell Laboratories in North Andover, Massachusetts. The many learned engineers, physicists, and technicians that I worked with at AT&T Bell Laboratories during the past 9 years provided information, equipment, and measurements during the various phases of this project and their assistance is respectfully acknowledged. I am grateful to Dr. A. Giger, Dr. M. Emshwiller, W. A. Robinson, and R. P. Slade, for their examples, suggestions, ideas, and criticisms, all of which generated interest in this topic and helped me to formulate theories and experiments. I am especially thankful to Dr. G. Alley, who recruited me into the microwave radio, introduced me to the problem of multipath propagation, and fostered in me an appreciation and enjoyment of scientific analysis and experimentation. Overall, AT&T Bell Laboratories has

been an immense source of technical knowledge and facilities that provided me with an incredible opportunity to perform simulations and experiments and to learn about digital communications systems.

The efforts of three people in particular have been essential to the completion of the dissertation, and they deserve special thanks. Dr. Kondagunta Sivaprasad has been a source of inspiration and guidance to me since I first studied in his classes during my sophomore year. Without his patience and faith in me, I would not have attempted to complete a dissertation. Dr. Iftekhar Rahman has been both a generous and devoted colleague, and an attentive and thoughtful teacher, from when I first worked with him at AT&T Bell Laboratories. Without his corrections and suggestions, I would not have been able to complete the dissertation. My present technical manager, George Lentz, has been a caring and supportive mentor during the conclusion of the program. Without his concern and encouragement, I would not have completed the degree.

Most of all, I would like to thank my family. The endless years of love and patience from my wife Janet, the unfailing adoration from my son Michelangelo, the inspiring sense of pride from my parents, the admiration and respect from my brother and sisters, the thoughtful words of encouragement from my parents-in-law, and the best wishes of many others, have all left a lasting impression in my heart and soul.

I thank you all.

FOREWARD

The main topics of this dissertation are addressed as follows.

Modelling and performance of digital radio systems are reviewed in chapter 1. Commonly used models are described, modelling parameters are defined, and literature of related work in the field is surveyed. Microwave link design and system performance objectives are also discussed.

Field measurements are reviewed in chapter 2. Features of the experimental link are reviewed. Measurement and collection hardware and software are described. Signal measurements are then defined and typical field data are presented. The field measurements are compared with other published experimental data. The data from this experiment is used later to show the validity of the modelling, and to develop analysis methods.

A comprehensive system model for terrestrial line-of-sight QAM digital radio is introduced in chapter 3. This is achieved by dividing the system into three linear and time-invariant subsystems. The subsystem blocks are transmitter, channel, and receiver. This enables the examination of specific performance issues for each sub-system (such as signalling, distortion, and detection). The overall system performance is then generated from the cascade of these sub-systems.

Channel models are developed in chapter 4. Radio propagation is reviewed and common modelling techniques are surveyed. Four particular types of models are applied to the experimental link in order to fully examine channel distortions and compare modelled and measured data. A forward multipath model is applied to identify terrain parameters which cause interference to terrestrial digital microwave radio links. A forward multipath

model is then developed to simulate channel distortions using the forward scattering parameters. An inverse multipath model is then developed for the extraction of forward multipath model parameters from measured channel data. Lastly, a statistical model is used to determine the distributions of the forward multipath parameters and characterize the resulting channel effects.

In chapter 5 a modem channel model is defined based on the analyses of chapter 4. A static multipath interference signature for modem performance characterization is then reviewed. An additional signature for dynamic multipath effects on modem performance is then introduced. Static and dynamic signature algorithms are developed based on the objectives and measures described in chapters 1 and 2. The hardware and software configurations are described. Measured modem signatures for various multipath conditions are then examined to determine the extent to which channel model parameters affect modem performance.

The system characteristics of the receiver are covered in chapter 6. Quadrature amplitude modulation is reviewed, and the receiver functionality is described. System considerations, such as equalization, detection, and recovery of the signal are discussed, and procedures to account for these processes are developed.

Signal distortion is summarized in chapter 7. The sub-system models are integrated to study the interference produced by multipath propagation. The effect of channel distortion on the QAM signal is modelled by examining the time response of the transmission channel. The effects of channel distortion are reviewed, and a metric is developed for quantifying the effect of multipath parameters on QAM signal quality. Measured data and estimated results are then examined for several cases.

Conclusions and recommendations are discussed in chapters 8 and 9.

TABLE OF CONTENTS

DEDICATION	iii
ACKNOWLEDGEMENTS	iv
FOREWARD	vi
LIST OF FIGURES	xi
ABSTRACT	xviii

CHAPTER	PAGE
INTRODUCTION	1
I SYSTEM PERFORMANCE AND MODELLING	7
Introduction	7
1.1 System Performance	7
1.2 System Models	10
1.3 Motivation	13
II FIELD MEASUREMENTS	15
Introduction	15
2.1 Field Experiment	15
2.2 Link Description	17
2.3 Configuration	19
2.4 Antenna Systems	21
2.5 Performance Monitoring	23
2.6 Data Collection	26
2.7 Summary	30

III	SYSTEM MODEL	32
	Introduction	32
	3.1 Digital Radio Communication Systems	32
	3.2 Filter Models	35
	3.3 Channel Model	40
	3.4 Receiver Model	46
	3.5 Summary	47
IV	RADIO CHANNEL MODEL	49
	Introduction	49
	4.1 Overview	49
	4.2 Forward Multipath Model	53
	4.3 Inverted Multipath Model	78
	4.4 Statistical Multipath Model	87
	4.5 Summary	104
V	MODEM PERFORMANCE	106
	Introduction	106
	5.1 Digital Radio Performance Characterization	107
	5.2 Multipath Signatures	109
	5.3 Channel Model	111
	5.4 Signature Theory	119
	5.5 Signature Algorithm	125
	5.6 Implementation	129
	5.7 Discussion of Model and Results	130
	5.8 Evaluation of a 64 QAM System	178
	5.9 Summary	181

VI	SIGNAL ANALYSIS	184
	Introduction	184
	6.1 QAM Digital Signal Theory	185
	6.2 Receiver Implementation	187
	6.3 System Considerations	191
	6.4 Summary	198
VII	DISCUSSION	201
	Introduction	201
	7.1 Channel Distortion	202
	7.2 Channel Reconstruction	204
	7.3 Second Path Delay	212
	7.4 Signal Distortion	218
	7.5 Multipath Interference	220
	7.6 Summary	225
VIII	CONCLUSIONS	227
IX	RECOMMENDATIONS	228
	LIST OF REFERENCES	231
	APPENDIX	236
	LIST OF ABBREVIATIONS	242

LIST OF FIGURES

<u>figure</u>	<u>page</u>	<u>title</u>
2-1	18	Salton-Brawley California Line-of-Sight Microwave Link Terrain Elevation Profile
2-2	20	Digital Radio Field Measurement Block Diagram
2-3	22	Digital Radio Antennae Configuration
2-4	25	RF Spectrum Monitor Block Diagram
2-5	27	Field Experiment Block Diagram
2-6	29	Remote Data Collection Flow Chart
3-1	34	Digital Radio System Block Diagram
3-2a	36	Time-Domain Transmitted Signal
3-2b	37	Frequency-Domain Transmitted Signal
3-3a	38	Time-Domain Nyquist Filter Response
3-3b	39	Frequency-Domain Nyquist Filter Response
3-4	43	An Illustration of Multipath Propagation Using Two Rays
3-5	48	The QAM Receiver Block Diagram
4-1a	57	Index of Refraction (dry component) as a Function of Temperature and Humidity
4-1b	58	Index of Refraction (wet component) as a Function of Saturated Vapour Pressure
4-1c	59	K-factor as a Function of the Gradient of the Index of Refraction in the Lower Atmosphere
4-2a	64	Local Geometry of Ground Reflection
4-2b	65	Surface Roughness

4-3a	70	Forward Multipath Model: case 1a
4-3b	71	Forward Multipath Model: case 1b
4-3c	72	Forward Multipath Model: case 1c
4-3d	73	Forward Multipath Model: case 1d
4-4a	75	Forward Multipath Model: case 2a
4-4b	76	Forward Multipath Model: case 2b
4-4c	77	Forward Multipath Model: case 2c
4-4d	78	Forward Multipath Model: case 2d
4-5a	86	Measurement of a Typical Multipath Event in the 6GHz Band at Brawley, California (Unprotected Antenna)
4-5b	87	Measurement of a Typical Multipath Event in the 6GHz Band at Brawley, California (Space Diversity Antenna)
4-6a	89	Analysis of a Typical Multipath Event in the 6GHz Band at Brawley, California (Unprotected Antenna)
4-6b	90	Analysis of a Typical Multipath Event in the 6GHz Band at Brawley, California (Space Diversity Antenna)
4-7	93	Distribution of Delay Difference
4-8	94	Distribution of Second Ray Strength
4-9	97	Angle of Arrival Discrimination Due to Antenna Gain Selectivity
4-10a	98	Single Frequency Fade Time Below Level Measured and Computed (Unprotected Antenna)
4-10b	99	In-Band Power Difference Time Below Level Measured and Computed (Unprotected Antenna)
4-11a	101	Single Frequency Fade Time Below Level Measured and Computed (Space Diversity System)
4-11b	102	In-Band Power Difference Time Below Level Measured and Computed (Space Diversity System)

4-12a	103	Single Frequency Fade Time Below Level Measured and Computed (Angle Diversity System)
4-12b	104	In-Band Power Difference Time Below Level Measured and Computed (Angle Diversity System)
5-1	113	The Effect of the K-factor on Second Path Delay and Cancellation Frequency
5-2a	116	Signal Level in the Frequency Domain as a Function of the Broadband Attenuation Parameter A
5-2b	117	Signal Level in the Frequency Domain as a Function of the Null Depth B
5-2c	118	Signal Level in the Frequency Domain as a Function of the Delay Difference τ
5-3a	133	Static Multipath Signature: case 1
5-3b	134	Static Multipath Signature: case 2
5-3c	135	Static Multipath Signature: case 3
5-3d	136	Static Multipath Signature: case 4
5-3e	137	Static Multipath Signature: case 5
5-3f	138	Static Multipath Signature: case 6
5-4a	139	Static Multipath Signature: case 7
5-4b	140	Static Multipath Signature: case 8
5-4c	141	Static Multipath Signature: case 9
5-4d	142	Static Multipath Signature: case 10
5-4e	143	Static Multipath Signature: case 11
5-4f	144	Static Multipath Signature: case 12

5-5a	145	Dynamic Cancellation Depth Signature: case 1
5-5b	146	Dynamic Cancellation Depth Signature: case 2
5-5c	147	Dynamic Cancellation Depth Signature: case 3
5-5d	148	Dynamic Cancellation Depth Signature: case 4
5-5e	149	Dynamic Cancellation Depth Signature: case 5
5-5f	150	Dynamic Cancellation Depth Signature: case 6
5-6a	152	Dynamic Null Frequency: case 1
5-6b	153	Dynamic Null Frequency: case 2
5-6c	154	Dynamic Null Frequency: case 3
5-6d	155	Dynamic Null Frequency: case 4
5-6e	156	Dynamic Null Frequency: case 5
5-6f	157	Dynamic Null Frequency: case 6
5-7a	158	Dynamic Null Frequency: case 7
5-7b	159	Dynamic Null Frequency: case 8
5-7c	160	Dynamic Null Frequency: case 9
5-7d	161	Dynamic Null Frequency: case 10
5-7e	162	Dynamic Null Frequency: case 11
5-7f	163	Dynamic Null Frequency: case 12
5-8a	165	Bit Error Performance as a Function of Dynamic Cancellation Depth: case 1
5-8b	166	Bit Error Performance as a Function of Dynamic Cancellation Depth: case 2
5-8c	167	Bit Error Performance as a Function of Dynamic Cancellation Depth: case 3

5-8d	168	Bit Error Performance as a Function of Dynamic Cancellation Depth: case 4
5-8e	169	Bit Error Performance as a Function of Dynamic Cancellation Depth: case 5
5-8f	170	Bit Error Performance as a Function of Dynamic Cancellation Depth: case 6
5-9a	171	Bit Error Performance as a Function of Dynamic Null Frequency: case 1
5-9b	172	Bit Error Performance as a Function of Dynamic Null Frequency: case 2
5-9c	173	Bit Error Performance as a Function of Dynamic Null Frequency: case 3
5-9d	174	Bit Error Performance as a Function of Dynamic Null Frequency: case 4
5-9e	175	Bit Error Performance as a Function of Dynamic Null Frequency: case 5
5-9f	176	Bit Error Performance as a Function of Dynamic Null Frequency: case 6
5-10	177	Comparison of the 10^{-3} and 10^{-6} Static Signatures
5-11	180	Typical Time from Protection Switch Request to Completion
6-1	193	Multipath Channel Response in the Time Domain with Receiver Carrier Detection
6-2	195	Multipath Channel Response in the Frequency Domain with Receiver Carrier Detection
6-3	197	Multipath Channel Response in the Time Domain with Receiver Timing Recovery
6-4	199	Multipath Channel Response in the Frequency Domain with Receiver Timing Recovery

7-1	205	Multipath Channel Response in the Frequency Domain (10 dB cancellation depth, at the channel center, with 6.3 nanosecond delay)
7-2	206	Multipath Channel Response in the Time Domain (10 dB cancellation depth, at the channel center, with 6.3 nanosecond delay)
7-3	207	Effect of Timing Recovery, Carrier Detection, and Sampling on the Multipath Channel Response (10 dB cancellation depth, at the channel center, with 6.3 nanosecond delay)
7-4	209	Comparison of the Simulated and the Reconstructed Multipath Channel Responses in the Frequency Domain (10 dB cancellation depth, at the channel center, with 6.3 nanosecond delay)
7-5	210	Measured Multipath Channel Response in the Time Domain (10 dB cancellation depth, at the channel center, with 6.3 nanosecond delay)
7-6	211	Comparison of the Measured and the Reconstructed Multipath Channel Responses in the Frequency Domain (10 dB cancellation depth, at the channel center, with 6.3 nanosecond delay)
7-7	215	Comparison of the Measured and the Reconstructed Multipath Channel Responses in the Frequency Domain (10 dB cancellation depth, 5 MHz from the channel center, with 6.3 nanosecond delay)
7-8	216	Comparison of the Measured and the Reconstructed Multipath Channel Responses in the Frequency Domain (10 dB cancellation depth, at channel center, with 10 nanosecond delay)
7-9	217	Comparison of the Measured and the Reconstructed Multipath Channel Responses in the Frequency Domain (20 dB cancellation depth, 15 MHz from the channel center, with 6.3 nanosecond delay)
7-10a	221	Peak Distortion versus Cancellation Depth and Second Path Delay Difference

7-10b	222	Mean-square Distortion versus Cancellation Depth and Second Path Delay Difference
A-1	240	Hewlett Packard Multipath Fade Simulator Multipath Channel Response in the Frequency Domain Usable Bandwidth
A-2	241	Hewlett Packard Multipath Fade Simulator Multipath Channel Response in the Frequency Domain Comparison of Theoretical and Simulated

ABSTRACT

A SYSTEM MODEL FOR MULTIPATH INTERFERENCE ON TERRESTRIAL LINE-OF-SIGHT QAM DIGITAL RADIO

by

Charles Henry Bianchi

University of New Hampshire, December, 1995

A comprehensive system model for characterizing the effects of multipath propagation on digital radio systems in the 4 to 6 GHz band is shown in this thesis. The effects of terrain-induced multipath propagation in the presence of atmospheric anomalies are studied using data from experimental microwave links in the field and in the laboratory. This technique, which treats multipath propagation as digital signal distortions caused by interference from ground reflections, has not been shown previously. A forward multipath propagation model is used to identify the critical propagation parameters for a QAM signal. A normalized two ray channel model is developed to approximate the frequency response produced by interference from a ground reflection in a narrow band. The effectiveness of this channel model is evaluated using measured data from the test radio link in the field. The channel parameter values are also estimated from these data. Using the channel model, the channel distortions are simulated in the laboratory. The performance of the laboratory test link is characterized to identify the critical parameters for a QAM receiver model. This receiver model is then used to simulate digital signal distortions and a metric is developed for digital signal distortion as a function of multipath interference.

INTRODUCTION

Digital communication may be broadly described as an estimation of pulses that are propagating through a channel. Depending on the sophistication of the system, information may be digitized, encoded, and converted to a pulse. The data stream then modulates a carrier and is transmitted in a specific frequency band. It is then transported through a medium and is detected at a receiver. The receiver performs the inverse of the transmitter in order to estimate the transmitted information.

The channel is in a range that can be considered to be linear and time-invariant. The transmitter and receiver are then be treated as a complementary pair with their overall response providing a best fit of the channel characteristics. The system response thus compensates for the channel distortions. The best estimate is obtained when the system is perfectly matched to the channel, and the integrity of the information is maintained.

Radio channel distortions are generally characterized by an analysis of nonlinearities in the frequency domain. These nonlinearities are inherent to transmission and propagation at microwave frequencies. They include flat and dispersive fading on the link, linear and parabolic amplitude and phase distortion in the channel, intermodulation in amplifiers, reflections in antennae and waveguides, and interference into the signalling frequency band from other sources. These will disturb the match of transmitter and receiver to the channel and degrade the quality of information transmission. The strength of some distortions, and the instabilities of others, make it

difficult for systems subjected to these impairments to meet network objectives without active countermeasures.

As a result, there has been extensive work in the modelling of communication channels. Characterization of signal distortions allowed system designs to be better matched to the transmission channel. Many of the original channel studies were motivated by impairments in analog radio systems. This included the effects of both propagation loss and interference.

Models developed more recently have been both physical and statistical in nature. Physical path models have been designed to simulate ground scatter and atmospheric refraction. Physical channel models have been designed to match signal distortions. Statistical models have been designed to estimate impairments and predict outage. They all have been motivated by the need to design improvements and countermeasures, as well as to set objectives and quantify limitations.

This study will examine the channel response in the frequency domain and will discuss its relation to distortions in the time domain. Signal information is used to characterize the communication system status during both normal and stressful conditions. Identification of failures, distortions, and interfering phenomena is obtained from channel data. Intelligent tests using detection and synchronization information can reduce the manpower necessary for installation. They can also eliminate the need for test equipment (delay sets, spectrum analyzers). Automation of many operation and maintenance functions will result. In general, remote diagnostic capabilities would be made more powerful.

Quadrature amplitude modulation (QAM) is used internationally for spectrally efficient transport of long-haul telecommunications traffic. Digital

radio systems incorporate QAM on medium and high capacity microwave links in the 2 to 8 GHz frequency range. Radio system design, operating conditions, and performance limitations are similar in the 2 - 8 GHz radio band.

There has been extensive work in both modelling communication channels and in the analysis of impairments for, first, analog and, then, digital radio in the open literature. Diffraction effects are not considered as they contribute to propagation only in shadowed regions, and are not critical to line-of-sight transmission where substantial clearance of obstructions is generally required. Signal interference and path obstruction are generally avoided by thorough route design practices. Hence, the main cause of dynamic distortion and cancellation of the intended signal in terrestrial line-of-sight radio communication is the unstable interference from terrain and atmospheric reflections.

The development and implementation of a comprehensive model for the effect of multipath interference in digital radio systems is the objective of this dissertation. This approach is useful for determining digital signal distortions due to ground reflections. Using a forward scattering approach, terrain-induced multipath propagation is examined for an experimental microwave link. A normalized two ray channel model is then developed. With field measurements, this channel model is evaluated, and its parameters are estimated. The radio system is then tested with a simulated channel in the laboratory to measure the system response and identify critical parameters. The channel model is used to simulate digital signal distortions. A metric is then developed for digital signal distortion based on the channel model.

In this dissertation, the performance of terrestrial line-of-sight quadrature amplitude modulation digital radio in the presence of multipath fading is analyzed. A system model is developed based on microwave link characteristics and microwave channel data. The performance of a typical 64 QAM system is measured so as to obtain realistic values for the model parameters and to compare the modelled results to the measured data. Signal level and digital performance data were measured in the field on a 6 GHz AT&T digital microwave link, and a digital radio system was tested and characterized in the AT&T Digital Microwave Radio Laboratory.

The topics addressed in this dissertation are arranged into 9 chapters as follows.

Modelling and performance of digital radio systems are reviewed in chapter 1. Commonly used models are described, modelling parameters are defined, and literature of related work in the field is surveyed. Microwave link design and system performance objectives are also discussed.

A field experiment for the collection channel and performance data is described in chapter 2. The experiment was implemented on a digital microwave radio link that had poor digital performance and that was known to be subject to frequent multipath propagation conditions. The data show the presence of multipath interference due to ground reflections to be a serious impairment to the performance of digital radio systems.

In chapter 3, a comprehensive system model is proposed to characterize the effect of multipath interference on digital communications systems. It is based on modelling the overall system as a cascade of subsystems. The

mechanisms of the pulse shaping filter, the multipath channel, and the QAM receiver, are analyzed and modelled separately.

The multipath channel is analyzed in chapter 4. A forward multipath channel model is developed based on the forward multipath characteristics of microwave link geometry. It is a normalised two ray model with three controlling parameters: the cancellation depth, the cancellation frequency, and the second ray delay difference. The values of these parameters and their distribution functions are estimated from field measurements using an inversion of the forward multipath channel model. The results compare favourably to the published data. The cancellation depth is a function of the second ray strength. A sufficiently strong second ray is found to be necessary for multipath interference to be possible. However, a coherent secondary wavefront as created by a stable second path delay is critical to the establishment of multipath interference. The location and movement of the cancellation frequency is shown to be a function of small and random perturbations of this second ray delay.

Digital modem performance is characterized as a function of the two ray parameters defined in chapter 5. Both static and dynamic channel conditions are simulated to evaluate the two ray channel model as well as to identify the limitations of QAM system performance. While all three of the multipath parameters control performance, it is shown that the delay has the most extensive effect.

In chapter 6, QAM theory is reviewed, and a QAM receiver model is developed. This model accounts for system effects such as detection, synchronization, and equalization. The QAM receiver model allows for estimation of the receiver output from the input channel.

The receiver model is verified and integrated with the channel model into an overall system model in chapter 7. The system model is then evaluated by recovering the second path delay of the multipath channel at the receiver output. The relationship between the channel model parameters and the digital performance is examined by comparing QAM signal distortions for various multipath interference cases. The second path delay is shown to be the controlling factor in limiting the performance of a QAM system subject to multipath interference.

CHAPTER I

SYSTEM PERFORMANCE AND MODELLING

Introduction

In this chapter the background literature and industry performance standards for digital microwave radio systems are reviewed. In section 1.1 system performance parameters are defined for high-capacity communication links and performance objectives are reviewed. In section 1.2 commonly used models are described, modelling parameters are defined, and literature of related work is surveyed. In section 1.3, the motivation for this dissertation is summarized.

1.1 System Performance

Radio channel distortions are generally characterized in the frequency domain. They are inherent to transmission and propagation at microwave frequencies. They include attenuation and multipath fading on the link, linear and parabolic amplitude and phase distortion in the filters and amplifiers, reflections in antennae and waveguides, intermodulation in amplifiers, and interference into the signalling frequency band. Attenuation fading lowers the signal with respect to noise and erodes the noise margin in signal detection above the background noise. Multipath fading causes dispersion in the affected channels. In Quadrature Amplitude Modulation (QAM) systems this causes cross-vector distortions resulting in cross-talk between the in-phase and quadrature signals. Channel amplitude and phase

distortions cause a combination of attenuation and cross-talk effects. In general, multipath results in a signal summation and cancellation pattern in the transport medium. The channel response due to the presence of reflections is therefore a combination of amplitude and phase distortions that may alter or destroy the intended signal. Intermodulation and interference introduce foreign signals into the communication channel which combine with the intended signal, changing its characteristics. As can be seen, increased attenuation, distortion, or interference all result in an increased probability of decision error at the receiver.

Decision error at the receiver is measured by the customer as information or bit error. The most common measure of digital transmission quality is the **Bit Error Ratio (BER)**, which is the ratio of errored bits to transmitted bits during a specified observation time. The bit error ratio is the basis for most digital performance objectives. The **International Consultative Committee for Telephony and Telegraphy (CCITT)** Recommendation G.821 defines three time-based parameters for performance of ISDN (**Integrated Services Digital Network**) unidirectional channels: **Errored Seconds (ES)**, **Severely Errored Seconds (SES)**, and **Degraded Minutes (DM)**. Seconds having one or more bit errors are ES. The objective is for ES not to exceed 0.32% of the time during any month. Seconds having a BER $> 1E-3$ (1 or more errored bits per 1000 transmitted bits) are SES. The objective is for SES not to exceed 0.054% of the time during any month. An SES is considered an outage. Ten or more consecutive SES are considered unavailable seconds. Digital trunk transmission systems typically lose frame detection after 10 consecutive SES. Minutes having a BER $> 1E-6$ (1 or more errored bits per 1000000 transmitted bits) are degraded minutes. The objective is for DM not

to exceed 0.4% of the time during any month. Obviously, random and unstable distortions, such as multipath fading, make it difficult to design radio links which are assured of meeting the above mentioned objectives. In addition, the progression to higher order modulation schemes for more efficient spectrum usage results in greater system sensitivity to distortion and noise. The need for appropriate system modelling is apparent from both the system design and quality perspectives.

In digital microwave radio, a number of the previously stated distortions are addressed by link design guidelines. The received signal level is a function of the transmitted signal power level, the line-of-sight path length, the clearance over obstructions, the transmit and receive antenna gains, and the transmit and receive waveguide lengths. These are all constrained by a link budget of maximum affordable and available power. Internal reflections are controlled by component design and inspection and by channel equalization. Intermodulation is controlled by limiting the nonlinearity in the system components. Interference is controlled by proper route design, signal polarization, and channel allocation. Multipath, on the other hand, being a function of the lower atmosphere characteristics and/or the local topography, is not well controlled by link design, but may be alleviated with countermeasures such as antenna diversity, channel diversity, channel equalization, and error correction. The prediction and subsequent correction of distortions is the main motivation for simulation and modelling of the multipath interference effects in the radio channel.

1.2 System Models

There has been extensive work in the modelling of multipath channels. The early channel studies, motivated by impairments in analog radio systems included only the effects of both propagation loss and interference. Motivated by the need to predict performance, design improvements and countermeasures, and verification of system objectives, physical and statistical channel models have been developed. The physical channel models simulate ground scatter and atmospheric refraction. The physical channel models match only the channel distortions. The statistical models estimate impairments and predict outage.

Many of the previous models are limited to analysis of atmospheric multipath phenomena and neglect multipath interference due to ground reflections, which is the limiting factor in the performance of digital line-of-sight radio channels. This has been pointed out by Olsen, Martin, and Tjelta [1] in their paper on multipath effects in microwave links. They analyzed the effect of atmospheric propagation parameters such as attenuation, refraction, wavefront coherence, and scintillation on signals reflected from the ground. They proposed that atmospheric effects weaken the direct signal and therefore magnify the effect of the ground reflection on the direct signal in the communication channel. From a review of the many published findings, they pointed out that, although attention has been predominantly given to atmospheric propagation effects, the results strongly indicated that ground reflection is the dominant factor and suggested that channel models should incorporate both the stable ground reflection and the atmospheric perturbation effect.

One of the earlier efforts to model multipath propagation was made by W. D. Rummler [2]. Signal level statistics in a 30 MHz channel were measured in the 6 GHz band. The data were analyzed to estimate two ray model parameters. The analysis was not used to predict digital radio performance. A subsequent study [3] fixed the second path delay at 6.3 nanoseconds and allowed the cancellation frequency and the direct and second ray amplitudes to vary. While this model produced transfer functions which agreed with the measured channel, a universally fixed second path delay is not consistent with propagation on microwave links in general as the delay is a function of the specific second path length.

An early approximation of the effect of multipath propagation on digital communications was performed by W. C. Jakes [4]. The distribution of the second path delay was estimated based on the expected geometry of atmospheric multipath rays. The delay characteristics were then related to inter-symbol interference in order to predict system performance. Spaced antenna diversity was suggested as an effective countermeasure. Jakes did not address the effect of ground reflections.

M. Shafi [5] simulated a non-deterministic three ray model for multipath propagation in order to evaluate diversity system performance. Probability distribution functions were assigned to the secondary amplitudes and delays. A montecarlo simulation was executed and the output statistics of single frequency signal level and two frequency signal difference were accumulated for the experiment. Outage was estimated from the time-below-level statistics of these two measures. The results were compared to radio link measurements at Palmetto, Georgia (USA). Shafi was mainly concerned with atmospheric multipath, and outage was not correlated to the physical

channel but only to single and dual frequency data points which were simulated randomly.

Campbell et al. [6] performed a performance measurement and prediction experiment on a 16 QAM digital radio in Australia. A two ray model was implemented with random distributions for the cancellation frequency, second ray delay, and second ray amplitude. Furthermore, multipath was restricted to atmospheric reflections. Single frequency fading and digital outage were measured and compared to the predicted data. The validity of the modelled data was found to be a function of the accuracy of the assumed delay distribution. Furthermore, single frequency fading data are not sufficient to adequately model channel nonlinearities.

Similarly, Martin [7] performed simulations of a 2 ray channel and compared them to both laboratory simulated modem performance and to field measured modem performance. However, outage was estimated from single frequency signal level and from the difference in signal level between measurements at two frequencies. Signal measurements at two frequencies only allows estimation of linear distortions. Nonlinear distortions, such as multipath, can not be estimated from two data points. As a result, Martin underestimated system outage because the actual multipath delays were less than the simulated values.

Lavric et al. [8] simulated the effect of multipath fading on digital radio using the Rummler channel model. Only atmospheric multipath was addressed in this study. Second ray amplitude and cancellation frequency were varied while the second ray delay was fixed to 6.3 nanoseconds. This results in a non-physical channel implementation. Similarly, Kafedziski [9] used the Rummler channel model to predict the probability of bit error for

QAM radio. The relevance of accurate and physically real channel parameters was not discussed.

Hubbard and Riley [10] measured the performance of an over-water digital radio link. They found that impairments were correlated with periods of dynamic multipath conditions and that high BER was coincident with a high rate of change of estimated second ray delay. They also found that the resulting rate of change of channel distortion was faster than would be measured by traditional single frequency signal level and two frequency signal level difference data.

Two frequency response channel models and one time-response channel model were studied by Haggman [11]. He used single frequency signal level and signal level difference data to validate the results. However, the models were not extended to predict performance.

A new channel model based on digital signal behaviour was proposed by Fechtel [12]. The variation in digital receiver tap values was simulated according to a delayed pulse model of propagation. The BER was then estimated for various signal to noise ratios. The intent was to develop a simulator for the cellular radio multipath propagation environment. The study did not measure or use physical channel information, and it did not specifically address ground reflection interference for line-of-sight radio links.

1.3 Motivation

As has been shown, much of the existing work has been focussed on atmospheric multipath propagation. The early studies were limited to the effects of propagation loss and interference. Physical and statistical channel models were later developed for the characterization of the response and the statistics of the multipath channel. Both the deterministic and statistic

channel models required a priori knowledge of the channel characteristics for a specific site.

It is evident from the literature [1-12] and from the data published in this dissertation that ground reflections play an important role in the performance of line-of-sight terrestrial microwave radio systems. Furthermore, many of the experiments performed thus far have either concentrated on characterizing linear variations in channel power, or gathering statistics for radio system performance. These experiments have resulted in subsystem models for either the physical link or the channel, and have been implemented with fixed delays and/or random distributions.

In this dissertation, a comprehensive model is developed to relate the physical geometry of a specific microwave link to the performance of line-of-sight radio. It is composed of a channel and a receiver model. The channel model is based on the parameters of atmospheric refraction and ground reflection at microwave frequencies and is compared to field measurements. The receiver model is based on QAM signal theory. The two subsystem models are integrated and used to relate channel parameters to signal distortions.

CHAPTER II

FIELD MEASUREMENTS

Introduction

In this chapter the digital radio field measurements and experimental microwave line-of-sight link topography are reviewed. Measurement and collection hardware and software are described. Signal and performance measures are defined and typical field data are discussed. The field measurements are compared with other published experimental data, and will be used in chapter 4 to develop, evaluate, and validate the channel model for multipath interference.

In section 2.1 the digital radio performance characterization experiment is described. In section 2.2 the microwave link characteristics are identified. The equipment configuration is described in section 2.3, and the antenna system is described in section 2.4. The performance monitoring and data collection processes are reviewed in sections 2.5 and 2.6, and relevant radio system data are examined in section 2.7.

2.1 Field Experiment

In order to characterize and evaluate digital radio systems in operation, a field experiment was performed on an AT&T 64 QAM digital microwave radio system. Located in the Imperial Valley of California between Salton and Brawley, the link was subjected to severe radio fading year-round, thus making it an excellent test bed for studying the effects of multipath

interference on digital communication systems. The experiments were initiated in January of 1987 and continued until August of 1989 in order to observe and characterize seasonal (slow) variations.

There have been a number of papers reporting on the results of line-of-sight microwave radio experiments [14-20]. In these papers, the performance results vary; however the signal characteristics are generally consistent. As antennae type and placement, equalizing techniques, combiner algorithms, and path lengths, topographies, and climates vary widely, each system configuration and link design must be considered individually. None of these studies provided detailed real-time channel measurements for application to a channel model. In contrast, the complexity and duration of the Salton/Brawley experiment provides substantial information on the effect of multipath propagation on microwave radio.

In this experiment, one objective was to evaluate 64 QAM microwave digital radio systems operating in the 4 and 6 GHz frequency bands [13]. In the presence of severe and dynamic fading phenomena, active countermeasures were necessary in order to provide acceptable performance in digital radio systems. Countermeasures such as protection switching, equalization, and error correction systems were evaluated in the experiment. Antenna and channel protection switching systems were implemented using different combining algorithms. In addition, adaptive slope and transversal equalization, and forward error correction systems were monitored.

An additional objective was to characterize line-of-sight radio propagation in the 4 to 6 GHz frequency bands in order to design countermeasures more efficiently and to estimate digital performance more accurately. Both radio channel data and system performance data were

monitored in the 6 GHz band. Narrow band power levels, power difference ratios, and digital performance were processed for each configuration. As measurements of real-time channel data were triggered by the occurrence of degraded performance, the measured signal distortions coincided with digital impairments.

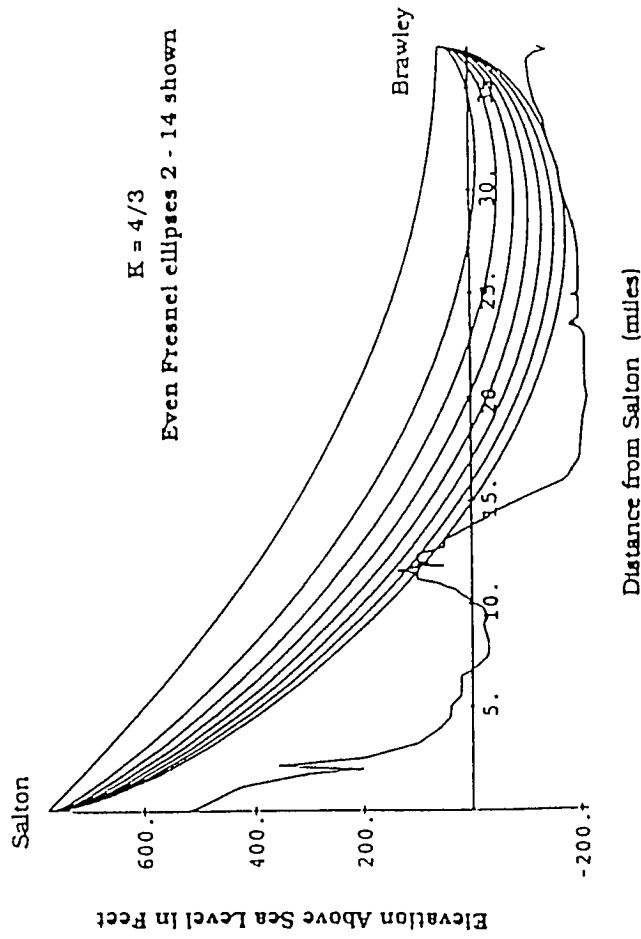
The tested link was used to develop a forward scattering model which is described in section 4.1. The critical path parameters for multipath interference are identified in the process. Some real-time fade events recorded during this experiment are used to evaluate a physical channel model in section 4.2. In addition the distributions of signal power levels and channel power differences measured during this experiment are used to evaluate the channel model in section 4.3.

2.2 Link Description

The 37 mile path between the Salton and Brawley radio stations traverses a desert area, much of which is below sea level. The path profile is shown in Figure 2-1. The area from about mid-path to Brawley is irrigated farm land and is very flat. As shown on the profile, the region around 31 miles from Salton is tangent to the 14th Fresnel zone at $K = 4/3$. This region gives rise to a dominant ground reflection at both receiving antennas. At Brawley the ground reflection is received at a nominal angle of 0.4 degrees with respect to boresight and at Salton at a nominal angle of 0.08 degrees. These angles change as the propagation effects change. Changes in local humidity produced by widespread irrigation of farmlands coupled with nocturnal and diurnal variations in temperature typical of desert areas may give rise to substantial stratification with both sub-refractive and super-refractive gradients occurring in the lower atmosphere. Combined with the

figure 2-1

Figure 2-1: Salton-Brawley California
Line-of-Sight Microwave Link Terrain Elevation Profile



dominant ground reflection present on this hop, such conditions frequently produce severe multipath fading.

2.3 Configuration

Figure 2-2 shows the typical field measurement configuration at the Brawley experimental receiver site.

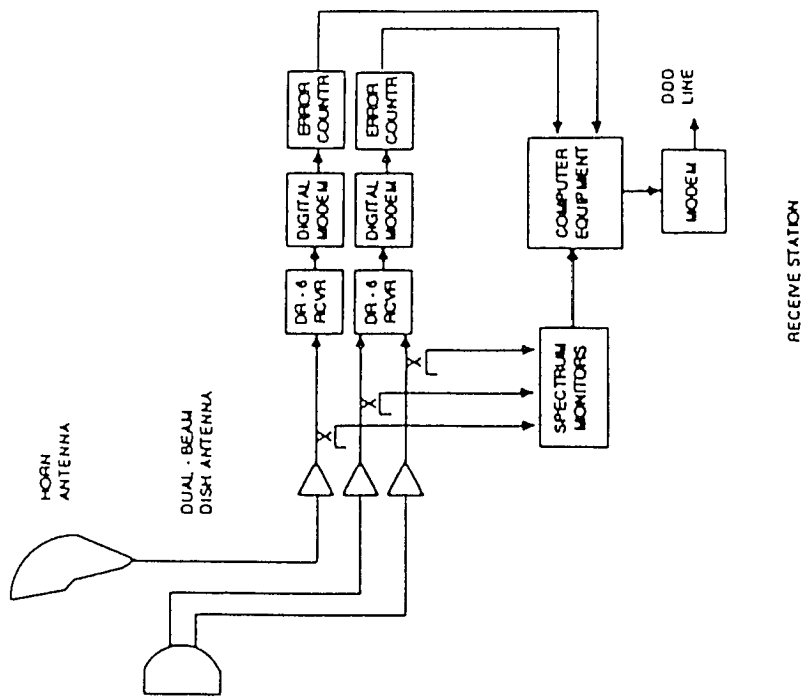
Performance experiments with AT&T digital radio began on the Salton to Brawley 6 GHz link in January of 1987 using a dual-beam **Angle Diversity** (AD) dish antenna developed for AT&T Bell Laboratories by Seavey Engineering. In this initial experiment the output of the antenna was connected to a network that generated two pairs of diversity signals. A pair of beams was displaced in the elevation plane. At the end of February the diversity receiver was connected to the main and space diversity antennae.

In September 1987 the reference unprotected pyramidal horn antenna in Brawley was modified. A new reference unprotected conical horn was installed. Before modification, the pyramidal horn antenna was connected to WC281 circular waveguide in a standard arrangement with polarization separating networks at the bottom of the tower. The new conical horn antenna was installed with polarization networks connected directly to the antenna flange. The signals were then brought down the tower using flexible elliptical waveguide. This change in the main reference antenna substantially improved the performance of the unprotected receiver. Multimoding occurred in the horn antenna [21-24]. In this scenario, echoes propagated in the circular waveguide and their long delay times degraded the system performance.

In April of 1988 the frequency and the polarization of the 6 GHz radio channel from Salton to Brawley were changed. Also **Radio Frequency** (RF)

figure 2-2

Figure 2-2: Digital Radio Field Measurement Equipment Block Diagram



spectrum monitors were introduced so that each antenna beam could be monitored before selection by the diversity combiner in the digital radio receiver. A pseudo-random bit stream was generated by a test-pattern generator. This was applied to an interface board which supplied the transmitter. The receiver, using another interface board, directed the received bit stream to an error detector. The errors were monitored with a counter. In November of 1988 data collection on the dual-beam AD dish at Brawley was replaced with monitoring of a standard **Space Diversity** (SD) implementation. In March of 1989 the receiving modems were re-configured. The custom interface boards were replaced with standard 45 Mbs (DS-3) interfaces. Error performance was measured by monitoring bit errors supplied by the digital modems.

The Brawley to Salton 6 GHz experiments started in May of 1988. The only major equipment change in this direction of transmission occurred in November of 1988 when monitoring of the two-antenna AD system with **Vertical Offset** (VO) was terminated and monitoring of space diversity began. This experiment used complete digital terminals with DS-3 test set inputs. Error performance was measured by monitoring bit errors supplied by the digital modems. The modems were re-configured for standard DS-3 transmission in November of 1988.

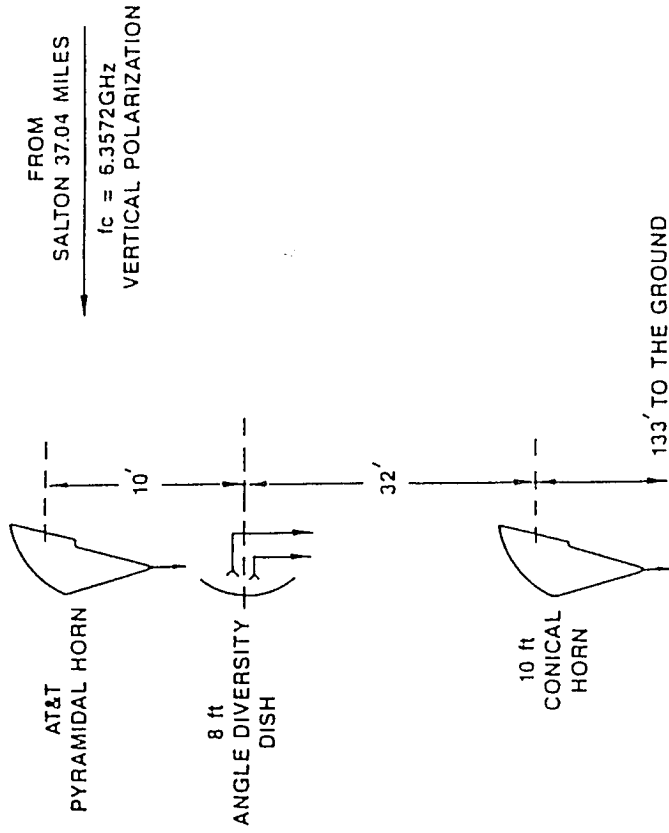
2.4 Antenna Systems

Figure 2-3 shows the spatial relationships of the antennas on the towers at Brawley and Salton, respectively.

The dual/tilted beam AD parabolic dish uses two feeds displaced above and below the focal point to create two beams separated in the elevation plane by 1.7 degrees. These 8 foot dishes are single-band antennas capable of being

figure 2-3

Figure 2-3: Digital Radio Antennae Configuration



operated with both vertical and horizontal polarization. The crossover point of the two beams is approximately 6 dB down from the gain at each beam peak. The antenna is oriented to provide equal nominal receive signal levels from the two beams.

Measurements made in Gainesville Florida showed that angle diversity with two tilted parabolic dish antennae having a vertical separation provided better performance than when the two beams had no vertical separation [17]. The VO-AD configuration was tested in Salton between May and October of 1988. Two 8 foot high performance dish antennas were used. The upper dish antenna was tilted above boresight by 0.85 degrees and the lower antenna, which was 12 feet below, was tilted below boresight by 0.85 degrees. The VO-AD antenna beams were thus oriented in the same directions and had the same beam widths as those of the AD antenna which was simultaneously monitored on the tower at Salton.

Space diversity was implemented using horn reflector antennas with a 42 foot vertical spacing at Brawley and a 36 foot vertical spacing at Salton. In both locations the SD antenna was a conical horn and the primary (unprotected) antenna was initially a pyramidal horn.

2.5 Performance Monitoring

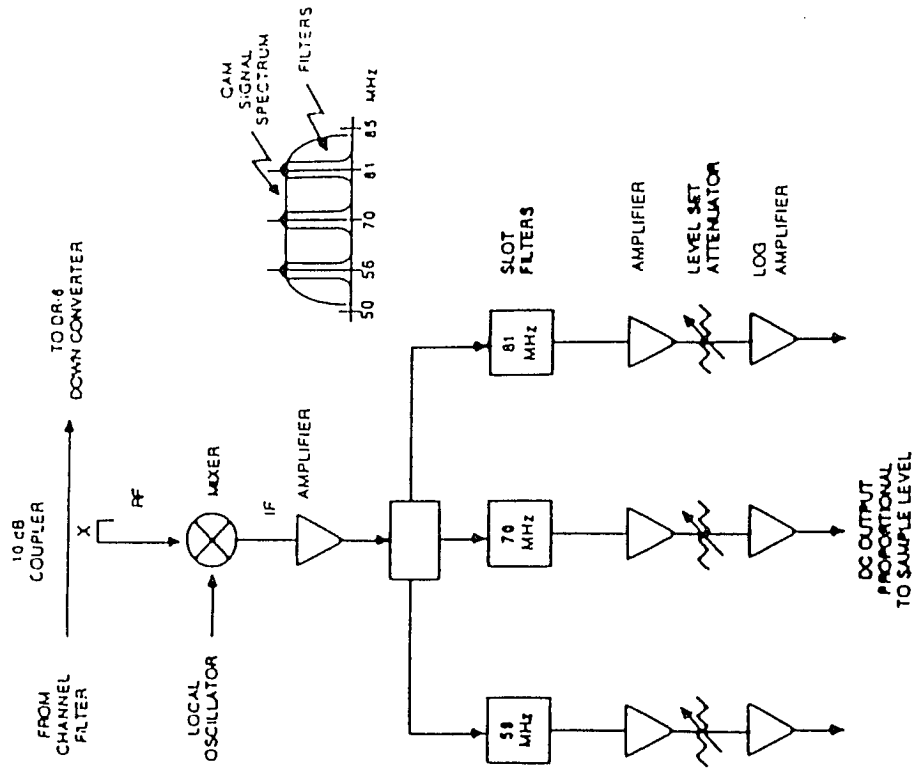
There were four time periods of data for the Salton to Brawley 6 GHz experiment: 9 April - 30 October 1988, 1 January - 19 February 1989, 4 April - 16 May 1989, and 1 June - 31 August 1989. There were four time periods of data for the Brawley to Salton 6 GHz experiment: 27 May - 31 October 1988, 16 December 1988 - 19 February 1989, 7 April - 15 May 1989, and 1 June - 31 August 1989.

The RF spectrum monitor block diagram is shown in figure 2-4. The signal to be monitored is coupled off after the channel dropping bandpass filter and then mixed down to the **Intermediate Frequency (IF)** of 70 MHz. After amplification the signal is split and applied to three 1 MHz wide bandpass filters. The filter outputs are then amplified and fed to a log amplifier where the digital spectrum signal power is detected and transformed into a dc voltage. The slot filter frequencies shown are those chosen for the RF channel in the 6 GHz band. The IF spectrum monitor does not have a mixer and the signal to be monitored is coupled off using a hybrid at IF just before the **Automatic Gain Control (AGC)** amplifier. The spectrum monitors are calibrated by applying a digital spectrum with known power levels and measuring the corresponding DC output voltages.

Single Frequency Fade (SFF) and **In-Band Power Difference (IBPD)** statistics are given in the form of **Time-Below-Level (TBL)** curves. Log(seconds) versus fade depth in dB, and Log(seconds) versus IBPD in dB are shown for each direction: Salton to Brawley, and Brawley to Salton. The SFF and IBPD statistics were continuously monitored and recorded at a nominal sample rate of 8 times per second while the system was operative. Data affected by equipment malfunction, craft activity or software maintenance were excluded. The time periods given for the various antennas and locations reflect consecutive blocks of time during which the accuracy of the data was verified and the configuration of the equipment was consistent. During March of 1989, software at all sites was modified to include a second of measurement data prior to the beginning of each error event. At the end of May, 1989, software was again modified to record received signal level in dBm from each filter. Prior to this, all measurements were recorded as fade depth

figure 2-4

Figure 2-4: RF Spectrum Monitor Block Diagram



in dB relative to the nominal received signal level. All channel monitors at the sites were re-calibrated at this time.

The performance monitor block diagram is shown in figure 2-5. Initially, a pseudo-random bit stream was generated using a test-pattern generator. This was applied to an interface board which supplied the transmitter. The receiver, using another interface board, provided the received bit stream to an error detector. The errors were monitored with a frequency counter which was polled by a remote computer. Eventually, the receiving modems were re-configured for transmission of 3 standard DS-3 signals in each direction. Error performance was then measured by monitoring bit errors supplied by the digital modems.

At each location, bit error ratio data are obtained from transmission analyzers by the remote computers. These data were then recorded sequentially into data files which are saved on site. At the end of each day, the previous 24 hours of data were retrieved by the polling computer at the Merrimack Valley laboratory. The data were processed for performance measures and examined on a daily basis. This information included bit error ratio (BER), errored seconds (ES), severely errored seconds (SES), unavailable seconds (UAS), loss of frame seconds, and degraded minutes (DM).

2.6 Data Collection

Two types of data were collected on each experiment. Event data was triggered when bit errors were being made and was used to analyze the operation of the radio system in the presence of multipath fading. Signal level data were collected continuously and were used to determine the frequency and nature of the fading on the hop and the performance of the antenna systems independent of the rest of the radio receiver.

figure 2-5

Figure 2-5: Field Experiment Block Diagram

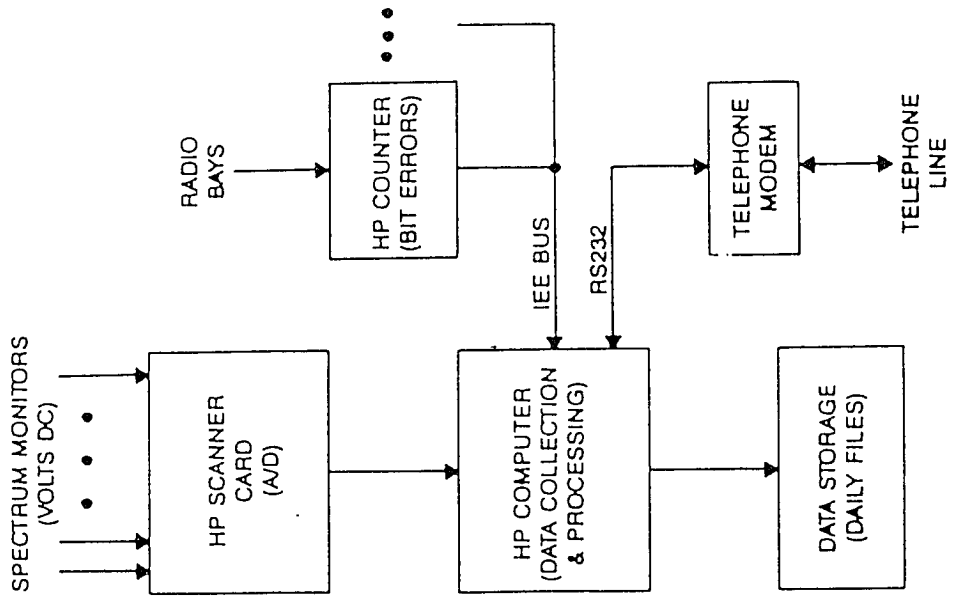


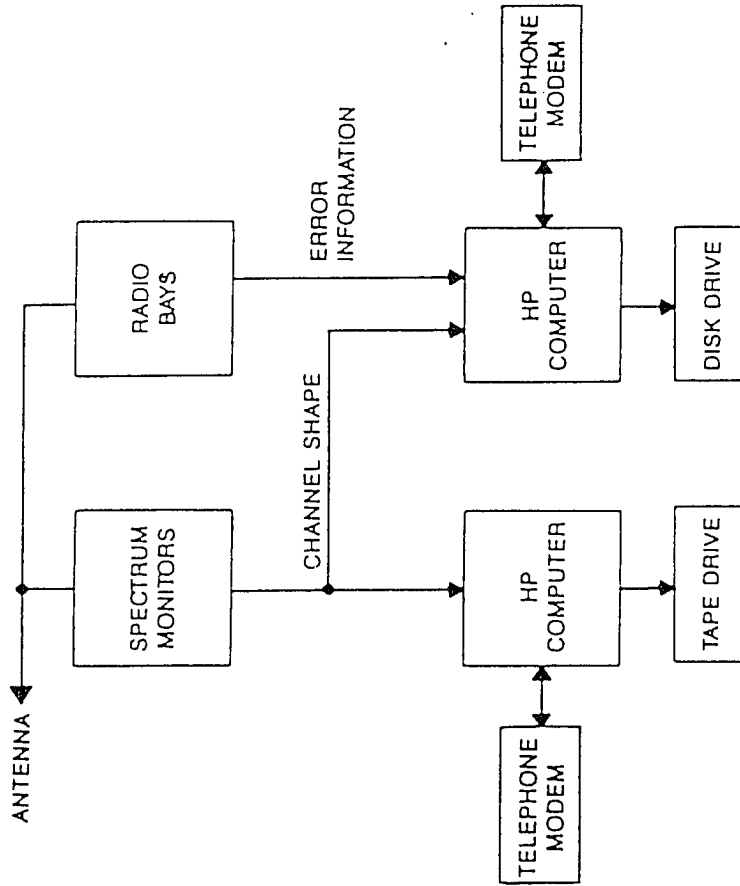
Figure 2-6 shows the data collection configuration for the Brawley DR-6 experiment after the RF spectrum monitors were installed. The combiner beam selection was monitored by connecting to the front panel display circuit. For the Salton DR-6 experiment, an error detector was not used and the bit error counter was connected to the bit error jack on the digital receiver. In addition, a second counter was used to record counts of frame losses. The counters were polled each second via an IEEE bus and a change in a counter reading triggered the recording of an event with bit errors. During an event, all data were recorded at approximately 8 times per second which permitted a detailed analysis of the propagation conditions during the time which errors occurred. In March of 1989 the monitoring programs were changed to record all the data for the one second period before errors were started as well as for the one second period after errors ended. Also, the sample rate of the counters was increased to approximately 3 times a second to better capture the beginning of an event.

Cumulative statistics were recorded by continually accumulating received SFF and IBPD data from the channel monitors. The IBPD was taken as the maximum difference in power level between the three channel filters (22 MHz separation between the outer samples at 6 GHz).

The data were transferred to Merrimack Valley Bell Laboratories for processing and analysis. Data associated with equipment malfunctions or local maintenance activity were eliminated during the processing.

figure 2-6

Figure 2-6: Remote Data Collection Flow Chart



2.7 Summary

For each experiment the radio equipment was tested using standard network practices [25]. The margins of error-free performance were both predicted and measured over-the-air. Values (in dB) are listed in Table 2-1. For each receiver location, the margins are listed according to antenna type, date of measurement, and signal polarization. The **Carrier to Noise ratio (C/N)** is the ratio of the signal power to the thermal noise power in the same channel. The predicted and measured thermal fade margins were similar. The **Carrier to Interference ratio (C/I)** is the ratio of the signal power to any interference power in the same channel. There were no interference sources measured or identified on the link.

Signal power level data were measured in a radio channel in real time at three frequencies during impaired digital performance. The signal power level data were referred to as the single frequency fade (SFF) data. Three 1 MHz bandpass filters were placed in the digital radio channel. The filter center frequencies were offset to 0 +/- 11 MHz from the channel center. The fade data represented the level in dB that the measured signal was below nominal.

The signal level data measured at three frequencies also allowed the determination of a nonlinear channel response. The maximum difference between the three SFF measurements in a channel at any given instant was recorded and referred to as the in-band power difference (IBPD). These shape data represented the maximum amount of linear slope in dB that was estimated for the channel.

The SFF data will be used in section 4.2 to compute the values of multipath channel model parameters. The probability distribution functions

for SFF and IBPD which were accumulated in the field experiment will be used in section 4.5 to verify the performance of the channel model for digital radio systems.

**TABLE 2-1
SIGNAL MARGINS**

<u>Site</u>	<u>Date</u>	<u>Polarization</u>	<u>Thermal Noise</u>		<u>Interference Noise</u>
			C/N		C/I
<u>Antenna</u>			<u>Calculated</u> (dB)	<u>Measured</u> (dB)	<u>Measured</u> (dB)
<u>Brawley</u>					
Main	3/87-8/87	Vertical	38	41	>65
Space Diversity		Vertical	38	39	>63
AD (V1)	3/87-10/88	Vertical	37	36	50
AD (V2)		Vertical	37	32	42
Main	9/87-4/88	Vertical	42	40	>65
Main	4/88-11/88	Horizontal	43	42	52
AD (H1)		Horizontal	37	36	41
AD (H2)		Horizontal	37	35	46
Main	11/88-8/89	Horizontal	45	41	47
Space Diversity		Horizontal	45	41	50
<u>Salton</u>					
Main	5/88-8/89	Vertical	43	48	70
AD (V1)		Vertical	33	38	>62
AD (V2)		Vertical	33	36	56
Space Diversity	11/88-8/89	Vertical	45	49	>73

CHAPTER III

SYSTEM MODEL

Introduction

In this chapter a system model for terrestrial line-of-sight QAM digital radio is defined. For simplicity, it is assumed to consist of three linear and time-invariant subsystems, namely, the transmit filter, the channel filter, and the receive filter. The overall system response is generated from a cascade of these subsystems. In section 3.1 the digital radio system and response are described. In section 3.2 the transmit and receiver filter models are defined. In section 3.3 the channel model is introduced and in section 3.4 the receiver model is discussed. In section 3.5 the overall digital radio system model is reviewed.

3.1 Digital Radio Communication System

The digital radio communication system consists of pulse shaping and sampling functions. Its response in the time and frequency domains is a function of the pulse shaping and sampling, the transmission path delay, and the channel distortions. For the purposes of this study, the transmitter and receiver are assumed to be linear and time-invariant subsystems. A shift in time of the input signal results in a corresponding shift in time of the output signal. Also, the additive and scaling properties of superposition apply to the outputs with respect to the inputs. The transmission path is thus treated as a filter having a linear and time-invariant response.

In this analysis, the digital radio communication channel is characterized by recording a series of simultaneous signal power measurements at three fixed and equi-spaced frequencies in the channel during periods of distortion, as was discussed in sections 2.5 and 2.6. Atmospheric phenomena are time-variant, and the resulting dynamic frequency response of the channel is approximated by the series of frequency response measurements in time. However, the time duration of each individual frequency response measurement is much less than that required for significant changes in atmospheric radio propagation conditions. The channel is therefore linear and time-invariant over the duration of each individual frequency response measurement.

The radio system is shown in figure 3-1. It consists of the **Transmitter** (XMT), the transmission channel, and the **Receiver** (RCV). The system under examination is an AT&T DR6-30-135 RT. It uses a 64 QAM scheme in the 6 GHz band. The channel bandwidth is approximately 25 MHz and the symbol interval is approximately 40 nanoseconds.

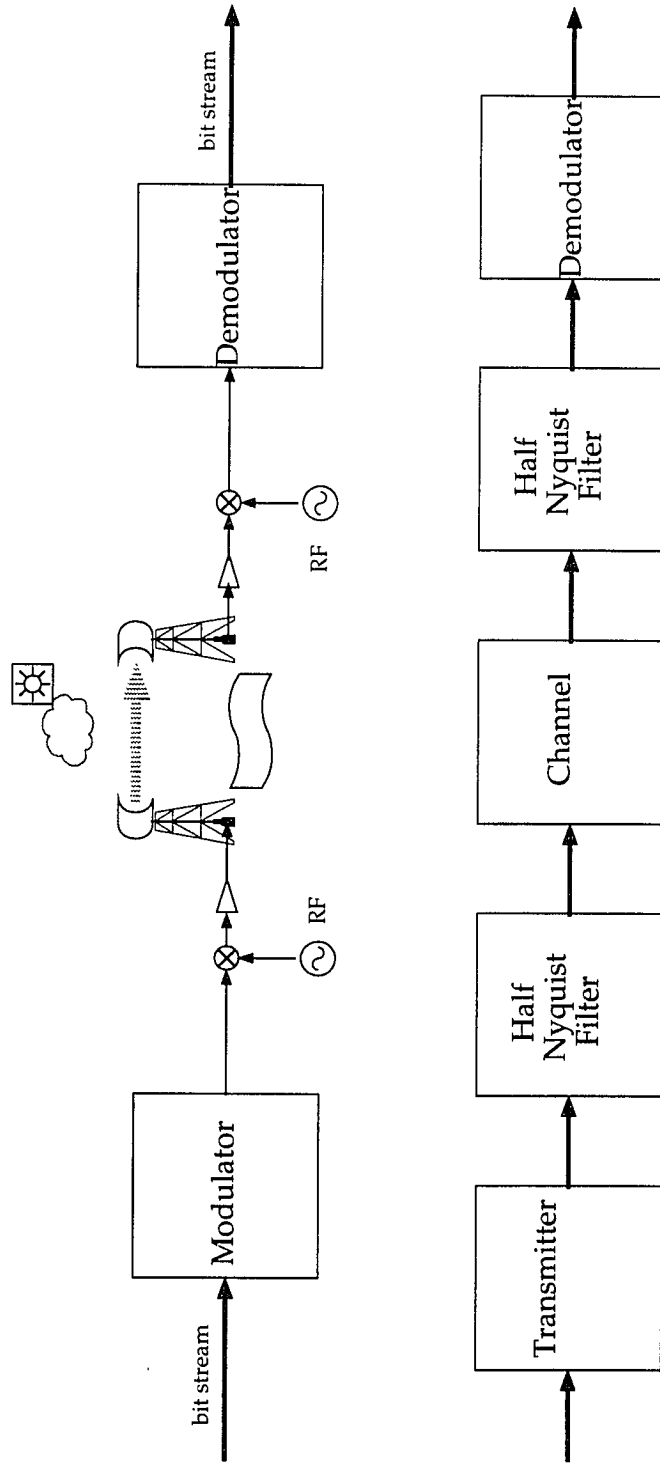
The system response to the input $x(t)$ in the frequency domain is the product of the transmit signal frequency characteristic $X(f)$, the transmit and receive filter transfer functions $W_x(f)$ and $W_r(f)$, and the channel transfer function $H(f)$,

$$Y(f) = X(f) W_x(f) H(f) W_r(f) \quad (3-1)$$

The system response to the input $x(t)$ in the time domain is the convolution of the transmitted signal $x(t)$, the transmit and receive Nyquist filter responses, $w_t(t)$ and $w_r(t)$, and the channel response $h(t)$,

figure 3-1

Figure 3-1: Digital Radio System Block Diagram



$$Y(f) = X(f) W_t(f) H(f) W_r(f) R(f)$$

$$y(t) = x(t) * w_{tx}(t) * h(t) * w_{rx}(t) * r(t)$$

$$y(t) = x(t) * w_x(t) * h(t) * w_r(t). \quad (3-2)$$

The frequency responses in (3-1) are the Fourier Transforms of the time responses in (3-2).

3.2 Filter Models

The DR6-30-135 transmitter produces a 40 nanosecond pulse. The pulse shape, shown in figure 3-2a, corresponds to a 25 MHz rectangular frequency response as shown in figure 3-2b. In the digital radio system as shown in figure 3-1 there are two Nyquist filters. Each implements a transfer function which is ideally equal to the square root of the overall Nyquist filter shape. In practice the filters are not identical. Since the system is linear and time invariant, the filters may be combined into a single transfer function for simulation purposes. The overall Nyquist filter time response is shown in figure 3-3a, with the frequency shape shown in figure 3-3b. The Nyquist filter response may be expressed as the product of the transmit and receive filter functions $W_x(f)$ and $W_r(f)$,

$$W(f_n) = W_x(f_n) W_r(f_n) \quad (3-3)$$

The normalized frequency f_n is the ratio of the signal frequency f to the Nyquist frequency f_s ,

$$f_n = \frac{f}{f_s} \quad (3-4)$$

The overall filter characteristic is represented by

figure 3-2a

Figure 3-2a: Time-Domain Transmitted Signal

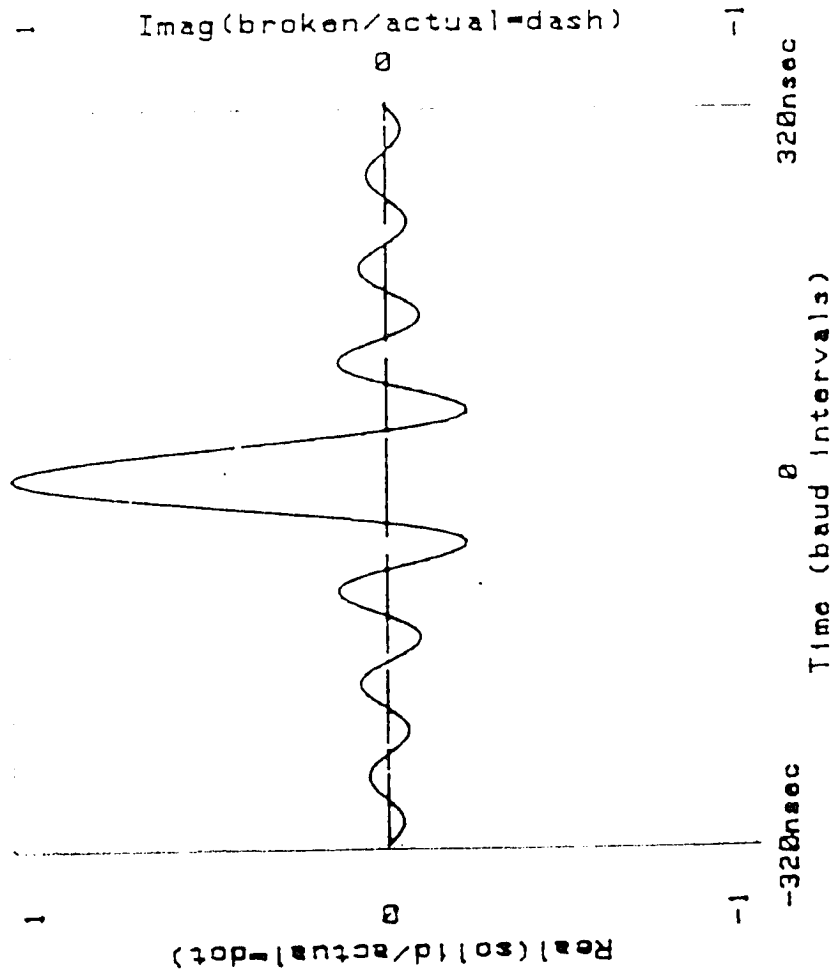


figure 3-2b

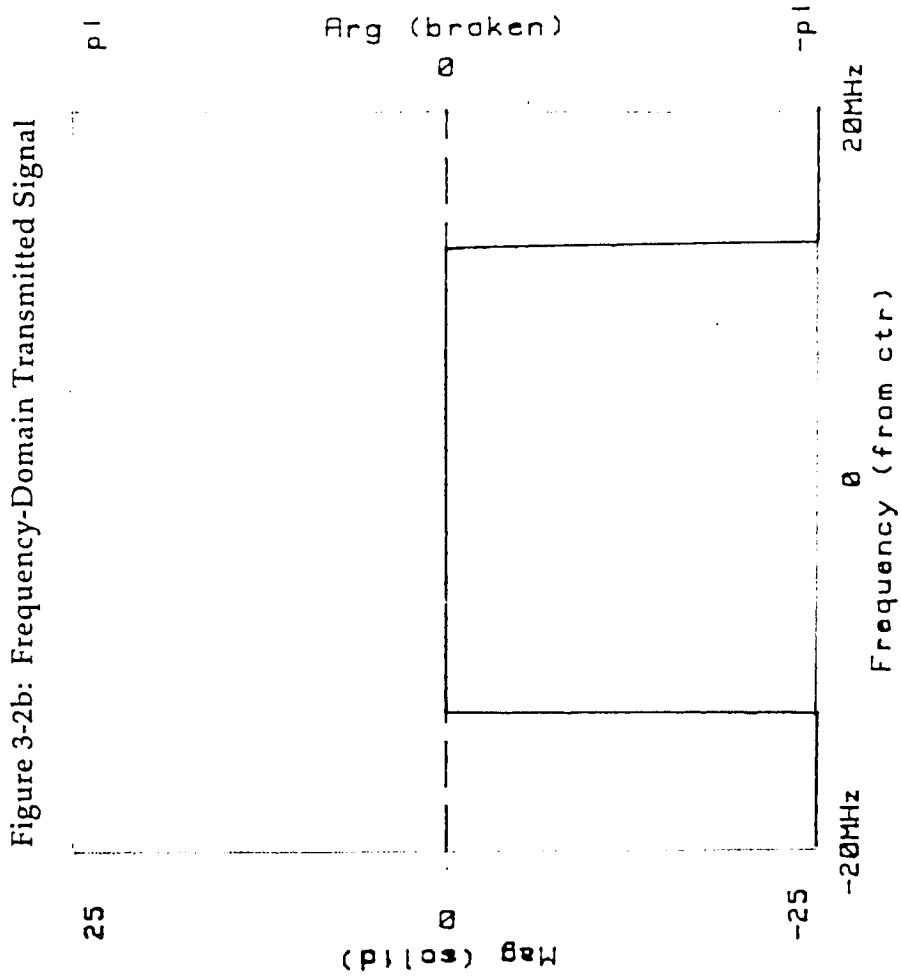


figure 3-3a

Figure 3-3a: Time-Domain Nyquist Filter Response

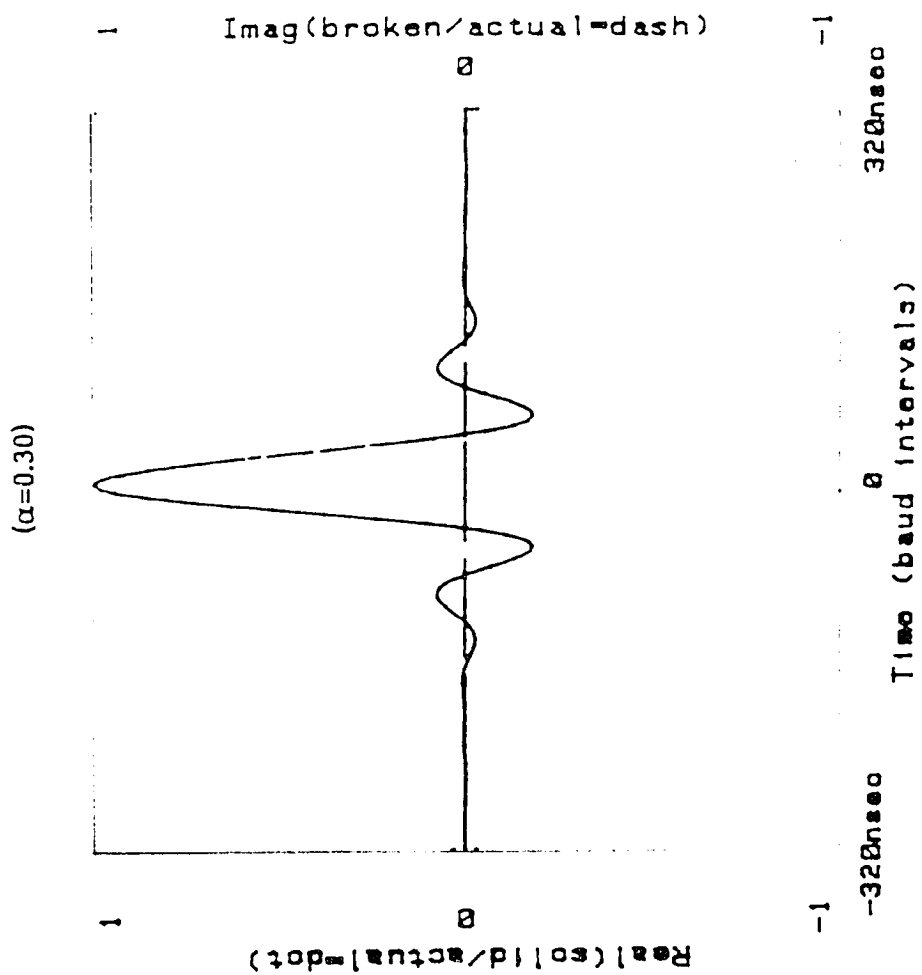
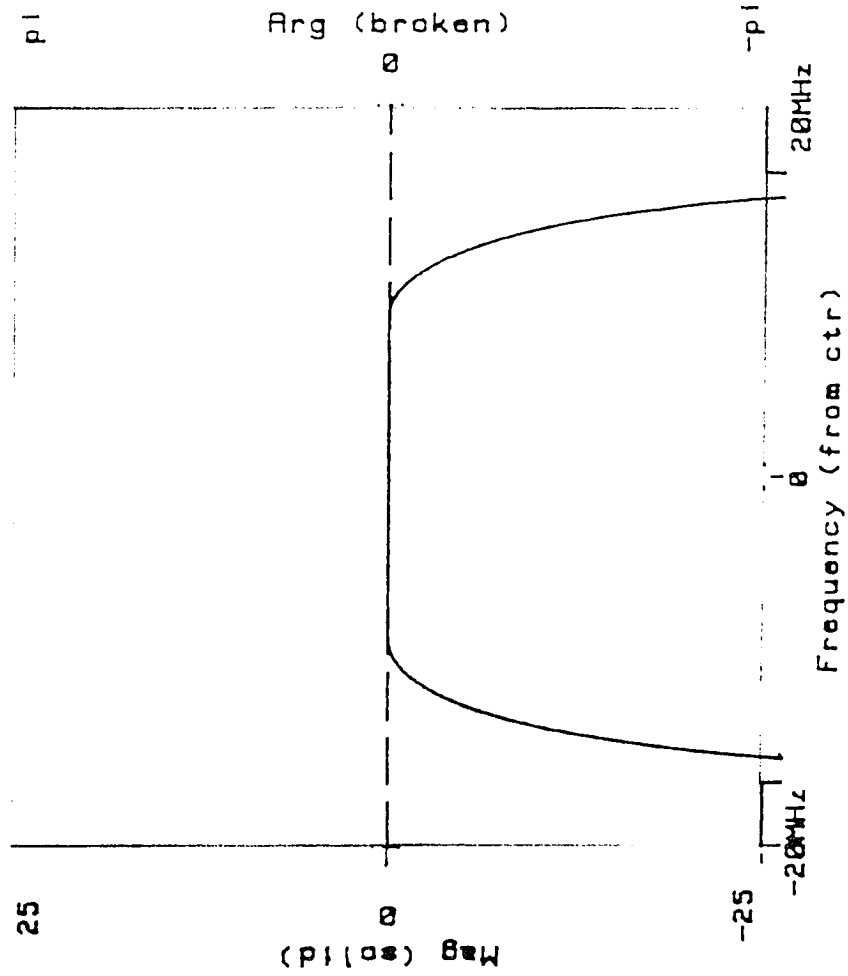


figure 3-3b

Figure 3-3b: Frequency-Domain Nyquist Filter Response

($\alpha=0.30$)



$$W(f_n) = 0, |f_n| \geq (1+\alpha), \quad (3-5a)$$

$$W(f_n) = \frac{1}{2} [1 - \sin(\frac{\pi(f_n-1)}{2\alpha})], (1-\alpha) \leq |f_n| \leq (1+\alpha), \quad (3-5b)$$

and
$$W(f_n) = 1, 0 \leq |f_n| \leq (1-\alpha), \quad (3-5c)$$

where α is the rolloff parameter [26]. For this system simulation α is 0.3.

3.3 Channel Model

Based on the nature of forward scattering on the terrestrial microwave link, a forward multipath model is developed for the radio channel. The received signal is approximated as the superposition of a direct signal and a second signal which is a reflected version of the direct signal. The model allows for simulation of a varying radio channel by selection of two ray parameters.

Phasors are used to approximate the vector addition of two interfering signals in a bandlimited channel. The two ray channel response is composed of a direct signal $\underline{\alpha}$ and a secondary (delayed) signal $\underline{\beta}$. The channel response in the presence of multipath interference is then approximated as the vector sum of these two phasors. The resultant phasor has magnitude σ and phase ϕ that are functions of the signal and interference vectors $\underline{\alpha}$ and $\underline{\beta}$,

$$\sigma e^{j\phi} = \alpha e^{j2\pi f\tau_\alpha} - \beta e^{j2\pi f\tau_\beta} \quad (3-6)$$

where τ_α is the propagation delay of the first ray and τ_β is that of the second. Normalizing the phase relationship to that of the direct ray results in a generalized representation for the composite signal,

$$\sigma e^{j\phi'} = \alpha - \beta e^{j2\pi f\tau'} \quad (3-7)$$

where the composite phase is

$$\phi' = \phi - j2\pi\tau_\alpha. \quad (3-8a)$$

delay difference is

$$\tau' = \tau_\beta - \tau_\alpha. \quad (3-8b)$$

A physical illustration of multipath propagation is shown in figure 3-4, where a secondary ray is reflected from the ground and arrives at the receiver after a delay of τ relative to the direct ray.

One of the causes of broad band attenuation and delay distortion is multipath propagation. The result of multipath propagation is a superposition of two or more delayed replicas of the same transmitted signal at the receiver. If the delayed replicas are out-of-phase, the subsequent cancellation results in signal loss.

For given amplitudes and delays, the composite signal has been written as a function of frequency as in equation (3-6). However, for broad band channels, signal cancellation is also a function of the delay difference as was discussed above. For signalling at a fixed bit rate (or in a fixed bandwidth),

there are discrete delay differences (odd integer half periods) yielding signal cancellation. If delay difference and frequency of cancellation are de-coupled, the two phasor composite of equation (3-6) may be recast as a two ray superposition. In a communication channel having a bandwidth much narrower than the overall multipath channel, the delay difference is approximately constant with respect to frequency. By assuming a fixed delay difference as a function of frequency, the two ray cancellation is expressed as a function of offset frequency from a given cancellation frequency. Independent selection of both delay and cancellation frequency are allowed with this model.

From equation (3-7), the generalized transfer function of the two ray model normalized in frequency for a narrowband channel is

$$H(f-f_0) = \alpha - \beta e^{j2\pi(f-f_0)\tau} \quad (3-9)$$

The parameter α , represents the strength of the direct signal. The parameter β , represents the strength of the second path signal. The delay difference τ , represents the delay of the second path signal with respect to the direct signal. The f_0 is the frequency of the signal cancellation. The expression $f-f_0$ represents the offset of the observation frequency from the frequency of the minimum signal power. The frequency of the signal power minimum is commonly referred to as the cancellation or "notch" frequency. It corresponds to the location of minimum signal power in the frequency domain. Strong second ray interference results in substantial signal cancellation. Both the signal power loss at a frequency f (narrow band) due to

Figure 3-4: An Illustration of Multipath Propagation Using Two Rays

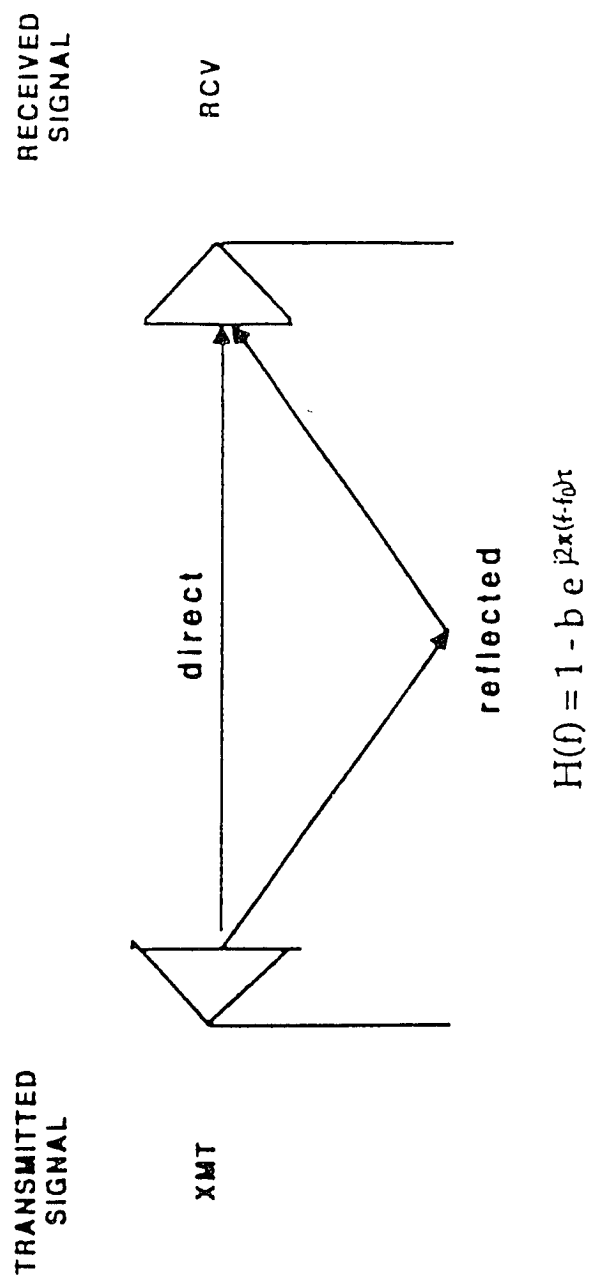


figure 3-4

f_0 , and the distortion across the channel (broadband) due to τ , cause impaired communication in the affected channel, as described earlier.

Line-of-sight microwave radio propagates in a half-space that is bounded by land or water. The energy reflected from the earth varies, depending upon the topology and the propagation characteristics of the lower atmosphere. Fluctuations in the refractivity of the lower atmosphere cause variations in the relative strength of the ground reflection β . The secondary delay τ , or path length also varies.

The transfer function of the narrowband two ray model in equation (3-9) may be expressed in terms of broadband and narrowband attenuation as

$$H(f-f_0) = a (1 - b e^{j2\pi(f-f_0)\tau}) \quad (3-10)$$

where the parameter a represents the broadband or "flat" attenuation, and the parameter b represents the strength of the secondary signal normalized to the direct. When $f = f_0$, $H(f-f_0) = a (1-b)$, where $(1-b)$ represents the maximum IBPD, and a represents the signal power at the minimum.

In order to focus on the channel slope only, the transfer function of equation (3-10) may be scaled by the broadband attenuation resulting in the normalized two ray model,

$$H(f-f_0) = 1 - b e^{j2\pi(f-f_0)\tau} \quad (3-11)$$

with the parameters as in equation (3-10). As before, the parameter b represents the strength of the secondary signal. In this case the direct signal is the reference, and the second signal is normalized to it. At the minimum

($f=f_0$), the expression $(1-b)$ represents the "cancellation depth" or the maximum IBPD.

There are two possible scenarios for dynamic multipath fading as modelled by two rays in this study. There may be a second signal of varying strength, or a second path of varying delay.

For the case of varying second signal strength, b is allowed to change. However, the offset notch frequency $f - f_0$, broadband attenuation a , and delay τ of the second signal with respect to the direct signal are fixed. The result is a changing notch depth. The process represents a propagation environment where there is a boundary that is stable in position as a function of the propagation wavelength. However the reflected energy is not stable in strength. A stable refractive index gradient in the lower atmosphere will give rise to a constant secondary path delay. A discontinuity or abrupt change in the refractive index gradient at some fixed altitude may give rise to refracted rays. An example would be the formation of a homogeneous layer in the lower atmosphere. Such a layer would be transient in nature and vary in height and density. On the other hand, the formation of a coherent reflecting area on exposed ground is a much more predominant and stable source of reflected energy. As the ground becomes more coherent in its reflectivity, there is an increased reflection coefficient. The result is a stronger secondary ray. Changes in the effective bending of rays within the lower atmosphere may cause focusing or defocusing effects. The result is a modulation of the secondary ray strength.

For the case of the second path of varying delay, the reflection phase is allowed to change. The result of phase or delay change is a variation of the exponential term $\tau(f - f_0)$. In reality, the secondary ray delay τ is varying.

However, the phase change is also reflected in variation of the signal power minimum f_0 . The relative change in delay is very small and so it is treated as a constant. A boundary having a stable reflectance amplitude but an unstable position as a function of the propagation wavelength would cause notch movement. Non-stable path length is very likely a result of a changing refractive index gradient in the lower atmosphere. This effect modulates the path length of a signal reflected from the ground.

In a minimum phase state, a notch offset frequency sweeping upward represents an increasing broadband notch separation. The result is a decreasing positive second ray delay. On the other hand, for the non-minimum phase state a notch offset frequency sweeping upward represents a decreasing negative second ray delay. The direction of change in delay (less negative) is opposite to the direction of change for a minimum phase state (less positive). A mirror image relationship results for second path delay as a function of channel phase and cancellation frequency. A minimum phase fade with increasing notch frequency has a second path delay gradient that is equivalent to that of a non-minimum phase fade with decreasing notch frequency.

3.4 Receiver Model

The QAM digital receiver model block diagram is shown in figure 3-5. The model for the QAM receiver takes the channel output at IF, and performs the **Carrier Detection (CD)** and the **Timing Recovery (TR)** functions on the resulting signal. In the AT&T 64 QAM receiver, there are two stages of equalisation; the **Adaptive Slope Equalizer (ASE)**, and the **Digital Transversal Equalizer (DTE)**.

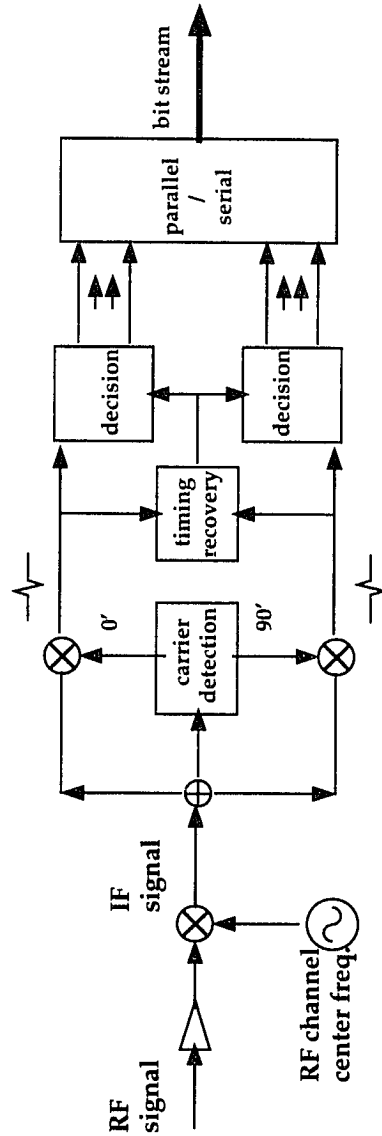
In addition, there are two feedback control paths from the **Digital Transversal Equalizer** (DTE); one is to the **Demodulator** circuit (DEMOM) for CD, and the other is to the **Analog to Digital Converter** (A/D) for TR. The receiver functions are discussed in chapter 6.

3.5 Summary

A model for the digital radio transmission system is developed which consists of transmitter, channel, and receiver filter functions. The transmitter and receiver are signal shaping filters. Using a two ray model, the channel is treated as a variable notch filter. Channel distortions are characterized in chapter 4. The overall system is linear and time-invariant, so that the effect of channel distortions is cascaded to the receiver where digital performance is estimated. The effects of distortions on the receiver are analyzed in chapter 5. System performance in the presence of distortions is evaluated in chapter 7.

figure 3-5

Figure 3-5
QAM Digital Receiver Block Diagram



CHAPTER IV

RADIO CHANNEL MODEL

Introduction

In this chapter, a channel model is developed that takes into account the cancellation effect of coherent interference. It includes the physical aspects of microwave propagation in the lower atmosphere. The model is verified by comparing its characteristics to real channel measurements. It is then incorporated into the overall system model.

In section 4.1, the principles of line-of-sight microwave communication are discussed, and other modelling techniques are reviewed. In section 4.2, a forward multipath model is developed to predict multipath parameters from the link geometry. In section 4.3, the multipath channel model is inverted to recover the multipath parameters from channel measurements. In section 4.4, a statistical behaviour of multipath propagation is simulated. In section 4.5, the channel modelling techniques and results are reviewed.

4.1 Overview of Line-of-sight Microwave Radio

The radio channel on a microwave radio link is the free-space line-of-sight path between the transmitting and receiving antennae. In the 6 GHz band, as described in chapter 2, path lengths vary from 5 to 95 miles. Propagation of electromagnetic waves with centimeter wavelengths may be

approximated by geometrical optics techniques at these distances. Signal loss is mainly due to spherical spreading of the wavefront.

Atmospheric anomalies lead to signal distortion. These are generally caused by variations in the index of refraction in the lower atmosphere. The lower atmosphere may be viewed as a lossy waveguide when the gradient of the index of refraction is non-linear. A change in the gradient may cause defocusing or additional spreading of the wavefront. This results in additional attenuation of the signal. On the other hand, a change in the sign of the gradient may cause focusing or concentration of the wavefront. This results in signal superposition or surging. These phenomena are somewhat unusual and infrequent. Focussing is generally associated with atmospheric ducting, which requires very stable and enduring weather conditions. Atmospheric phenomena by themselves are not the dominant causes of impairment in digital radio systems and are not addressed in this study.

The earth is the lower boundary on a terrestrial microwave link. The transition in impedance from air to ground, or air to water, provides a reflection coefficient of near unity for the airborne signal. The likelihood of signal reflection from ground or water is very high. The fixed nature of the earth makes a stable reflection possible in the presence of stable weather conditions, giving rise to coherent interference. Coherent interference results in substantial impairment to a digital communication system. So there is a pressing need for the development of an appropriate channel model to analyze the performance of the digital modem.

Of the many techniques that have been used to study the radio propagation in the lower atmosphere, the most relevant are the diffraction models, guided wave models, refraction models, and channel models.

Diffraction models compute the field at terrain obstacles and transitions. Guided wave models treat the link as a lossy waveguide. Refraction models use ray tracing to estimate the received signal. Channel models use parameters, which may or may not be related to propagation, to simulate the communication channel.

The Geometrical Theory of Diffraction has been applied to radar propagation modelling near airports [27]. It uses Huygens technique for equivalent source modelling above knife edges. The path terrain profile is estimated as a series of plates and edges. The variations in topography over a long link are not preserved by the plate/edge estimated profile. While valuable for predicting field strength near obstacles in the propagation path, it cannot be used to model refracted and/or reflected signals for point-to-point communication links.

Waveguide models have also been developed for propagation in the lower atmosphere [28]. These examine the modes of propagation as solutions to the wave equations in the lower atmosphere. The solutions are dependent on the index of refraction, as it determines the upper and possibly lower boundaries of the waveguide. This approach has been instrumental in understanding the effect of ducting phenomena. However, as with the other methods, it does not lend itself well to digital performance prediction.

Ray tracing has been used in many studies to estimate radio propagation loss [29]. It is an invaluable tool for studying the effects of refraction on wavefronts. Rays are drawn from the transmitter to the receiver as functions of launch and reflection angles. These angles are modified by the index of refraction. However, this method does not provide a field-strength solution. The radio signal does not propagate as a finite

number of rays. Ray-tracing, at best, estimates a piecewise linear wavefront. Since it does not lend itself well to correlation with digital performance, it is not appropriate as a system model.

Channel modelling has been a commonly used approach for estimating the performance of radio systems [30-33]. Both physical and mathematical models have been developed to characterize the behaviour of radio channels in the presence of multipath fading. Random variations of the values of model parameters are used to statistically simulate channel distortion. The resulting channel performance can be used to predict overall system performance. The reliability of statistical models depends on the validity of the model and on the accuracy of the parameters. Furthermore, if the channel model parameters cannot be related to digital signal performance, then the channel model is not appropriate as part of an overall system model.

The purpose of this chapter is to develop and define a channel model for eventual integration into the overall system model. Radio propagation is reviewed and common modelling techniques are surveyed. The experimental link design and data are analyzed in order to characterize channel distortions and to compare modelled and measured channel and performance data. A forward multipath model is applied to identify terrain parameters which cause interference to terrestrial digital microwave radio links. An inverse multipath model is determined for extraction of forward multipath model parameters from measured channel data. In addition, a statistical model is used to examine distributions of the forward multipath parameters and to compare the modelled and measured channel. The objective is to characterise the multipath interference that may be induced by ground reflections on a typical digital radio link. This characterisation will

provide a better understanding of the nature and likelihood of channel distortions due to multipath interference. The radio channel model developed in this chapter is a subsystem of the overall digital radio system model.

4.2 Forward Multipath Model

In this section, a forward multipath model is developed by examining transmission of the signal from the source over the air to the receiver. The terrain is treated as a piecewise linear scatterer that may give rise to many reflected signals at the receiver and interfere with the direct signal. The lower atmosphere variations are expressed as changes in the gradient of the index of refraction. They are treated as displacement of the propagation paths for the direct and reflected rays. The principles of geometrical optics are used to compute reflected rays. The reflecting areas of ground and their respective parameters are identified by the simulation. These are compared to measured data from an experimental microwave link.

As the simplest case, for example, the multipath may be approximated by a direct ray or path of transmission, and a single secondary ray or path, as is shown in chapter 3. Here the ground acts as a perfect reflector with angles of incidence and reflection satisfying Snells Law. The signal at the receiver is then the sum of the above two signals as in equation (3-9)

$$H(f-f_0) = \alpha - \beta e^{j2\pi(f-f_0)\tau} \quad (4-1)$$

where the parameter α , represents the strength of the direct signal. The parameter β , represents the strength of the second path signal. The delay difference τ , represents the delay of the second path signal with respect to the

direct signal. The f_0 is the frequency of the signal cancellation. The expression $f-f_0$ represents the offset of the observation frequency from the frequency of the minimum signal power.

This approach is applied to the terrestrial microwave link analysis by dividing the path profile into reflecting ground segments, each giving rise to a secondary path. In order to determine the parameters of reflection, the conditions of propagation in the lower atmosphere must also be included.

In the lower atmosphere, the radio refractivity N is defined by

$$N=(n-1) \cdot 10^6 \quad (4-2)$$

where n is the index of refraction of the atmosphere. For a constant refractivity index, the path of the ray is a circle of radius R where

$$1/R = dN/dh \cdot 10^6 \quad (4-3)$$

and h is the height above the earth [35] .

A transformation of variables allows a change of perspective, from curved earth to flat earth. A ray of radius R propagating above the earth has a modified radius R_m above the flat earth;

$$1/R_m = 1/R + 1/a \quad (4-4)$$

where $a = 6370$ km (earth radius). For a constant refractivity index, the path of the ray is a circle of radius R_m where

$$1/R_m = dM/dh \cdot 1E-6 \quad (4-5)$$

where M is the modified radio refractivity for flat earth propagation, related to N by

$$M = N + (h/a) \cdot 1E-6 \quad (4-6)$$

The ratio of modified to actual earth radius is defined as the effective earth radius factor,

$$K = R_m / a \quad (4-7)$$

Normal daytime propagation conditions in the lower atmosphere exist when $K = 4/3$ or $dN/dh = -39$ N-units/km. A small negative gradient in the refractivity of the atmosphere causes the radio waves to follow the curvature of the earth.

Sub-refractive propagation occurs when dN/dh is greater than -39 N-units/km and less than infinity. In this case K is greater than 0.5 and less than $4/3$. It causes an upward bending of rays or an apparent bulge in the earth surface. Power fading results from the additional spreading of the wavefront. Diffraction losses result in cases of obstruction fading from earth bulge.

Super-refractive propagation occurs when dN/dh is less than -39 N-units/km and greater than -157 . In this case K is greater than $4/3$ and less than infinity. The earth appears to be flat or concave, causing rays to hit the

earth before arriving at the receiver. Power fading results from the additional spreading of the wavefront. Multipath interference results in cases of increased or enhanced ground reflections.

Variations in K on a microwave link are caused by changes in the index of refraction as a function of altitude. The index of refraction is composed of dry and wet components, N_{dry} and N_{wet} [36]. The composite is a function of pressure, humidity, and temperature. The dry component increases in value with both temperature and humidity, as is shown in figure 4-1a. The wet component increases with saturated vapor pressure, as is shown in figure 4-1b.

In the modelling of radio propagation for line-of-sight microwave radio, the gradient of the index of refraction is assumed to be linear in the lower atmosphere (100 meters) and constant along the microwave link. As a result, the K factor of equation (4-7) is used for the ratio of the radius of propagation of radio waves above the earth to the actual radius of the earth. Equations (4-2) through (4-7) illustrate the relationship between the index of refraction and the K factor. As the gradient of the index of refraction becomes less positive, the K factor increases. When the gradient becomes negative, the K factor exceeds one. This is shown in figure 4-1c.

In this dissertation, an effective earth radius factor, assumed to be constant over the path, is used to model linear variations in the refractive index gradient as a function of altitude. Terrain elevation points are then adjusted to account for the effective change in path length. A method for path profile linearisation is developed to identify potentially coherent reflecting areas as well as areas of shadowing and possible obstruction. The adjusted linearised profile is treated as a combination of reflecting plates and

figure 4-1a

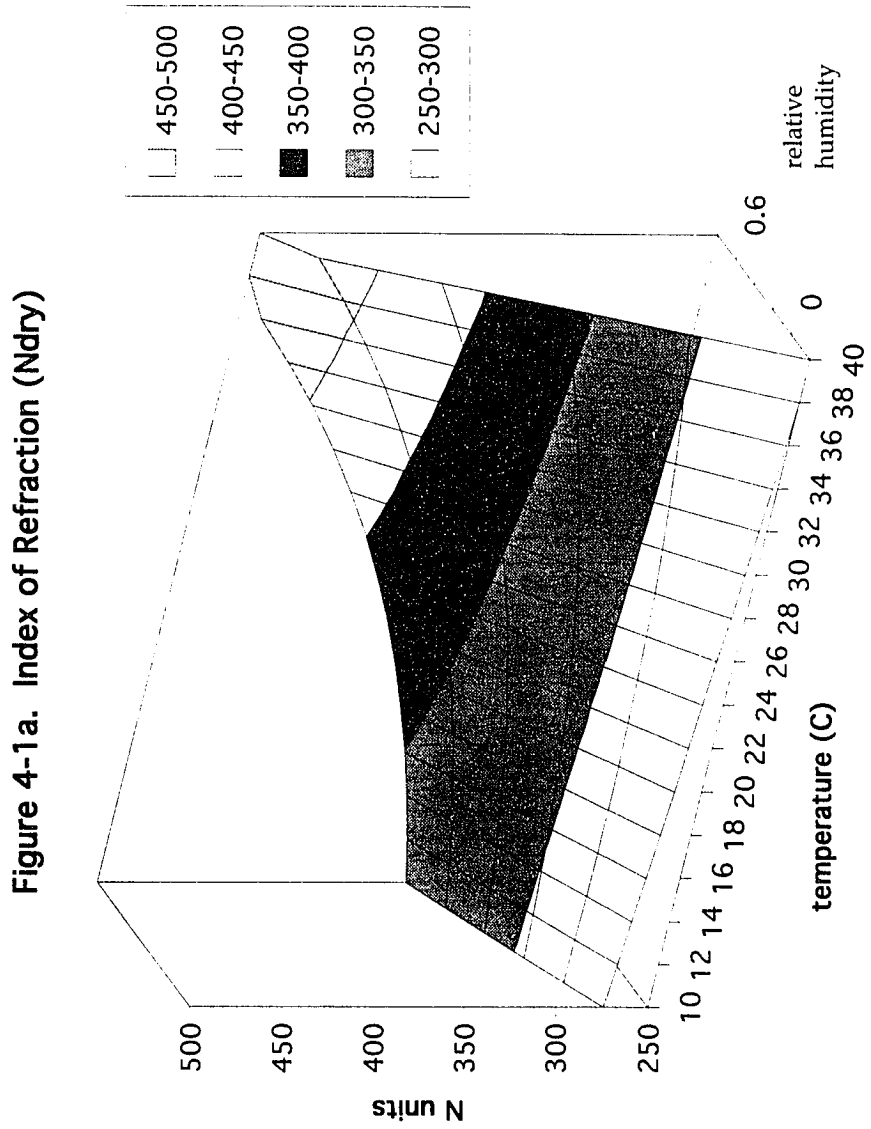


figure 4-1b

Figure 4-1b. Index of Refraction (Nwet) and saturated pressure

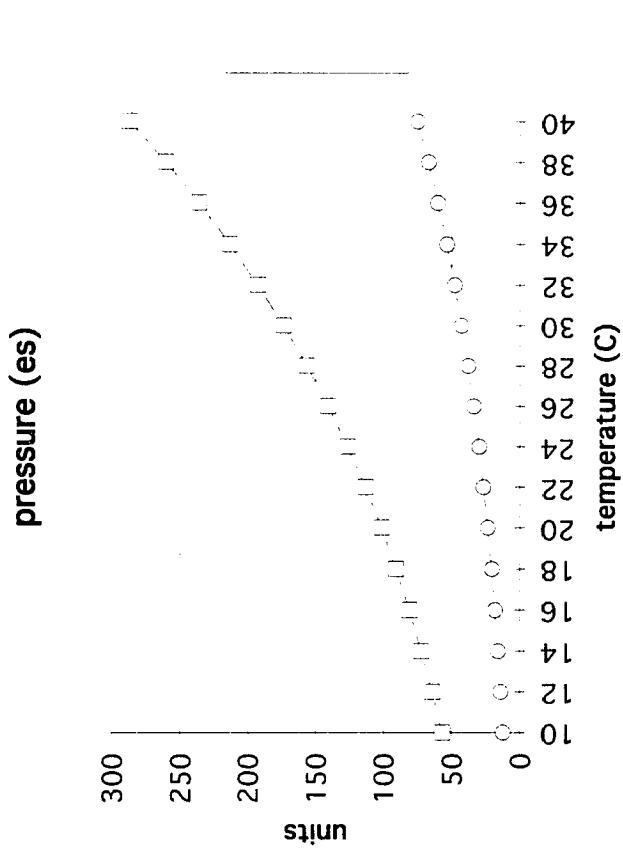
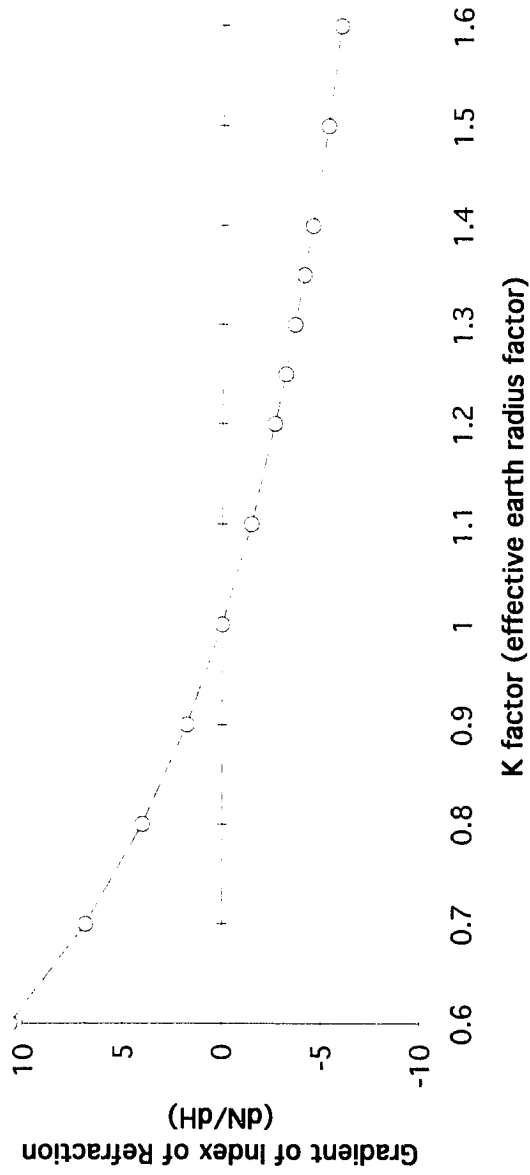


figure 4-1c

Figure 4-1c. Gradient of the Index of Refraction in the lower atmosphere (100m) as a function of a constant K factor



wedges from which the reflected wavefront is computed. The effects of directive antenna data are included to allow for simulation of real radio systems.

The coordinate system is cartesian. The origin is at sea level under the first antenna. The horizontal axis is to sea level under the second antenna. The earth bulges upward above the horizontal axis.

The terrain elevation profile is plotted for a flat earth. Line-of-sight propagation is along the direct optical path (straight line) from the transmitting to the receiving antenna. For the flat earth profile, the direct path is fixed. In the absence of atmospheric refraction, the direct path is perpendicular to the radius of the earth, and the optical (apparent) and physical (actual) terrain locations are equal. Atmospheric refraction bends the propagation paths of the radio waves (e.g. earth bulge). The result is a displacement of the optical terrain location. Thus, for the flat earth profile the optical terrain elevation varies as a function of atmospheric refraction.

Secondary rays will be delayed according to the length of the propagation path. The path of the secondary ray is defined as the sum of straight line segments (hypotenuse) from antenna to ground segment to antenna.

Reflecting segments are assigned an altitude above sea-level which includes earth bulge effects. The terrain elevation data are mapped to a flat earth profile. The distance from each reflecting segment to an antenna is measured horizontally. The path length is a straight line segment from the transmitting antenna to the reflection point, and from the reflection point to the receiving antenna.

The propagation paths are straight lines in cartesian coordinates. Subrefraction and super-refraction are treated as parabolic distortions of the local terrain altitude above sea level. The terrain elevation data are entered as a series of elevations along the path of transmission. These elevations are displaced for the desired gradient of the index of refraction (or K factor) by computation of the modified earth radius. A front-end subroutine then computes a series of straight-line segments of 0.01 miles in length to approximate the profile. The slope of the segment is defined by the difference in elevation of the endpoints after accounting for earth bulge condition.

Each segment may be shadowed or obstructed from view of either antenna by the surrounding terrain. The first pass of the analysis is a clearance profile. Illumination conditions of the local ground are determined by sweeping the profile from each end. A monotonic decrease of the angle of arrival at the ground segment from one antenna compared to the angle of departure from the ground segment to the other antenna implies a non-shadowed condition. Visibility is the first parameter of the forward multipath model.

For worst case analysis, each exposed ground segment is considered a reflecting surface having a reflection coefficient equal to unity. In fact, for grazing angles of incidence, the reflection coefficient of ground is very close to unity for microwave radio frequencies and for both vertical and horizontal polarisations [34]. The reflection coefficient is the second parameter of the forward multipath model.

This model could be further required to allow for reflection coefficient variation on a per-segment basis. The conductivity of the particular type of terrain being illuminated could be taken into account, as well as variation in

frequency, polarisation, and angle of incidence. However, these variations are very small with respect to the parameters of this study. For digital radio propagation modelling, the effect of a more precise (and slightly reduced) reflection coefficient would merely be an interferer of slightly less amplitude.

The amplitude of a travelling wave is reduced by the distance from the source squared because of the spherical propagation of a wavefront in free space. The direct signal strength is therefore attenuated by the path length travelled from the transmit to the receive antennae. The secondary signal travels a different path and is attenuated by a different amount. For the purposes of this model, the direct signal amplitude is normalised to unity, and the secondary signal amplitude is scaled by the difference in path length squared. A third parameter for the forward multipath model is amplitude.

The launched and detected signals are also scaled by an approximate antenna pattern with the peak aligned with boresite and normalized to unity. The direct signal strength is therefore attenuated by the transmit and receive antenna patterns. The antenna contribution is simply a function of the departure and arrival angles. On the other hand, the secondary path is attenuated by the transmit and receive antennae, and by the directivity of the reflecting surface. Assuming the exposed earth to be a near-perfect reflector, Snell's law is applied for ray tracing. However, the path from the transmitter to the reflecting ground segment and the path from that same ground to the receiver may not have equal arrival and departure angles. In other words, the receiver may be off boresite for the reflection path. Since each ground segment provides an aperture for an image source, the reflection is treated as a windowed image of the actual source. As with the direct path, the reflection path is scaled by an approximate antenna pattern with the peak signal at

boresite normalised to unity. For the secondary path, the antenna contribution is a function of the departure, incidence, reflection, and arrival angles. Thus, a fourth parameter for the forward multipath model is directivity. The reflection geometry for a second (ground reflection) path is illustrated in figure 4-2a.

Also important to the reflection criterion is the smoothness of the surface area. If the ground segment is rough with respect to the wavelength of propagation, the reflection will be scattered, or diffuse. If it is smooth with respect to the wavelength of propagation, the reflection will be mirror-like, or specular. As a rule, the Rayleigh criterion [35] is used to distinguish smooth from rough surfaces. As is shown in Figure 4-2b, the difference in path length Δl may be written as a function of the variation in local surface height h and the angle of incidence on the local surface area α ,

$$\Delta l = 2h \sin\alpha \quad (4-8)$$

In general, any surface for which the path lengths of reflected rays vary by much less than a wavelength, λ ,

$$h(\sin\alpha) / \lambda \rightarrow 0$$

is considered smooth.

A microscopic smoothness criterion of $\pi/4$ or

$$\Delta l < \lambda/8 \quad (4-9)$$

applied over an individual ground segment results in a surface height

Figure 4-2a: Local Geometry of Ground Reflection

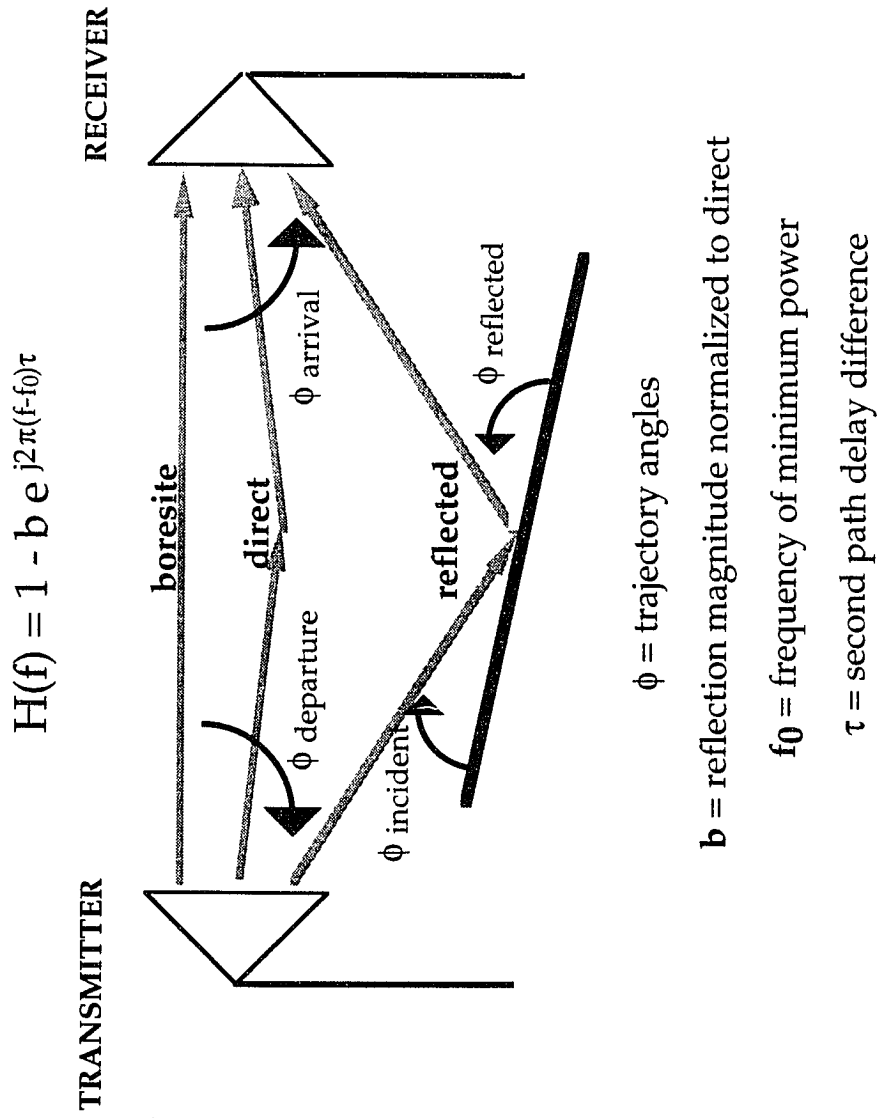
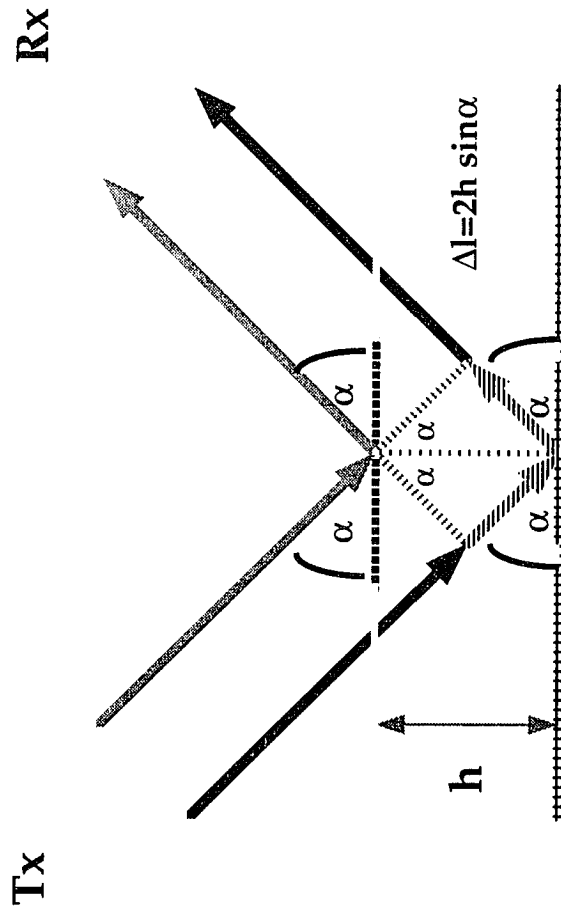


figure 4-2a

figure 4-2b

Figure 4-2b: Surface Roughness



difference limit of

$$\Delta h < \lambda / 16 (\sin\alpha)$$

If $\lambda = 0.05$ meters, $\alpha = 0.05$ degrees then $\Delta h < 0.0625$ meters. The roughness of a ground segment is a fifth parameter for the forward multipath model.

A roughness factor $f(\sigma_h)$ [36] may be used to scale the smooth earth reflection coefficient for an approximation of reflection from a moderately rough surface,

$$f(\sigma_h) = \exp\{-1[4\pi\sigma_h (\sin\alpha)/\lambda]^2/2\} \quad (4-10)$$

where σ_h is the standard deviation of ground height. This could be incorporated into the multipath model on a per-segment basis to allow for modelling of roughness variations. Limited roughness, however, reduces the amplitude of the specular reflection and the resulting interfering signal.

Similarly, the macroscopic smoothness of several consecutive segments is an important factor in determining the convergent nature of the reflecting area. If several adjacent segments satisfy a criterion such as (4-9), then they are merged into a larger area of specular reflection. The rays reflected from such an area are all in phase, giving rise to a continuous and contiguous reflected wavefront. For digital radio, the resulting interference will be coherent and signal-like. The stability of superposition will be a function of the stability of the propagation path, composed of the reflecting ground or water and the lower atmosphere. The addition of multiple signals at the receiver will result in summation and cancellation that is a function of

the delay difference of the propagation paths. If the above-mentioned criterion are exceeded, then the overall area will act as a diffuse reflector. The resulting interference from this type of reflection will be non-coherent and noise-like. In the channel of concern, it will be weak because the noise is broadband. The result will be a slight increase in the random noise power. The convergence of adjacent ground segments or the resulting coherence of the reflected wavefront is thus a sixth parameter for the forward multipath model.

In summary, second path clearance and reflector smoothness are necessary for a reflected signal to be generated. If a surface area is illuminated and sufficiently smooth, it will serve as a reflector for a secondary path. However, coherence is the most important parameter for interference to occur once the path is established. If the reflected wavefront is coherent, then the reflected signal will interfere with the direct coherent signal. The interference will result in channel distortion and loss of performance. Because of the threshold effect of digital decisions, variations in reflection coefficient or antenna discrimination will not affect the loss of performance. They only affect the amount of signal attenuation at the cancellation frequency. In fact, it is more important to properly characterise the second path delay, as adjacent surfaces that create constant delay paths form a coherent wavefront.

Forward multipath results for the Salton to Brawley link in southern California are listed in Table 4-1. The line-of-sight path is indicated by the coarse dotted line, and the boresight direction of the antennae (aligned at $K=4/3$) is indicated by the fine dotted line. The line-of-sight path is 37 miles in length. The path parameters are: angle of departure (from the

transmitter), angle of arrival (at the receiver), angle from specular (at the reflecting surface segment), terrain height, and delay (of the reflection path relative to the line-of-sight path). The terrain elevation is plotted for each surface segment with a solid line. The remaining parameters are computed and are super-imposed onto the terrain elevation profile when the respective ground segment is in sight of the transmitter and receiver. The angle of departure is indicated by the fine dashed line. The angle of arrival is indicated by the coarse dashed line. The angle from specular is indicated by the solid line broken by one dash. The delay is indicated by the solid line broken by two dashes. Terrain which gives rise to coherent reflection is indicated by a convergence of constant delay and constant angle (from specular) profiles.

For example, the terrain elevation profile for $K=2/3$ is plotted in Figure 4-3a with the resulting multipath parameters. The terrain (solid line) slopes downward from Salton to Brawley, with a significant hill providing some blockage at approximately one third of the distance from Salton to Brawley. The direct signal path is not obstructed. Note that the antenna alignment for the transmitter and receiver is normally performed during standard propagation conditions ($K=4/3$). As a result, the line-of-sight for $K=2/3$ (coarse dot) is below the line-of-sight (fine dot) for $K=4/3$. Therefore the direct signal for $K=2/3$ is attenuated by the antenna gain offset from the maximum gain direction at $K=4/3$. The multipath parameters are plotted for the sections of the length which are visible to both the transmitter and receiver. This occurs along the last third of the distance from Salton to Brawley. In this area, the angles of departure (coarse dash) and arrival (fine dash) are small and nearly equal, indicating that the effect of antenna discrimination is

insignificant. Furthermore, the angle from specular (dash dot) is nearly zero over the first half of the reflecting area indicating angles of incidence and reflection from the ground that are equal. The reflection is specular and mirror-like, and the delay (dash dot dot) is nearly constant and approximately equal to 0.8 nanosecond over the first half of the reflecting area. Therefore, an interfering signal is possible due to a coherent wavefront with an 0.8 nanosecond delay reflected from the first half of the last third of the distance from Salton to Brawley.

Table 4-1

<u>Figure</u>	<u>K factor</u>	<u>Receiver Elevation</u>
4-3a	2/3	141
4-3b	1	141
4-3c	4/3	141
4-3d	5/3	141
4-4a	2/3	178
4-4b	1	178
4-4c	4/3	178
4-4d	5/3	178

Figures 4-3 (a-d) show the path simulation for a Salton antenna height of 780 feet and a Brawley antenna height of 141 feet. In figure 4-3a, $K=2/3$. Over approximately 10% of the path near Brawley, the angle of reflection from specular is very close to 0 degrees. Over the same area, the delay is approximately 0.8 nanoseconds, indicating a possibly coherent reflection source. In figure 4-3b, $K=1$, and the situation is very similar. The delay is slightly increased to 1.2 nanoseconds, as would be expected with the increased gradient in index of refraction. The angle from specular is approximately zero for the reflected wavefront directed at the receiver. At $K=4/3$ in figure 4-3c,

figure 4-3a

Figure 4-3a: Forward Multipath Model

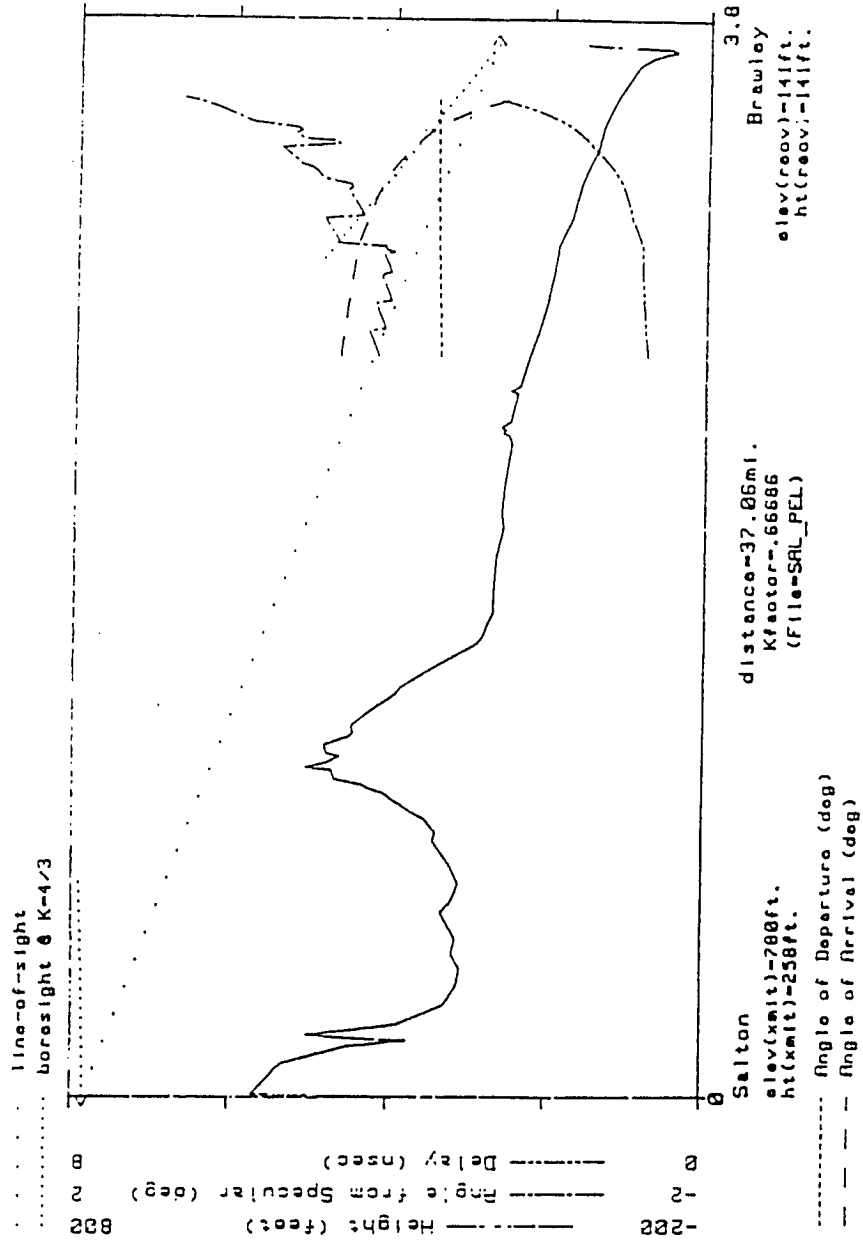


figure 4-3b

Figure 4-3b: Forward Multipath Model

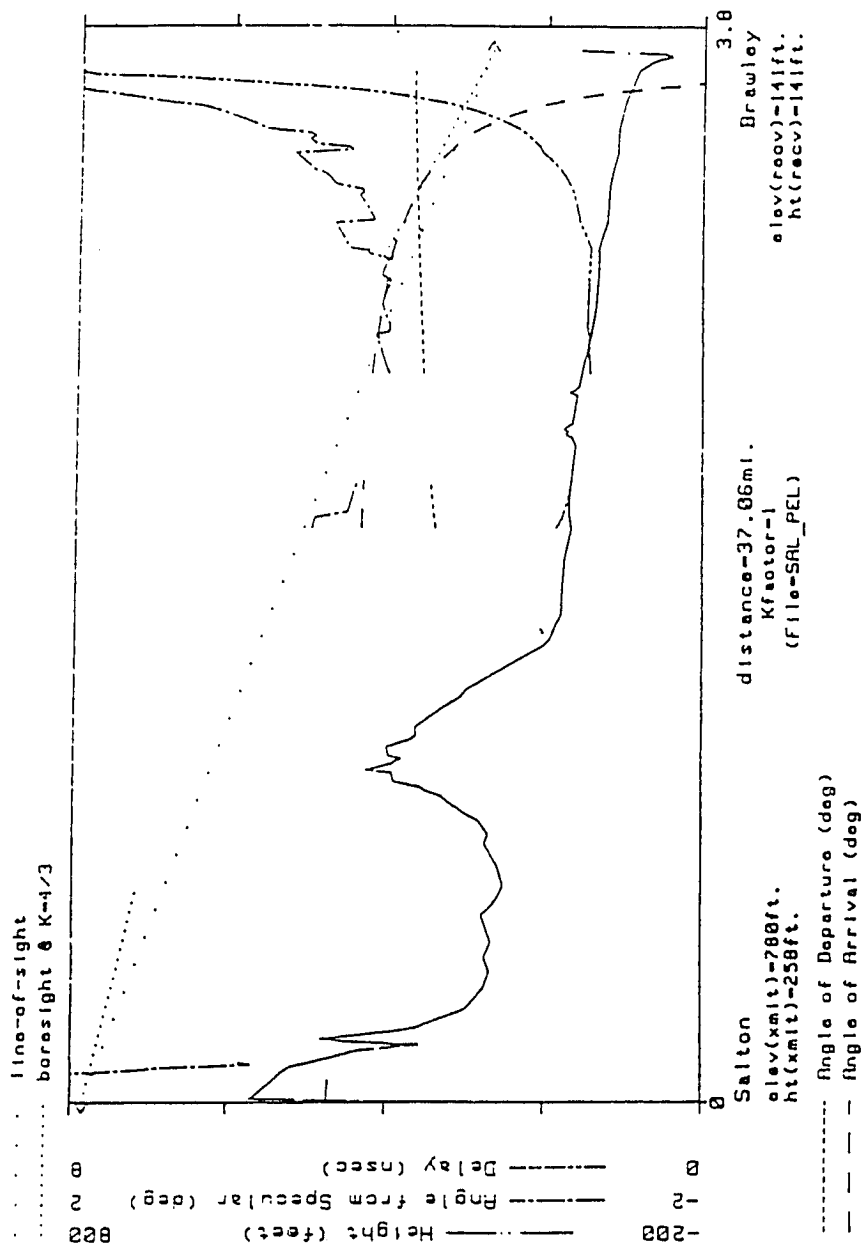


figure 4-3c

Figure 4-3c: Forward Multipath Model

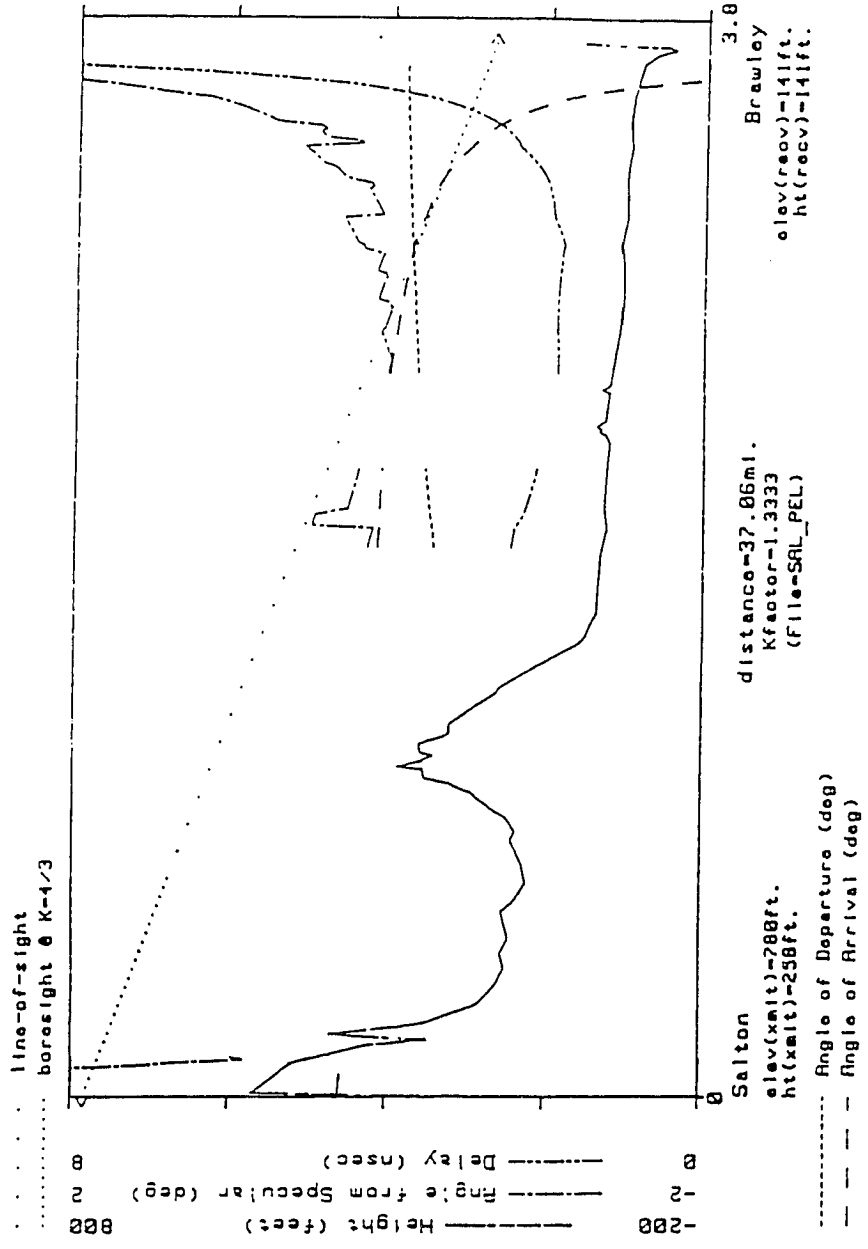
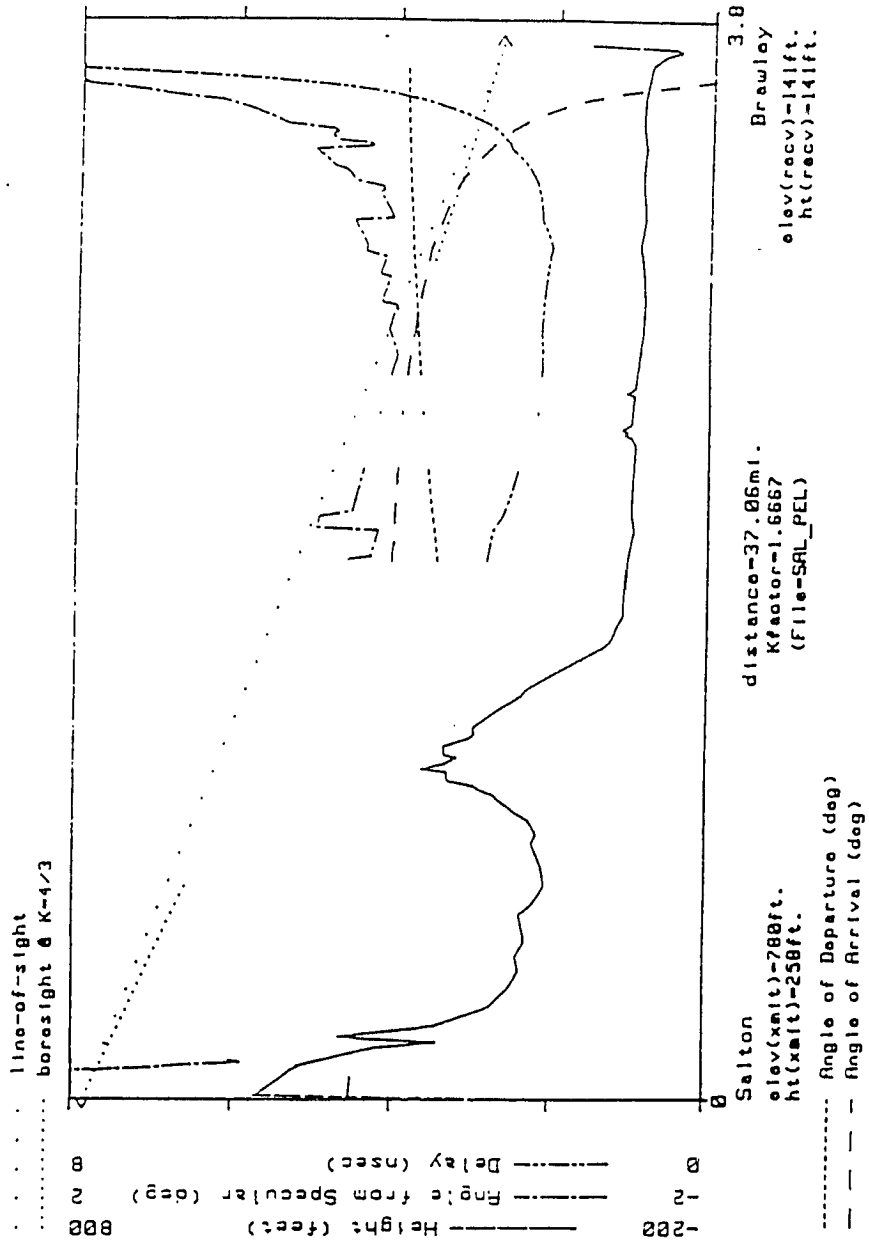


figure 4-3d

Figure 4-3d: Forward Multipath Model



the delay is again slightly greater at 1.6 nanoseconds with a very nearly specular reflection angle. In this case, a second reflecting area becomes exposed adding approximately 5% to the path length. For $K=5/3$ in figure 4-3d, the delay increases to 2.2 nanoseconds with a near specular reflection. Here the original reflecting area has grown in size to approximately 15% of the path length; a second reflecting area remains exposed. Throughout the propagation regime of figures 4-3 (a-d), the simulation shows evidence of probable interference from ground reflections. Furthermore, the variation in delay of the reflection path would suggest a distribution of cancellation frequencies, or, in other words, broadband cancellation effects.

An additional example of the simulation is shown for a Salton antenna height of 780 feet and a Brawley antenna height of 178 feet in figures 4-4 (a-d). In figure 4-4a, $K=2/3$. Over approximately 10% of the path near Brawley, the angle of reflection from specular is close to 0 degrees. As before, the delay is approximately 1 nanosecond over the same area. In figure 4-4b, $K=1$, and the delay increases to 1.6 nanoseconds, as would be expected with the increased height and gradient in index of refraction. The angle from specular is again approximately zero directed at the receiver. At $K=4/3$ in figure 4-4c, the delay increases again to 2.0 nanoseconds with a very nearly specular reflection angle. A second reflecting area is again exposed; comprising an additional 5% of the path. For $K=5/3$ in figure 4-4d, the delay increases to 2.4 nanoseconds with a near specular reflection. Here the original reflecting area has grown in size to approximately 15% of the path length and the second reflecting area remains exposed. As in 4-3 (a-d), the propagation regime of figures 4-4 (a-d) shows evidence of probable interference from ground reflections. The change in antenna height does not diverge or

figure 4-4a

Figure 4-4a: Forward Multipath Model

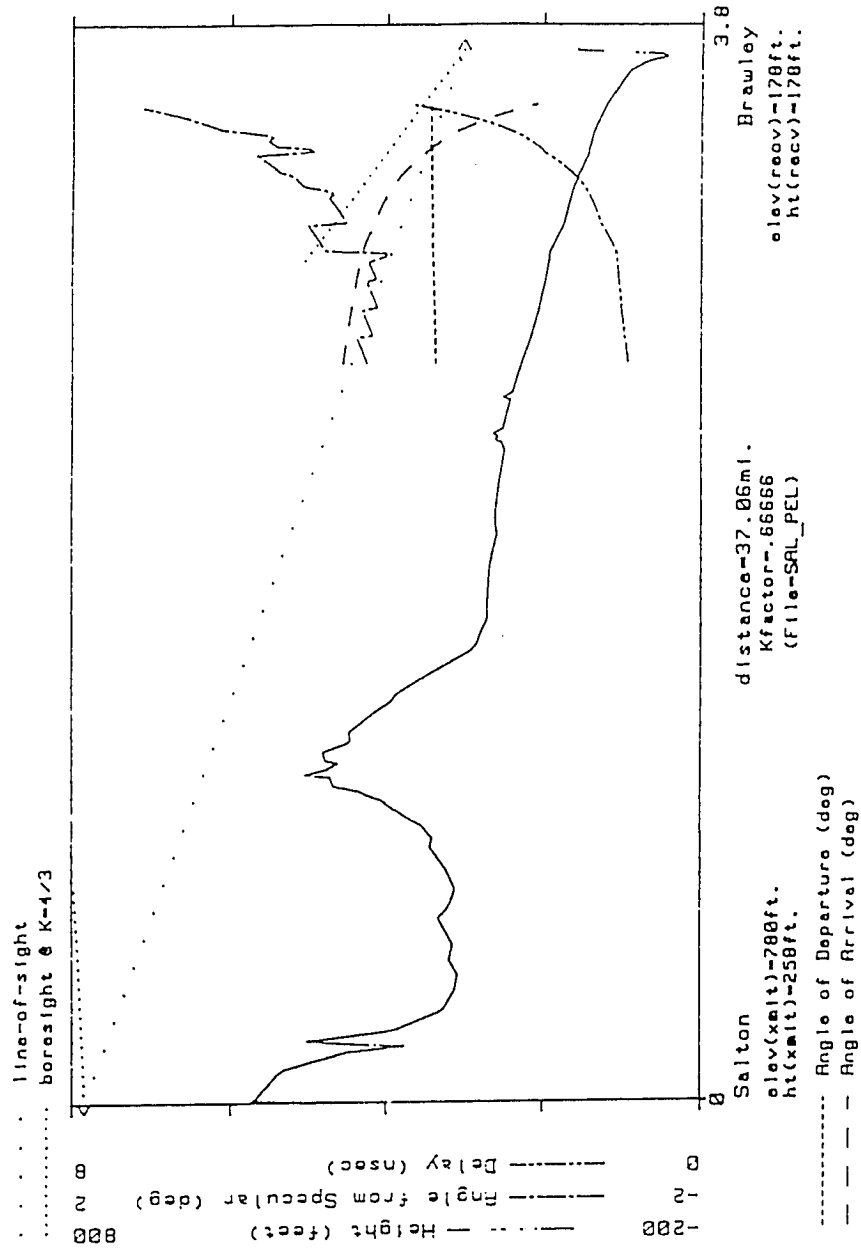


figure 4-4b

Figure 4-4b: Forward Multipath Model

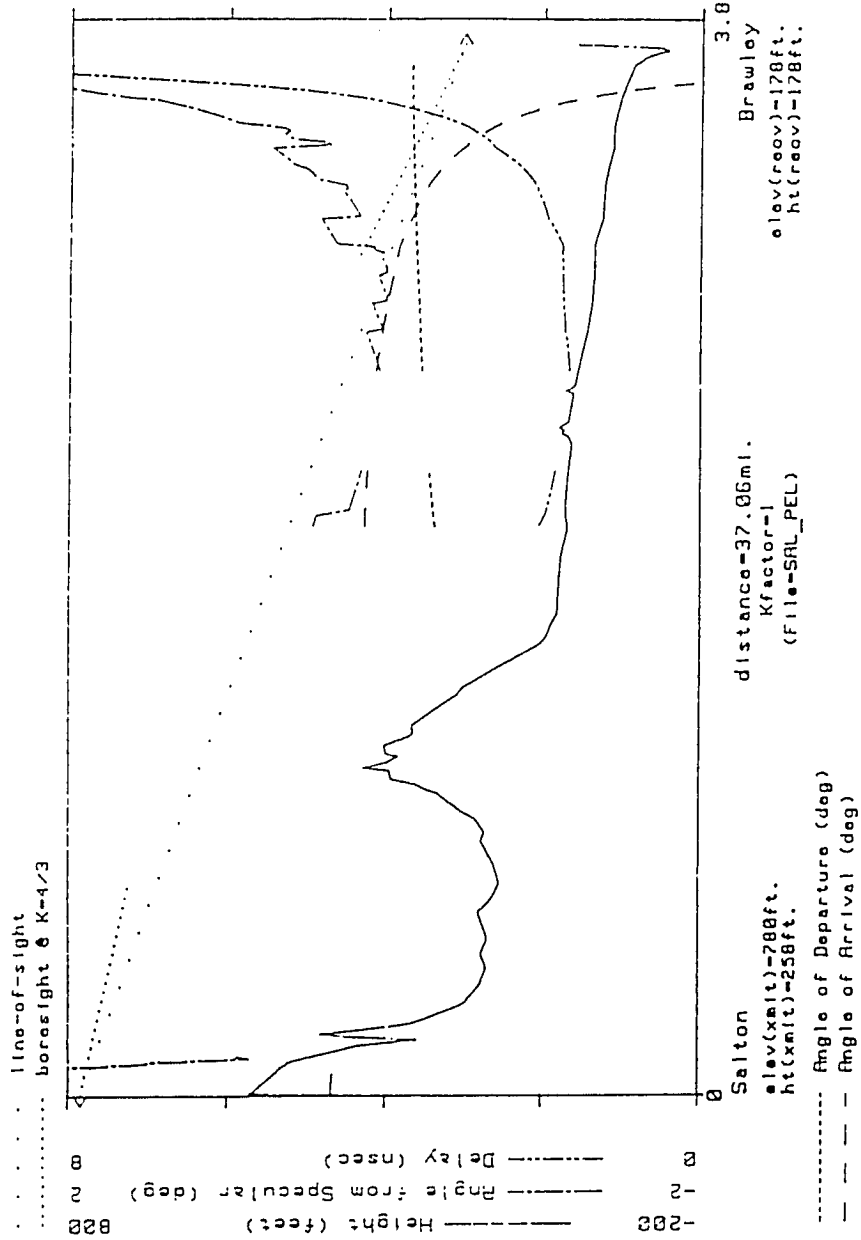


figure 4-4c

Figure 4-4c: Forward Multipath Model

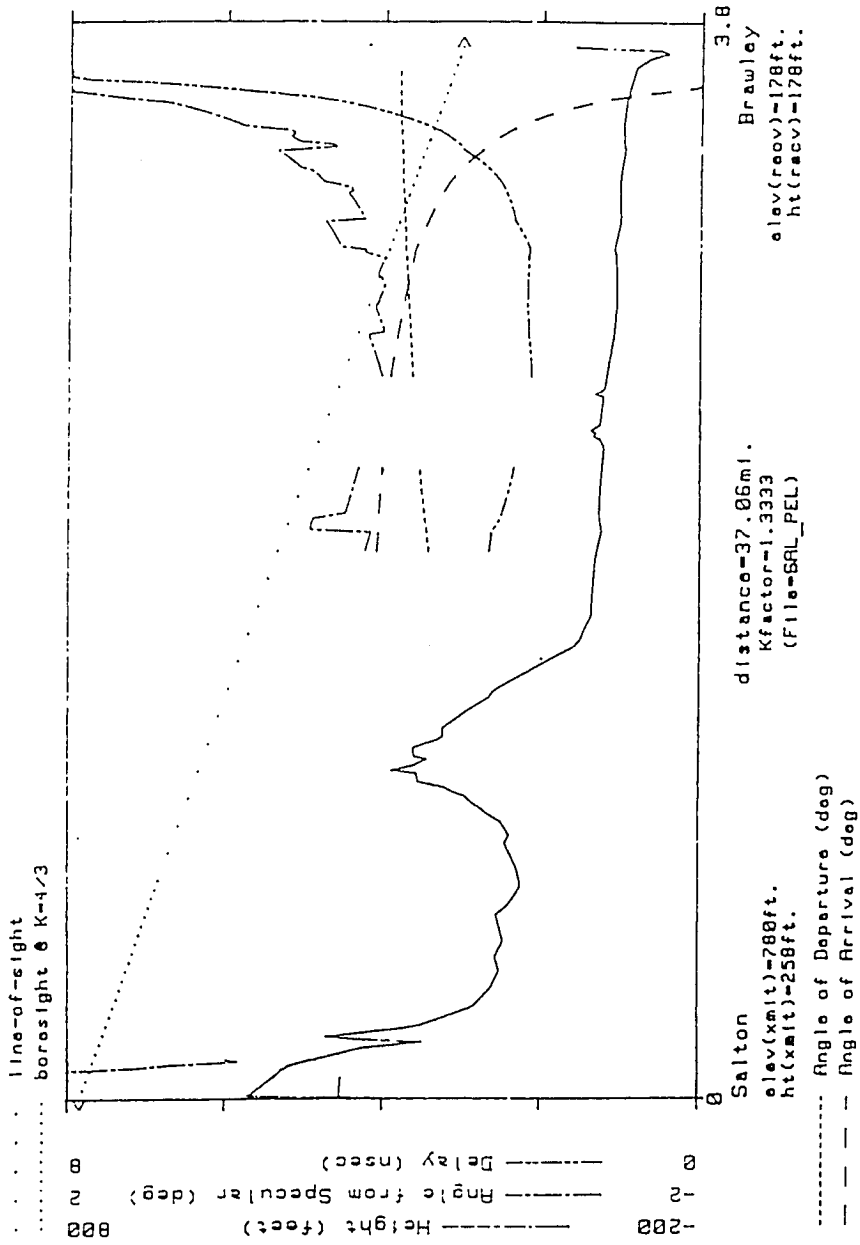
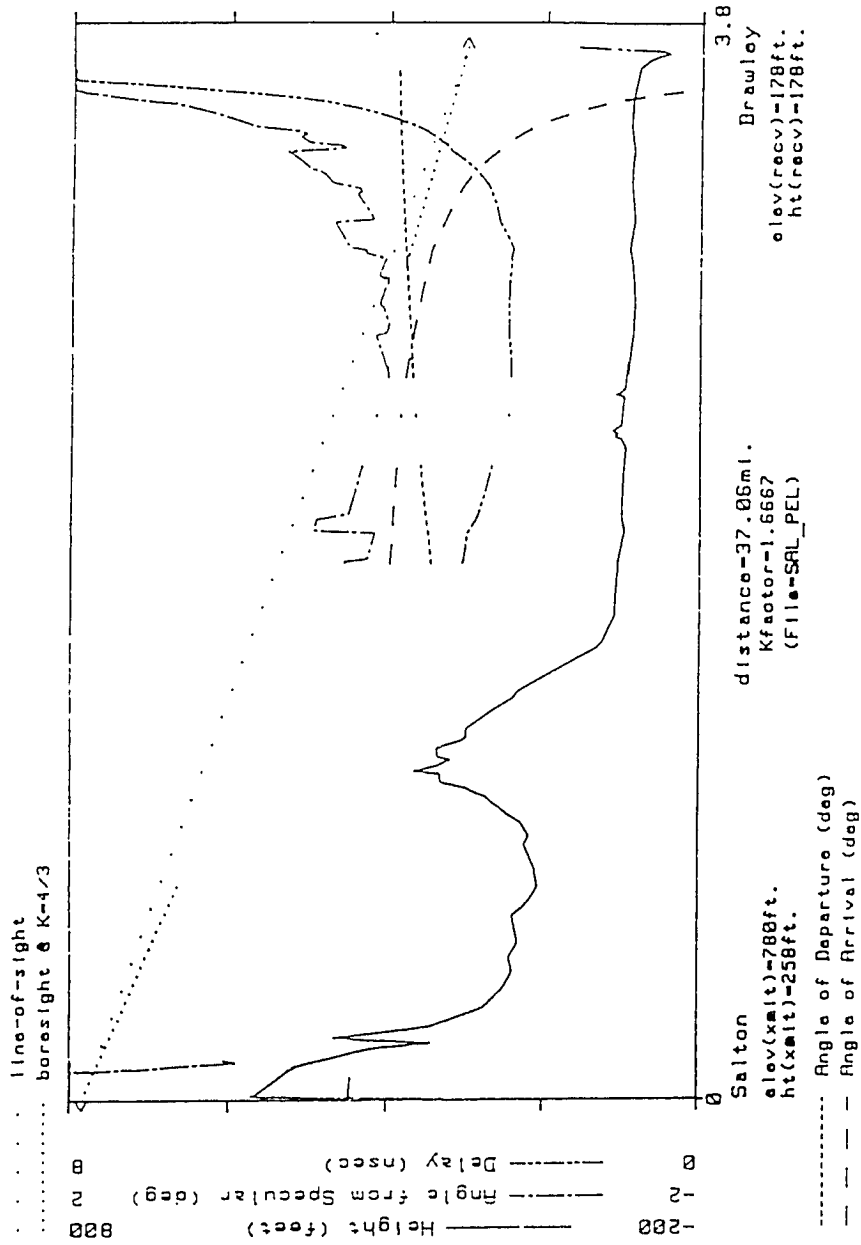


figure 4-4d

Figure 4-4d: Forward Multipath Model



defocus the reflected energy. It serves only to increase the delay of the reflection paths.

The forward multipath parameters for multipath propagation due to ground reflections are: (1) amplitude of the transmitted signal, (2) visibility of the exposed ground, (3) reflection coefficient of the exposed ground, (4) roughness of the exposed ground, (5) directivity gain for the path trajectory, and (6) coherence of the reflected wavefront. As is shown in the path analyses, it is essential to identify and analyze the sources of secondary paths. Visibility and directivity are easily established by a linearized terrain profile analysis. Coherence may be obtained by computed the secondary path length or delay profile. A measurable area of exposed and smooth ground or water having a constant delay profile is a reflection candidate. If the coherent reflecting area is present for normal k factors, then the link has a very high risk of multipath interference. On the other hand, if the coherent reflecting area is present for extreme K factors only, then the risk of multipath interference is low.

4.3 Inverted Multipath Model

In order to determine the parameters of the forward multipath model, the characteristics must be compared to the observable behaviour of the radio channel. In this section, an inverse multipath model is developed. The inverse model allows for estimation of the channel transfer function developed in chapter 3. A direct signal and an interfering signal are approximated at the receiver. While the parameters of the model are not easily measured, they must be recoverable from the channel data in order for the model to successfully approximate the channel. To recover the parameters, the two ray cancellation model of chapter 3 is inverted. The

model is set equal to the channel power, and solutions for the various parameters are obtained in terms of measured levels. Recovery of the parameters is equivalent to identification of the interference for cases of good channel approximation, as is shown.

Linear and parabolic power distortions of the channel transfer function are characterized using a second order approximation,

$$|H(f_n)|^2 = p_0 + p_1 f_n + p_2 f_n^2 \quad (4-11)$$

where p_0 , p_1 , and p_2 represent the zero order (constant), first order (linear), and second order (parabolic) coefficients of the power of the channel transfer function. The normalized frequency f_n is the ratio of frequency to channel bandwidth.

The coefficients may be determined using a least mean squares parabolic regression technique. The data points are the received signal power values measured by the three channel filters at the frequencies f_1 , f_2 , and f_3 , respectively. The least mean squares technique minimizes the difference between the second order polynomial and the data points. The coefficients are computed by solving the system of equations

$$\begin{bmatrix} 1 & f_1 & f_1^2 \\ 1 & f_2 & f_2^2 \\ 1 & f_3 & f_3^2 \end{bmatrix} \begin{bmatrix} p_0 \\ p_1 \\ p_2 \end{bmatrix} = \begin{bmatrix} |H(f_1)|^2 \\ |H(f_2)|^2 \\ |H(f_3)|^2 \end{bmatrix} \quad (4-12)$$

Solutions were restricted to cases having a cancellation frequency falling inside the digital radio channel bandwidth. For such situations, there was

only one solution to the system, and it was not necessary to evaluate the stability of the equations.

The two ray approach may be used to simulate the shape of the radio channel. The dispersive part of multipath fading may be simulated using a normalized two ray model as in section 3.3, having the transfer function

$$H(f-f_0) = 1 - b e^{j2\pi(f-f_0)\tau} \quad (4-13)$$

The offset cancellation frequency $f-f_0$, is the frequency relative to the position of the signal power minimum. The parameter b , represents strength of the second ray and the τ , represents the delay difference of the second ray with respect to the direct ray.

The power in the channel is expressed as the magnitude squared:

$$|H(f-f_0)|^2 = 1 - 2b \cos(2\pi(f-f_0)\tau) + b^2 \quad (4-14)$$

As the cancellation frequency approaches the frequency of observation, the offset cancellation frequency approaches zero and the first and second derivatives of (4-14) may be approximated as follows:

$$\frac{\partial |H(f-f_0)|^2}{\partial f} = 8b\tau^2\pi^2(f-f_0) \quad (4-15)$$

and

$$\frac{\partial^2 |H(f-f_0)|^2}{\partial f^2} = -8b\pi^2\tau^2 \quad (4-16)$$

for

$$(f-f_0) \rightarrow 0$$

The derivatives (4-15) and (4-16) may be used to estimate the offset cancellation frequency $f-f_0$, and the second ray strength b ,

$$(f-f_0) = \frac{\frac{\partial |H(f-f_0)|^2}{\partial f}}{\frac{\partial^2 |H(f-f_0)|^2}{\partial^2 f}} \quad (4-17)$$

and

$$b = 1 - \sqrt{|H(f-f_0)|^2 - \frac{1}{2} \frac{\left(\frac{\partial |H(f-f_0)|^2}{\partial f}\right)^2}{\frac{\partial^2 |H(f-f_0)|^2}{\partial^2 f}}} \quad (4-18)$$

The second derivative (4-16) and the second ray strength (4-18) may then be used to estimate the second ray delay,

$$\tau = \frac{\left(\frac{\partial |H(f-f_0)|^2}{\partial^2 f}\right)}{2b} \quad (4-19)$$

Given a parabolic approximation to channel power as shown earlier, it is possible to estimate the two ray model parameters specified above. The polynomial in (4-11) is an expansion about the channel center frequency. Three coefficients, p_0 , p_1 , and p_2 , are specified. The coefficients are related to the polynomial and its first and second derivatives at the reference frequency as follows:

$$|H(0)|^2 = p_0 \quad (4-20)$$

$$\frac{\partial |H(0)|^2}{\partial f} = p_1 \quad (4-21)$$

and

$$\frac{\partial^2 |H(0)|^2}{\partial^2 f} = 2p_2 \quad (4-22)$$

The two ray equation in (4-14) is a broadband expression for power. Near the notch, the three parameters $(f-f_0)$, (b) , and (τ) may be approximated by (4-17), (4-18) and (4-19). As the notch frequency nears the channel center, the polynomial approximation and the two ray model become comparable in validity. The two ray parameters may then be estimated directly from the polynomial coefficients. The offset notch frequency becomes

$$(f-f_0) = \frac{-p_1}{2p_2} \quad (4-23)$$

the second ray strength becomes

$$b = 1 - \sqrt{p_0 - \frac{1}{2} \left(\frac{p_1^2}{2p_2} \right)} \quad (4-24)$$

and the second ray delay becomes

$$\tau = \frac{2p_2}{2b} . \quad (4-25)$$

Physical measurements of multipath fading parameters and their variations have been well documented. Data have been published both internal to AT&T Bell Laboratories and in several references [38-41]. Various notch frequency speeds, some as fast as 100 MHz per second have been recorded. Notch depth speeds on the order of tens of dB per second, have also been noted.

Multipath transit delay data has also been published in several references. The data has varied widely. One reference gave a delay distribution with values less than 1 nanosecond for 95% of the measured time [40]. Another published specific delays of 5 to 8 nanoseconds for atmospheric events [10]. In terms of path length, Crawford and Jakes [4] measured changes from fractions of a foot to 10 feet. The corresponding variations in angle-of-arrival were 0.75 degrees above boresight to 0.8 degrees below.

A typical multipath event from Brawley, California recorded for 6 GHz radio is shown in figure 4-5. The three spectrum filters separated by +/- 11 MHz from the channel center are monitored. The sampling rate is approximately 8 times per second. An 11 second channel distortion event is shown at the two receiving antennae: figure 4-5a for the unprotected antenna, and figure 4-5b for the space diversity antenna. During both measurements, there was a notch moving through the band from high to low frequencies. This was shown by the gradual loss of signal in consecutive filters.

In a 2 ray fading scenario, the transfer function in the frequency domain may be viewed as a notch filter with varying position and magnitude of the notch or minimum. The channel distortions associated with an unstable minimum is traumatic to digital signalling. In a nonhomogeneous atmosphere, slight variations in wind speed, temperature, pressure, and humidity may occur simultaneously, resulting in both a phase and amplitude modulation of the received signals. Changes in relative phase between two received signals results in a movement of the cancellation frequency or notch. Changes in amplitude result in a variation of the notch depth. Slope fading generally occurs when the notch is outside the monitored channel but near the band edge. It is manifested by non-equal signal levels from each of the filters at the same instant in time, typically with the band centered filter output being less than one band-edge filter output and greater than the other. As the signal minimum approaches a channel in the frequency domain, the slope of the channel response becomes more severe. The band edge filter near the notch displays a large loss of signal. Eventually, the channel shape as given by the three filter outputs becomes nonlinear in dB.

A good example of multipath propagation phenomenon is shown in figure 4-5 (a-b). Initially in the spaced antenna channel, and then in the unprotected antenna channel, the signal power was faded and distorted. The normal QAM spectrum is flat across the channel, and rounded at the edges, as shown in figure 3-3b. The spectra in figures 4-5 (a-b) had a slope distortion as shown by the lower signal level in the upper filter output (f_3) and the higher signal level in the lower filter output (f_1). Movement of a signal minimum through a monitored channel is typically illustrated by the consecutive depression of each of the spectrum filter outputs in either

figure 4-5a

Center Frequency - solid 1

Lower Frequency - broken dot 2

Upper Frequency - broken dash 3

Figure 4-5a: Measurement of a Typical Multipath Event
in the 6GHz Band at Brawley, California
(Unprotected Antenna)

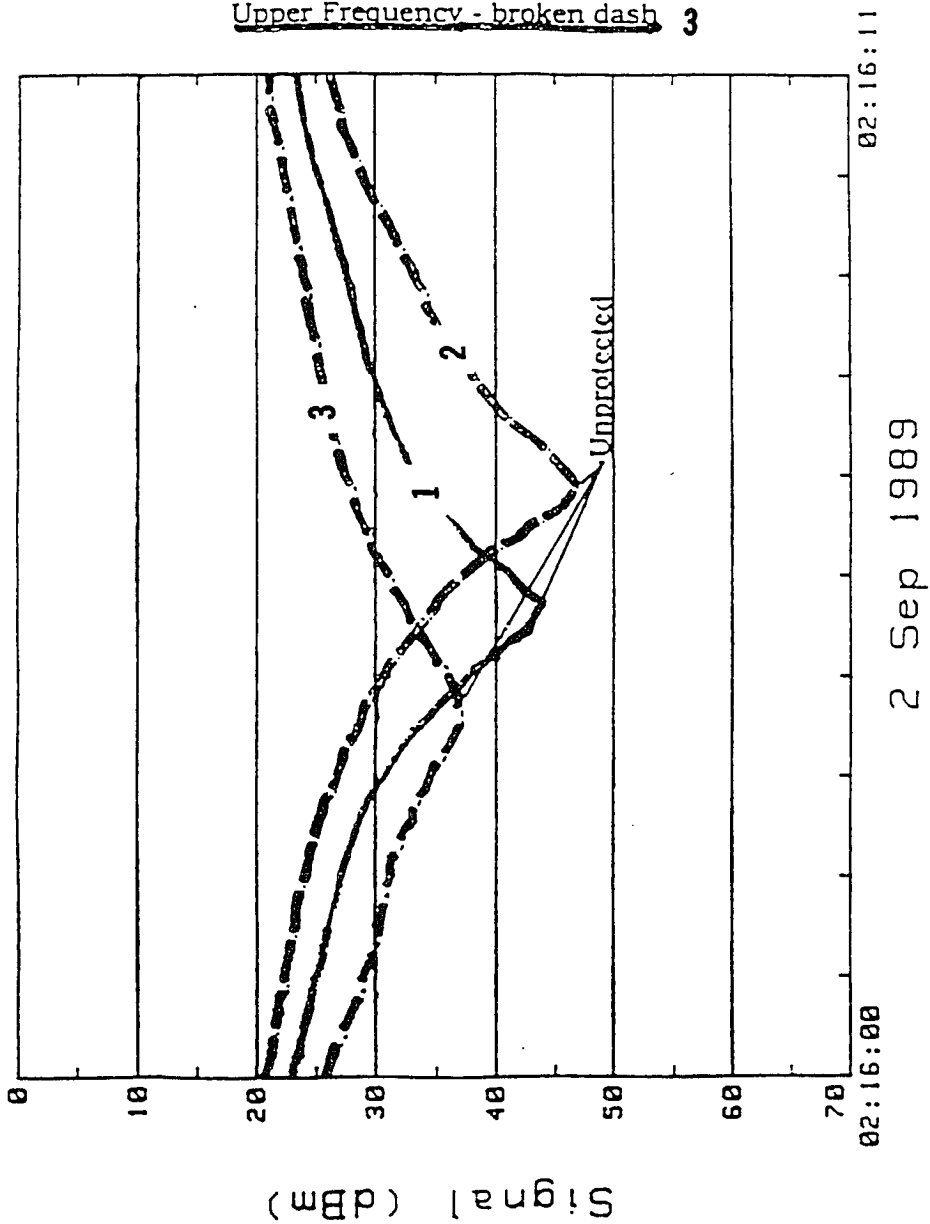


Figure 4-5b: Measurement of a Typical Multipath Event
in the 6GHz Band at Brawley, California
(Space Diversity Antenna)

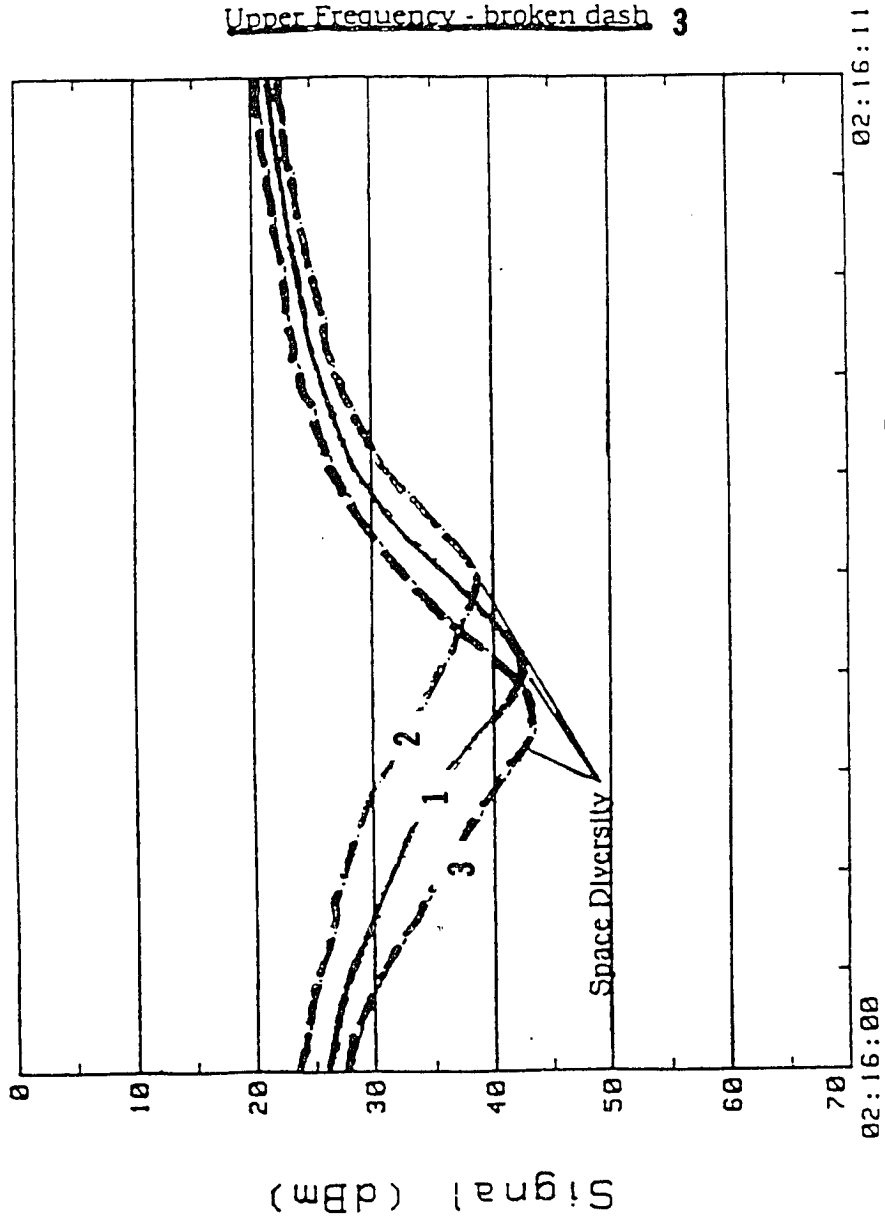


figure 4-5b
Center Frequency - solid 1

Lower Frequency - broken dot 2

Upper Frequency - broken dash 3

02:16:11

2 Sep 1989

02:16:00

ascending or descending order with respect to time as the notch sweeps to either higher or lower frequencies. A minimum rapidly moved from higher frequencies down through the spaced antenna channel. Seconds later a minimum moved similarly through the unprotected antenna channel. A signal minimum in the frequency domain is a severe shape distortion of the channel causing quadrature crosstalk and loss of information.

The event was analysed using the polynomial approximation to the normalized two ray model. This determined delay, depth, and frequency of the fade. As is shown in figures 4-6a and 4-6b, the normalized two ray model is solved for both the unprotected and space diversity ports. The analysis reveals minima moving approximately 15 MHz/second. At the unprotected antenna port, the second ray delay is approximately 2 nanoseconds for the duration of the event. Similarly, it is approximately 1 nanosecond at the space diversity port. The stability of the second ray delay is an important result of this analysis since it verifies the existence and dominance of the coherent interference signal. In general, the delays computed for this event fall within the range of the values published for other experiments (1 to 8 nanoseconds) [38-41].

4.4 Statistical Multipath Model

Based on the nature of multipath interference on the terrestrial microwave link, as defined previously, a statistical multipath model is developed for the radio channel. The two ray parameters can then be estimated from multipath channel data using the inversion method of section 4.2. The distribution of these parameter values are then used to establish ranges for random simulation of the two ray model. The channel is then

figure 4-6a

Figure 4-6a: Analysis of a Typical Multipath Event
in the 6GHz Band at Brawley, California
(Unprotected Antenna)

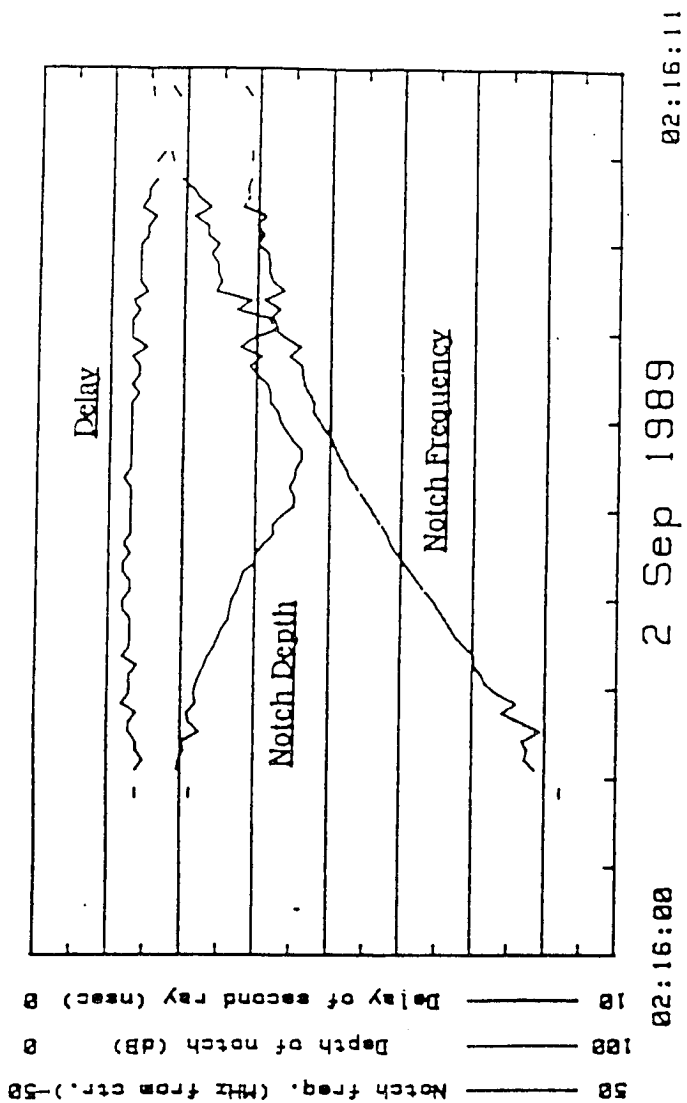
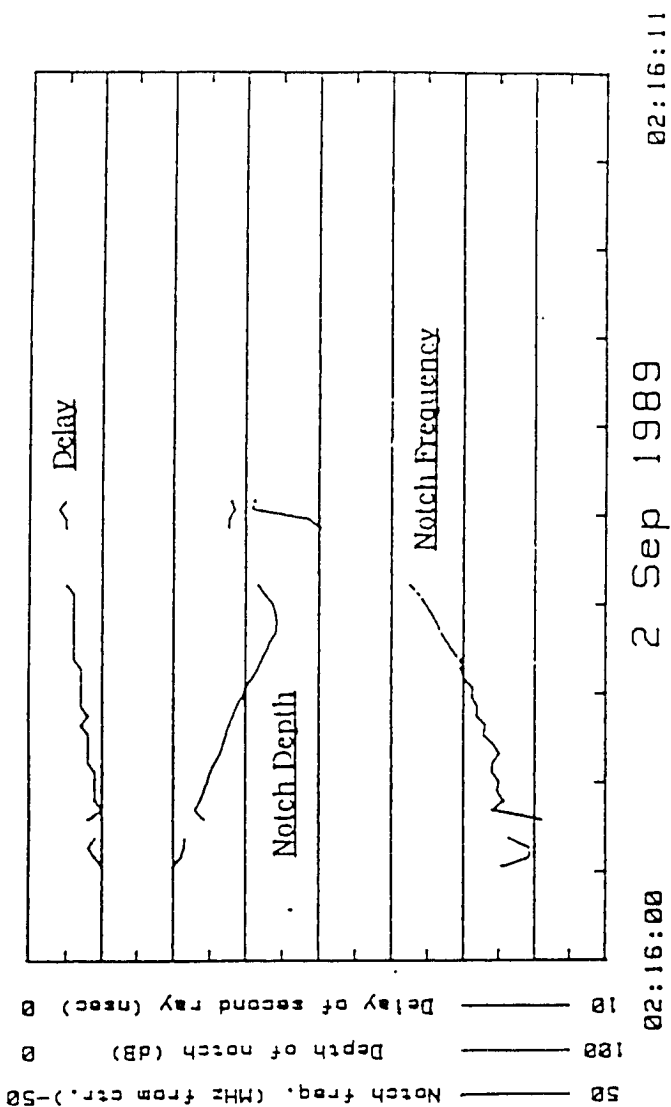


figure 4-6b

Figure 4-6b: Analysis of a Typical Multipath Event
in the 6GHz Band at Brawley, California
(Space Diversity Antenna)



simulated, and the fade data are compared to measured channel data.

The perturbation of the two ray cancellation model is used to approximate the random superposition of the direct signal and a secondary or reflected signal to simulate fading. The model allows for simulation of the signal strength and distortion from second ray magnitude and delay. Consequently, the effect of multipath interference is approximated and compared to measurements.

As before, the normalized two ray model is used to simulate channel power,

$$H(\Delta f) = 1 - b' e^{j 2\pi \Delta f \tau'} \quad (4-26)$$

where the direct ray strength is normalized to unity and the second ray strength is scaled to that of the direct. The three variables used to shape the channel are the b' , f' , and τ' . The b' represents the amplitude of a second ray normalised to the direct ray amplitude. The frequency parameter is offset from the signal minimum location or the cancellation frequency, f_0 , and is defined as $\Delta f' = f - f_0$. The delay difference τ' is relative to the direct path. The two ray propagation regime was shown in figure 3-4.

In order to simulate the statistics of multipath fading using the two ray model, the statistics of the model parameters must be determined or estimated. Multipath data from Brawley, California were recorded for 6 GHz radio and were processed for two ray fading parameters. The data were recorded for two parabolic dish feeds from September to November of 1987. Values of second ray strength b' and delay difference τ' were computed using the inverse method of the previous section. These are accumulated in figures

4-7 and 4-8. The figures show total samples versus parameter value.

The distribution of second ray strength is approximately uniform, ranging from 0.8 to 1.0 nanoseconds. The formation of a coherent reflecting area on exposed ground provides a stable source of reflected energy. As the ground becomes more coherent in its reflectivity, there is an increased reflection coefficient. The result is a significant and stable secondary path. Changes in the effective bending of rays within the lower atmosphere may cause focusing or defocusing effects. The result is a variation of the secondary ray strength. As the cancellation depth is a function of the direct and second ray strengths, the second ray strength is estimated from the cancellation depth in the signal power versus frequency domain. The estimate is most precise when the cancellation frequency is located in the channel that is being measured. Movement of the actual cancellation frequency into and out of the channel results in the variation of the estimated value. Note that a second ray strength of 1.0 will yield a total cancellation of signal at the cancellation frequency. Values of second ray strength near 1.0 are consistent with the ground cover and exposure of this link.

The distribution of delay difference peaks at approximately 0.8 nanoseconds for V1, and at approximately 1 nanosecond for V2. The distributions for both antennae have well-defined shapes, suggesting distinct secondary paths. The formation of a coherent reflecting area on exposed ground provides a stable source of reflected energy. Changes in the effective bending of rays within the lower atmosphere may cause variation of the secondary path length. The secondary signal phase is changing. The result is a changing notch frequency ($f - f_0$). The secondary ray delay τ is also varying, however, its relative change is very small. A boundary having a stable

Figure 4-7: Distribution of Delay Difference

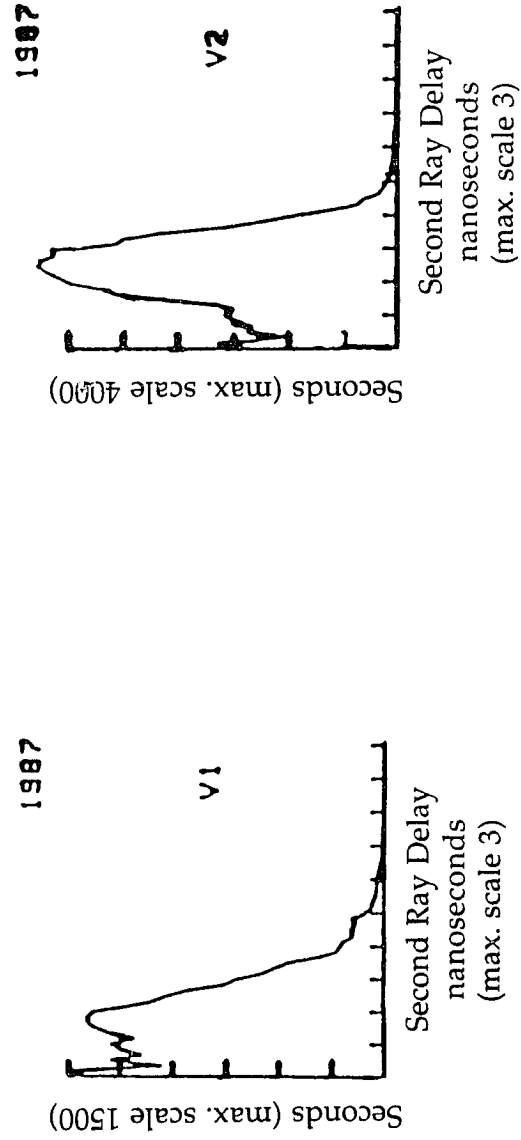


figure 4-7

Figure 4-8: Distribution of Second Ray Strength

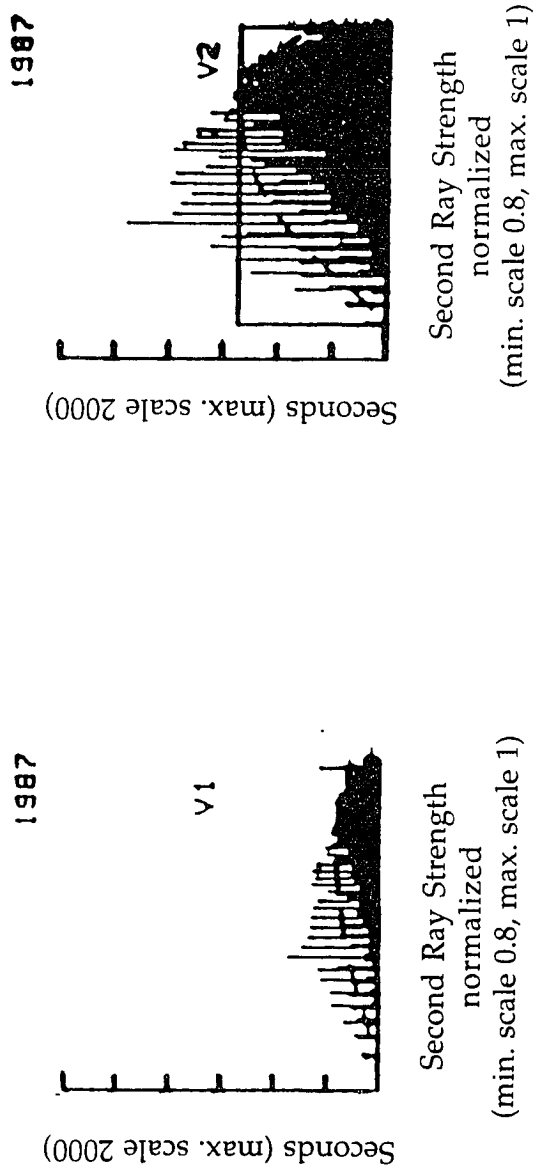


figure 4-8

reflectance amplitude but an unstable position as a function of the propagation wavelength would cause notch movement. Non-stable path length is very likely a result of a changing refractive index gradient in the lower atmosphere. This effect modulates the path length of a signal reflected from the ground. Values of delay difference from 0.8 to 1.2 nanoseconds are consistent with the characteristics of this link, as well as with the analyses of the previous sections.

In order to simulate random multipath interference, the model parameters are varied according to the distributions estimated above. The probability density function of the second ray strength is modelled to have a uniform distribution from 0.85 to 1.0. The probability distribution function of delay difference is modelled to have a sinusoidal variation from 0.5 to 1.5 nanoseconds with a peak at 1 nanosecond. Based on the random delay, the angle of arrival was estimated. The secondary ray was then scaled by the receive antenna gain for that angle of arrival, as illustrated in figure 4-9. The simulation is performed for three antenna systems: unprotected, space diversity, and angle diversity. For each system, the channel power is modelled according to equation 4-26. The parameters are varied according to the distributions for $1E+6$ random combinations. For each trial, the signal power is computed at three points in band. The frequencies correspond to the spectrum monitor frequencies used in the field measurements. In the case of space and angle diversity, receiving system selects one of the two antenna ports. Generally, diversity protection algorithms select the channel having the greater average power. The SFF and IBPD distributions, defined in section 2.5, are then computed and accumulated. These distributions are compared

to measured data in figures 4-10(a-b) - 4-12(a-b) for the various antenna systems.

Single frequency fading results for the unprotected antenna are shown in figure 4-10 (a). The computed distribution follows the trend of the measured distribution. This indicates that the shape of the delay distribution used is realistic. However, there is nearly an order of magnitude difference in the amount and depth of signal cancellation. The poor modelling of the second ray strength results in the poor estimation of the cancellation depth. The in-band power difference results shown in figure 4-10 (b) indicate similar results. While the simulated distribution follows the measured in trend, the amount and depth of dispersion are not matched. Again, incorrect second ray strength ultimately causes incorrect cancellation depth simulation, limiting the accuracy of the power difference estimate. Similar results are shown for the space diversity system. Single frequency fading is shown in figure 4-11 (a). The computed distribution does not compare well to the measured distribution. The difference in the amount and depth of signal cancellation increases with cancellation depth. As before, poor modelling of the second ray strength causes poor estimation of the cancellation depth. The results for diversity systems are compounded by the average power selection algorithm. It is selecting between two incorrectly modelled channels to simulate the fading and dispersion, thus compounding the incorrect depth. In this case, the unprotected and space antennae have similar gain patterns. The system takes advantage of phase discrimination to mitigate multipath interference. The in-band power difference results shown in figure 4-11 (b) indicate similar results. Again, incorrect second ray strength ultimately causes incorrect cancellation depth simulation, limiting the accuracy of the power difference

figure 4-9

Figure 4-9: Angle of Arrival Discrimination Due to Antenna Gain Selectivity

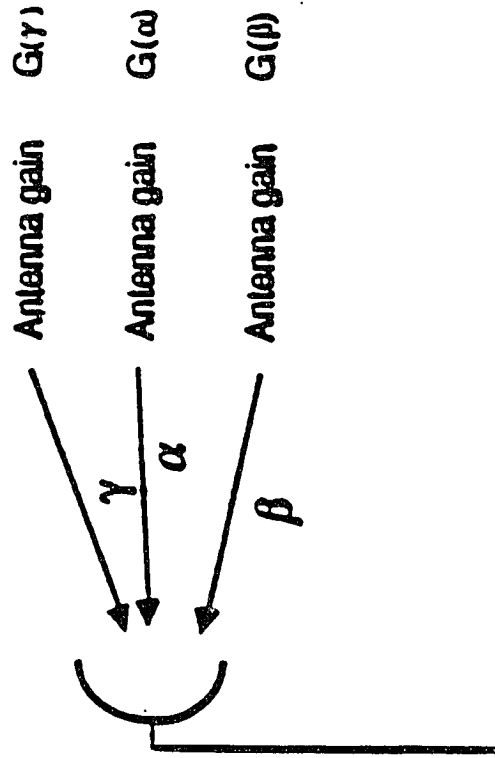


figure 4-10a

Figure 4-10a: Single Frequency Fade Time Below Level
Measured (dash) and Computed (solid)
(Unprotected Antenna)

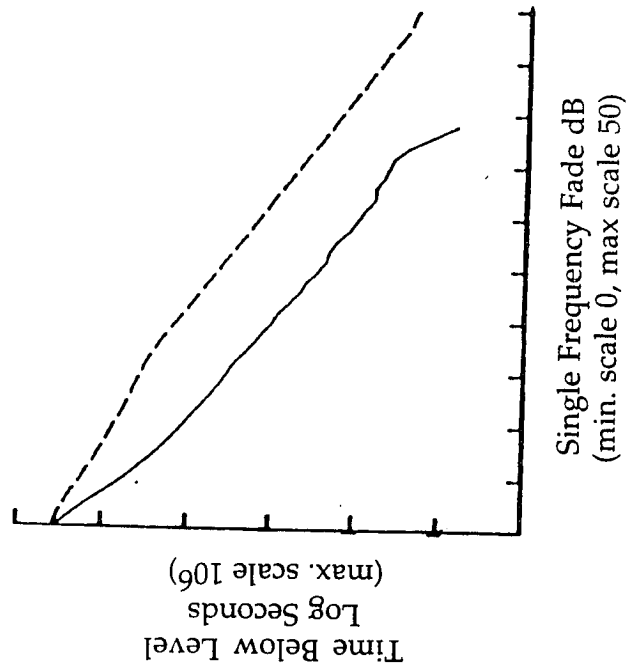
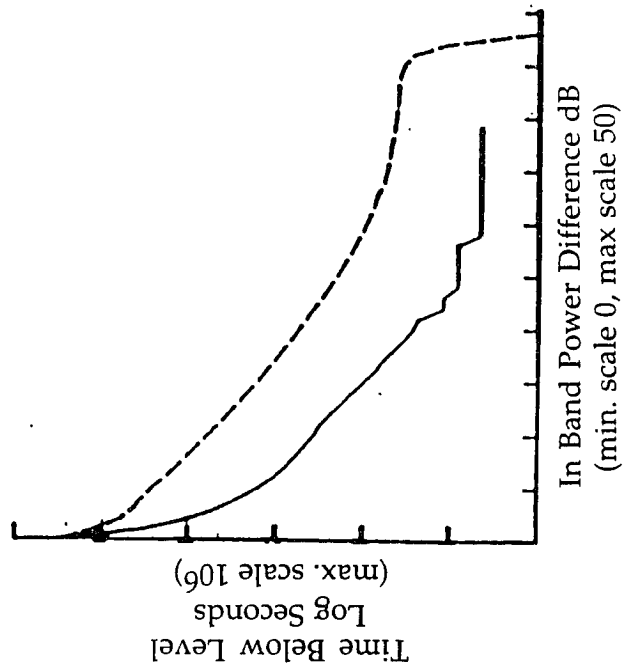


figure 4-10b

Figure 4-10b: In-Band Power Difference Time Below Level
Measured (dash) and Computed (solid)
(Unprotected Antenna)



estimate. Lastly, results are shown for the angle diversity system. Single frequency fading is shown in figure 4-12 (a). The computed distribution is even less well matched to the measurements than for the previous systems. The difference in the amount and depth of fading increases with the cancellation depth. As before, poor modelling of the second ray strength causes poor estimation of cancellation depth. The error is compounded by the average power selection algorithm. It is selecting between two incorrectly modelled channels to simulate the fading and dispersion, thus compounding the incorrect fade depth. In this case, the angle diversity antennae have different gain patterns, biased according to angle of arrival. The system takes advantage of gain discrimination to mitigate multipath interference. The in-band power difference results shown in figure 4-12 (b) indicate similar results. Again, incorrect second ray strength ultimately yields an incorrect value of the cancellation depth, limiting the accuracy of the power difference estimate.

The simulation performed in this section is an illustration of the limitations of statistical modelling. Atmospheric phenomena, such as multipath interference on a terrestrial microwave link, are random in nature and therefore difficult to predict in a precise manner. Only ranges and constraints can be established and fine-tuned. Even when the model parameters are physically valid, such as the case of a two ray model, the behaviour of these parameters cannot be characterized. This naturally would allow one to question the validity of applying a statistical two ray model, as there is an inherent uncertainty in selecting proper distribution functions and simulation techniques.

figure 4-11a

Figure 4-11a: Single Frequency Fade Time Below Level
Measured (dash) and Computed (solid)
(Space Diversity System)

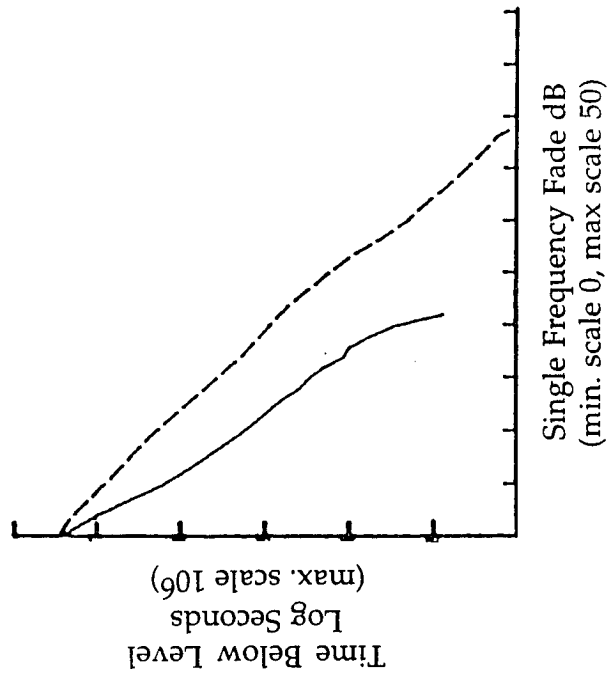


figure 4-11b

Figure 4-11b: In-Band Power Difference Time Below Level
Measured (dash) and Computed (solid)
(Space Diversity System)

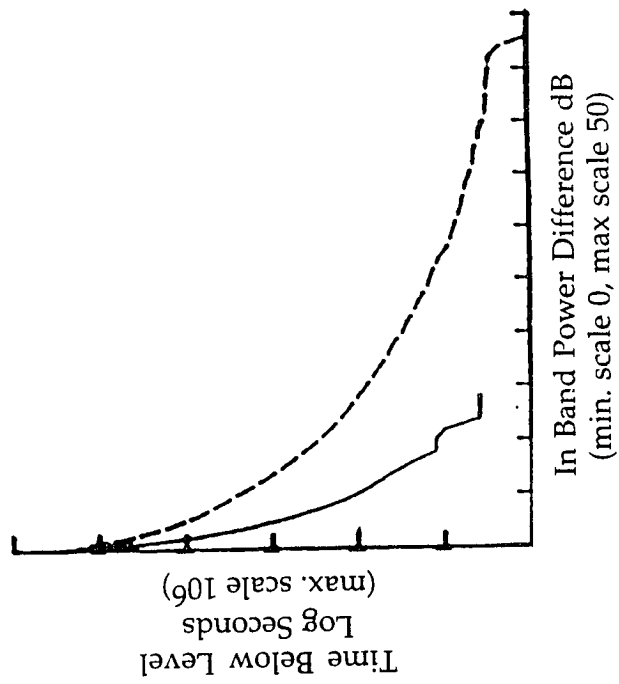


figure 4-12a

Figure 4-12a: Single Frequency Fade Time Below Level Measured (dash) and Computed (dot) (Angle Diversity System)

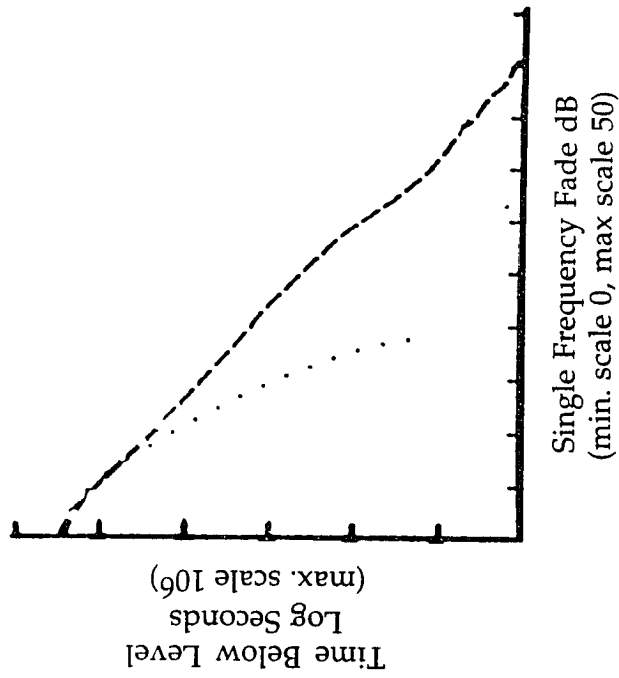
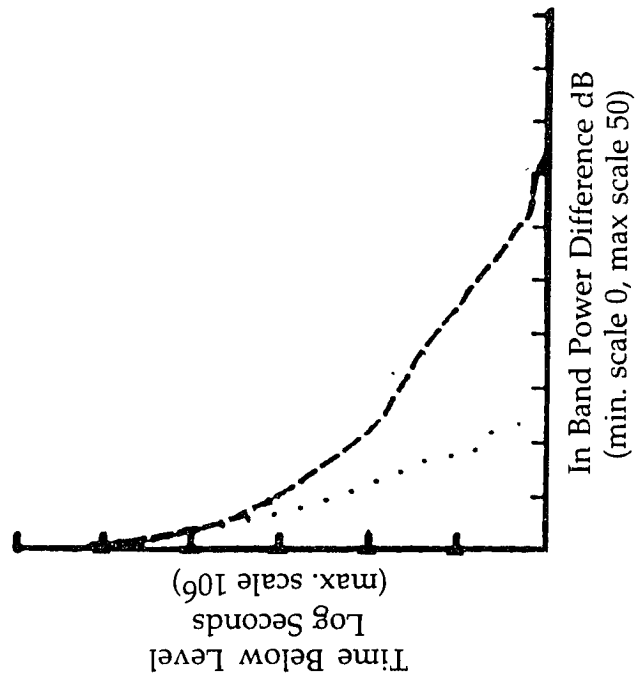


figure 4-12b

Figure 4-12b: In-Band Power Difference Time Below Level
Measured (dash) and Computed (dot)
(Angle Diversity System)



4.5 Summary

The various types of models discussed in sections 4.2 through 4.4 to the multipath problem allowed us to compare the results of the different analyses. The forward multipath model identified the path parameters for a typical line-of-sight microwave link. With the help of the forward model, typical values of the parameters were estimated, and made it possible to predict interference sources from ground reflections. An inverse multipath model was then established from the channel model. It enabled us to compute the two ray parameters from channel data. Finally, the statistical model allowed us to estimate the channel magnitude and shape based on random simulations using probability distribution functions for the two ray parameters.

While these approaches can predict the effects of multipath interference, the probability of multipath interference cannot be predicted thus far as the predominant physical propagation parameters are both random and unique to each line-of-sight path. However, the importance of the second ray delay difference to channel distortion was apparent in each analysis. A constant delay causes a coherent reflected wavefront to be formed travelling along a stable secondary path. At the receiver this wavefront acts as an interfering signal to the direct transmission. It is therefore appropriate to study both digital modem and digital signal responses as functions of the second ray delay.

CHAPTER V

MODEM PERFORMANCE

Introduction

In this chapter, a receiver channel model is defined, based on the analysis of chapter 4. A static multipath interference signature for modem performance is then reviewed and a new signature for the characterization of the effects of dynamic multipath interference is introduced. Signature algorithms for the evaluation of digital radio systems are then developed based on the objectives and measures described in chapters 1 and 2 and the hardware and software configurations are described. Modem signatures for various multipath conditions are measured and examined to determine the extent to which channel model parameters affect modem performance. In section 5.1 performance characterization of digital radio systems is reviewed. In section 5.2 the interference signature is introduced. In section 5.3 the multipath channel model is reviewed. In section 5.4 the static and dynamic signature theory is developed. In sections 5.5 and 5.6 the signature measurement software and implementation are described. In section 5.7 the signature method, channel model, and performance results are discussed. In section 5.8 the performance of QAM is analyzed. In section 5.9, the receiver performance in the presence of multipath interference is reviewed.

5.1 Digital Radio Performance Characterization

The desire to compare the performance of different digital radio systems and configurations requires evaluation of their capability for transmission in the presence of communication channel distortion. This has resulted in the development and use of interference signatures which produce variable multipath distortions in order to determine the thresholds of error-free performance [37].

Static signatures, referred to as M-curves in the literature, are obtained by varying the simulated channel parameters. The cancellation depth and the cancellation frequency are varied for a fixed second ray delay of 6.3 nanoseconds in order to determine the values required for a particular performance threshold. Typically, a channel unavailability criterion is selected, such as the threshold of outage, a BER of 10^{-3} . A static implementation of modem signature, such as the M-curve, is used to baseline the performance of an unprotected radio system. Any point on the threshold curve defines a set of fixed parameters which result in the desired performance criterion. The two ray channel model developed in chapter 4 is used to develop the signature. The power at the channel minimum, or so-called "notch depth", and frequency of the channel minimum, or "notch frequency" are two relevant parameters for control. Location of a strong notch with frequency in-band is analogous to creating an interfering signal that is a delayed replica of the direct signal, with the delay equal to an odd integer multiple of the the signalling half-period (i.e. out-of-phase). The resulting channel distortion causes a loss of information. The static signatures simulate the multipath channel with fixed parameter values and are sufficient for determining the threshold of performance for a modem.

Real multipath phenomena are unstable, as was shown in the examples of chapter 4. The two ray parameters vary, causing distortions which sweep through the communication band very quickly. Countermeasures are designed (1) to avoid these severe channel outages by protection switching, (2) to correct for less severe impairments using error correction codes, and (3) to compensate for moderate channel distortions by adaptive equalization. The ability of a radio system, with or without countermeasures, to perform in the presence of active multipath fading is not adequately simulated with the static signature.

A dynamic signature is developed in this chapter in order to simulate the effect of a dynamic multipath channel on radio system performance. The signature is a threshold curve identifying the regions of parameter changes over which signal transmission is impaired. From the analysis of the two ray channel model, it is clear that the important parameters for digital signal distortion are the "notch depth" (cancellation depth) and the "notch frequency" (cancellation frequency). The movement of a cancellation frequency through the channel is analogous to the variation of the path length or delay of an interfering signal that is a delayed replica of the direct signal. This is typically the result of variations in the gradient of the atmospheric index of refraction along the path. The deepening of a cancellation is analogous to an increase of the ratio of the secondary to direct signal power. This is typically caused by de-focussing of the direct signal or focussing of the secondary signal by a nonlinear gradient in the atmospheric index of refraction. In either case, the dynamic channel distortions causes a loss of information. The results of this chapter will show that QAM performance depends strongly on the second path delay.

5.2 Multipath Signatures

A static multipath signature characterizes modem performance in the presence of fixed fade conditions. In the case of the two ray channel model, the parameters are cancellation frequency, second ray amplitude, and second ray delay. The presence of substantial signal cancellation in the channel generally results in system outage. Second ray amplitude determines the cancellation depth. Substantial signal attenuation or cancellation due to a second path results in digital outage. Path length determines both the overall shape of the two ray channel and the location of the cancellation frequencies. Smaller delay results in greater separation of minima in the frequency domain, and consequently determines the amount of shape in the band. The presence of substantial shape in the channel frequency response generally results in digital errors by causing cross-talk between the quadrature vectors. For the static signatures [43], the cancellation frequency is selected and the ratio of secondary to direct signal power is varied until a specified BER is obtained. The ratio of signal power determines the "notch depth". The critical notch depth is identified for each cancellation frequency of interest. The second ray delay is typically fixed to 6.3 nanoseconds for this signature.

Results of dynamic testing have been reported in the literature. One form of signature is an iso-error curve [41]. It gives a trajectory of constant BER performance with respect to variations in fade parameters. This is a direct extension of the M-curve into time and does not allow for the evaluation of protection switching. Another method [42] allows for variations of the notch frequency. The notch is varied about a fixed frequency. It is a type of M-curve that tests adaptive equalizers. It also does not evaluate protection switching.

A dynamic multipath signature characterizes modem performance in the presence of active and changing fading conditions. In the case of the two ray channel model, this involves the dynamic cancellation frequency, the dynamic second ray amplitude, and the dynamic second ray delay. Variation of the second ray amplitude changes the cancellation depth and results in direct signal de-focussing or secondary signal focussing. These dramatic changes in signal level result in digital errors. The variation of path length sweeps the cancellation frequencies and changes the overall shape of the channel. As a result, channel slopes change as minima move into and out of the band. For example, as the delay increases, the minima narrow and their separation decreases in the frequency domain. Consequently, the signal power extrema in a fixed band increase with delay. Dynamic distortions in the channel frequency generally cause digital outage by impairing carrier detection and timing recovery processes.

The dynamic signature couples the dimension of time onto the static signature. It also provides a simulated test scenario that closely resembles the multipath fade environment. Three dynamic signatures are developed in this dissertation. They are threshold curves which identify the region of error-free performance for a radio system. The first case is a BER threshold curve for the rate of change of the cancellation depth \mathbf{B} (secondary to direct signal power ratio \mathbf{b}) as a function of cancellation frequency $\mathbf{f_0}$ for a fixed second ray delay τ . The second case is a BER threshold curve for the rate of change of the cancellation frequency as a function of cancellation depth for a fixed second ray delay. The third case is a bit error threshold curve for the rate of change of both cancellation depth and frequency.

The signature analysis and the data that follow will show that: (1) the signatures are independent of the phase state, (2) the signatures are independent of broadband attenuation for values appreciably less than the fade margin, (3) the dynamic "notch depth" curve is independent of second ray delay and is mainly a function of the difference in 10^{-3} and 10^{-6} M-curves, (4) the dynamic "notch frequency" curve, like the static curve, is related to the second ray delay, and (5) that the radio system suffers fewer switching errors as the second ray delay is decreased.

5.3 Channel Model

It was shown in section 3.3 that interference produced by multipath propagation may be approximated by using a two ray model as in equation (3-9),

$$H(f-f_0) = a (1 - b e^{j2\pi(f-f_0)\tau}) \quad (5-1)$$

where the parameter **a** represents the broadband or flat fade component which attenuates both signals. Similarly, the parameter **b** represents the secondary signal normalized to the direct. As before, $f - f_0$ is the offset frequency of observation f from the cancellation frequency f_0 .

Rummler [3] used equation (5-1) with the delay difference arbitrarily fixed to 6.3 nanoseconds. The remaining three parameters, **a**, **b**, f_0 , were adjusted to fit the channel shape. As was previously discussed in section 1.2, multipath fading is hardly ever the result of two ray fades with delays of 6.3 nanoseconds [1-12]. This conclusion is supported by the data collected for this study, as is shown in figure 4-7.

In a two ray channel, the response is minimum phase if the larger ray arrives before the smaller ray, as was described in section 3.3. It is non-minimum phase if the smaller ray arrives first.

For the two ray model, there is a direct relationship between the second ray delay τ , and the n^{th} cancellation frequency f_0 [43],

$$\tau (n) = n / 2 f_0. \quad (5-2)$$

The two ray cancellation results in a series of signal minima in the frequency domain. The separation frequency of these minima is proportional to the inverse of the delay difference. From equation (5-2), the frequency separation is related to the second ray delay, or vice-versa. As a result, the rate of change for the notch frequency is related to the rate of change for the second ray delay.

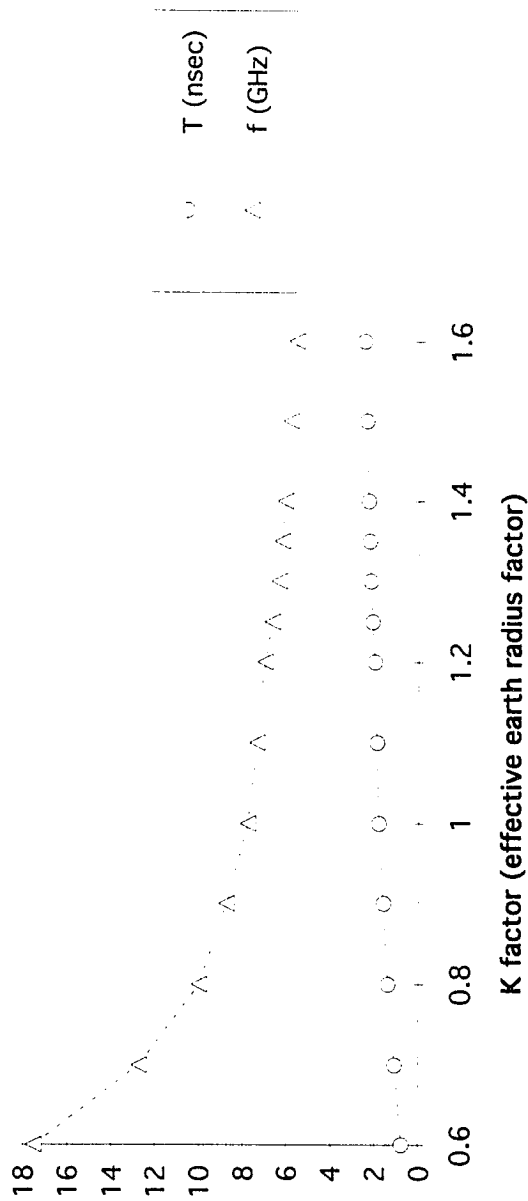
On a microwave link with a ground reflection, changes in the K factor cause a spatial displacement of the ground reflection, and therefore a change in the effective path length. The result is a variation in second path delay and a movement of the cancellation frequency. This result is shown in figure 5-1. The overall change in K factor from 0.6 to 1.6 yields an overall movement of the cancellation frequency of approximately 10 GHz.

The fade is in a minimum phase state if the larger ray arrives before the smaller ray. It is in a non-minimum phase state if the smaller ray arrives first.

The normalized two ray implementation discussed in section 4.2 is used to simulate the dispersive part of multipath fading in equation (4-13). Similar to equation (5-1), the second ray strength \mathbf{b} is scaled to that of the

figure 5-1

Figure 5-1-1: Second Path Delay and Signal Cancellation Frequency as a Function of Effective Earth Radius



direct, however in this case the direct ray strength a is normalised to unity. The three variables used to shape the channel are similarly b , f , and τ . The variable b is more commonly referred to as the cancellation depth B , where

$$B = -20 \text{ Log}_{10}(1 - b) \quad (5-3)$$

Similarly, the parameter a of (5-1) is more commonly referred to as the flat fade A , where

$$A = -20 \text{ Log}_{10}(a) \quad (5-4)$$

Physically acceptable values of delay and second ray strength from field measurements are used. However, the attenuation component a of the generalized two ray model is not considered.

The generalized implementation of equation (3-10) is compared to the normalized two ray implementation of equation (3-11) used in this dissertation. Comparison at the cancellation frequency results in the following relationships for the respective parameters (generalized parameters a , b , τ , f_0 versus normalized parameters b' , τ' , f_0'):

$$f_0' = f_0 \quad (5-5)$$

$$B' = A + B, \text{ and} \quad (5-6)$$

$$\tau' = (a b \tau) / b' \quad (5-7)$$

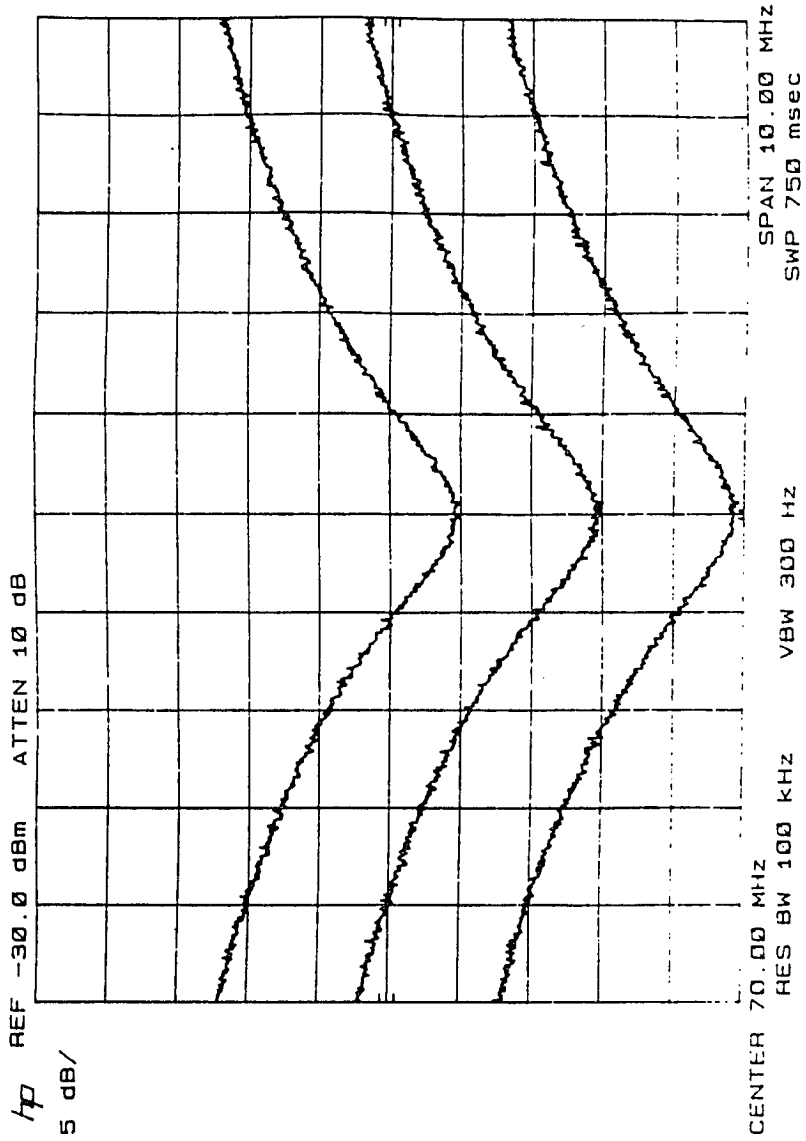
Physical measurements of multipath fading parameters and their variations are documented in section 4.3. Various cancellation frequency movements, some as fast as 100 MHz per second, have been recorded. Cancellation depth changes on the order of tens of dB per second have also been noted [43, 47-50]. Multipath delay difference data have also been published in several references. As discussed in section 4.3, second path delay measurements vary widely, from 1 to 8 nanoseconds [10, 40]. Analysis for typical multipath events performed in section 4.4 revealed notch movements in the range of 15 MHz/second for second ray delays of 1 - 2 nanoseconds at one antenna, and 0.5 - 1 at another.

The differences in channel shape from a two ray fade with varying flat fade components **A** are shown in figure 5-2a. The shape of the channel is shown to remain consistent. However, the signal level at any frequency is shown to drop corresponding to the attenuation value **A**.

The results of changing notch depths **B** on the effective channel are shown in figure 5-2b. As is expected, **B** corresponds to signal level at the channel power minimum. However, the effect of **B** on the channel shape diminishes with increasing distance from the cancellation frequency.

The difference in channel shape that results from simulating a two ray fade with differing delay values τ is plotted in figure 5-2c. As is shown, the delay τ has the most dramatic effect on the overall channel shape. For different values of τ , channel shapes are similar at the notch frequency only. There is substantial difference in both shape and signal strength for channels of different delay. The Rummler implementation yields a channel shape that is constrained by the 6.3 nanosecond delay. The broadband shape of the Rummler implementation is not applicable to modelling multipath

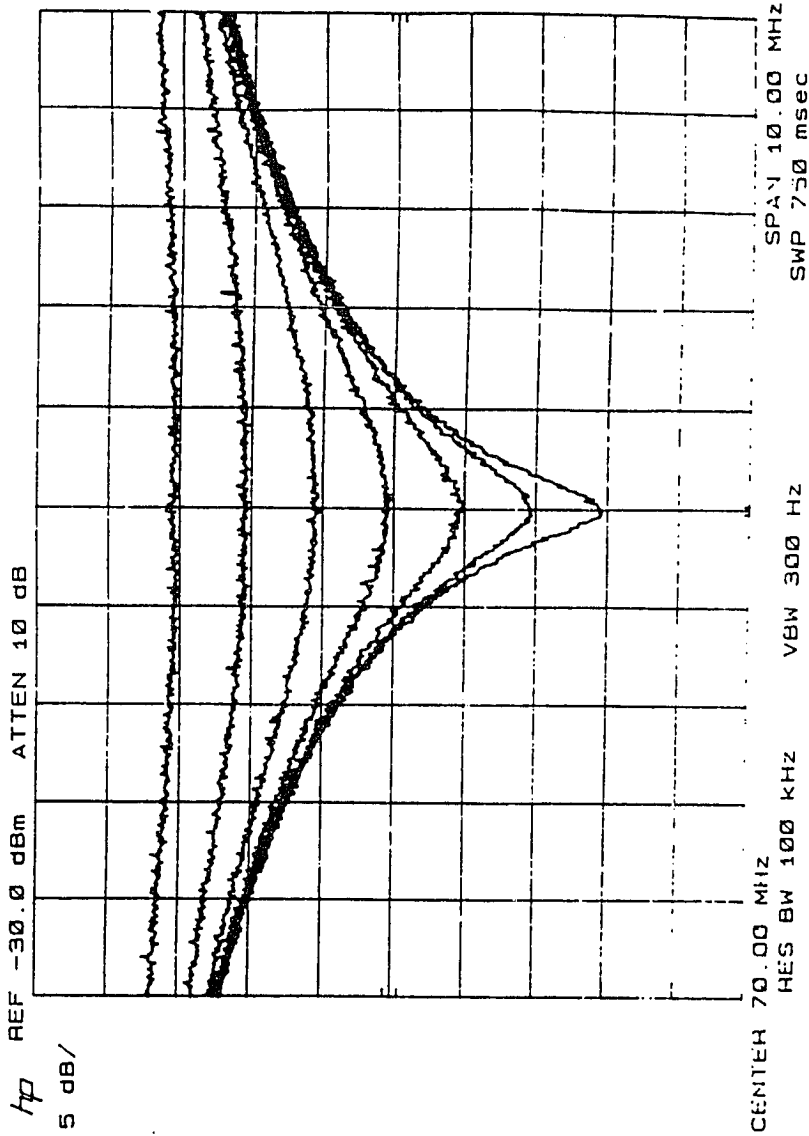
Figure 5-2a: Signal Level in the Frequency Domain
as a Function of the Broadband Attenuation Parameter A



$\tau = 6.3 \text{ ns}$
 $B = 30 \text{ dB}$
 $A = 0 \text{ dB}$
 $A = 10 \text{ dB}$
 $A = 20 \text{ dB}$

figure 5-2a

Figure 5-2b: Signal Level in the Frequency Domain
as a Function of the Null Depth B



A = 0 dB

$\tau = 6.3$ ns

B = 10 dB *figure 5-2b*

B = 15 dB

B = 20 dB

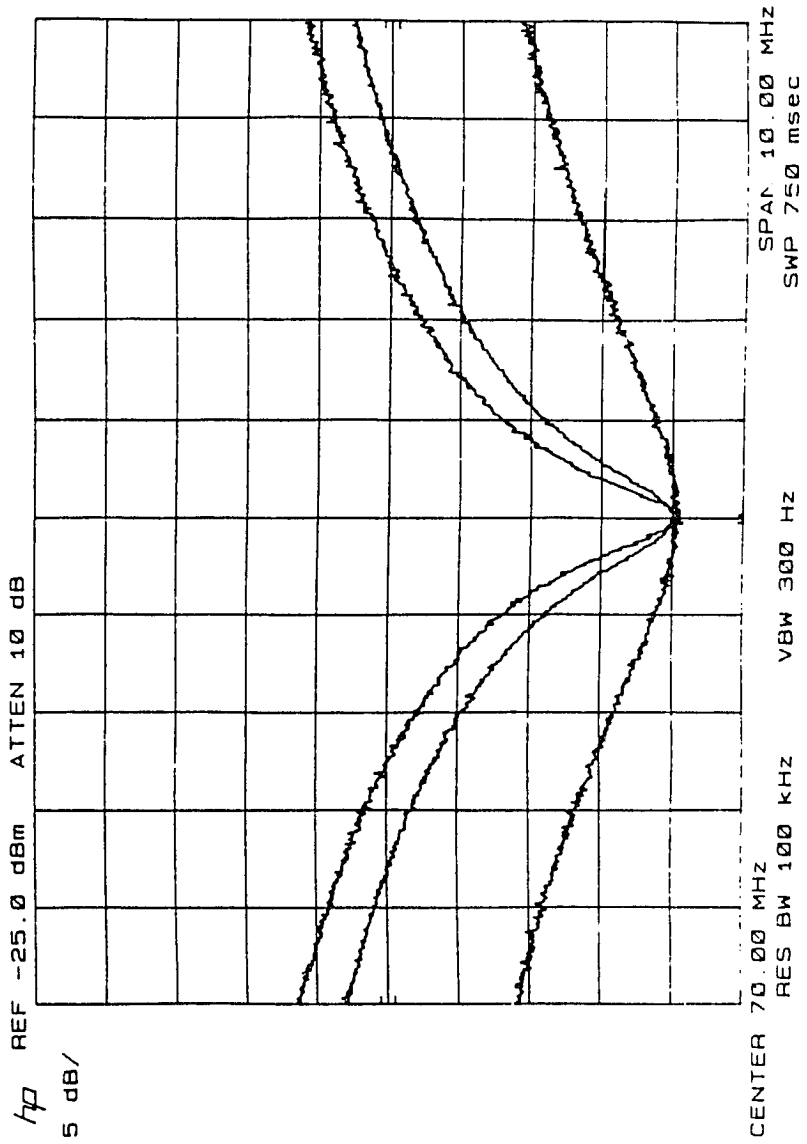
B = 25 dB

B = 30 dB

B = 35 dB

B = 40 dB

Figure 5-2c: Signal Level in the Frequency Domain
as a Function of the Delay Difference τ



A = 0 dB

B = 40 dB

$\tau = 6.3$ ns

$\tau = 4.0$ ns

$\tau = 1.0$ ns

figure 5-2c

channels in general because of the delay variations that are possible.

A physically realistic propagation environment must be simulated to adequately stress the radio system. This is necessary to evaluate performance and to identify those factors which limit operation.

A modem performance signature that incorporates more accurately the effects of multipath propagation is developed in this chapter. Inclusion of an attenuation component allows the variation of the thermal noise floor to be considered [37]. Selection of the value of second ray delay allows simulation of physically real and different second ray paths. Sweeping of the "notch frequency" simulates the effect of variations in delay caused by perturbations in atmospheric refraction. Modulation of the "notch" depth simulates the effect of variations in signal strength caused by atmospheric focussing effects. The simulation of these dynamic effects allows a complete characterization of channel behavior as a function of both frequency and time. The increased degrees of freedom and the variation of parameters in time and frequency result in a model that more closely resembles the effect of multipath propagation on line-of-sight communications.

5.4 Signature Theory

In general terms, the two ray model introduced in section 3.3 may be viewed as a sum of a direct signal phasor $\underline{\alpha}$ and an interfering phasor $\underline{\beta}$,

$$\sigma e^{j\phi} = \alpha e^{j\omega\tau_\alpha} - \beta e^{j\omega\tau_\beta} \quad (5-8a)$$

where τ_α is the propagation delay of the direct signal and τ_β is that of the second. Normalizing the phase relationship to the direct signal results in a generalized representation for the composite signal,

$$\sigma e^{j\phi'} = \alpha - \beta e^{j\omega\tau'} \quad (5-8b)$$

where the delay difference is

$$\tau' = \tau_\beta - \tau_\alpha. \quad (5-8c)$$

The composite ray \underline{L} may be substantially weaker than the direct ray $\underline{\alpha}$ [43].

More precisely, the direct signal has a magnitude α , and the interferer has magnitude β and phase $\omega\tau$ relative to the direct. This results in a composite phasor of magnitude L and angle ϕ ,

$$L = \left(\alpha^2 + \beta^2 + 2 \alpha \beta \cos \omega \tau \right)^{\frac{1}{2}}, \quad (5-9a)$$

$$\phi = \tan^{-1} \left\{ \frac{(\beta \sin \omega \tau)}{(\alpha + \beta \cos \omega \tau)} \right\}. \quad (5-9b)$$

Comparison to the two ray model of (5-1) yields

$$\omega = 2 \pi (f - f_0) \quad (5-10a)$$

$$\alpha = a \quad (5-10b)$$

$$\beta = -b. \quad (5-10c)$$

For the normalized model the variables are,

$$\alpha = 1 \quad (5-11a)$$

$$\beta = -b'. \quad (5-11b)$$

Defining the signal strength at the cancellation frequency as,

$$\lambda = \alpha - \beta, \quad (5-12)$$

and expanding equation (5-9a) as a power series about the cancellation frequency f_0 yields

$$\mathbf{L} \approx \mathbf{L}(f - f_0) + 2\pi(f - f_0)\dot{\mathbf{L}}(f - f_0) + (2\pi(f - f_0))^2 \frac{\ddot{\mathbf{L}}(f - f_0)}{2}. \quad (5-13)$$

At the cancellation frequency, equation (5-9a) and its derivatives are found to be:

$$\mathbf{L}(f - f_0) = \lambda \quad (5-14a)$$

$$\dot{\mathbf{L}}(f - f_0) = 0 \quad (5-14b)$$

$$\ddot{\mathbf{L}}(f - f_0) = \left(\frac{\alpha\beta\tau^2}{\alpha - \beta} \right). \quad (5-14c)$$

For deep fades, λ is small and $\beta = (\alpha - \lambda) \simeq \alpha$. For the normalized model, $\alpha = 1$. At the cancellation frequency, $\alpha\beta \simeq 1$. The cancellation depth versus frequency characteristic becomes

$$\mathbf{L} \approx \lambda + \left(\frac{1}{2} \right) (2\pi(f - f_0))^2 \left(\frac{\tau^2}{\lambda} \right). \quad (5-15)$$

In order to express (5-15) as a function of only the cancellation frequency, the cancellation depth and second ray delay are removed from consideration. In the analysis of nonlinear channel distortion, the absolute channel amplitude is not as important as the difference in amplitudes throughout the channel, Consequently, both sides of equation (5-15) are normalised for amplitude,

$$\frac{\mathbf{L}}{\lambda} \approx 1 + \left(\frac{1}{2}\right) (2 \pi (f - f_0))^2 \left(\frac{\tau}{\lambda}\right)^2. \quad (5-16)$$

For a first order approximation, the relationship between λ and τ is assumed to be linear so that

$$\lambda = m \tau, \quad (5-17)$$

then expression (5-16) becomes

$$\frac{\mathbf{L}}{\lambda} \approx 1 + \left(\frac{1}{2}\right) (2 \pi (f - f_0))^2 \left(\frac{1}{m}\right)^2. \quad (5-18)$$

The equation (5-18) is a function of the offset frequency $(f - f_0)$ and of the amplitude to delay ratio m [43]. Signatures for similar systems with different delays are therefore related by this scale factor m .

To estimate the effect of cancellation frequency movement on the performance characteristic (5-17), the cancellation frequency f_0 may be expressed as a function of time,

$$f_0(t) = v_f t + f_1. \quad (5-19)$$

The parameter v_f represents the cancellation frequency velocity

$$v_f = \frac{(f_2 - f_1)}{(t_2 - t_1)}. \quad (5-20)$$

The parameters t_1 and f_1 are the initial time and frequency. The t_2 and f_2 are the final time and frequency. The linear variation is a limitation of the test equipment.

The derivative of (5-18) with respect to time has the expected dependence on cancellation frequency velocity v_f . It is also dependent on the ratio of normalised amplitude to delay m ,

$$\frac{\dot{L}}{\lambda} = 2 (2 \pi m)^2 (v_f^2 t - v_f f + v_f f_1). \quad (5-21)$$

Thus, the overall dynamic cancellation frequency characteristic is related to delay by m^2 . This scale factor is the ratio of cancellation depth to second ray delay. The result is a signature shape that is dominated by the second ray delay for deep fades. The performance curve for dynamic cancellation frequency is a function of the second ray delay, or of the secondary path length characteristics. For multipath interference with changing cancellation frequencies, system performance is independent of the atmospheric focussing. The dynamic cancellation frequency signature is a non-linear function of the cancellation frequency velocity and of the factor m^2 , and as a result, its behaviour is not related to that of the static signature.

In order to express (5-15) as a function of only the cancellation depth, the cancellation frequency and the second ray delay are removed from consideration. If the relationship between $f - f_0$ and τ is linear, then

$$p = 2 \pi (f - f_0) \tau. \quad (5-22)$$

Expression (5-15) becomes

$$\mathbf{L} \approx \lambda + \frac{1}{2} \left(\frac{p^2}{\lambda} \right). \quad (5-23)$$

The shape, characterised by the second order approximation of equation (5-23), represents system performance in the presence of static, or fixed parameter, multipath interference. It is a function of cancellation depth λ and of the product of offset cancellation frequency and delay p . Signatures for similar systems with different delays are therefore related by this scale factor p .

In order to estimate the effect of change in cancellation depth on the performance characteristic (5-23), the cancellation depth λ is assumed to be a linear function of time,

$$\lambda(t) = v_\lambda t + \lambda_1. \quad (5-24)$$

The parameter v_λ represents the cancellation depth velocity

$$v_\lambda = \frac{(\lambda_2 - \lambda_1)}{(t_2 - t_1)}. \quad (5-25)$$

The parameters t_1 and λ_1 are the initial time and frequency. The t_2 and λ_2 are the final time and frequency. The linear variation is a limitation imposed by the test equipment.

The derivative of (5-23) with respect to time is composed of two terms which are dependent on cancellation depth velocity v_λ . One term is also dependent on the product of offset frequency and delay p ,

$$\dot{\mathbf{L}} = v_\lambda - \frac{p^2}{2} \left(\frac{v_\lambda}{(v_\lambda t + \lambda_1)^2} \right). \quad (5-26)$$

For deep fades or small λ_1 , the expression (5-26) becomes

$$\dot{\mathbf{L}} \approx v_\lambda - \frac{p^2}{2 v_\lambda t^2}. \quad (5-27)$$

The dependence of the dynamic cancellation depth characteristic on the frequency and delay product is limited to the second term of equation (5-27). It is diminished by the denominator term, which is the product of depth velocity and time squared. The resulting signature is dominated by the first term, and is relatively independent of second ray delay. The performance curve for dynamic cancellation depth is a function of the depth velocity only, or of the focussing effect of the atmosphere. For multipath interference with changing cancellation depths, system performance is independent of the secondary path length. The dynamic cancellation depth signature is mainly a function of cancellation depth velocity, and its behaviour is therefore related to the static signature for different values of cancellation depth.

5.5 Signature Algorithm

For the static signature, the two ray parameters are fixed and the resulting system performance (BER) of the radio is measured. The effect of dynamic variations on BER is not examined. In a dynamic signature, radio performance is examined in terms of line BER (before protection) or DS-3 bit errors (after protection). Fade parameters are varied at a fixed rate. In this section, a static signature measurement based on BER is implemented. In addition, two dynamic signatures based on bit error performance are developed and measured. A dynamic "notch depth" signature, a dynamic "notch frequency" signature, and a bit error performance curve for dynamic depth and frequency, are all shown.

The energy reflected from the earth is a function of the path topology. The terrain may be viewed as an amalgam of random scatterers producing diffuse reflections of the source. If the terrain is smooth when compared to the wavelength of the incident energy, a coherent image is formed and a specular reflection results [44].

For the static signature using equation (5-1), values of \mathbf{a} , \mathbf{b} , \mathbf{f}_0 , τ , and phase state are selected for a desired channel shape. These are programmed in a multipath fade simulator. The radio performance is examined in terms of a threshold BER, as is done for the M-curve [43]. Generally $\mathbf{a}=1$, and $\tau=6.3$ nanoseconds. The notch position is incremented from just below the lower cutoff frequency of the channel to just above the upper cutoff frequency. At each frequency, the "notch depth" is increased by incrementing \mathbf{B} . This is repeated until the desired threshold BER is measured. The different static multipath signatures which were measured are related by equation (5-18).

The dynamic "notch frequency" signature sweeps through a band of 60 MHz. The test fixes the attenuation, the strength, and the delay of the secondary ray with respect to the direct ray. However, the secondary path or reflection phase is changing. The result is a changing "notch frequency" ($f - f_0$). In reality, the secondary ray delay τ also changes. However, it is inversely proportional to the spacing between adjacent notches. Its relative change is very small and so it is treated as a constant for the simulation. A boundary having a stable reflection coefficient but an unstable position as a function of the propagation wavelength would cause notch movement. Non-stable path length is very likely a result of a changing refractive index gradient in the lower atmosphere. This effect modulates both the direct and reflected signals. The parameters a , τ , phase, and initial and final notch positions f_0 in equation (5-1) are all fixed. For each notch position pair, a sweep time is programmed. The sweep time is calculated according to the desired speed of the notch frequency change. The sweep time is decremented, resulting in incremented notch frequency speed. The process is repeated until bit errors are detected for that particular notch notch frequency pair. Bit errors are monitored at the DS-3 output of the receiver terminal. The signature is measured for discrete values of notch depth B from a lower to upper limit. The different dynamic cancellation frequency signatures which were measured are related by equation (5-21).

The dynamic "notch depth" signature changes the depth from an initial to a final value by varying the second signal amplitude. This occurs at a specific frequency within the radio channel. In equation (5-1), the offset "notch frequency" ($f - f_0$), attenuation a , and second ray delay τ , are all constant. However, the secondary ray strength b is changing. This results in a

changing "notch depth". The process represents a propagation environment where there is a boundary that is stable in position as a function of the propagation wavelength. However the reflected energy is not stable in strength. A stable refractive index gradient in the lower atmosphere will give rise to a constant secondary path delay. A discontinuity or abrupt change in the refractive index gradient at some fixed altitude may give rise to refracted rays. An example would be the formation of a homogeneous layer in the lower atmosphere. Such a layer would be transient in nature and vary in height and density. On the other hand, the formation of a coherent reflecting area on exposed ground is a much more predominant and stable source of reflected energy. As the ground becomes more coherent in its reflectivity, there is an increased reflection coefficient. The result is a stronger secondary ray. Changes in the effective bending of rays within the lower atmosphere may cause focusing or defocusing effects. The result is a modulation of the secondary ray strength. The signature fixes the two ray parameters a , τ , and phase, as well as initial and final "notch depths" B . The "notch frequency" ($f - f_0$) is incremented from just below the lower cutoff frequency of the channel to just above the upper cutoff frequency. At each position, a sweep time is programmed. The sweep time is calculated for a desired speed of "notch depth" change. The sweep time is decremented, resulting in incremented "notch depth" speed. The process is repeated until bit errors are detected for that particular "notch frequency" and "notch depth" speed pair. Bit errors are monitored at the DS-3 output of the receiver terminal. The different dynamic cancellation depth signatures which were measured are related by equation (5-27).

The bit error performance curve represents a sweep of both notch frequency and notch depth. The parameters α , τ , phase state, initial and final notch positions f_0 , and initial and final notch depths B are all fixed. A sweep time is programmed for an initial speed of the notch frequency change. This sweep time specifies the speed of corresponding notch depth change. Once the simulation is complete, the DS-3 bit errors are recorded and plotted. The sweep time is decremented, resulting in incremented notch frequency and notch depth speeds. The DS-3 bit error burst is again recorded. The procedure is repeated until a maximum speed is reached. The exercise does not produce a three-dimensional signature. It gives an indication of system response to simultaneous variation of two fade parameters, notch depth and notch frequency.

5.6 Implementation

The static and dynamic signatures are measured using a Hewlett-Packard series 300 computer workstation. The software is composed of approximately 2500 lines of commented code written in the Hewlett-Packard interpretive basic program development environment. It is menu-driven and is divided into subroutine modules.

Software modules actively control an HP 11757A Multipath Fade Simulator via the IEEE-488 instrument bus. In this application, the HP 11757A is placed in the IF path between output of the RF Downconverter and the input of the Linear Delay Equalizer. The Fade Simulator allows variation of the two ray parameters. Attenuation A ranges from 0 to 40 dB. Notch depth B ranges from 0 to 40 dB. Second ray delay τ ranges from 1 to 25 nanoseconds. Notch frequency f_0 ranges from 40 to 100 MHz. An HP 3781B

Pattern Generator is used for signal generation. The HP Multipath Fade Simulator is discussed in Appendix A.

A $(2^{20} - 1)$ length DS-3 (hi) pattern with framing is supplied to the transmit terminal input. The signal is detected at the receiver terminal output with an HP 3782B Error Detector.

The signatures are obtained by measuring the bit error performance produced by the channel distortion of interest. In order to measure the bit error performance, an HP 5316B Universal Counter is connected to the DR6-135 Terminal Framer Hop CRC Errors output. A second HP 5316B is connected to the FL LS output to detect frame loss. Sometimes no CRC pulses are observed at the Hop CRC Errors jack when the receiving modem loses frame synchronisation. Two counters are used to detect such errored situations. The transitions of the Fade Simulator and the polling of the Universal Counters are controlled by the software. Measurement of the M-curve requires approximately 6 to 8 minutes.

The dynamic signatures and performance curves require measurement of binary errors on the DS-3 line. The HP 3782B Error Detector is connected to the DS-3 receive terminal output of the channel under measurement. An HP 5316B Universal Counter is then connected to the error output of the HP 3782B. Bit errors captured by the Error Detector are recorded this way. The transitions of the Fade Simulator, the measurement period gating of the Error Detector, and the polling of the Universal Counter are controlled by the software. The performance curve averages three individual error measurements for each notch depth and frequency speed pair. Measurement of the dynamic notch depth signature requires approximately 1 hour. Measurement of the dynamic notch frequency signature requires

approximately 1 hour and twenty minutes. Measurement of the dynamic notch depth and frequency performance curves requires approximately 10 minutes.

5.7 Discussion of Model and Results

The signature data are organized as in Table 5-1. The static multipath signatures are shown in figures 5-3 (a-f) - 5-4 (a-f). The dynamic "notch" or cancellation depth signatures are shown in figures 5-5 (a-f). The dynamic "notch" or cancellation frequency signatures are shown in figures 5-6 (a-f) - 5-7 (a-f). The bit error performance curve for dynamic depth and frequency are shown in figures 5-8 (a-f) - 5-9(a-f).

The static signature or M-curve represents a locus of points in the plane of channel power minimum or cancellation depth (dB) versus cancellation frequency (MHz). These are threshold curves for a specific BER (figures 5-3a-f, 5-4a-f). An examination of figures 5-3a-c reveals the behavior of the M-curve with respect to second ray delay. As the delay is decreased, the cancellation depth required to produce 10^{-3} BER increases. The same behavior is borne out in figures 5-4a-c for the 10^{-6} threshold. Changing the flat fade component from 0 dB to 10 dB (figures 5-3d, 5-4d) or 20 dB (figures 5-3e, 5-4e) does not seem to affect the curve. Curves for non-minimum phase state (figures 5-3f, 5-4f) are very similar to the minimum phase state curves (figures 5-3a, 5-4a).

The dynamic cancellation depth signature represents a locus of points in the plane of cancellation depth velocity (dB/sec) versus cancellation frequency (MHz). It is a threshold curve for bit errors in the presence of active system countermeasures (figures 5-5a-f). A sample is shown in figure 5-5a. Inspection of the curve reveals an area just below the band center where

depth transitions of up to 40 dB/sec do not cause bit errors after equalization and protection switching. An examination of figures 5-3a and 5-4a shows this area to be coincidental with the area of greatest difference in the 10^{-3} and 10^{-6} M-curves. This implies a greater warning effect for active countermeasures. Figure 5-10 illustrates this comparison. The vertical scale represents changes in cancellation depth. There are areas of greater vertical distance separating the curves. For a constant cancellation frequency, greater cancellation depth velocity is required to defeat the countermeasures. Variation in the second ray delay does not seem to result in much change from 6.3 to 4 nanoseconds (figures 5-5a, b). Still, it does result in a slightly more narrow characteristic for 1 nanosecond. Changes in flat fade depth of 10 or 20 dB (figures 5-5d, e) or phase state (figure 5-5f) do not change from the reference characteristic significantly (figure 5-5a).

Table 5-1. Organization of Figures for Chapter 5

		<u>for phase state</u>		<u>for delay (nsec)</u>			<u>for flat fade(dB)</u>		
		min	non	6.3	4.0	1.0	0	10	20
static signatures:									
10^{-3} M-curve	figs. 3:	a-e	f	a	b	c	a	d	e
10^{-6} M-curve	figs. 4:	a-e	f	a	b	c	a	d	e
dynamic signatures:									
notch dep.	figs. 5:	a-e	f	a	b	c	a	d	e
notch freq.									
incr. freq.	figs. 6:	a-e	f	a	b	c	a	d	e
decr. freq.	figs. 7:	a-e	f	a	b	c	a	d	e
bit error performance:									
incr. freq.	figs. 8:	a-e	f	a	b	c	a	d	e
decr. freq.	figs. 9:	a-e	f	a	b	c	a	d	e

figure 5-3a

Figure 5-3a: Static Multipath Signature

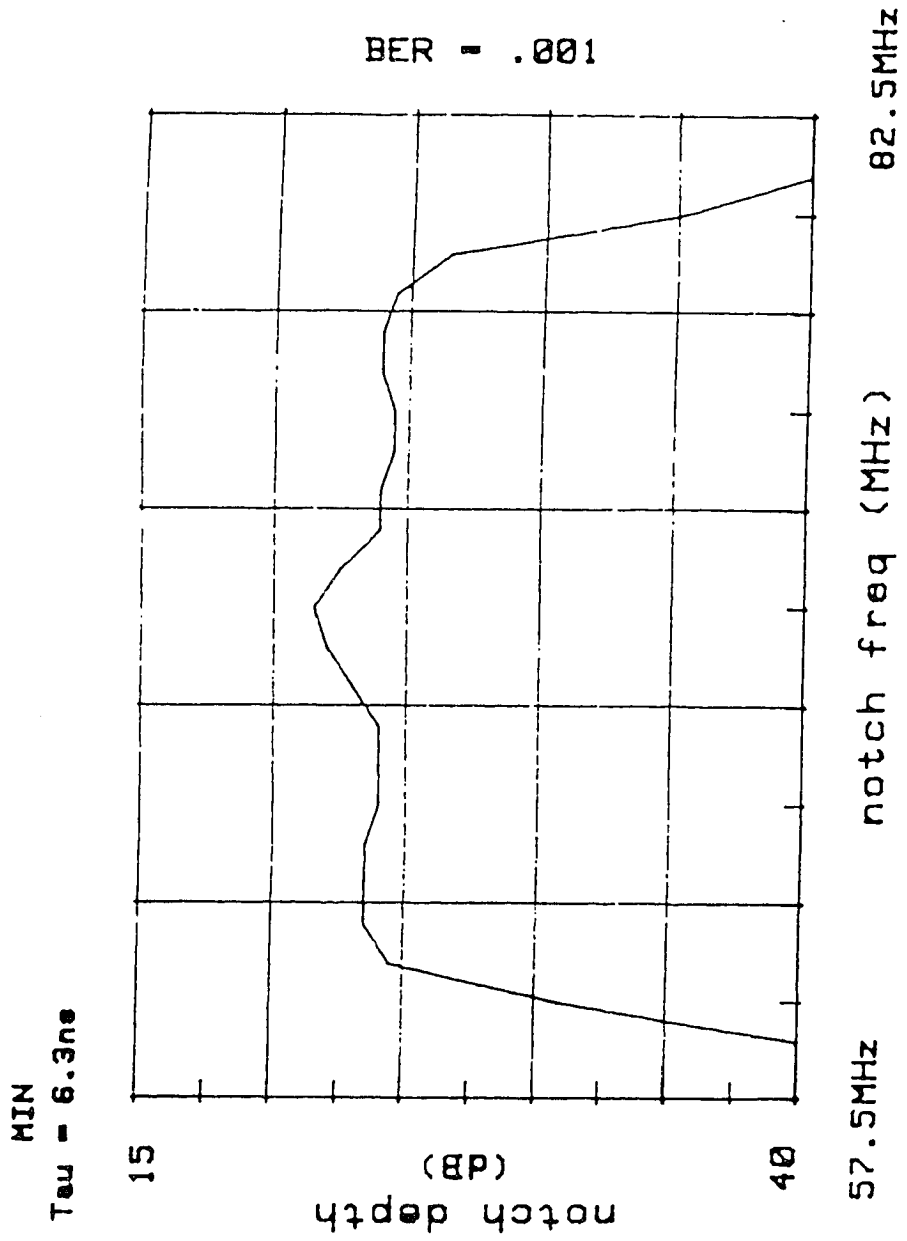


figure 5-3b

Figure 5-3b: Static Multipath Signature

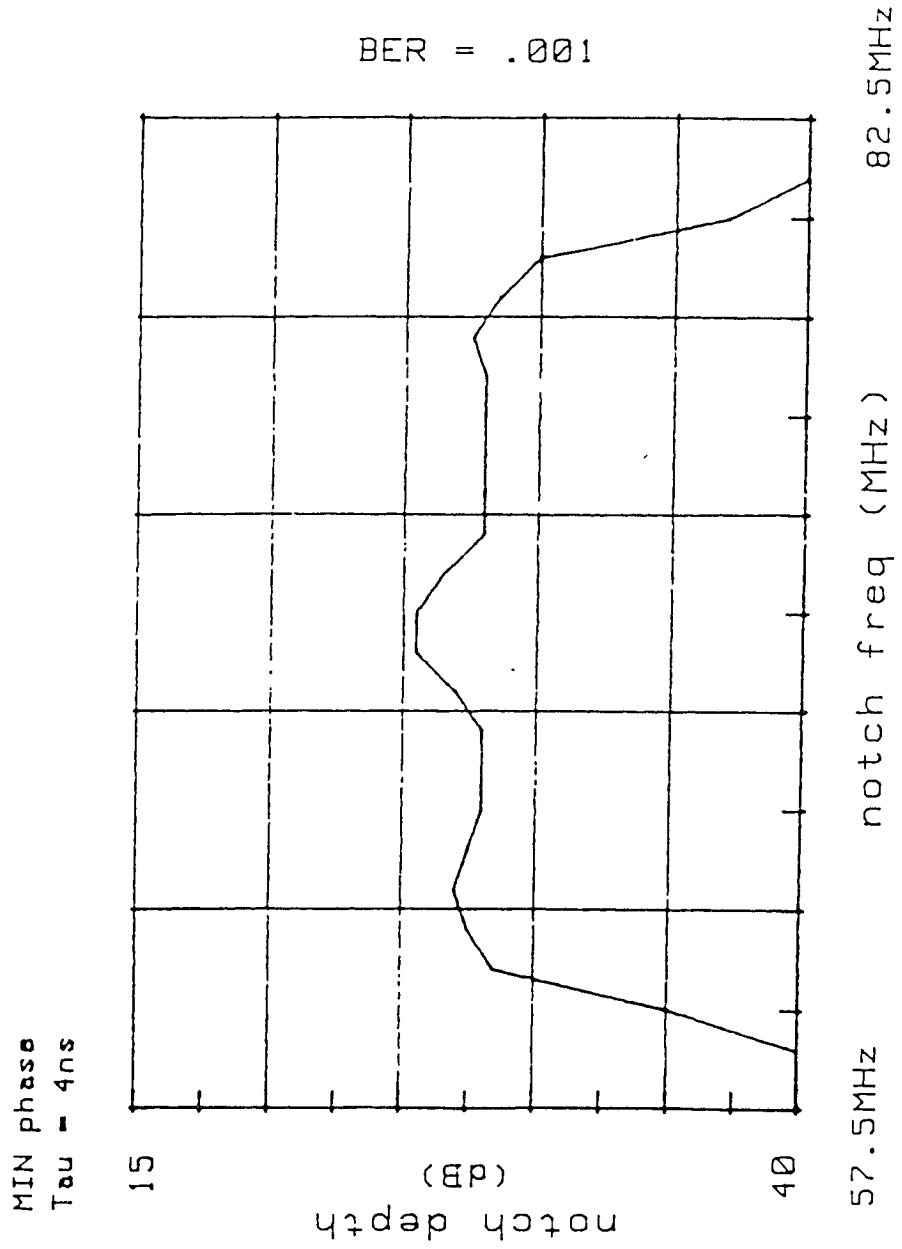


figure 5-3c

Figure 5-3c: Static Multipath Signature

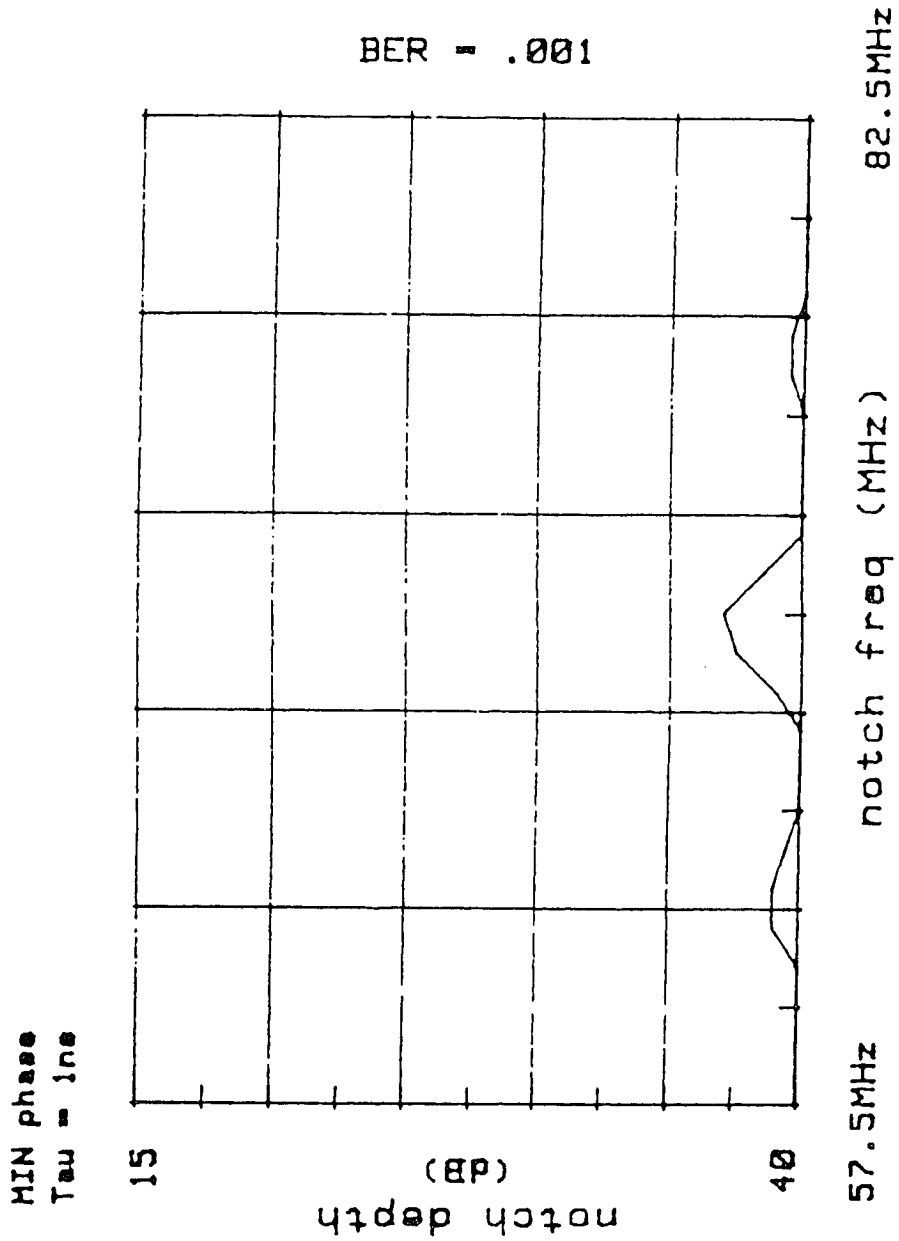


figure 5-3d

Figure 5-3d: Static Multipath Signature

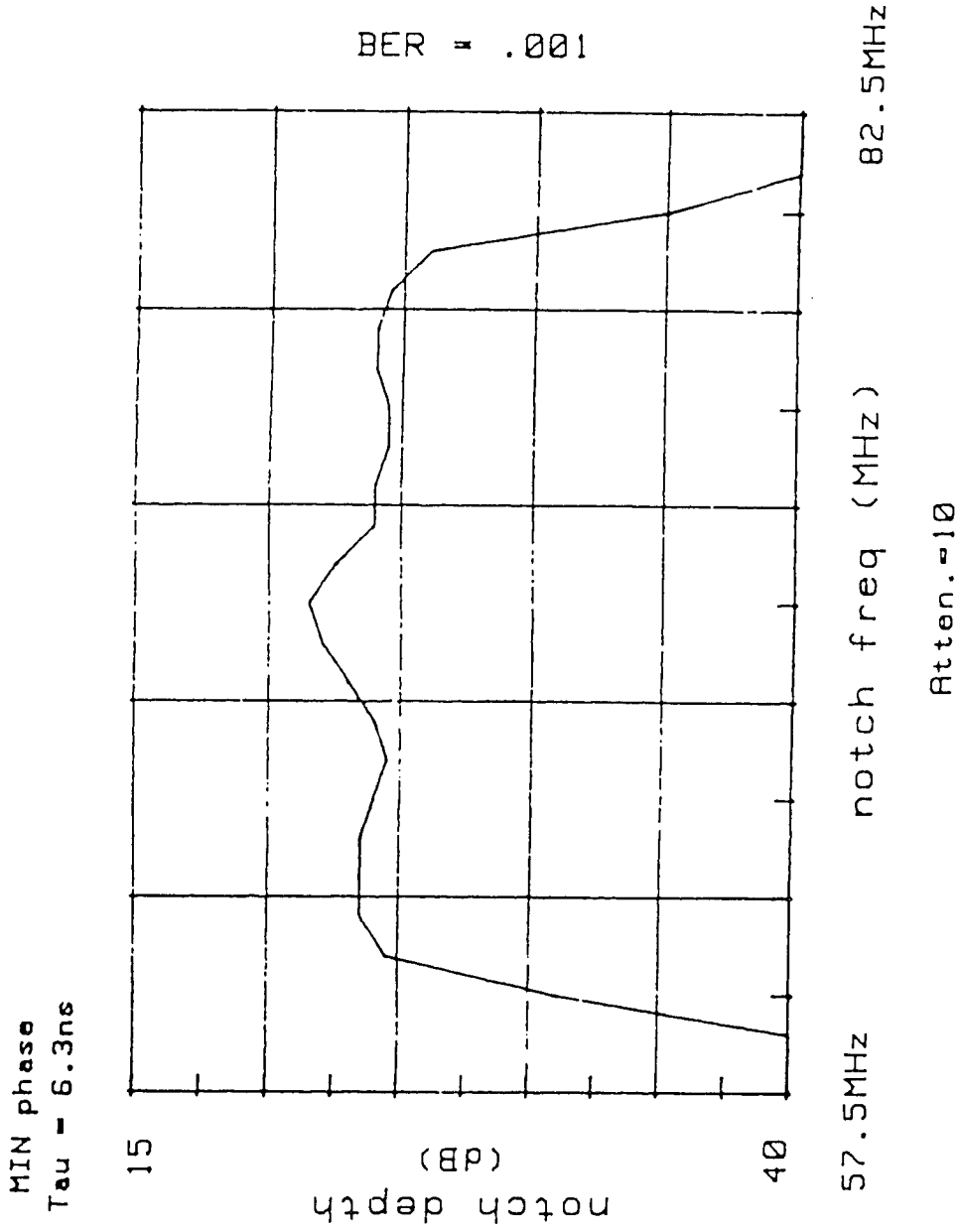


figure 5-3e

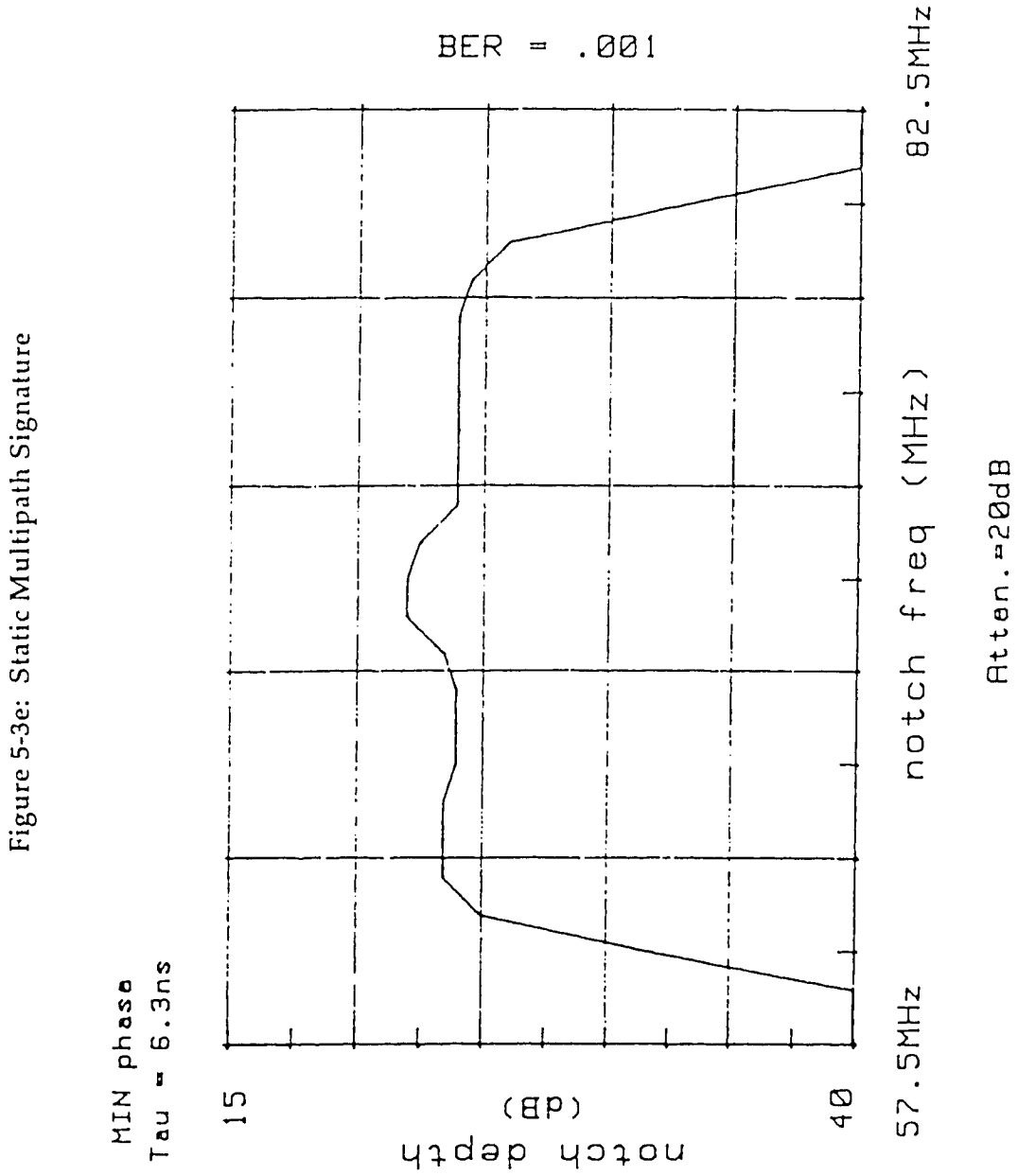


figure 5-3f

Figure 5-3f: Static Multipath Signature

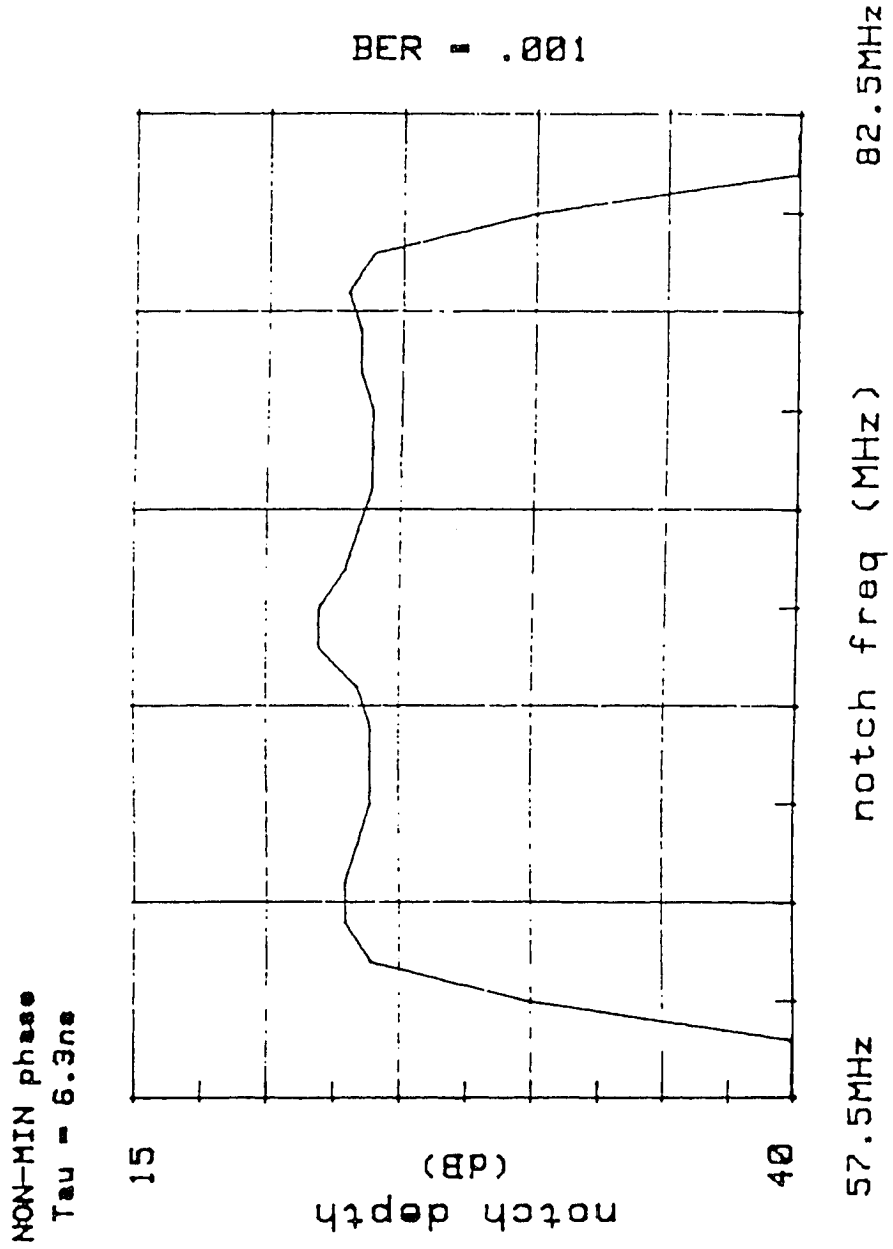


figure 5-4a

Figure 5-4a: Static Multipath Signature

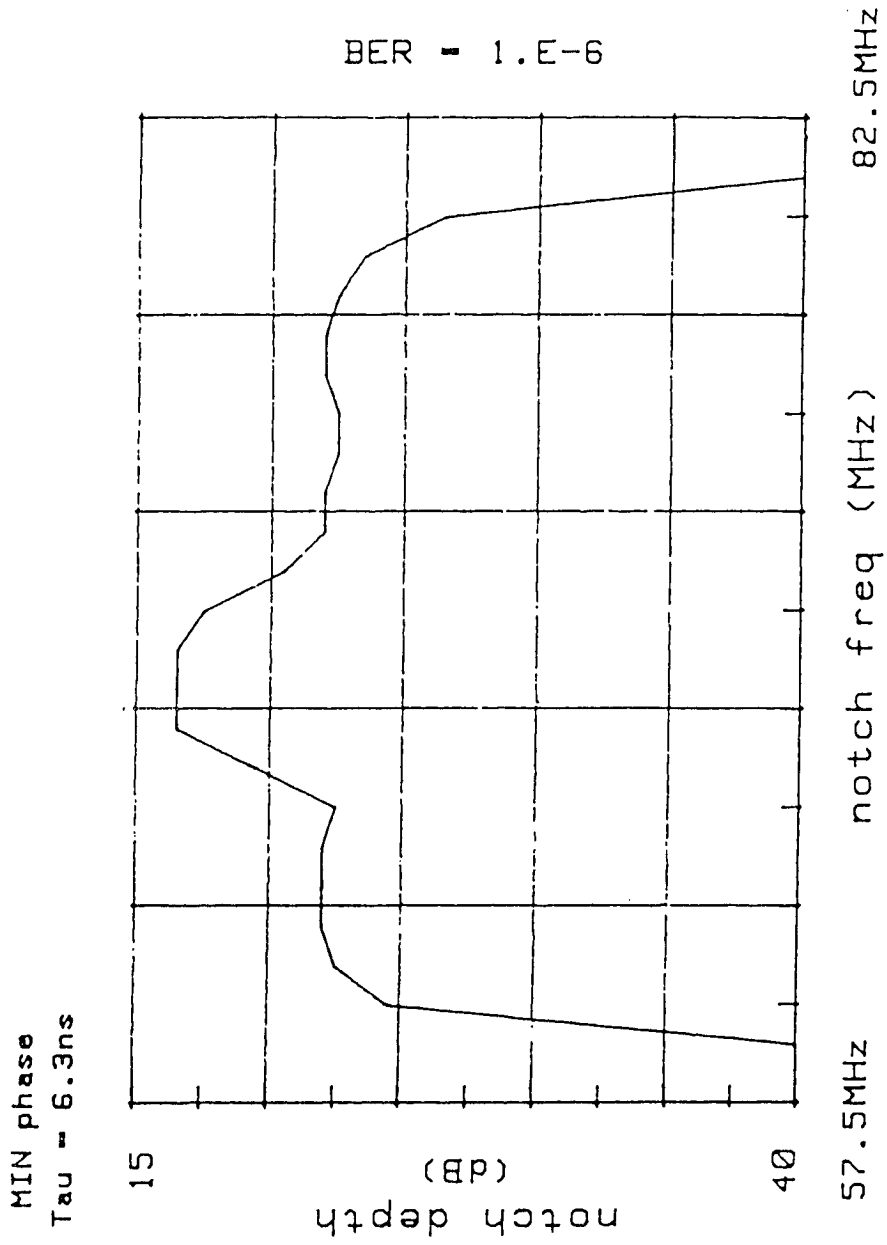


figure 5-4b

Figure 5-4b: Static Multipath Signature

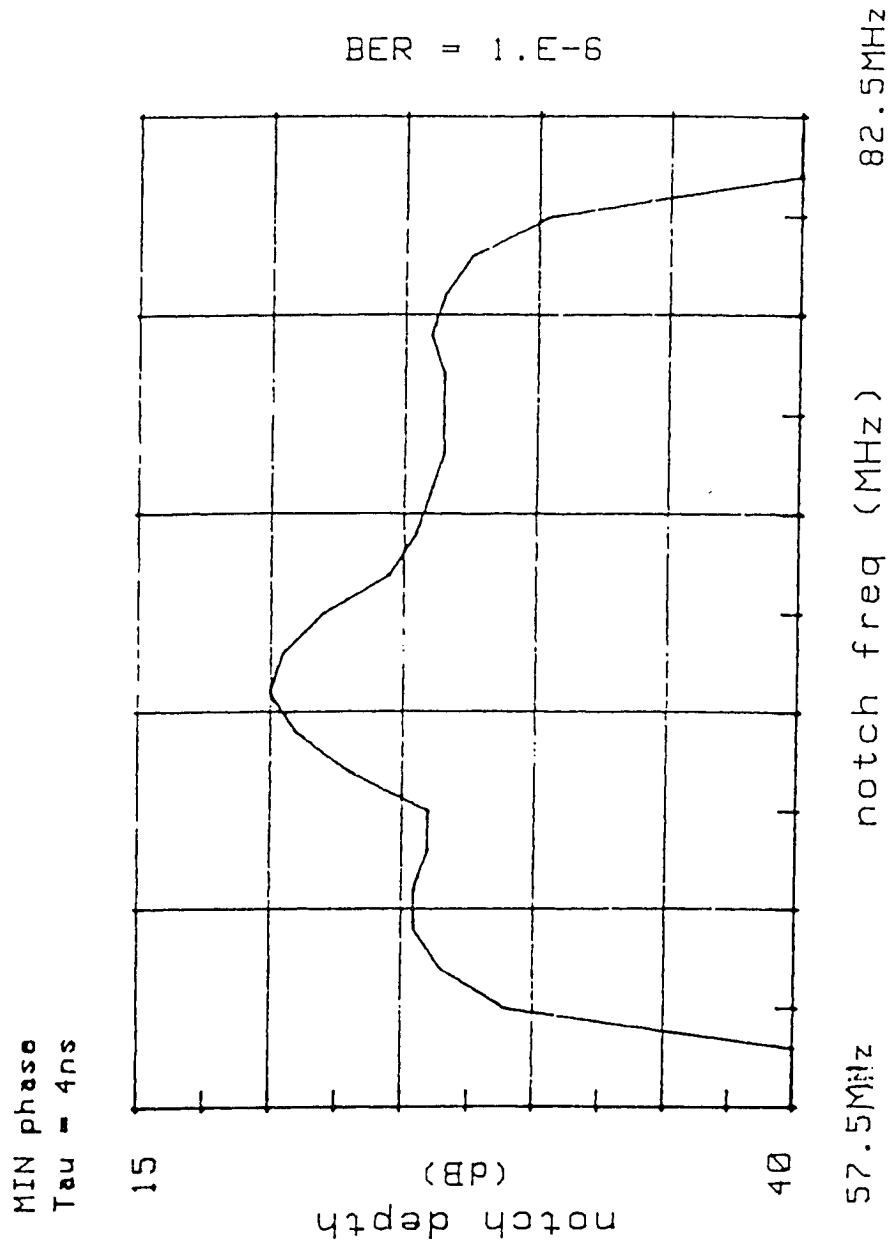


figure 5-4c

Figure 5-4c: Static Multipath Signature

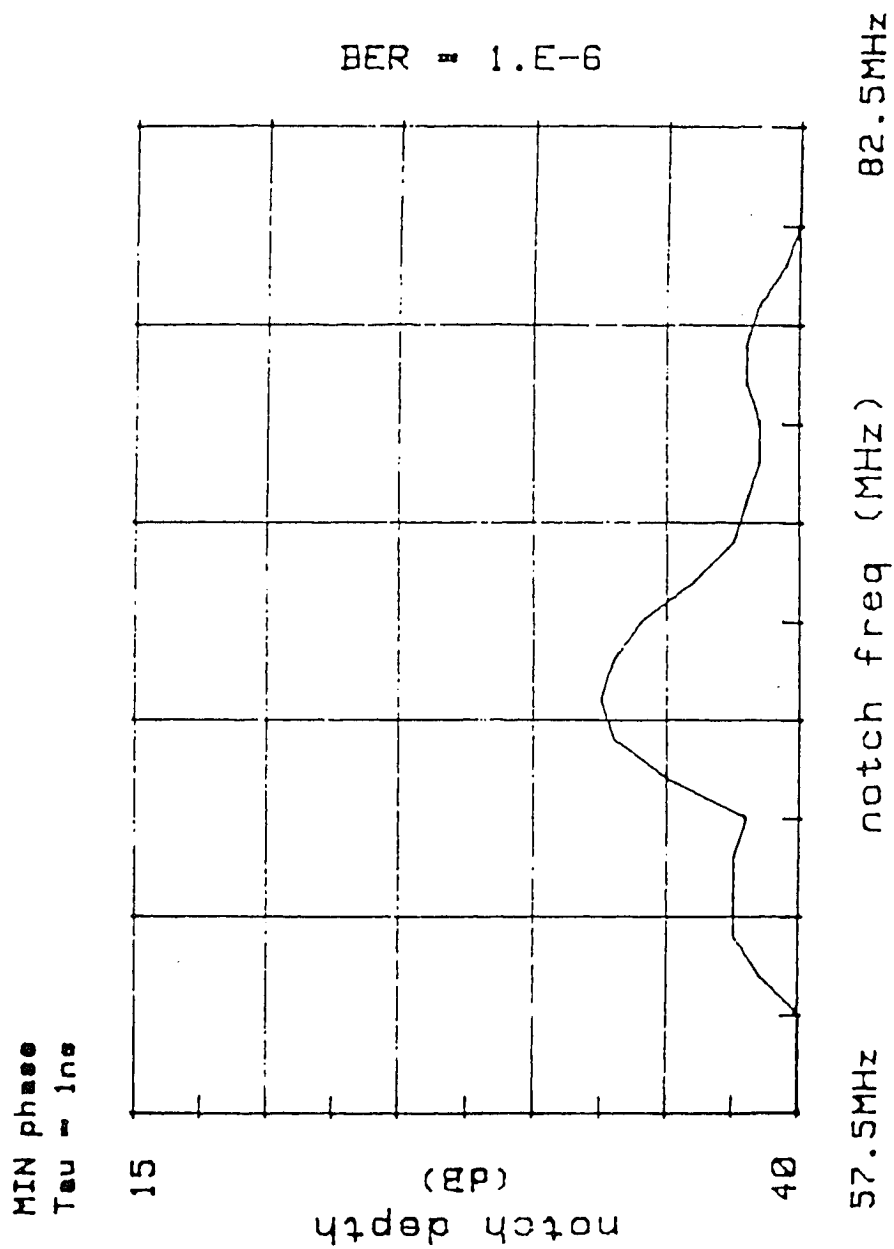


figure 5-4d

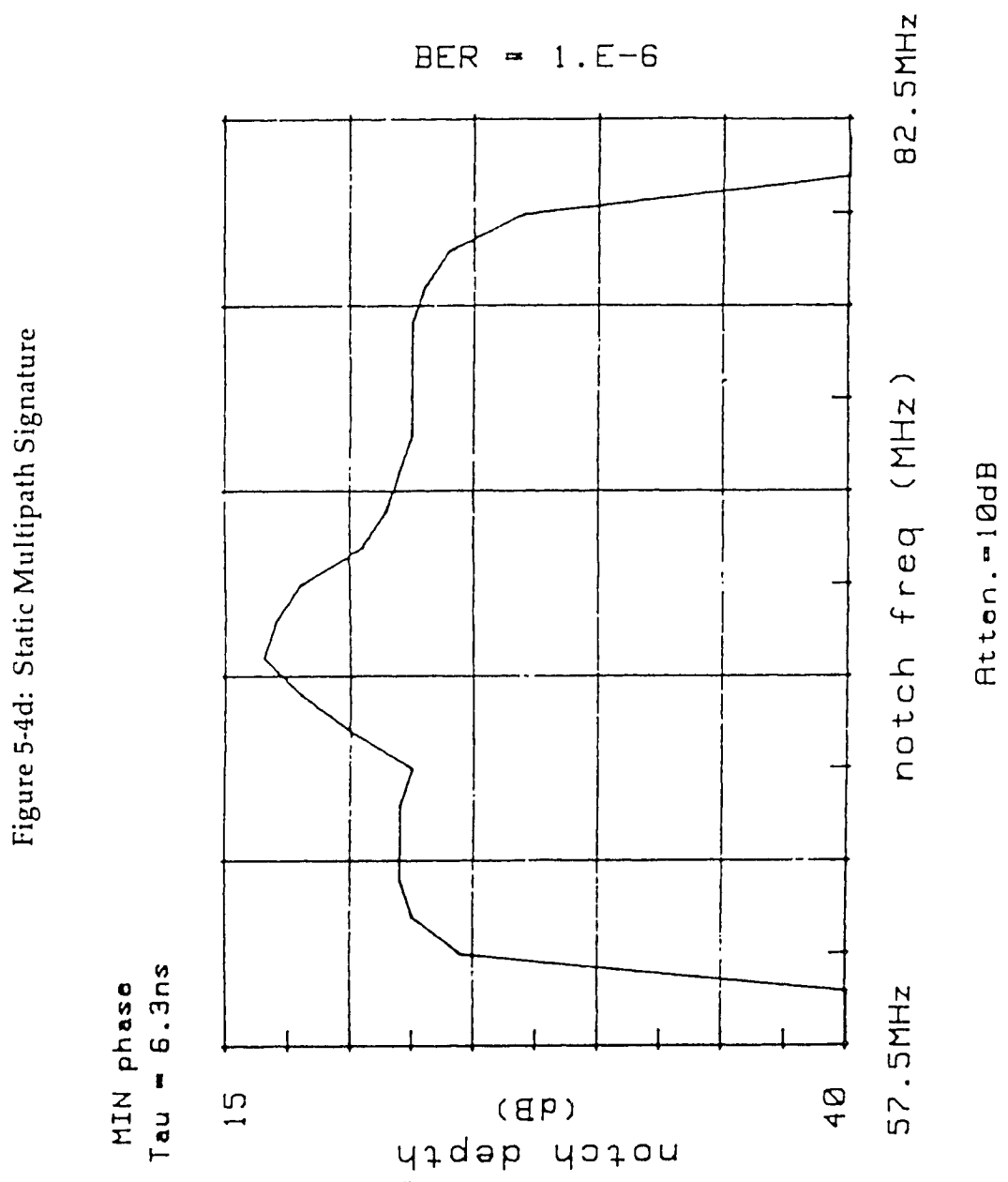


figure 5-4e

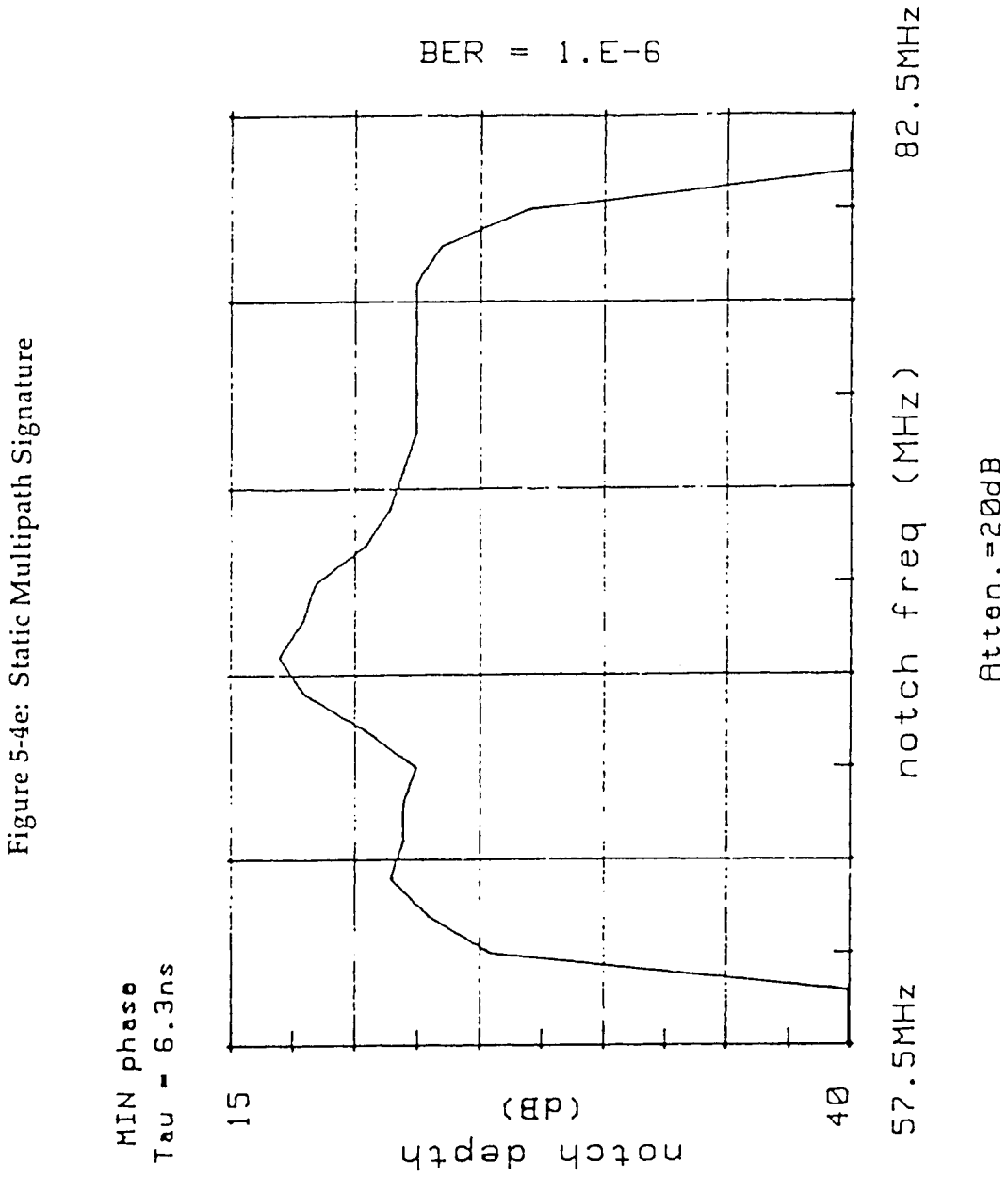


figure 5-4f

Figure 5-4f: Static Multipath Signature

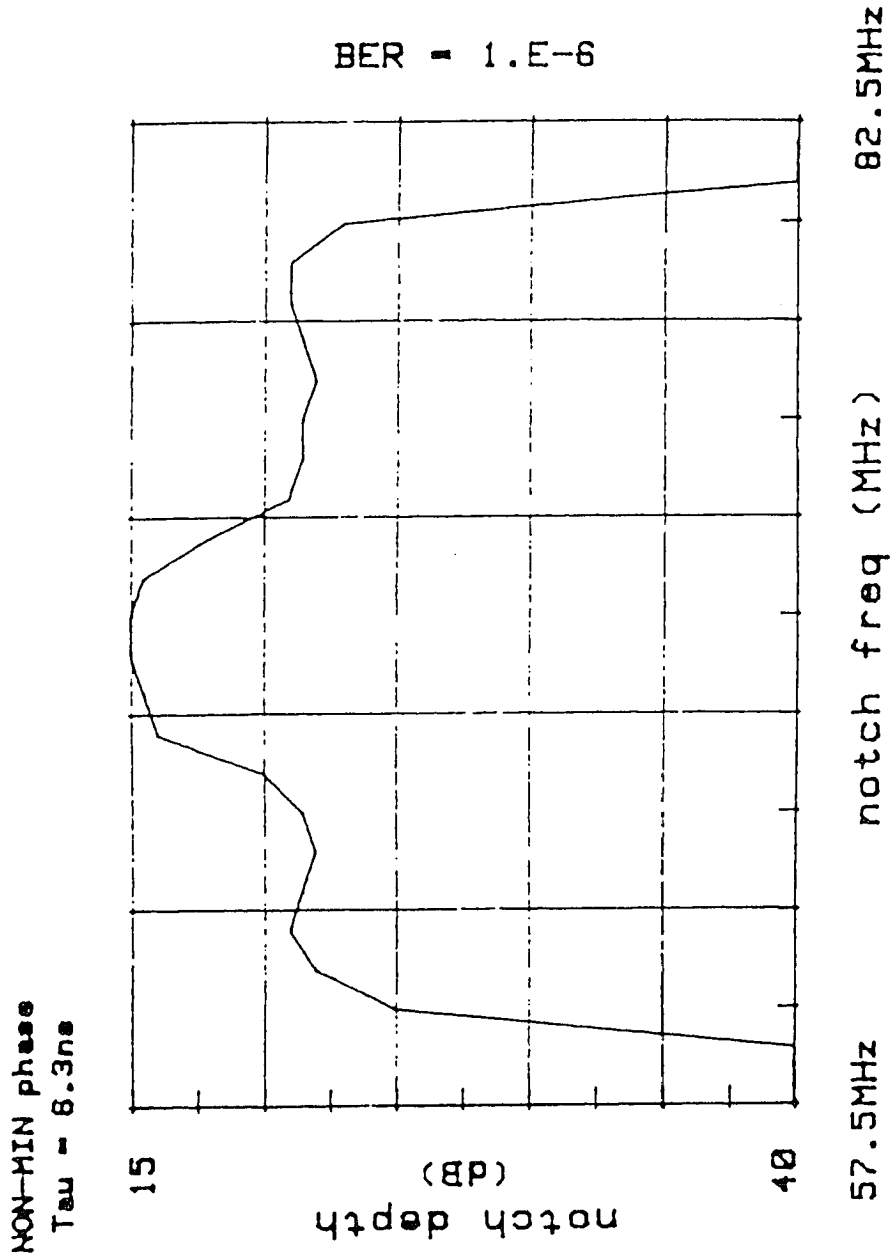


figure 5-5a

Figure 5-5a: Dynamic Cancellation Depth Signature

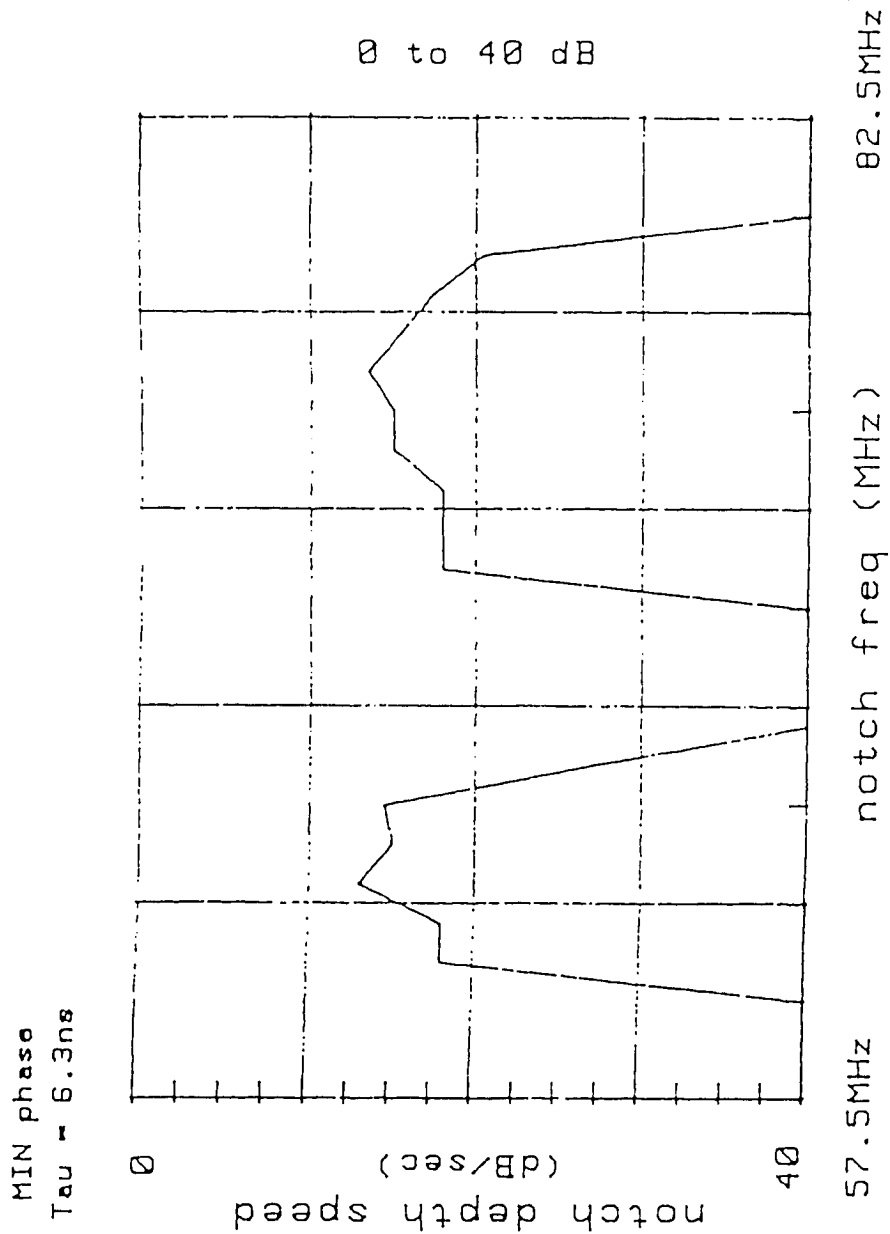


figure 5-5b

Figure 5-5b: Dynamic Cancellation Depth Signature

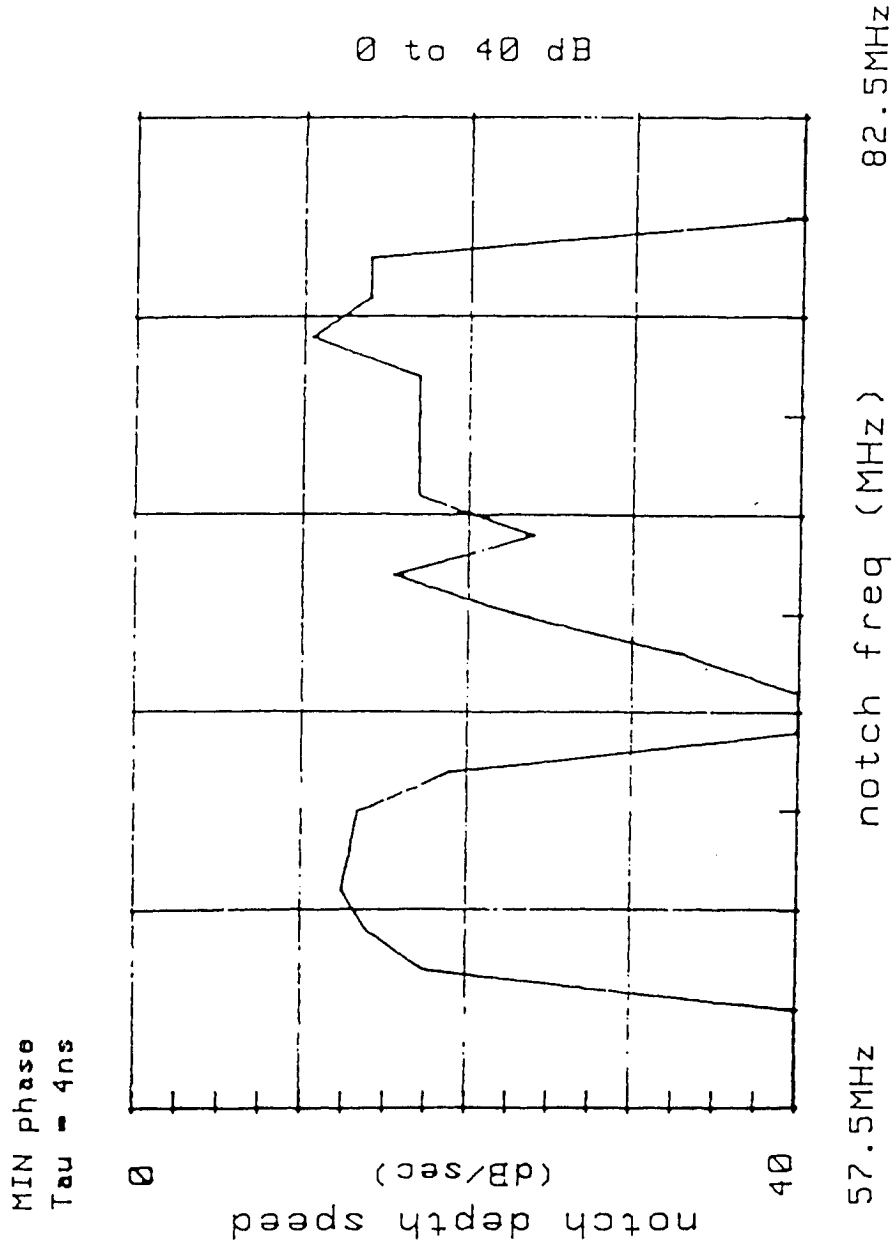


figure 5-5c

Figure 5-5c: Dynamic Cancellation Depth Signature

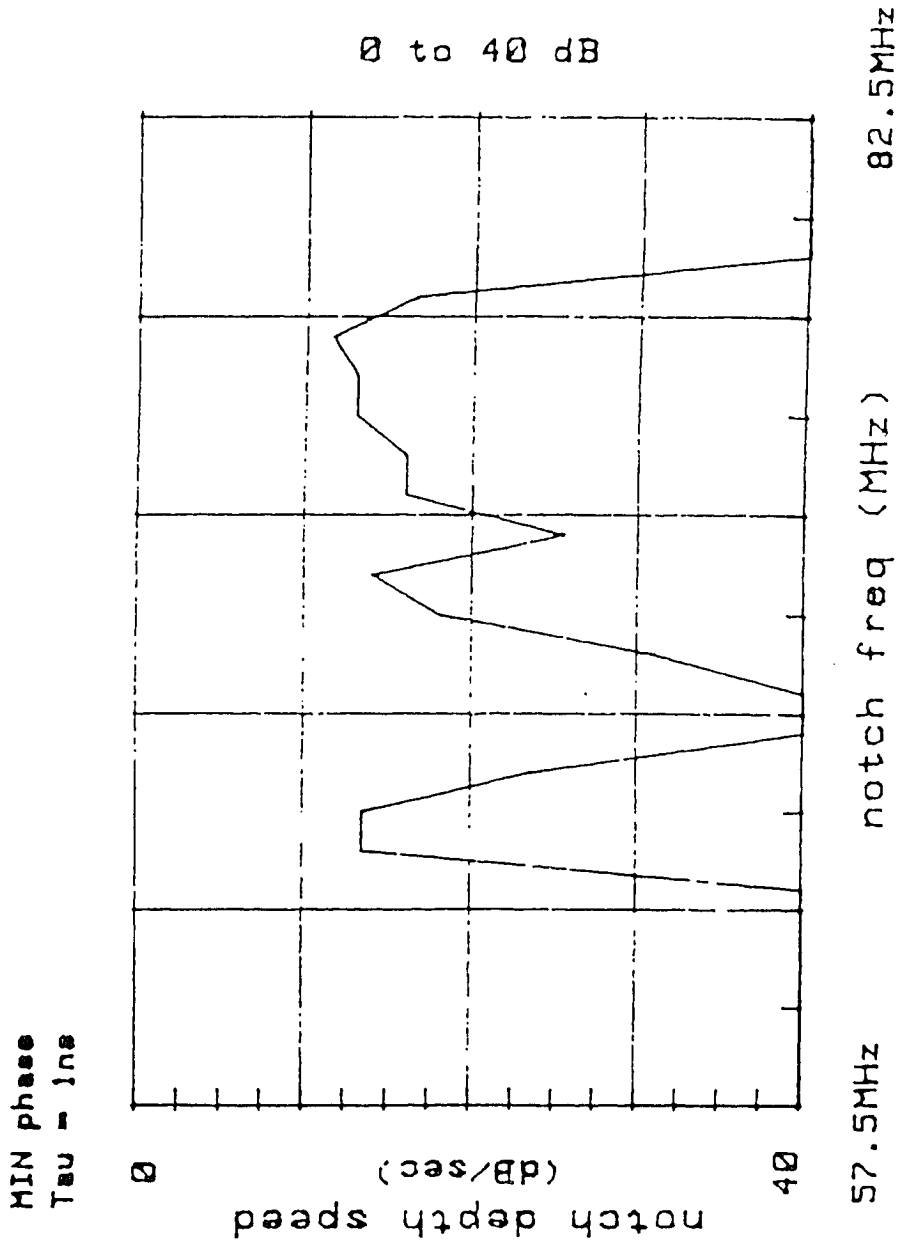


figure 5-5d

Figure 5-5d: Dynamic Cancellation Depth Signature

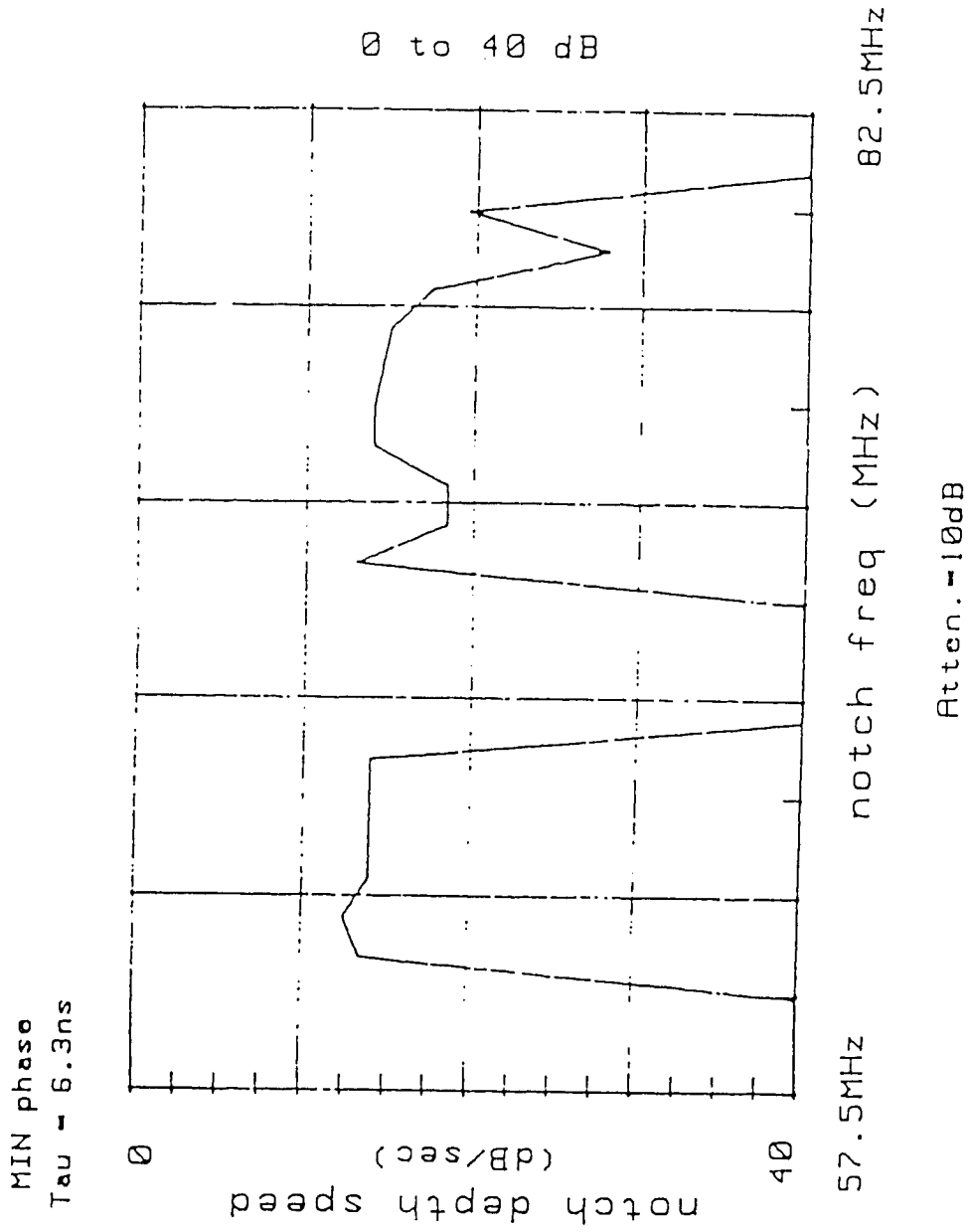


figure 5-5e

Figure 5-5e: Dynamic Cancellation Depth Signature

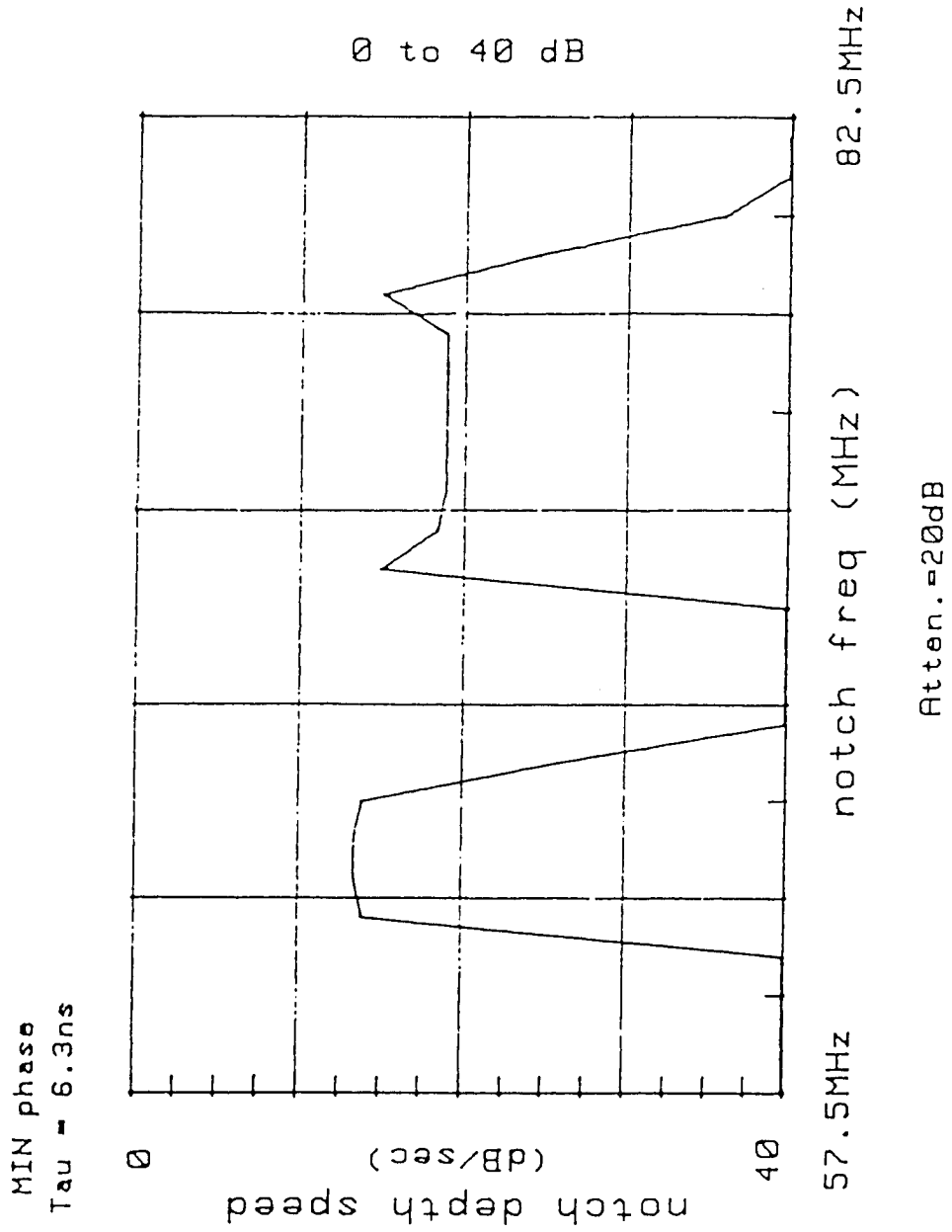
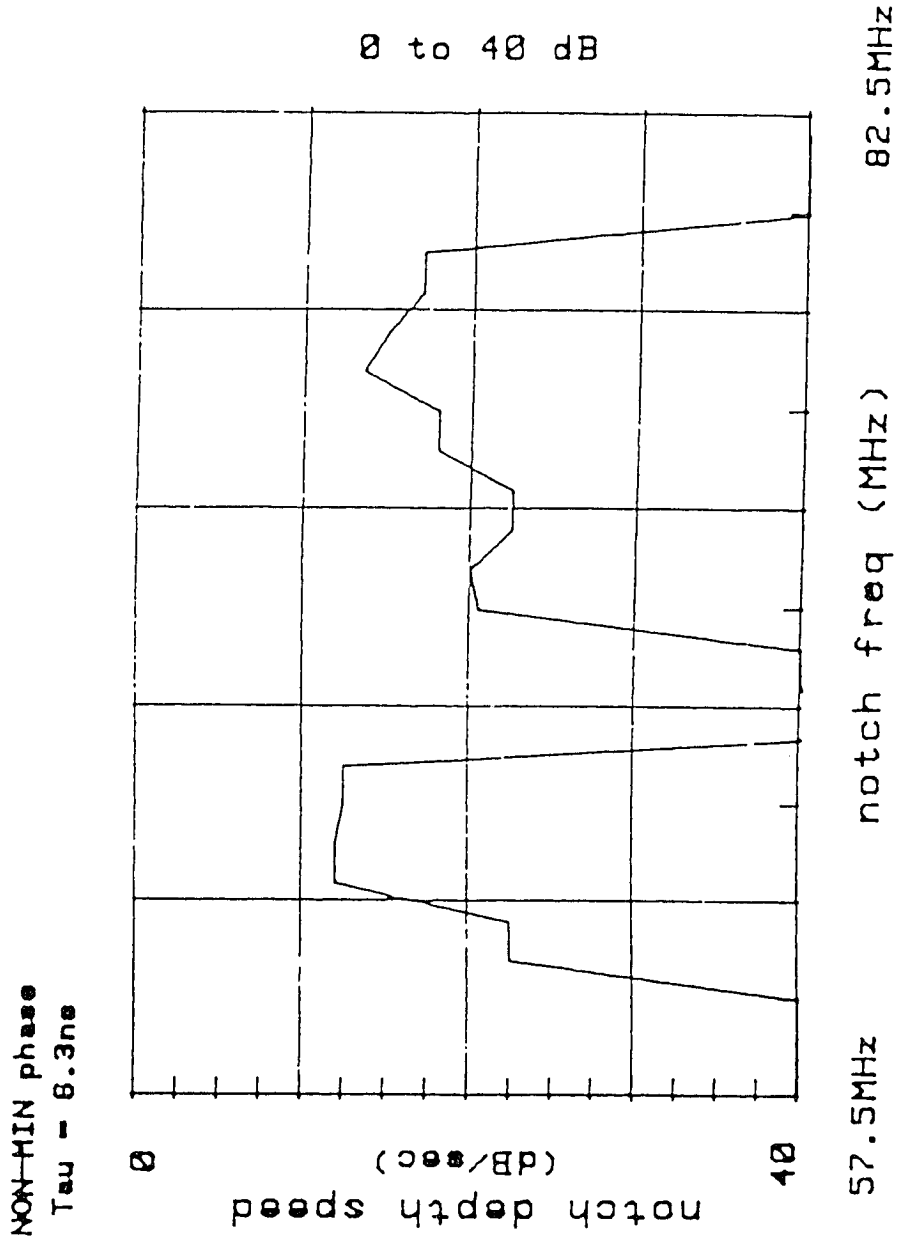


figure 5-5f

Figure 5-5f: Dynamic Cancellation Depth Signature



The dynamic cancellation frequency signature represents a locus of points in the plane of frequency velocity (MHz/sec) versus depth (dB). It is a threshold curve for bit errors in the presence of active system countermeasures (figures 5-6a-f, 5-7a-f). Figure 5-6a shows a typical response for a channel minimum sweeping from 40 to 100 MHz. Figure 5-7a similarly shows a response for movement from 100 to 40 MHz. An examination of figure 10 again illustrates the available time for a successful protection switch. The horizontal scale is represents changes in cancellation frequency. There are areas of greater horizontal distance separating the curves. For constant depth, greater frequency speed is required to defeat the protection switch. Comparison of figures 5-6b and c or 5-7b and c, reveals the variation in response with respect to second ray delay. A smaller value of delay results in a larger critical value of cancellation depth. The addition of flat fade depths of 10 or 20 dB (figures 5-6d,e or 5-7d,e) does not change the critical value of cancellation depth required to cause protection errors. Change in the phase state, however, does cause a slight change. Figure 5-6a represents a minimum phase condition for minima swept from 40 to 100 MHz. Similarly, figure 5-7f represents a non-minimum phase condition for minima swept from 100 to 40 MHz. Figure 5-6f represents a non-minimum phase condition for minima swept from 40 to 100 MHz. Figure 5-7a represents a minimum phase condition for minima swept from 100 to 40 MHz. These two figures are also quite similar. In the minimum phase superposition of two rays, a cancellation frequency sweeping upward in the frequency domain represents an increasing separation of minima in the broadband channel. This corresponds to a positive second ray delay that is decreasing in magnitude. In the non-minimum phase superposition, a cancellation frequency sweeping

figure 5-6a

Figure 5-6a: Dynamic Null Frequency

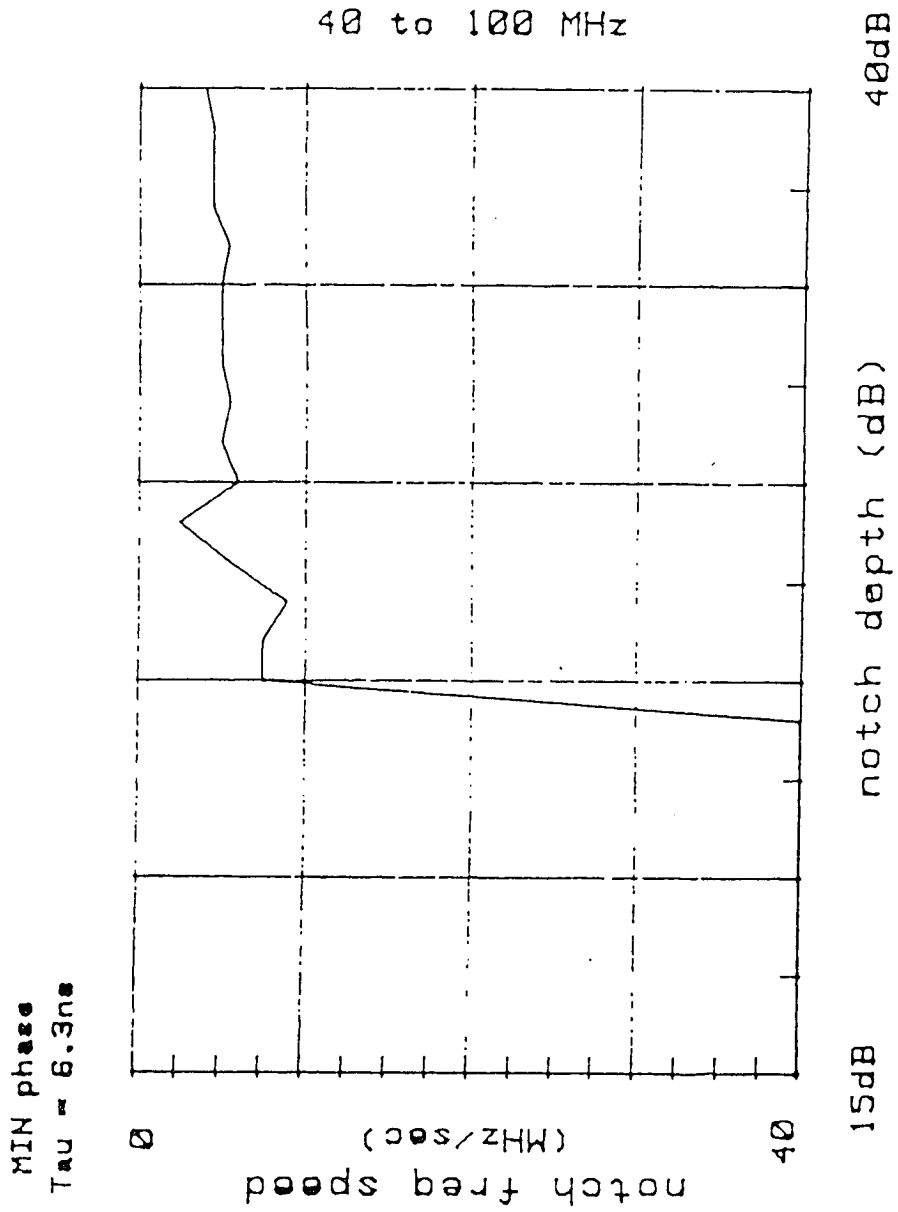


figure 5-6b

Figure 5-6b: Dynamic Null Frequency

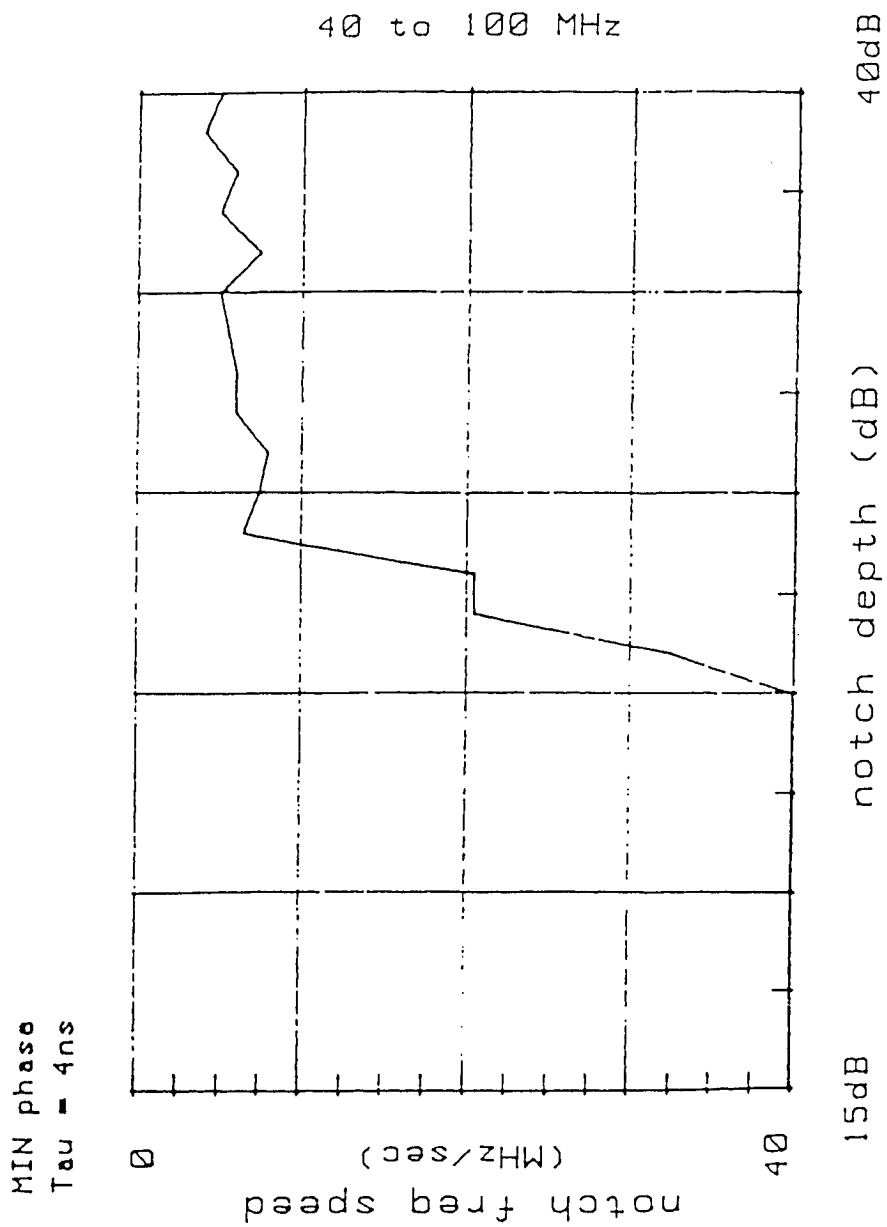


figure 5-6c

Figure 5-6c: Dynamic Null Frequency

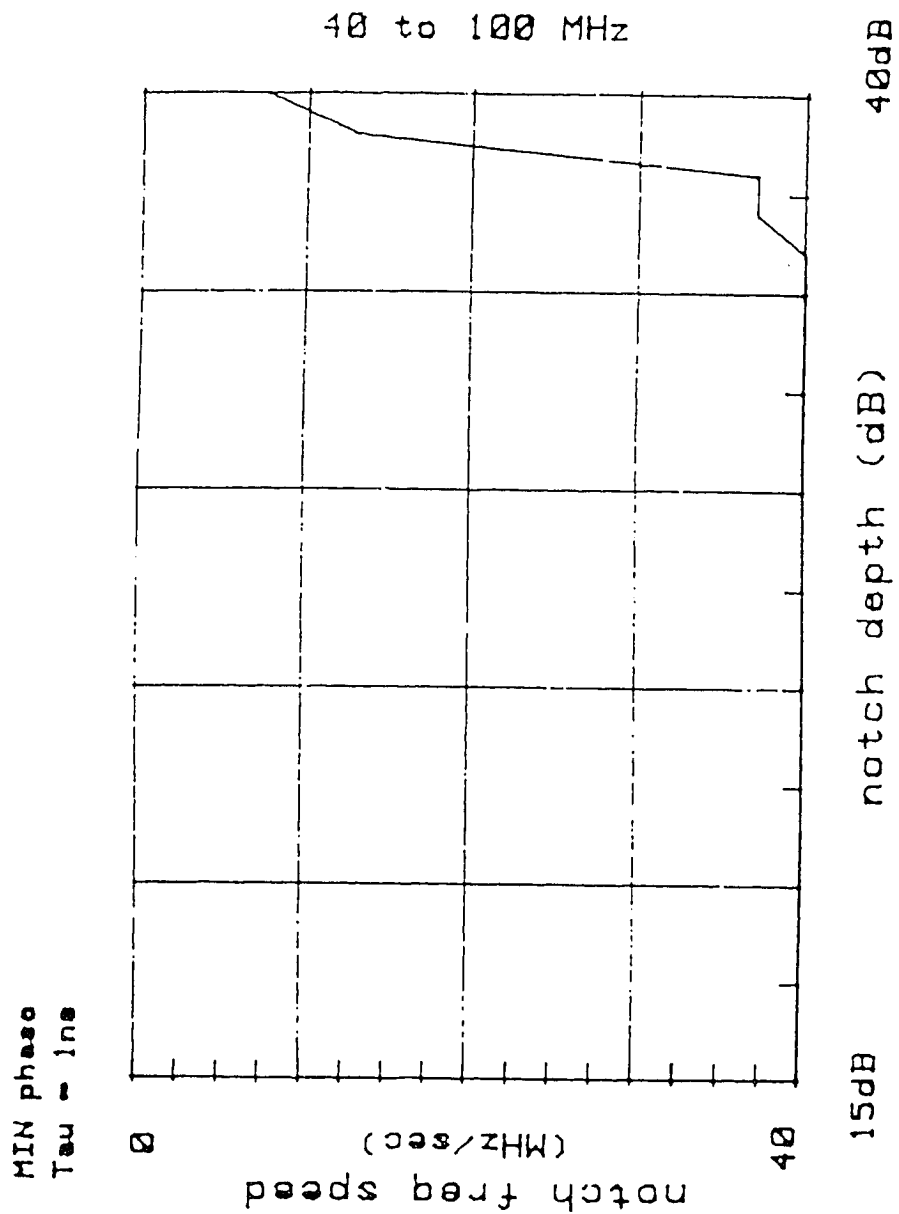


figure 5-6d

Figure 5-6d: Dynamic Null Frequency

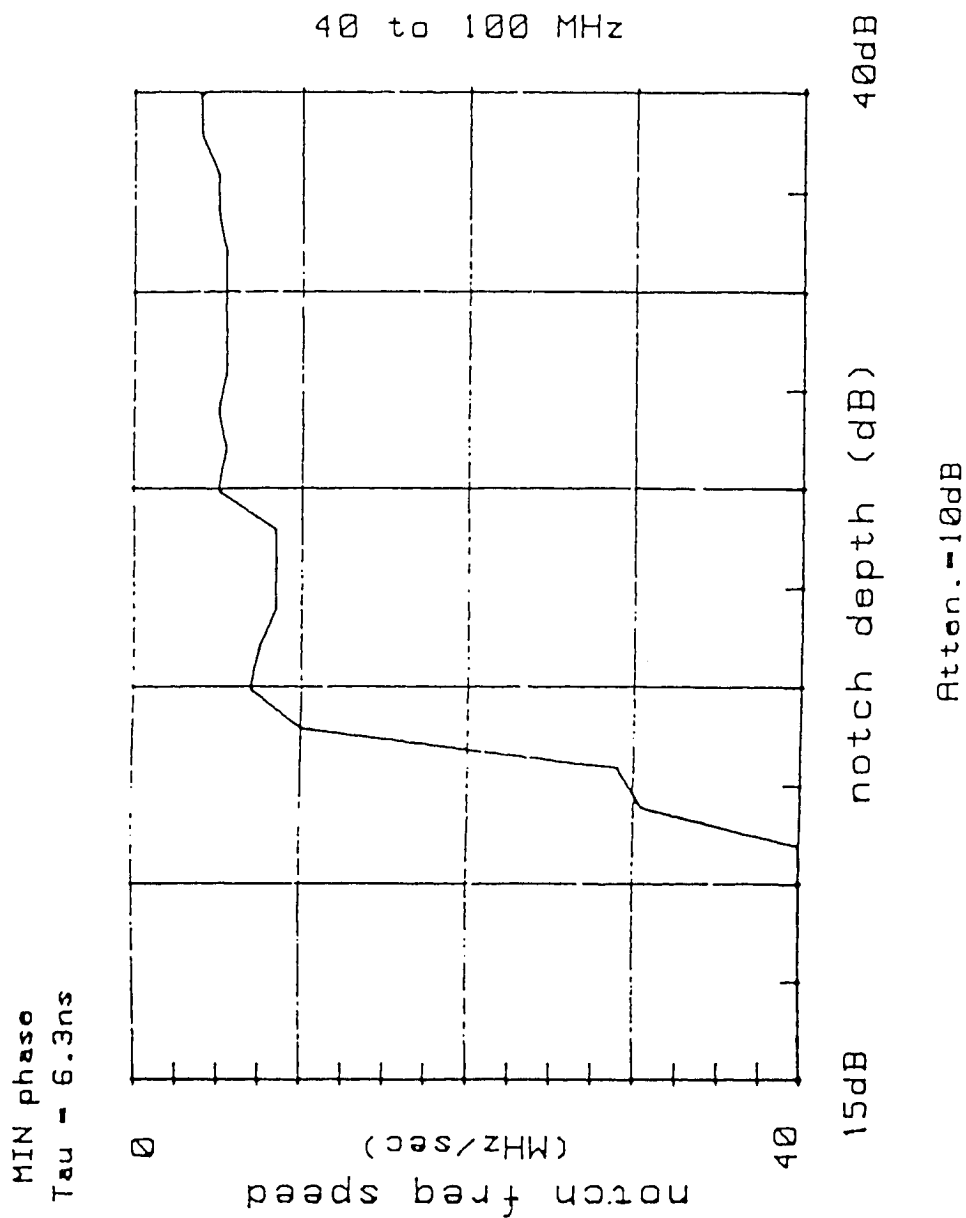


figure 5-6e

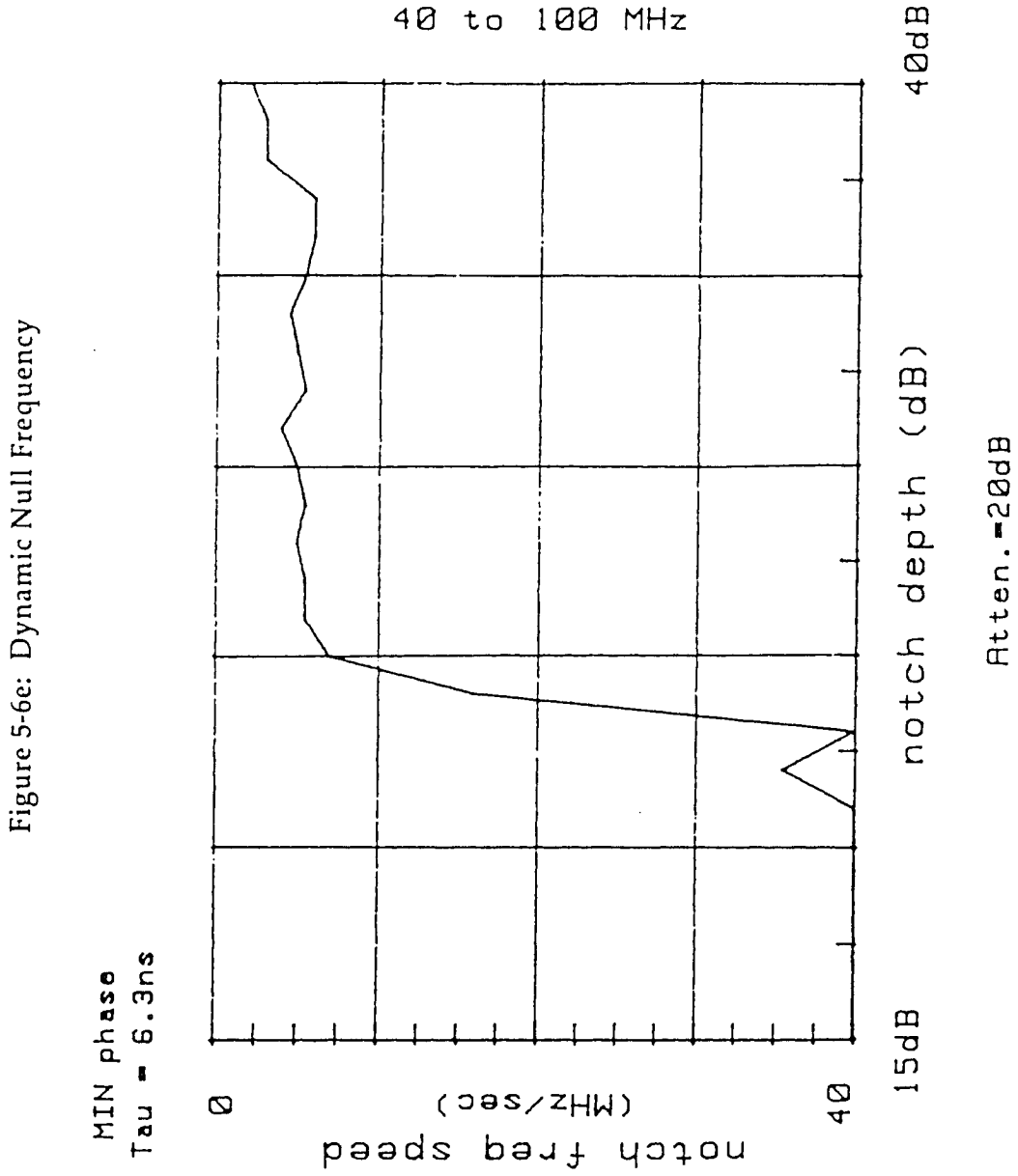


figure 5-6f

Figure 5-6f: Dynamic Null Frequency

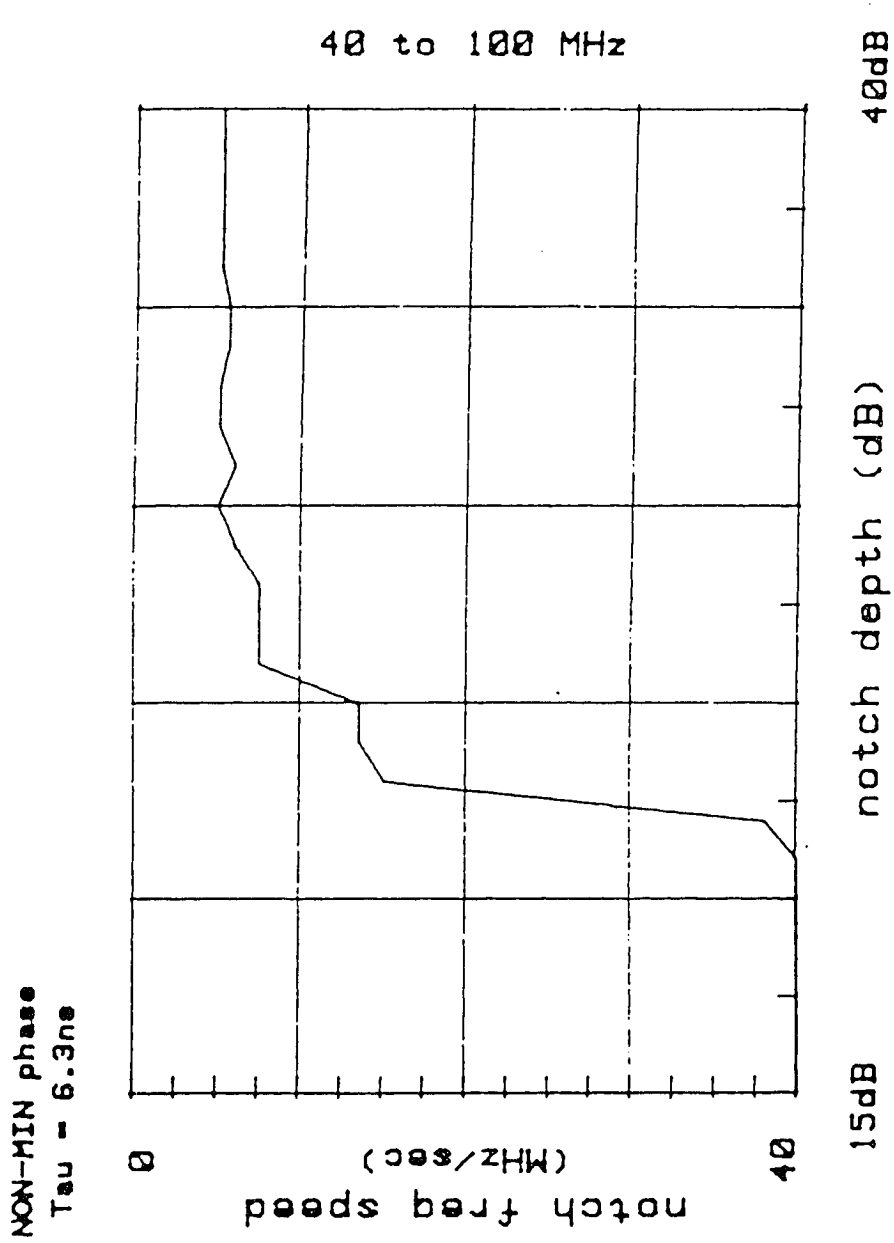


figure 5-7a

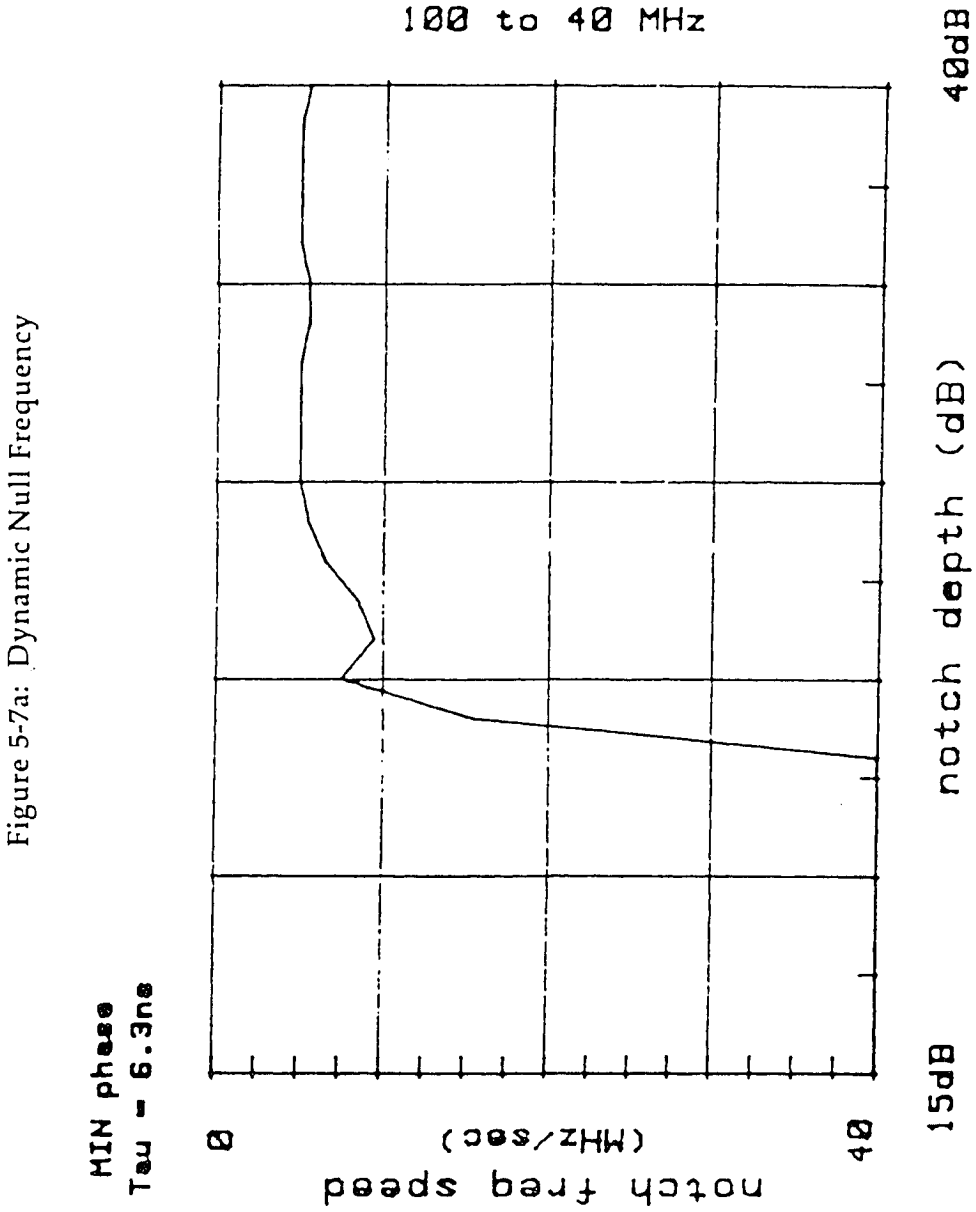


figure 5-7b

Figure 5-7b: Dynamic Null Frequency

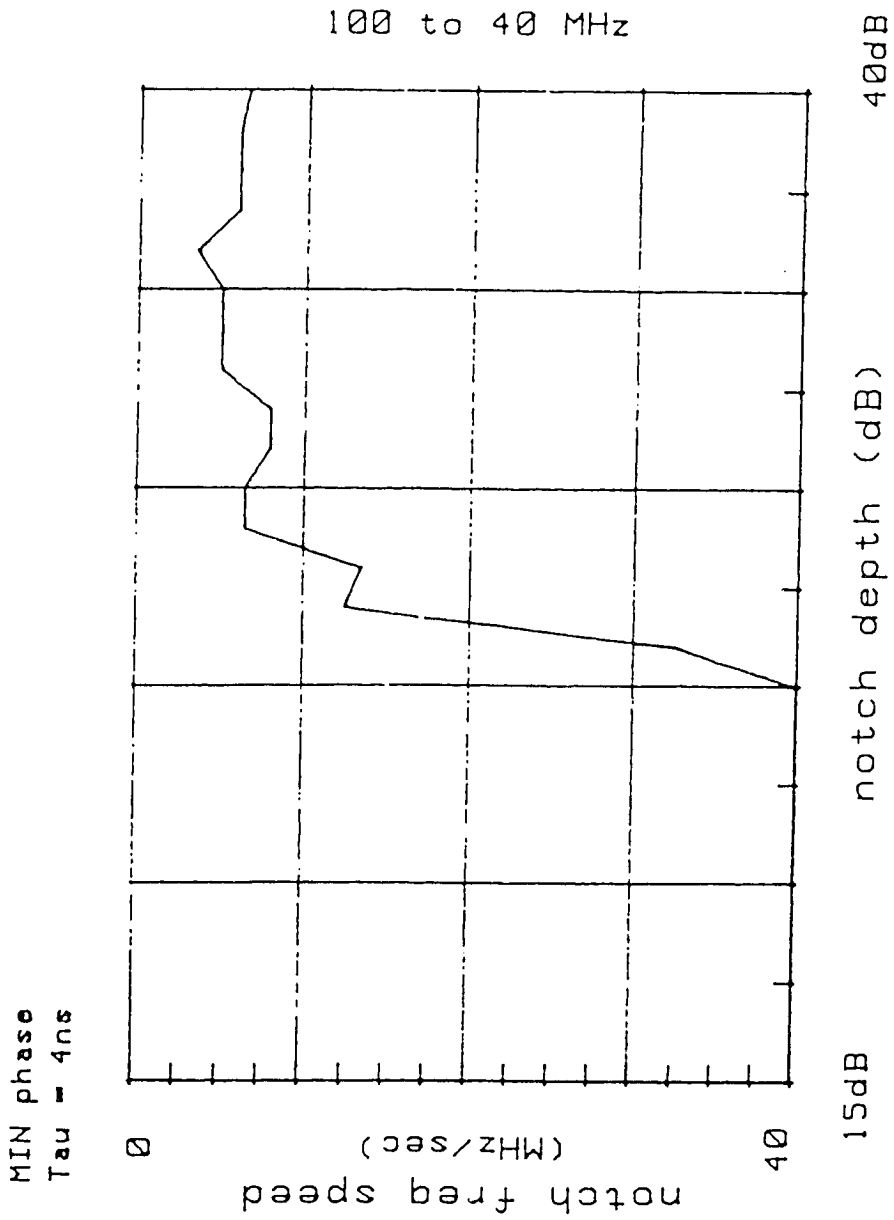


figure 5-7c

Figure 5-7c: Dynamic Null Frequency

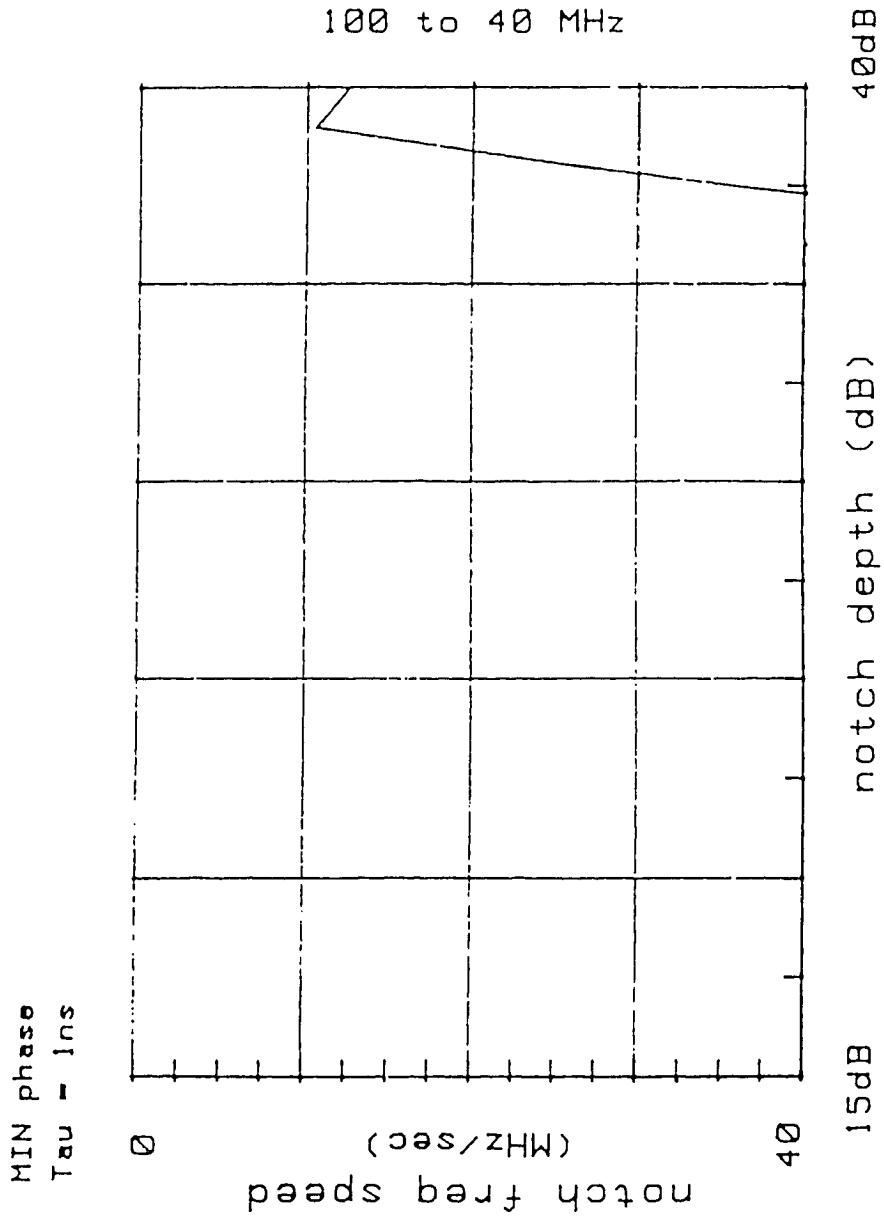


figure 5-7d

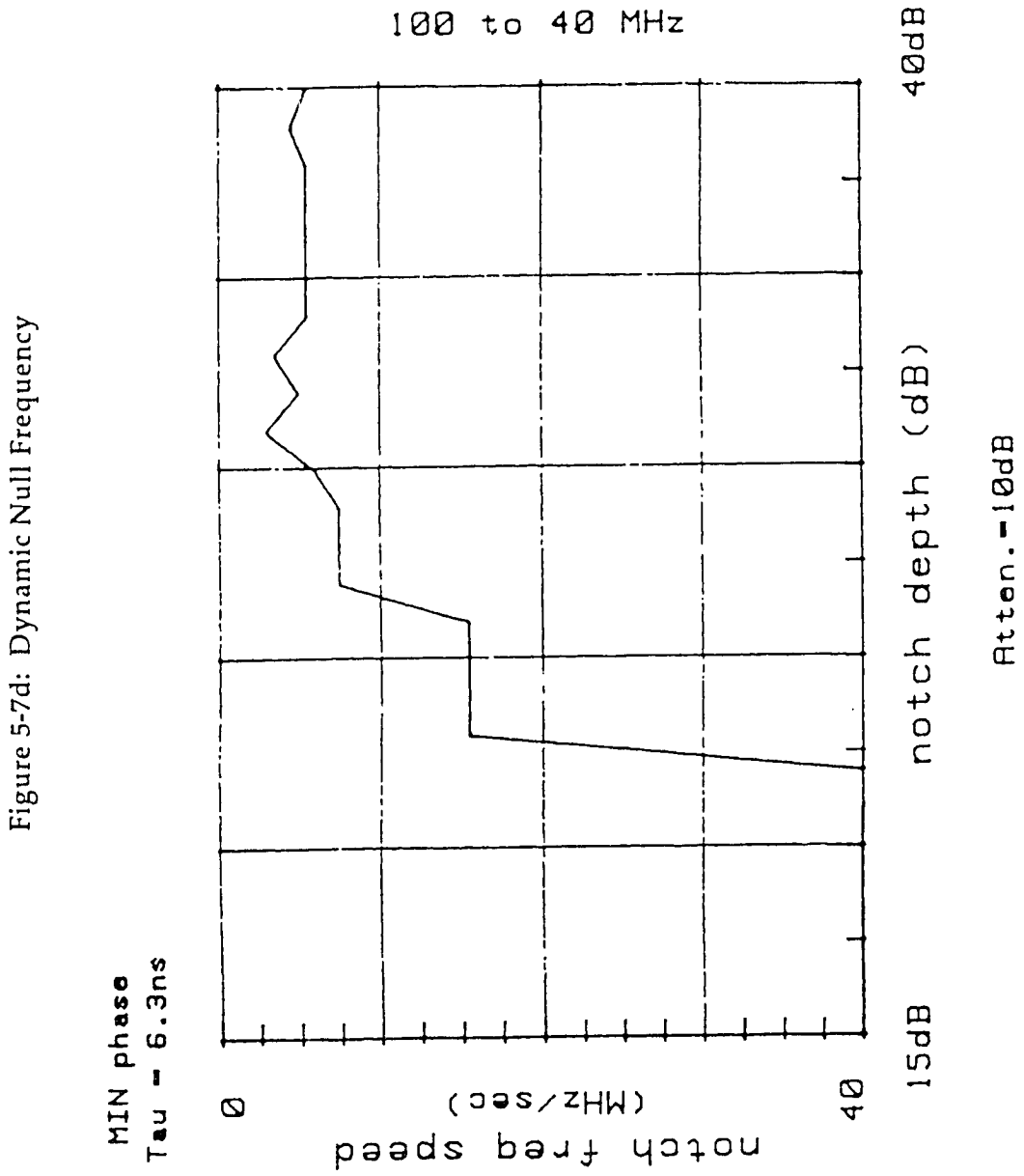


figure 5-7e

Figure 5-7e: Dynamic Null Frequency

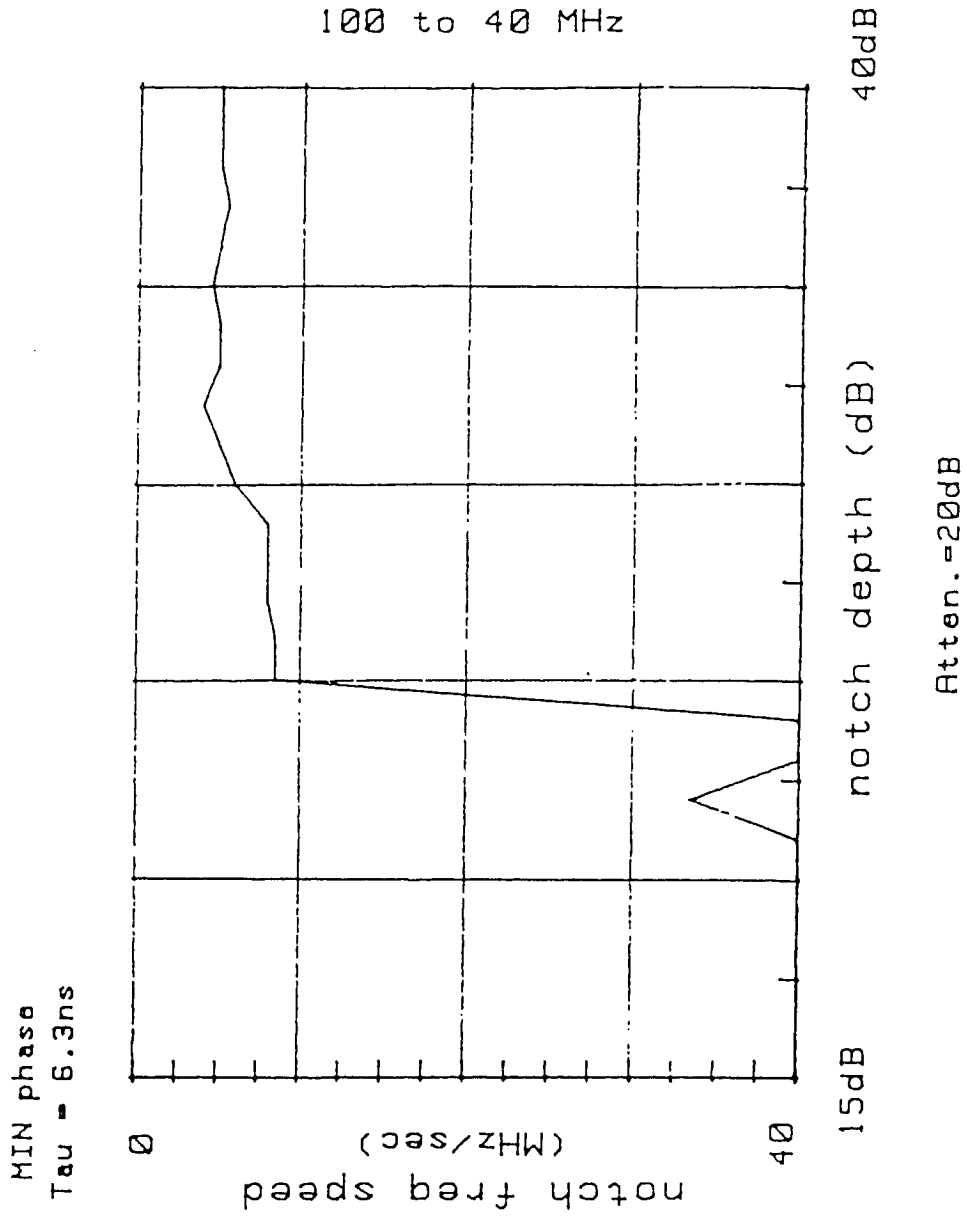
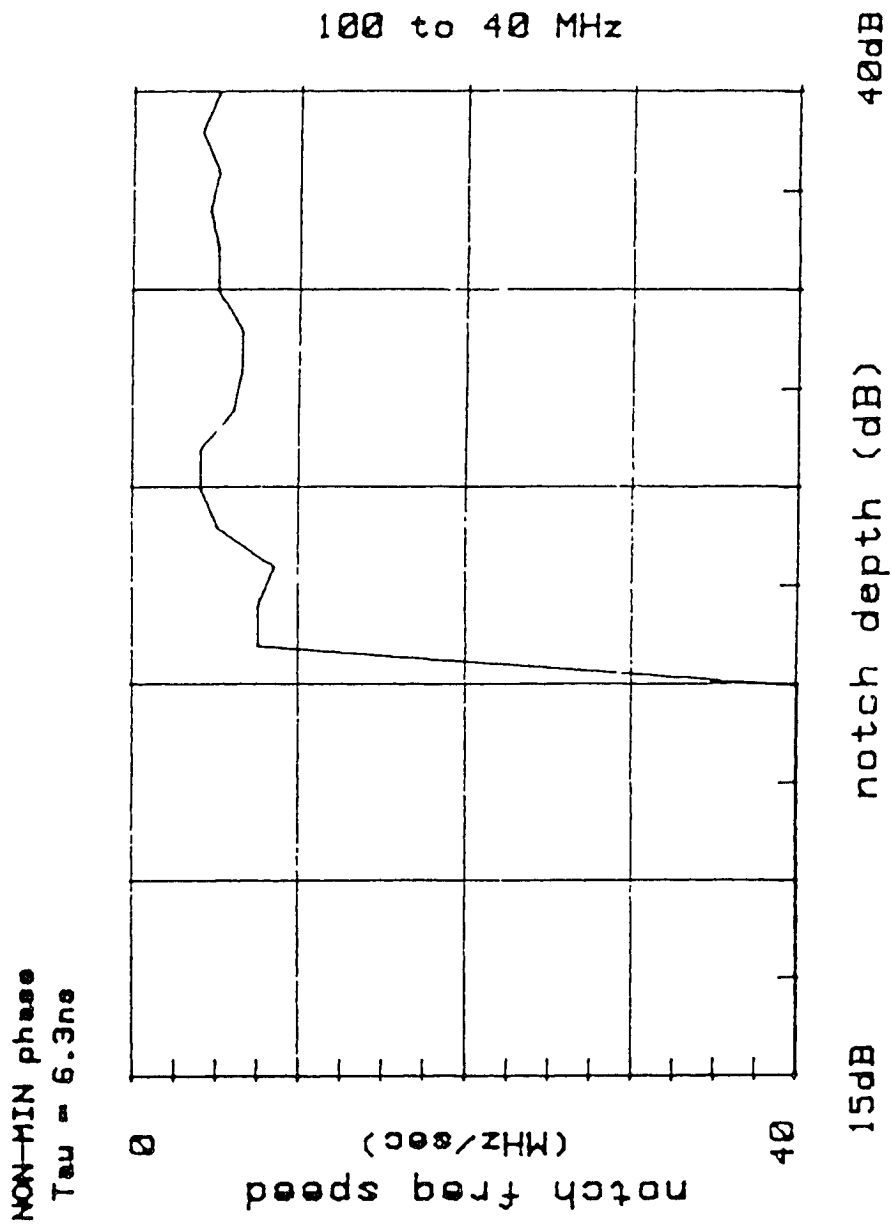


figure 5-7f

Figure 5-7f: Dynamic Null Frequency



upward in the frequency domain represents a negative second ray delay that is decreasing in magnitude. The direction of change in delay for the non-minimum phase condition (less negative) is opposite to the direction of change for the minimum phase condition (less positive). A mirror image relationship exists between the minimum phase with increasing frequency and the non-minimum phase with decreasing frequency.

The bit error performance curve represents a measurement of bit errors after protection. The cancellation frequency ranges are from 40 MHz to 80 MHz (figures 5-8a-e) or from 100 MHz to 60 MHz (figures 5-9a-e). The velocity ranges from 0 to 40 MHz/sec. There is a 20 dB variation in cancellation depth. The cancellation depth ranges from 20 dB to 40 dB. For either direction of cancellation frequency sweep, the cancellation depth will be 30 dB when the minimum arrives at the channel edge (60 or 80 MHz). Figures 5-8 and 5-9 show the log (base 10) of bit errors versus the cancellation frequency velocity (MHz/sec). Figures 5-8a,b and 5-9a,b show little difference with respect to a delay of 6.3 or 4 nanoseconds. But, examination of figures 5-8c and 5-9c shows that a delay of 1 nanosecond resulted in no bit errors for up to 40 MHz/sec cancellation frequency velocities. Addition of flat attenuation of 10 or 20 dB (figures 5-8d,e, 5-9d,e), or changes of two ray phase conditions (figures 5-8f, 5-9f), did not change the results significantly.

Comparison of the static multipath signatures in figures 5-3 (a-f) 5-4 (a-f) with the dynamic cancellation depth signatures in figures 5-5 (a-f) confirms the similarity discussed in section 5.3. The static signatures show outage (BER = $1E-3$) and impairment (BER = $1E-6$) to performance generally beginning at in-band cancellation depths of 15 to 20 dB. There is some moderate variation of critical depth as a function of second ray delay value for both static and

figure 5-8a

Figure 5-8a: Bit Error Performance as a Function of Dynamic Cancellation Depth

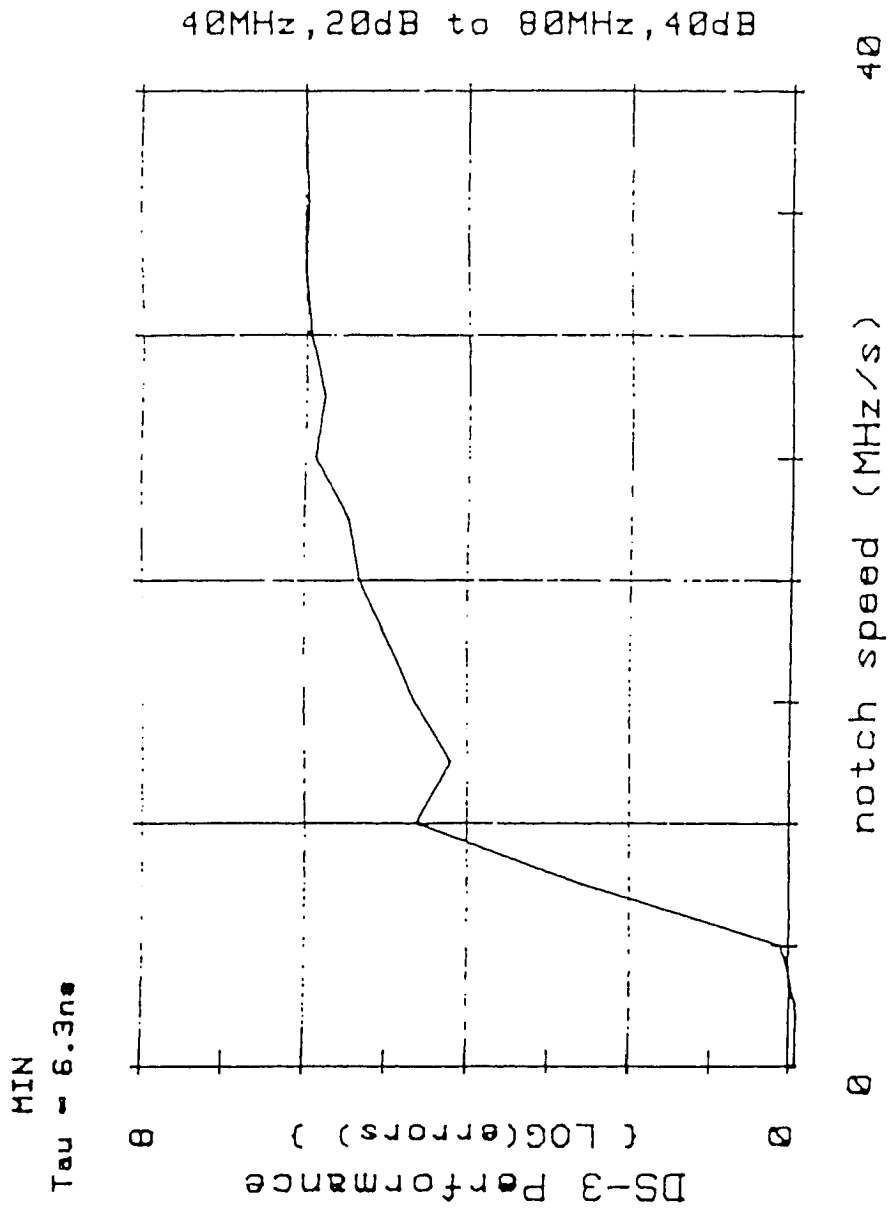


figure 5-8b

Figure 5-8b: Bit Error Performance as a Function of Dynamic Cancellation Depth

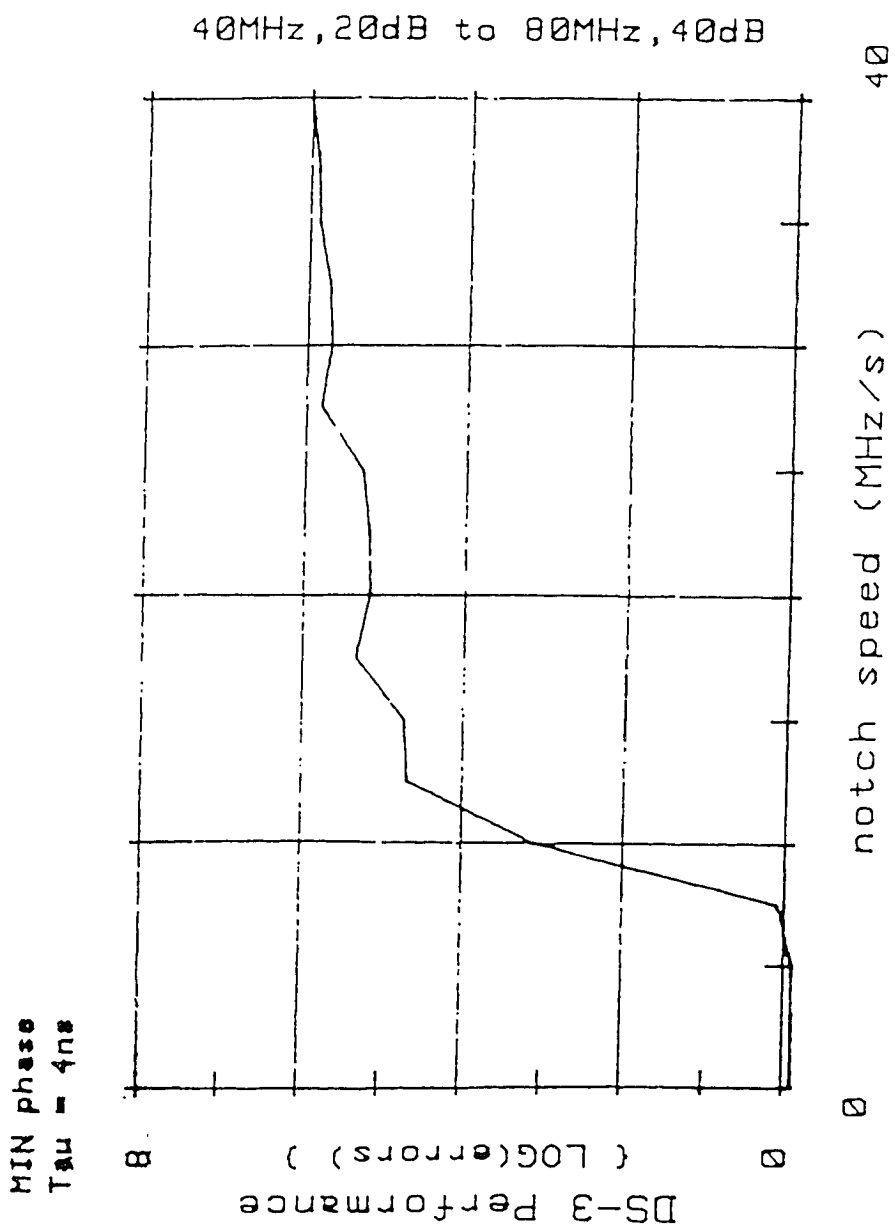


figure 5-8c

Figure 5-8c: Bit Error Performance as a Function of Dynamic Cancellation Depth

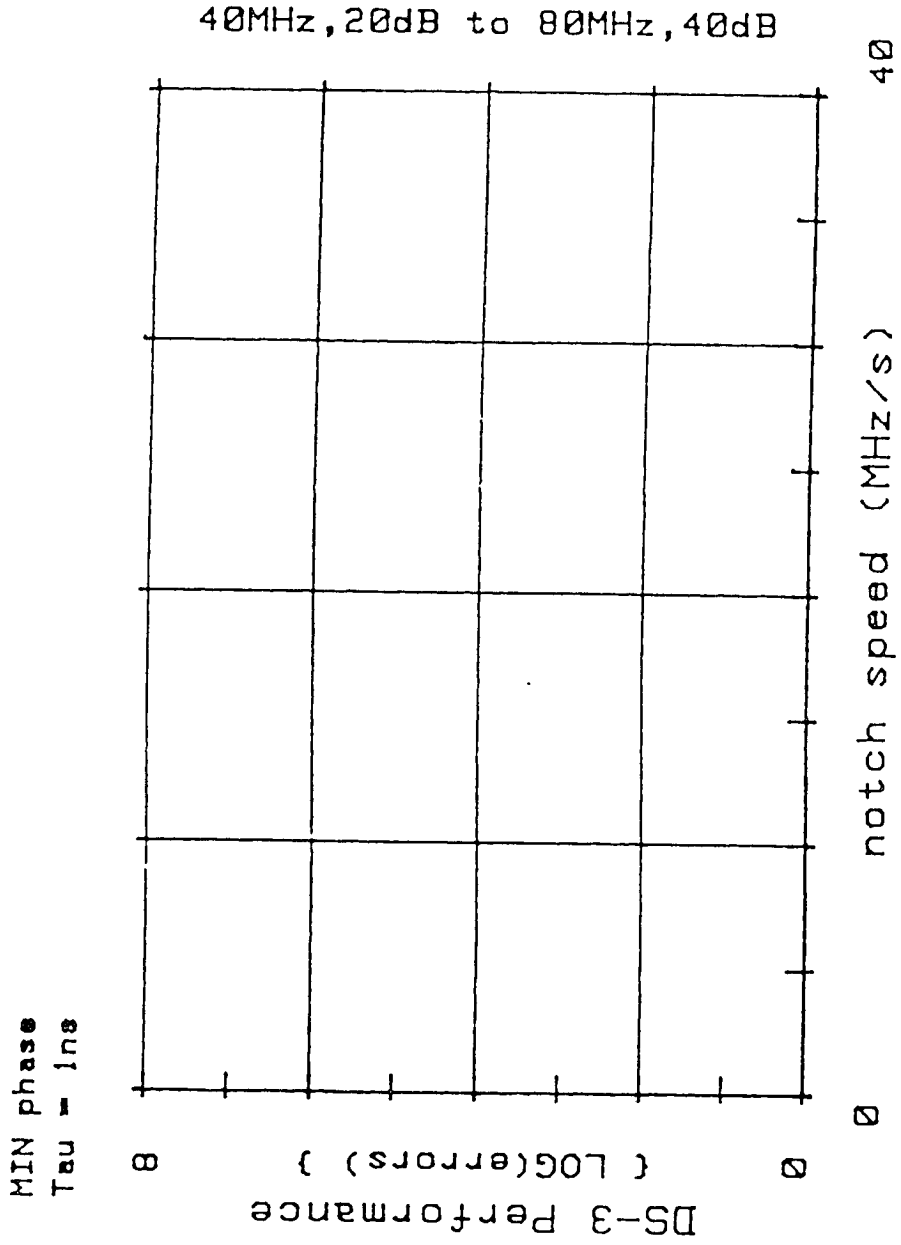


figure 5-8d

Figure 5-8d: Bit Error Performance as a Function of Dynamic Cancellation Depth

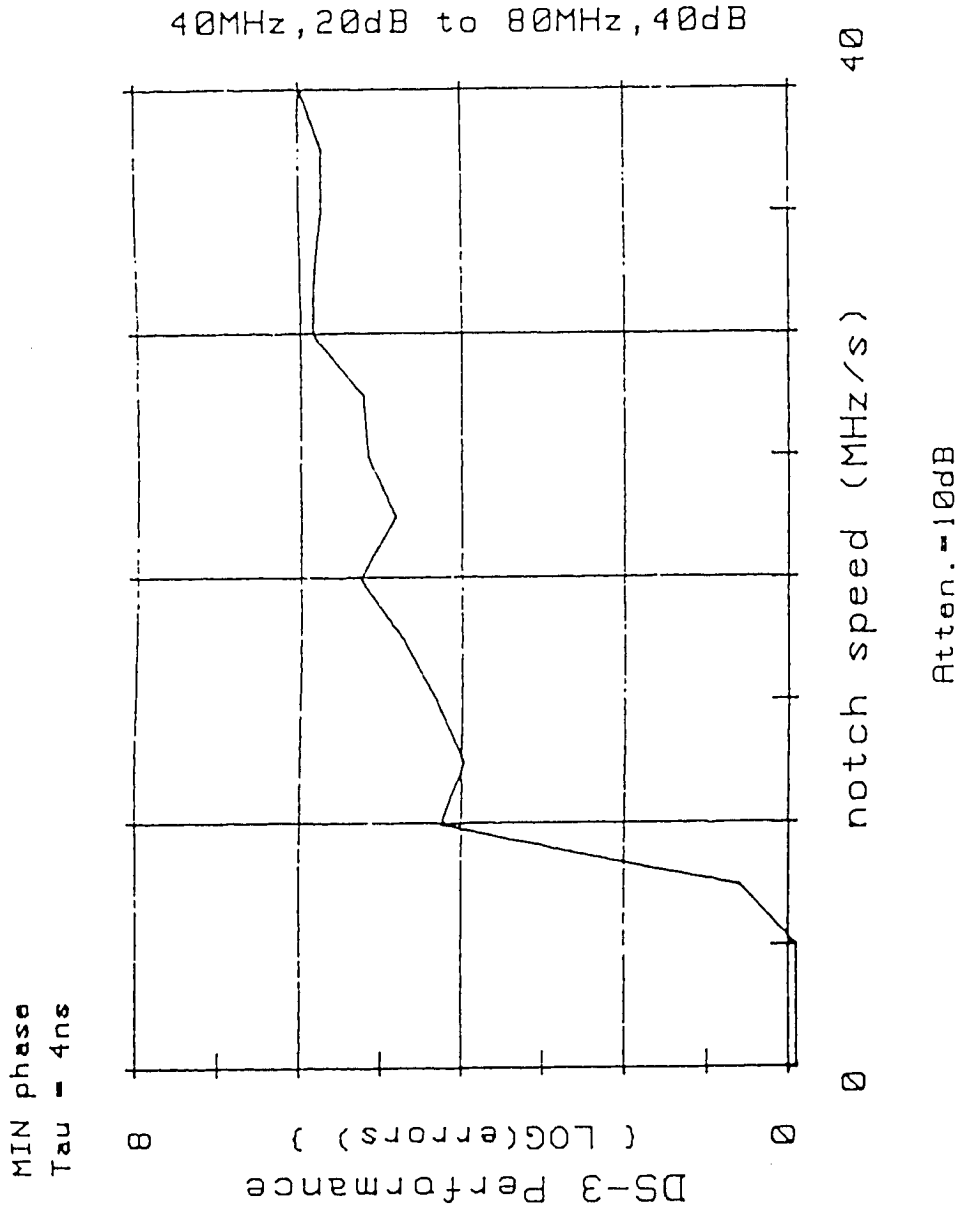


figure 5-8e

Figure 5-8e: Bit Error Performance as a Function of Dynamic Cancellation Depth

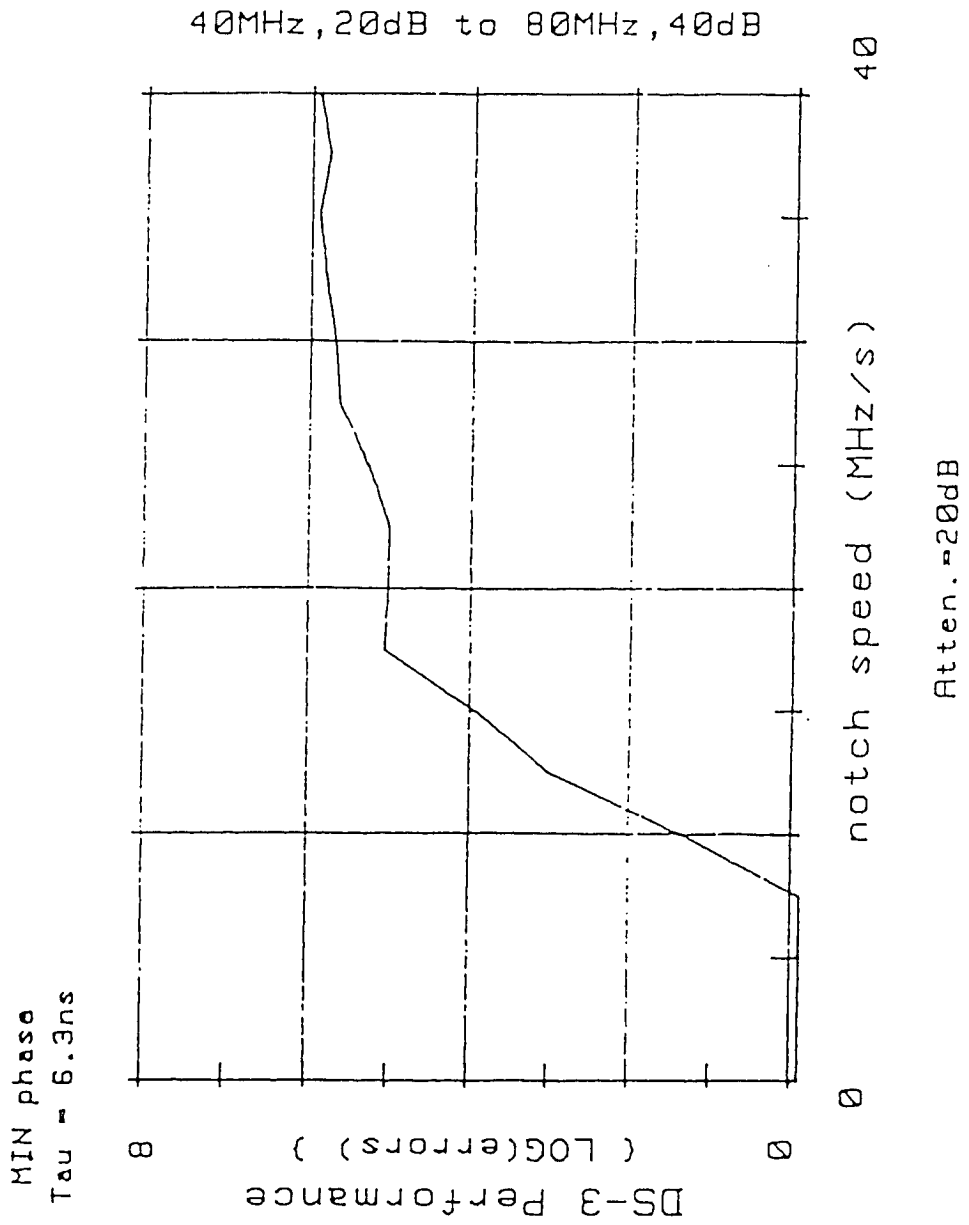


figure 5-8f

Figure 5-8f: Bit Error Performance as a Function of Dynamic Cancellation Depth

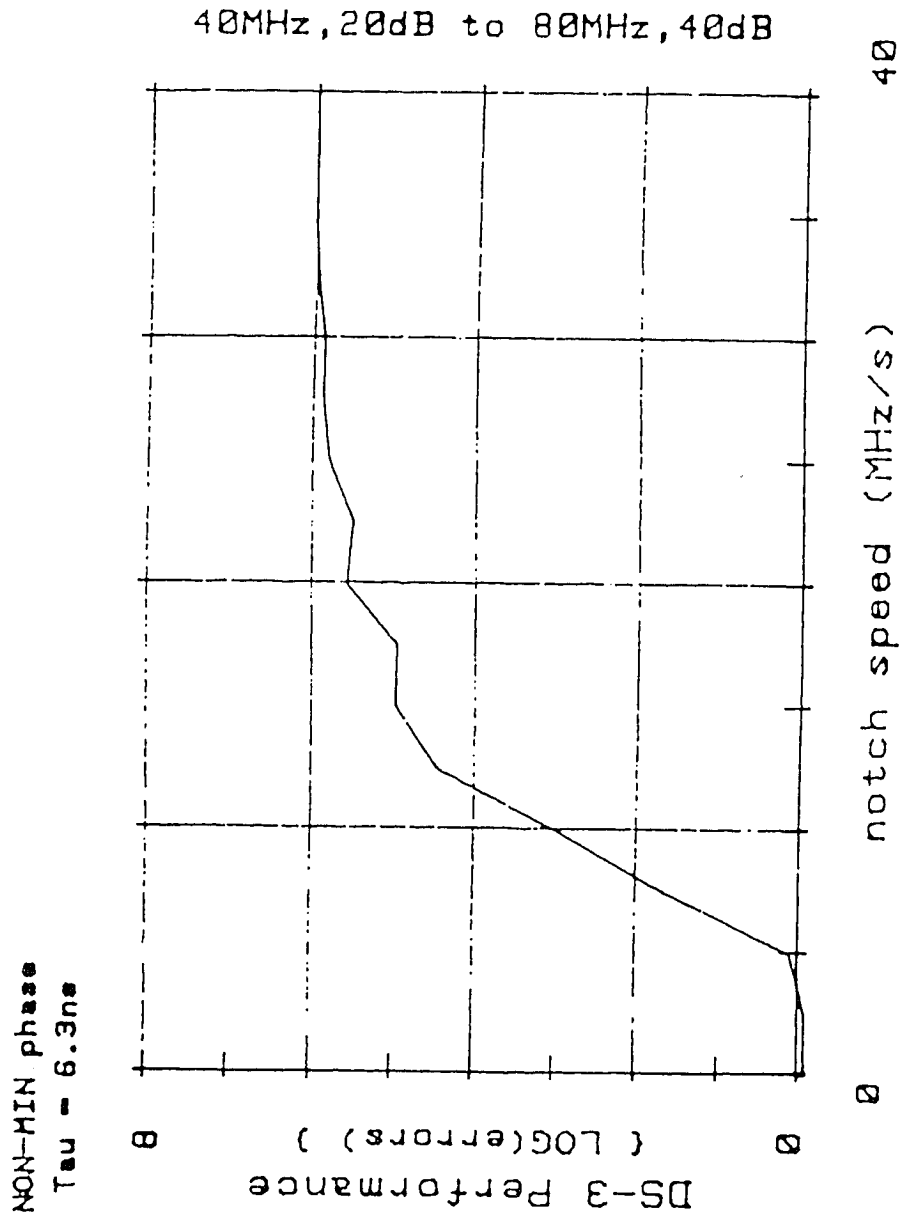


figure 5-9a

Figure 5-9a: Bit Error Performance as a Function of Dynamic Null Frequency

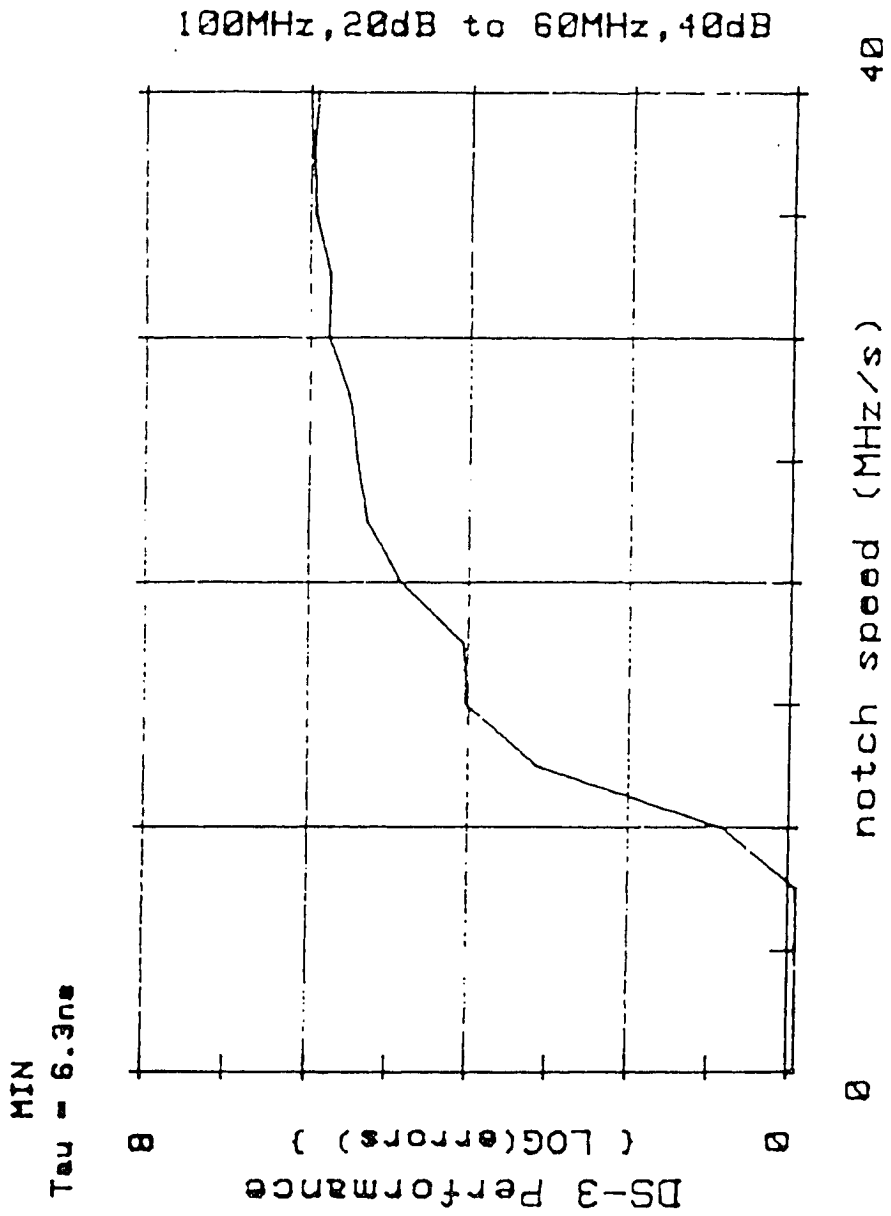


figure 5-9b

Figure 5-9b: Bit Error Performance as a Function of Dynamic Null Frequency

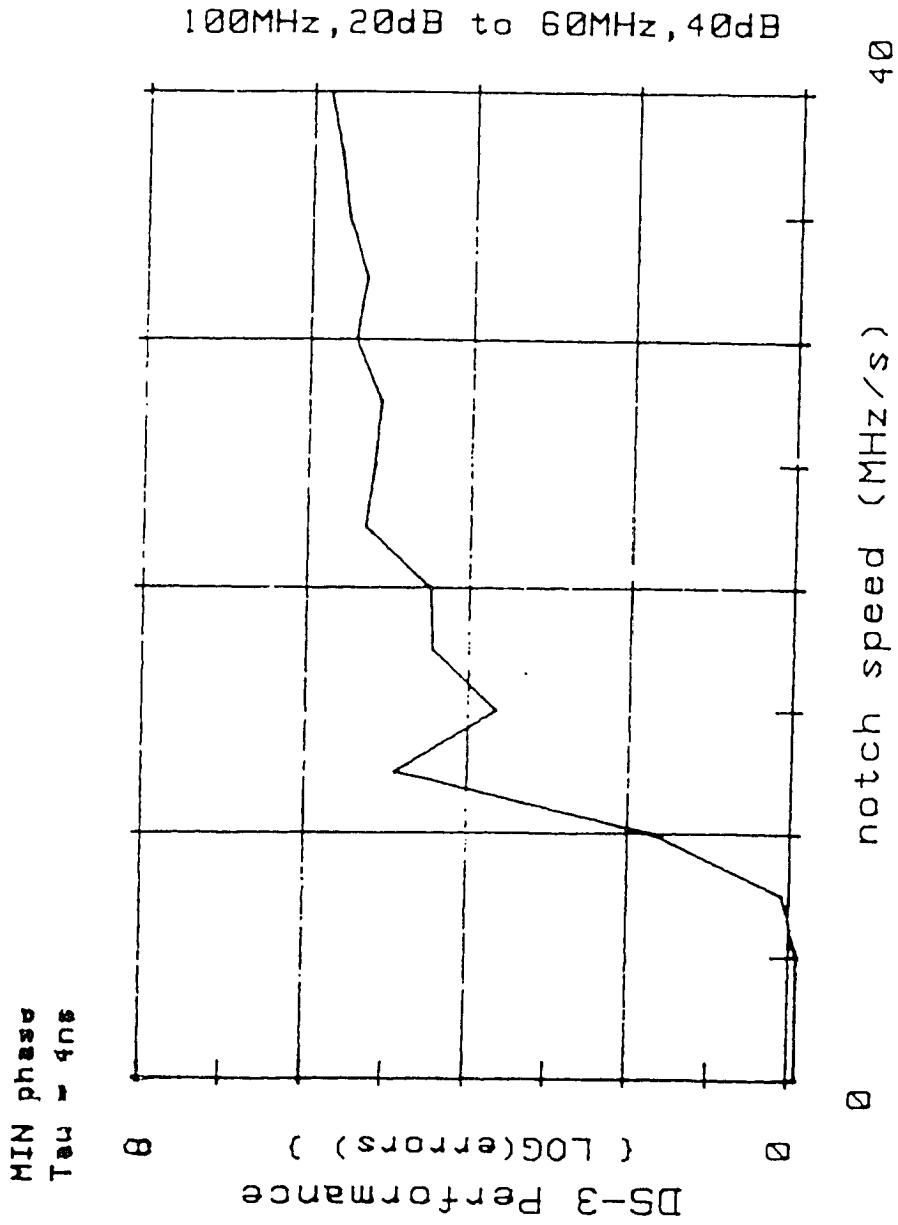


figure 5-9c

Figure 5-9c: Bit Error Performance as a Function of Dynamic Null Frequency

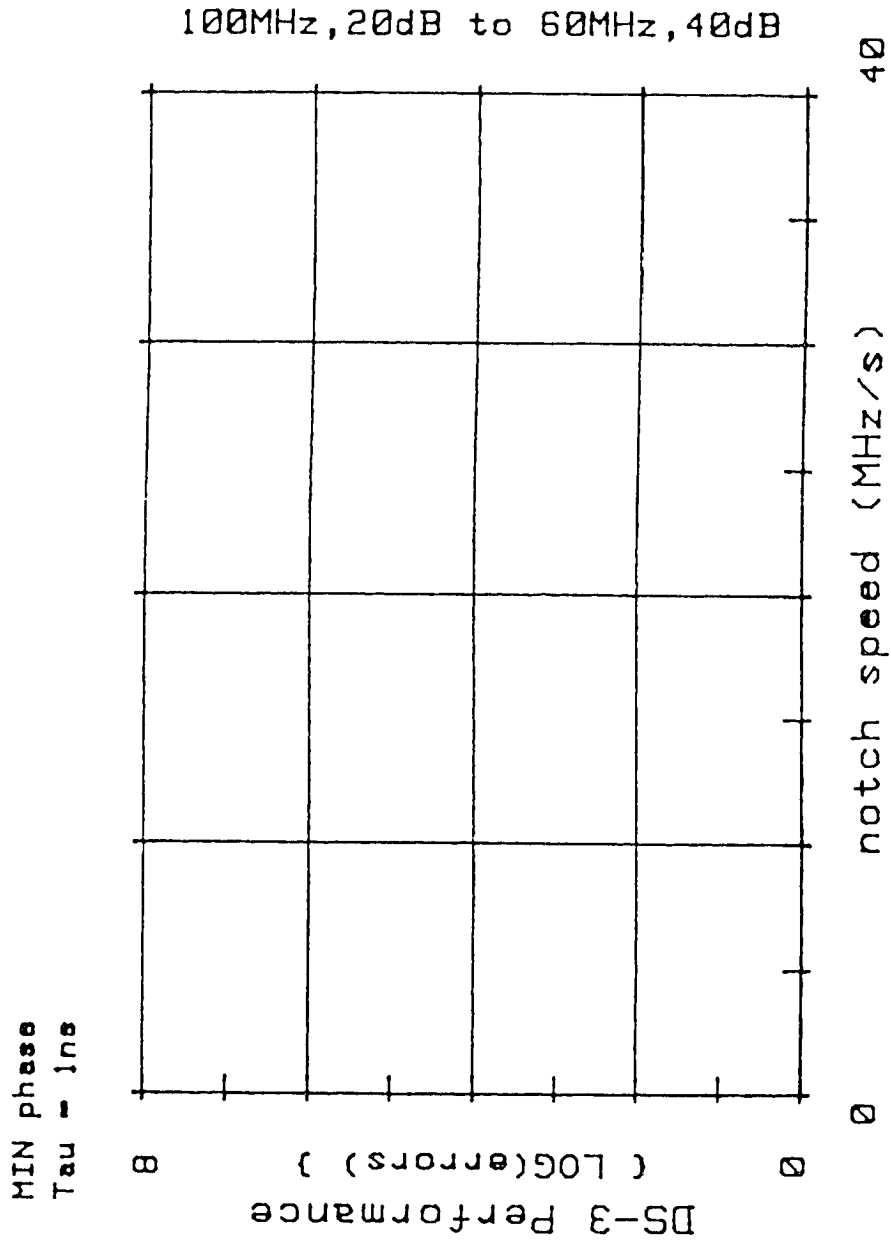


figure 5-9d

Figure 5-9d: Bit Error Performance as a Function of Dynamic Null Frequency

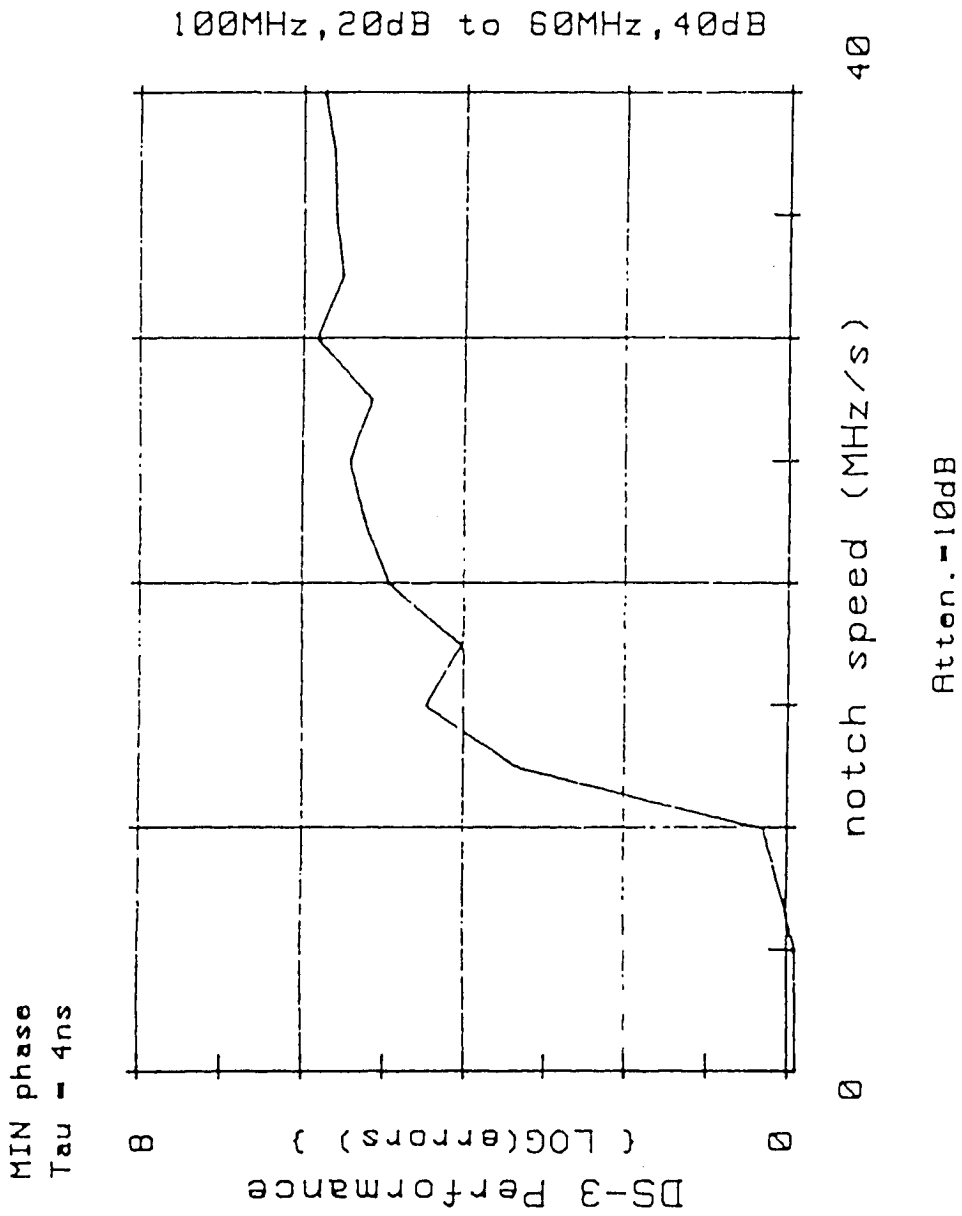


figure 5-9e

Figure 5-9e: Bit Error Performance as a Function of Dynamic Null Frequency

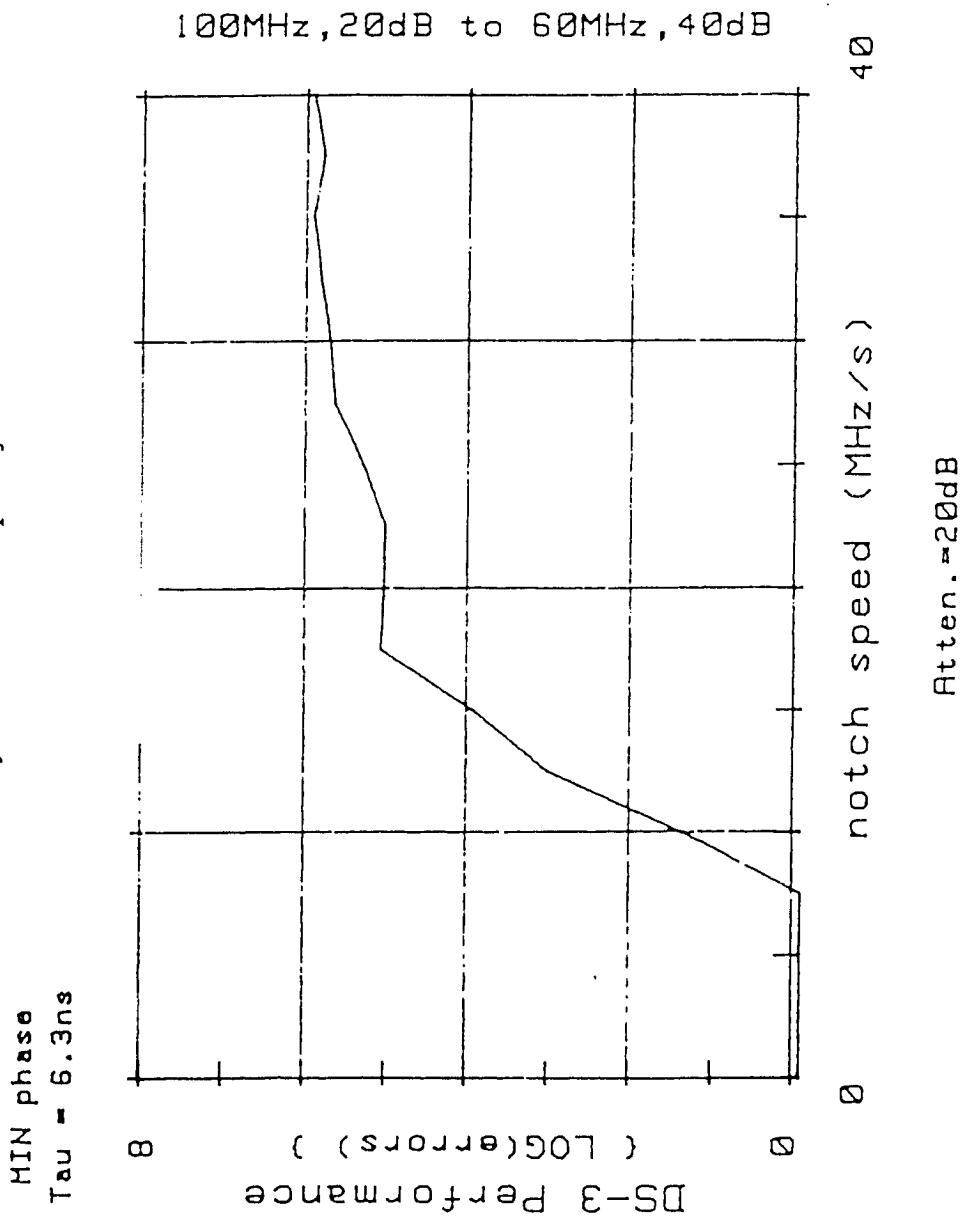


figure 5-9f

Figure 5-9f: Bit Error Performance as a Function of Dynamic Null Frequency

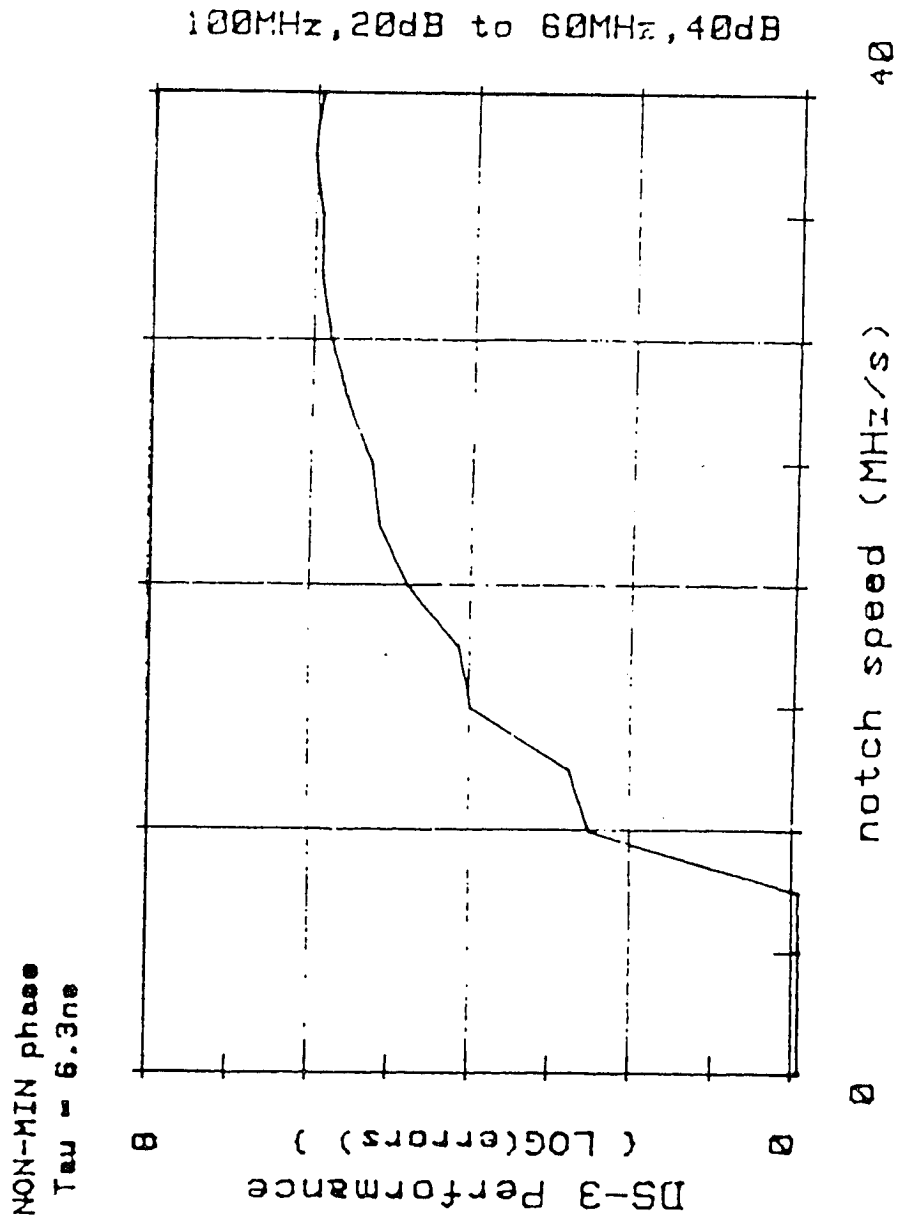
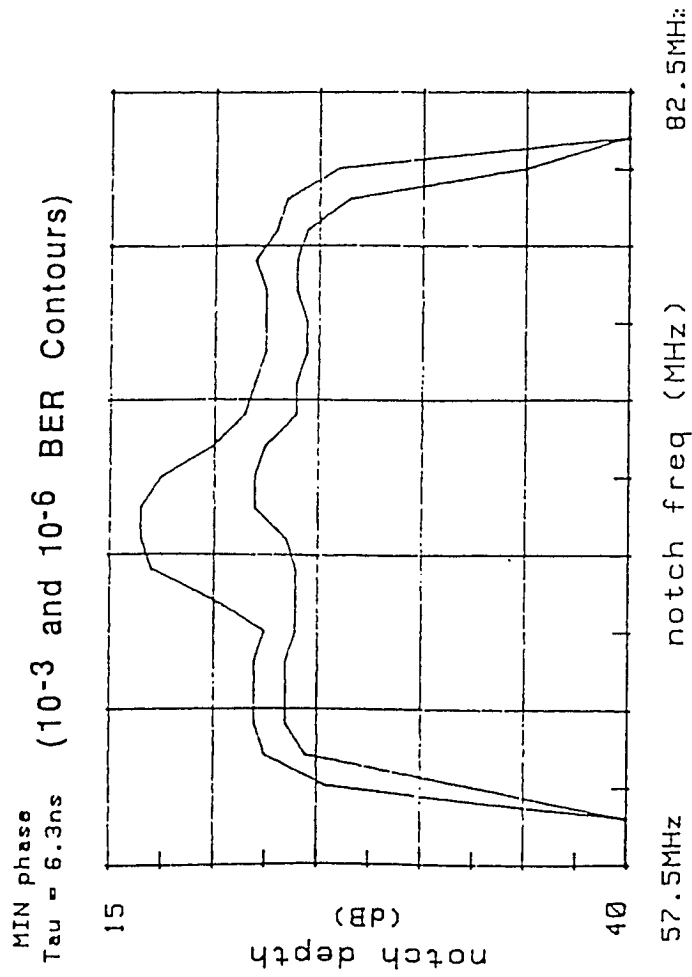


figure 5-10

Figure 5-10: Comparison of the 10^{-3} and 10^{-6} Static Signatures



dynamic signatures. This is consistent with errored performance at depth velocities of 10 to 20 dB per second. If in-band cancellation depths of 20 dB are obtained before active countermeasures are capable of correction or protection, impairment results.

Comparison of the static multipath signatures in figures 5-3 (a-f) - 5-4 (a-f) with the dynamic cancellation frequency signatures in figures 5-6 - 5-7 (a-f) also illustrates the behaviour discussed in section 5.3. The static signatures show outage ($BER = 1E-3$) and impairment ($BER = 1E-6$) to performance generally beginning at in-band cancellation depths of 15 to 20 dB. This is confirmed by the errored performance at cancellation depths of 10 to 20 dB in the dynamic signatures. However, two important observations are noted. Once a critical cancellation depth is reached, performance is errored for any cancellation frequency velocity exceeding approximately 3 - 7 MHz per second. This critical cancellation depth is shown to be a function of second ray delay. Similarly, comparison of overall results for small versus large delay reveals a significant performance difference due to the critical cancellation depth. For small delays, performance is error-free to nearly 40 dB cancellation depths. The test system is more successful at correction of and protection from the small delay multipath phenomena than from the large delay phenomena. The dynamic signature is necessary to evaluate performance of a system equipped with countermeasures and protection switching in a fading environment. The static signature does not characterize the end-to-end performance in the presence of dynamic distortions.

5.8 Evaluation of a 64 QAM System

The accuracy of the dynamic signature is dependent upon the timing cycle of the protection system. The time for completion of a protection switch

may vary. Switch completion time is dependent on the time of the request and the availability of a protection channel. A measurement of the variation in time for protection switch completion is shown in figure 5-11. The curve on the right represents a typical system response. The curve on the left represents an experimental system response. The curve in the middle represents the tested radio system. The mean time to switch completion is approximately 45 milliseconds.

For the dynamic cancellation frequency signature, the time interval for a notch sweep is decreased until switching errors occur. At this point, the threshold cancellation frequency velocity is

$$f_t = \frac{\Delta f}{\Delta t_t} \text{ Hz/sec.} \quad (5-28)$$

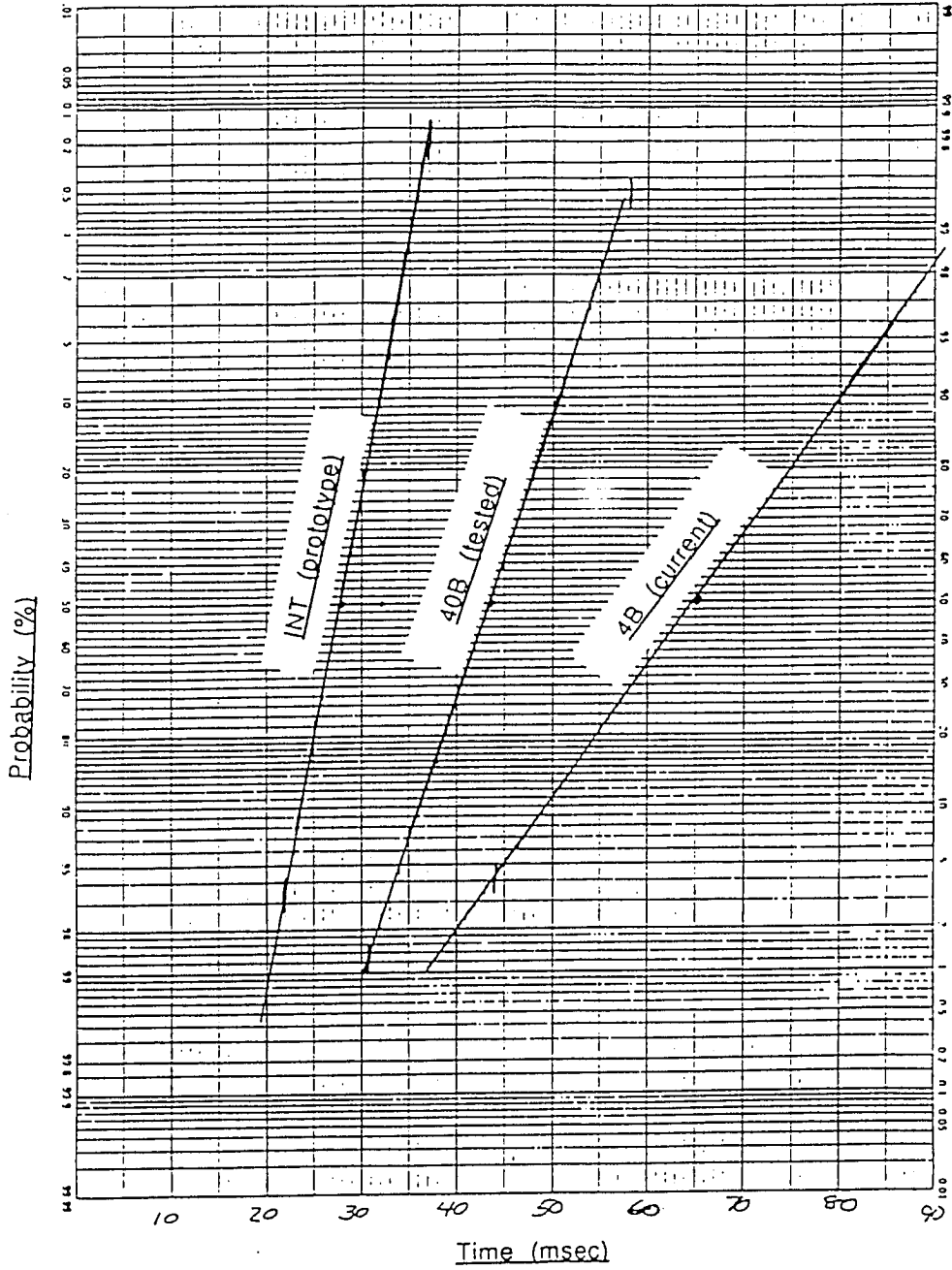
The numerator represents the change in cancellation frequency. The denominator represents the threshold time interval for the frequency change. Ideally, Δt_t is the minimum time during which the system can complete a protection switch without error. Variation in the protection switch completion time affects the threshold time interval. The threshold time interval is the sum of an actual elapsed time for a frequency sweep $\Delta t_{\Delta f}$ and the protection switch completion time δt ,

$$\Delta t_t = \Delta t_{\Delta f} + \delta t \text{ (sec)} \quad (5-29)$$

Ideally, the switch is instantaneous and the required δt is zero. The threshold frequency speed is proportional to the frequency transition time. In reality, δt varies as shown in figure 11. The result is a variation in measured threshold

figure 5-11

Figure 5-11: Typical Time from Protection Switch Request to Completion



speeds. As the switch time δt increases, the threshold notch frequency speed decreases.

Variations in performance measurement result from protection requests initiated at an unusually inconvenient point in time. An errorless switch was not possible. As is shown in figure 5-11, there is substantial variation in protection switch completion time. This phenomenon caused the coarseness in some of the results.

As the dynamics of fade activity increase, errors become more likely because a minimum may arrive in band before a switch can be completed. For the AT&T 6-GHz 135 Mbit/sec radio system, switch request occurs when the error rate reaches 14 error counts in less than 100 milliseconds (BER approximately 10^{-6}). If the time required for the BER to worsen from 10^{-6} to 10^{-3} is less than the switch completion time, errors will result. A comparison of static signatures for 10^{-3} and 10^{-6} (figure 10) will show an indication of the transition between switch request and outage. Coupled with knowledge of the fade dynamics, the range of variation in dynamic threshold may be specified.

5.9 Summary

The static multipath signature was examined with respect to second ray delay, phase of fade, and broadband attenuation. Emswiller [43] demonstrated that the static signature is linearly related to delay difference. The signature is independent of attenuation for values appreciably less than the fade margin. It is also independent of the phase of fade. The signature theory was extended to generate two dynamic signatures for the evaluation of radio system performance in the presence of multipath fading. In addition, a bit error curve for evaluating the performance of antenna and channel

protection switching systems in the presence of dynamic multipath interference was developed. The static signature, the dynamic signatures, and the bit error curve were used to evaluate an AT&T 64 QAM digital radio system.

The dynamic cancellation depth signature evaluated the effect of a changing cancellation depth with a fixed cancellation frequency. It identified the ability of the system to withstand changes in signal level at specific frequencies within the channel. As a result, it defined the transition from error-free to errored operation in terms of cancellation depth speed. The dynamic cancellation depth signature was shown to be a function of the difference between static signatures defined at the outage threshold (10^{-3}) and at the protection switch request threshold (10^{-6}). Critical depths in the static signature correspond to critical depth velocities in the dynamic signature. Some variation was found as a function of second ray delay. However, the performance appears to be independent of attenuation and of relative phase state. These signatures are representative of atmospheric focussing, where the ratio of the secondary to the direct ray is the critical parameter for interference to occur once a secondary path has established.

The dynamic cancellation frequency signature evaluated the effect of a changing cancellation frequency with a fixed cancellation depth. It demonstrated the ability of the system to withstand minima moving across a 60 MHz band. As a result, it defined the transition from error-free to errored operation in terms of cancellation frequency speed. The dynamic cancellation frequency signature is also linearly related to the second ray. Critical cancellation frequency velocity was shown to be a function of second ray delay. It is independent of attenuation that is appreciably less than the fade

margin. A relationship between the phase of the fade and the direction of notch frequency movement was also shown. This signature is representative of ground or atmospheric reflections, where the secondary path is established and the path length or delay is the critical parameter controlling interference in a particular frequency band.

The bit error performance signature examined the effect of a changing cancellation frequency with varying cancellation depth. It measured the error response of the system to various channel perturbations. Like the dynamic cancellation frequency signature and the static signature, it was related to the second ray delay. The bit error performance curve appears to be independent of attenuation and of the phase state. The dynamic signatures offer the capability of characterizing the performance of radio protection systems. The threshold of error-free operation may be identified in two dimensions. The signatures allow simulation of a dynamic multipath fading environment. The importance of the second ray delay to proper system evaluation is shown by the static and the dynamic multipath signatures. It has a marked effect on the threshold of outage and the probability of successful countermeasures.

CHAPTER VI

SIGNAL ANALYSIS

Introduction

Distortion of the communication channel corresponds to distortion of the transmitted signal. The result is incorrect estimation of the transmitted signal, and a subsequent loss of information. The relevant distortions, such as multipath interference, are generally characterized in the frequency domain, as was reviewed in chapter 4. However, if time domain data are available they are more directly related to system performance. In this chapter a signal model is established for the QAM receiver in order to study the relationship between channel distortions in frequency and system performance in time. A method for channel recovery from the receiver output is then developed. The channel recovery technique will be applied to the system model to evaluate the effects of multipath interference on QAM link performance in chapter 7.

The input to the QAM receiver is the output of the communication channel that was modelled in chapter 4. A QAM receiver channel model is developed and is then used to compute the time domain response of the receiver from frequency domain distortions at the QAM receiver input. As the effects of real time channel perturbations on signal quality and system performance appears at the output of the QAM receiver, the receiver model allows us to remove these effects.

The QAM digital signal theory is reviewed in section 6.1. The QAM receiver functionality is described in section 6.2. Implementation of system functions, such as equalization, synchronization, and sampling, are considered in section 6.3. The overall receiver model is reviewed in section 6.4.

6.1 QAM Digital Signal Theory

The quadrature amplitude modulation (QAM) signal consists of an **in-phase** (I) component and a **quadrature-phase** (Q) component. The I and Q components may be represented by vectors along the real and imaginary axes.. The resultant vectors form a symmetrical signal constellation in the phase plane. By mapping the signal states into orthogonal vectors, more information may be transmitted than by standard amplitude or frequency modulation. Consequently, each signal state has a real and an imaginary component corresponding to the I and Q vectors.

The detected signal at the QAM receiver filter output is expressed as

$$y(t) = y_I(t) + j y_Q(t) \quad (6-1)$$

where the y_I is the in-phase component and the y_Q is the quadrature-phase component. The pulse must not contribute energy at other symbol decision times so as not to affect other symbol decisions. The transmit pulse shape is therefore selected to minimise **Inter-Symbol Interference** (ISI). The pulse duration is equal to the symbol interval. The pulse is designed such that its amplitude is zero at non-zero symbol intervals. A $\sin(x)/x$ pulse shape, where $x=(\pi t/T)$, accomplishes the desired effect (see figure 3-2a). It has periodic zero crossings at symbol intervals of T and it has a maximum at zero.

The $\sin(x)/x$ pulse is equivalent to a rectangular shaped channel response (see figure 3-2b). Amplitude and delay distortion in the channel correspond to dispersion or spreading of the pulse in the time domain. Dispersion therefore results in ISI. Amplitude and delay distortion in the frequency channel also show up as phase distortion in the time domain. This may cause a decision error in the QAM system by moving the received signal vector into the wrong signal decision region.

In QAM systems, the detected signal is sampled at the symbol interval. A symbol decision is made at each sample time based on the estimated I and Q components. The voltage not associated with the transmitted symbol at that sampling instant results in ISI and contributes to decision error.

The sampled signal for each component in (6-1) may be written as

$$y_I(t) = \sum_{k=-n}^{k=+n} c_k^{IxI} s_I(t-kT) + j \sum_{k=-n}^{k=+n} c_k^{IxQ} s_Q(t-kT) \quad (6-2a)$$

$$y_Q(t) = \sum_{k=-n}^{k=+n} c_k^{QxQ} s_Q(t-kT) + j \sum_{k=-n}^{k=+n} c_k^{QxI} s_I(t-kT) \quad (6-2b)$$

The s_I and s_Q are the sampled signals corresponding to each component of the QAM signal. At any particular instant, the estimated signal is a snapshot of the transmitted symbol combined with signal contributions from past ($t > 0$) and future ($t < 0$) symbols. The signal vectors are sampled at decision times ($t = kT$, $k = \dots, -2, -1, 0, 1, 2, \dots$). The c_k are the coefficients for each signal vector. The T is the symbol interval length, and the k corresponds to the symbol interval of interest. The total number of samples is $N = (2n + 1)$. For the I vector, the c_k^{IxI} are the co-vector or real component coefficients, and the c_k^{IxQ}

are the cross-vector or imaginary components for non-zero symbol intervals kT . These co-vector coefficients represent the in-phase signal contributions to the respective components for all symbol intervals kT . Similarly, for the Q vector, the $c_k^{Q \times Q}$ are the co-vector or real component coefficients, and the $c_k^{Q \times I}$ are the cross-vector or imaginary components for time $t = kT$. These cross-vector coefficients represent the out-of-phase signal contributions to the respective components for all symbol intervals kT .

6.2 Receiver Implementation

A tapped delay line equalizer is one of the major components of a modern QAM digital receiver. It is used in carrier detection and timing recovery algorithms. Under stable conditions and equalization, the equalizer status is a function of the channel conditions.

The impulse response of a tapped delay line equalizer may be written as a sum of impulses at symbol intervals in time scaled by the corresponding equalizer coefficients:

$$d[n] = \sum_{m \in \langle N \rangle} d_m \delta(n-m), \quad (6-3)$$

where n is the discrete time, N is the total number of taps, and the d_m are the equalizer coefficients [45]. The corresponding frequency response is given by the discrete fourier series

$$D[k] = \frac{1}{N} \sum_{n \in \langle N \rangle} d[n] e^{j\left(\frac{2\pi}{N}\right)kn}, \quad (6-4)$$

where \mathbf{k} is the discrete frequency. If the input to the equalizer is defined in the discrete frequency domain as $\mathbf{Y}(\mathbf{k})$, and the output is defined as $\mathbf{Z}(\mathbf{k})$, then the equalizer response is

$$\mathbf{Z}[\mathbf{k}] = \mathbf{Y}[\mathbf{k}] \mathbf{D}[\mathbf{k}]. \quad (6-5)$$

If the equalizer is compensating properly, the response $\mathbf{Z}[\mathbf{k}]$ will be flat with a constant reference level \mathbf{A} , and the input channel to the equalizer becomes

$$\mathbf{Y}[\mathbf{k}] = \frac{\mathbf{A}}{\mathbf{D}[\mathbf{k}]}. \quad (6-6)$$

The input channel to the equalizer is written as a discrete fourier series,

$$\mathbf{Y}[\mathbf{k}] = \frac{1}{\mathbf{N}} \sum_{\mathbf{n}=\langle \mathbf{N} \rangle} \mathbf{y}[\mathbf{n}] e^{-j\left(\frac{2\pi}{\mathbf{N}}\right)\mathbf{k}\mathbf{n}} \quad (6-7)$$

where \mathbf{k} is the discrete frequency, $\mathbf{Y}[\mathbf{k}]$ are frequency coefficients, \mathbf{n} is the discrete time, $\mathbf{y}[\mathbf{n}]$ are the time samples, and \mathbf{N} is the number of samples. Since the purpose of the equalizer is to compensate for channel distortion, the coefficients are adjusted to compensate for distortions in the received signal. The equalizer coefficients $\mathbf{d}[\mathbf{n}]$ in time represent the inverted values of the sampled signal $\mathbf{y}[\mathbf{n}]$ in time:

$$\mathbf{d}[\mathbf{n}] = -\mathbf{y}[\mathbf{n}], \mathbf{n} \neq 0 \quad (6-8)$$

$$\mathbf{d}[\mathbf{n}] = \mathbf{y}[\mathbf{n}], \mathbf{n} = 0$$

The number of samples N is equal to the number of coefficients in the equalizer. The coefficients represent symbol-interval samples of the received signal in time. The input channel is therefore estimated by inverting the equalizer coefficients and transforming them from the time to the frequency domain.

The DR6-30-135 digital transversal equalizer has 11 baud-interval co-vector and 11 baud-interval cross-vector coefficients for both the I and Q vectors. Having co- and cross-vector coefficients allows the equalizer to compensate for both magnitude and phase distortions.

The zero time co-vector coefficient is normalized to a value of 1 because it corresponds the peak of the transmitted symbol signal. All other coefficients are normalized to this zero time co-vector peak value.

A zero forcing algorithm is used to control adjustment of the coefficients in the DR6-30-135 DTE. It drives the difference between received and estimated signals to zero [46]. The result of a converging adjustment algorithm is a set of coefficients which sufficiently respond to channel distortions. The set represents the sum of a complex valued pulse sampled at zero time and the inverses of complex valued pulses sampled at non-zero symbol intervals.

The channel response, as estimated by the DTE, is expressed in the frequency domain as was the equalizer channel in (6-7), by

$$Y[k] = \frac{1}{11} \sum_{n=-5}^{n=5} y[n] e^{-j\left(\frac{2\pi}{11}\right)kn} \quad (6-9)$$

with n as discrete time and k as discrete frequency. The $y[n]$ correspond to time samples and are related to the $c[n]$ as in (6-3).

In DR6-30-135 the adaptive slope equalizer (ASE) is implemented at IF using frequency domain techniques. An ASE can also be implemented as a fractionally spaced two-coefficient equalizer. The two coefficients are cross-vectors at + 1/2 and - 1/2 baud. The purpose of the ASE is to provide slope correction capability for the channel power. It therefore provides some compensation of the channel shape in frequency, or of the received pulse in time.

For the two tap ASE the channel may be expressed as in (6-7) but with two cross-vector (imaginary component) coefficient values at 1/2 symbol intervals, $y[-1/2]$ and $y[1/2]$,

$$Y[k] = \frac{j}{2}y[-\frac{1}{2}] \left\{ \cos\left(\frac{j\pi k}{2}\right) + j \sin\left(\frac{j\pi k}{2}\right) \right\} + \frac{j}{2}y[\frac{1}{2}] \left\{ \cos\left(\frac{j\pi k}{2}\right) + j \sin\left(\frac{j\pi k}{2}\right) \right\}. \quad (6-10)$$

In this case, the real and imaginary power components are written as,

$$\text{Re}\{Y[k]\} = \frac{-1}{2}y[-\frac{1}{2}] \left\{ \sin\left(\frac{j\pi k}{2}\right) \right\} + \frac{-1}{2}y[\frac{1}{2}] \left\{ \sin\left(\frac{j\pi k}{2}\right) \right\}, \quad (6-11)$$

and

$$\text{Im}\{Y[k]\} = \frac{1}{2}y[-\frac{1}{2}] \left\{ \cos\left(\frac{j\pi k}{2}\right) \right\} + \frac{1}{2}y[\frac{1}{2}] \left\{ \cos\left(\frac{j\pi k}{2}\right) \right\}, \quad (6-12)$$

The sine function in (6-11) gives rise to odd symmetry or slope in the real component, whereas the cosine in (6-12) yields even symmetry in the imaginary component. The effect of the ASE upon the received signal is related to that of the DTE. It has a limited ability to compensate for shape distortions in the channel. Compensation by the ASE may be of concern to DTE analysis as it is introduced to the signal before the DTE. Analysis of the effect of the ASE was included for completeness, but was not measured here.

6.3 System Considerations

There are limitations to channel estimation that are inherent to the AT&T radio system examined in this study. The transversal equalizer is related to the sampling characteristics in the time domain, as was shown above. Furthermore, the carrier detection and timing recovery operations affect the detected signal. There are $N=11$ coefficients for each vector of the DTE. The result is a set of 11 complex samples in the time domain. There is a direct correspondence between the sample spacing in time and the sequence length in frequency. The tap or sample spacing is 40 nanoseconds in the time domain with a total time span of 400 nanoseconds. The corresponding bandwidth in the frequency domain is therefore 25 MHz, with a sample spacing of 2.5 MHz. In terms of discrete delay, the DTE is capable of compensating for up to +200 or -200 nanoseconds in the time domain. This corresponds to a 5 MHz signal period in the frequency domain. On the low end, the DTE is capable of compensating for as little as +40 or -40 nanoseconds of delay. This corresponds to a 25 MHz signal period in the frequency domain. Therefore, delay distortion in the range of 5 to 25 MHz is directly resolved from the symbol interval samples. Delay greater than 200 nanoseconds (in the time domain), corresponding to a period less than 5 MHz (in the frequency domain), cannot be resolved because of the 2.5 MHz baud-spaced sampling. Delay less than 40 nanoseconds (in the time domain), corresponding to a period greater than 25 MHz (in the frequency domain), is resolved by estimation techniques.

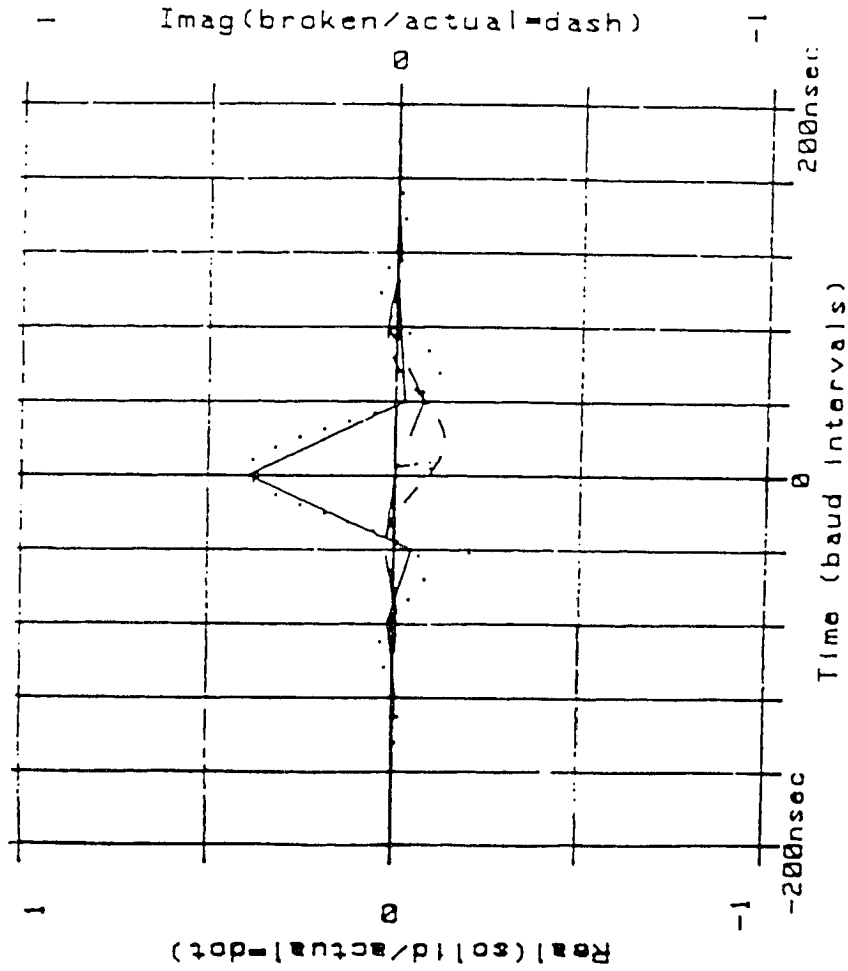
Carrier detection attempts to bring the detected signal closer to the transmitted signal by moving the signal vector in angle about the signal point. It therefore optimizes the phase component of the signal vector. In

doing so, it minimizes the cross-vector distortion ($I \times Q$) in the current signal state. This effect is equivalent to that of the zero-time cross-vector equalizer coefficient. In fact, the cross-vector information from the DTE drives the carrier detection circuit. It acts in opposition to the imaginary zero-time component of the received pulse. In order to prevent the DTE from interfering with carrier detection, the zero-time cross-vector coefficient is made inactive. The DTE assigns a zero to it.

An example of carrier detection in the presence of multipath distortion is shown in figures 6-1 and 6-2. An ideal pulse shape is simulated for transmission through both Nyquist filters and a transmission channel as described in chapter 3. In the transmission channel, two ray fade is simulated where a 10 dB deep minimum is placed 5 MHz below the channel center frequency. The second ray delay is 6.3 nanoseconds. The time response is shown in figure 6-1 and the frequency response in figure 6-2. The dotted curve represents the real component of the received pulse in time. The dashed curve represents the imaginary component. When the minimum is located at the center of the channel, the two ray transfer function is symmetrical. The magnitude has even symmetry and the phase has odd symmetry. When the minimum is not at the channel center, the two ray channel transfer function is non-symmetrical. In this example of a minimum 5 MHz below the center frequency, the two ray channel transfer function does not have symmetry. The peak is attenuated and the pulse shape is not symmetrical. The DTE coefficients represent symbol interval samples of the received pulse. The solid line connects points that represent DTE self-vector values (real parts of complex coefficients). The broken line connects points that represent DTE cross-vector values (imaginary parts of

figure 6-1

Figure 6-1: Multipath Channel Response in the Time Domain
with Receiver Carrier Detection
Two ray fade: $f_0 - f_{\text{car}} = -5$ MHz, depth=10 dB, delay=6.3 nsec
(original & sampled pulse)



complex coefficients). The broken line connects points that represent DTE cross-vector values (imaginary parts of complex coefficients). The carrier detection mechanism results in the difference in value of the cross-vector or imaginary component at zero time. In figure 6-1 it is approximately 0.1.

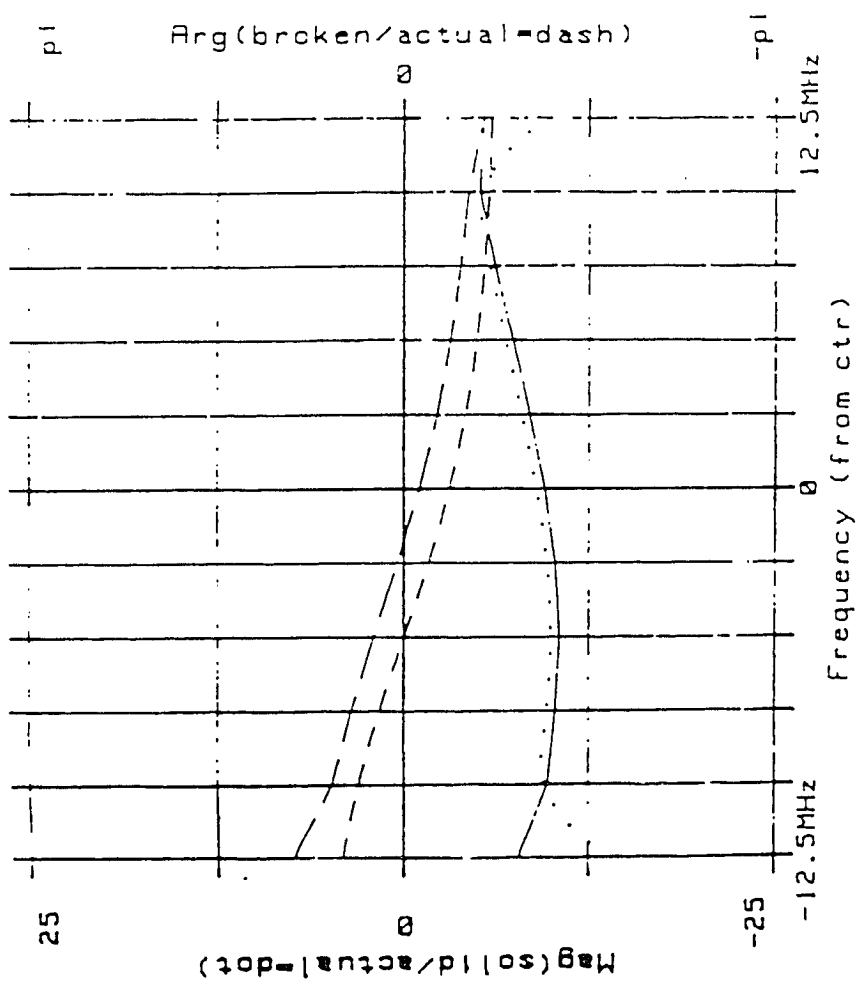
The channel is estimated from the coefficients. The imaginary component of the zero time sample is not available due to the carrier recovery algorithm used in DR6-30-135. If the assigned value of zero is used, the reconstructed channel will have noise. An impulse at zero time is added to the time response. The added impulse is of adequate strength to cancel the zero time cross-vector value. An imaginary impulse in the time domain is equivalent to a constant phase in the frequency domain. It is therefore equivalent to adding broadband phase noise to the signal in the frequency domain. The noise strength will be a function of the error in coefficient value. The result of such missing data is illustrated in figure 6-2. The dotted line shows the magnitude shape of the received channel in frequency. The dashed line shows the phase shape of the received channel in frequency. The reconstructed channel is computed from the DTE coefficient values shown in figure 6-1. In figure 6-2, the solid line shows the magnitude shape of the reconstructed channel. The broken line shows the phase shape. The error of the reconstructed channel phase with respect to the received channel phase is approximately constant through much of the channel.

In order to minimise the phase error, the zero time interval cross-vector coefficient is treated as missing information. It is best obtained by direct measurement. If the zero time interval cross-vector coefficient (or a related measure) is not accessible, it may be interpolated from the existing data points. This is implemented using a least mean squares fit to the data

figure 6-2

Figure 6-2: Multipath Channel Response in the Frequency Domain
with Receiver Carrier Detection

Two ray fade: $f_0 - f_{ctr} = 5$ MHz, depth=10 dB, delay=6.3 nsec
(original & recovered channel)



points as explained in section 4.3. The resulting polynomial is then evaluated at zero time to estimate the zero symbol interval cross-vector coefficient.

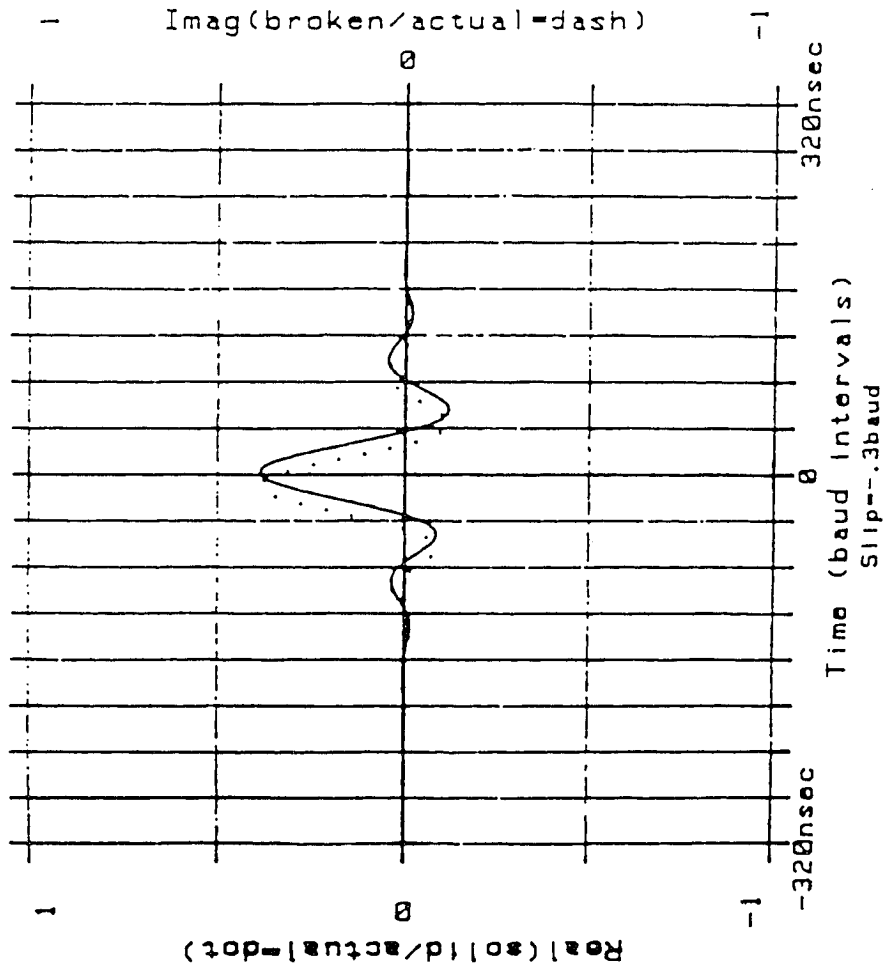
Timing recovery optimizes the sampling of the received pulse in time by aligning the peak of the pulse with the zero time reference axis. This is accomplished by shifting the pulse in time until the co-vector samples of the received pulse at the +1 and -1 symbol intervals are equal. The +1 and -1 baud-interval coefficients from the co-vector drive the timing recovery.

An example of timing recovery in the presence of multipath distortion is shown in figures 6-3 and 6-4. An ideal pulse shape is simulated for transmission through both Nyquist filters and a transmission channel as described in chapter 3. In the transmission channel, a two ray fade is simulated where a notch of 10 dB depth is placed at the channel center. The second ray delay is 6.3 nanoseconds. The time response is shown in figure 6-3, and the frequency response in figure 6-4. The dotted curve represents the real component of the received pulse in time. There is no imaginary component. The symmetrical two ray fade in the frequency domain has the time response described in earlier. The peak is attenuated in strength, and the pulse shape is real and non-symmetrical. The solid curve represents the real component of the pulse after the timing recovery algorithm is implemented. It is the replication of the received (dotted) pulse shifted by 0.3 symbol intervals. The actual pulse peak may not fall exactly on the zero time reference, but it is generally very close. The DTE coefficient values represent symbol interval samples of the pulse after timing recovery. The timing recovery mechanism shifts the data in time. In figure 6-3 the shift is approximately 0.3 symbol intervals. Linear shift of the time response by an amount t_0 corresponds to multiplication of the frequency response by a

figure 6-3

Figure 6-3: Multipath Channel Response in the Time Domain
with Receiver Timing Recovery

Two ray fade: $f_0 = f_{\text{car}}$ deplh=10 dB, delay=6.3 nsec
(original & shifted pulse)



related exponential factor of t_0 :

$$w(t-t_0) = W(f) e^{-j2\pi f t_0} \quad (6-13)$$

The shift in time corresponds to distortion of the phase component in frequency. To recover the phase response in the frequency domain, it is necessary to measure or estimate the amount of shift in the time domain due to timing recovery.

The result of timing recovery distortion is illustrated in figure 6-4. The dotted line shows the magnitude shape of the received channel in frequency. The dashed line shows the phase shape of the received channel in frequency. The reconstructed channel is computed from the DTE coefficients of the pulse shown in figure 6-3. In figure 6-4, the solid line shows the magnitude shape of the reconstructed channel. The broken line shows the phase shape. The error in the reconstructed channel phase with respect to the received channel phase varies with frequency, as anticipated by equation (6-13).

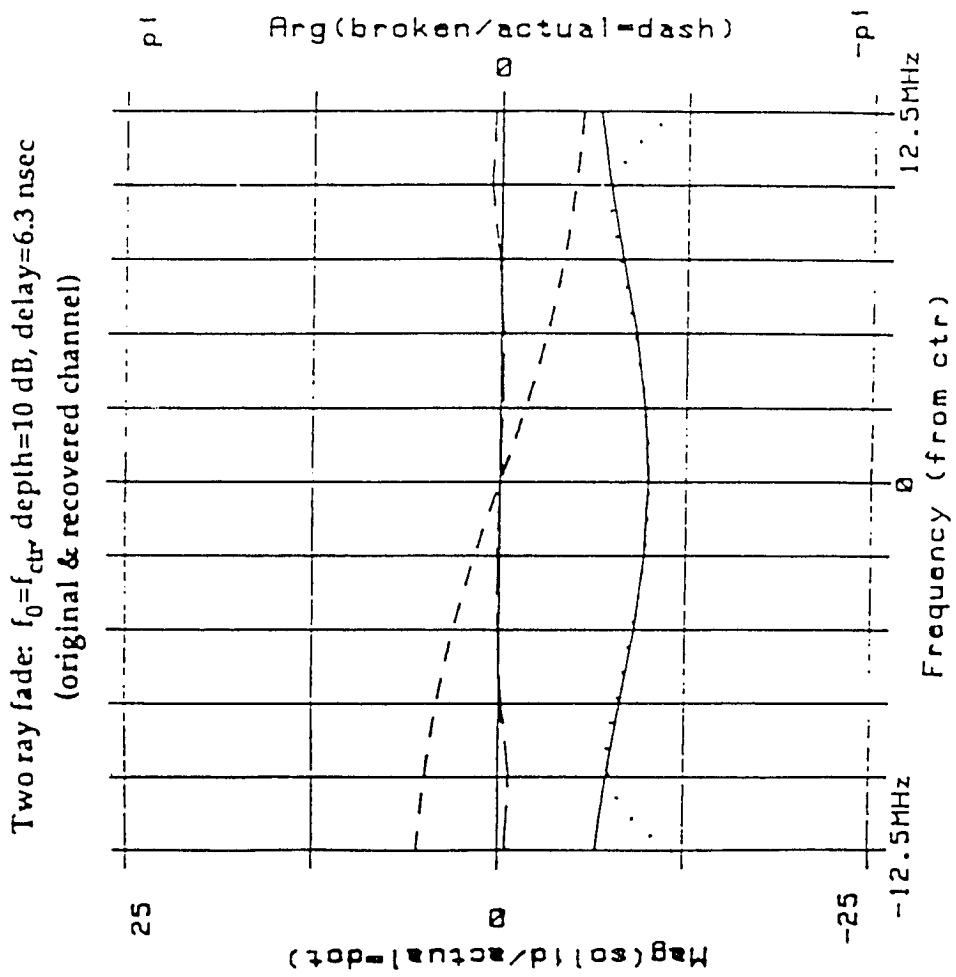
The timing recovery effect is best obtained by direct measurement. If the time shift (or a related measure) is not accessible, it may be estimated. If the distortion is known and simulated, the timing recovery is approximated. The estimated time shift is then used in expression (6-13) to remove phase distortion from the reconstructed channel.

6.4 Summary

The effect of distortion on a QAM signal was examined for multipath interference in a 25 MHz channel. The time domain response of this frequency domain channel was obtained in order to characterize signal distortions. Both simulated multipath data and measured digital radio data

figure 6-4

Figure 6-4: Multipath Channel Response in the Frequency Domain
with Receiver Timing Recovery



were used. The carrier detection and timing recovery responses for these signal data were approximated. The equalizer coefficients were used to estimate the system time response. The channel transfer function was then computed from these data, and compared to measured and/or simulated channels. This method will be applied in chapter 7 to model the effect of real time channel perturbations due to multipath interference. The results will be compared to measured channel data and will be used to relate multipath interference to digital signal quality.

CHAPTER VII

DISCUSSION

Introduction

In this chapter, the effects of multipath propagation on QAM link performance are discussed. The channel model, developed in chapter 4 and evaluated in chapter 5, is integrated with the receiver model, developed in chapter 6. The receiver model output is inverted to recover the channel in order to verify the functionality of the system model. QAM signal distortions are computed for various multipath distortions in order to illustrate the relationship between the channel model parameters and digital performance. The importance of secondary path delay as the controlling factor in the relationship of multipath interference to signal distortion are shown.

Channel distortions and their corresponding effects on signal quality are reviewed in section 7.1. Examples of channel reconstruction from time domain samples of received signals are given in section 7.2. A method for the estimation of second path delay is demonstrated in section 7.3 for various cases of multipath distortion. Peak and mean-square distortions are defined as measures of digital signal quality in section 7.4. These signal distortion measures are computed for various multipath channel distortions and related to the multipath channel parameters in section 7.5. The system model and performance results are reviewed in section 7.6, and future studies are suggested in section 7.7.

7.1 Channel Distortion

Multipath interference shows up as amplitude and phase distortion in the affected channels, and causes signal dispersion in the time domain. The performance of quadrature amplitude modulation is degraded by signal dispersion. The signal dispersion causes intersymbol interference which results in decision errors and loss of information. Intersymbol interference may therefore be examined as a function of the multipath channel model.

In multipath propagation, the secondary path gives rise to a delayed replica of the original signal. The second signal acts as an interferer to the desired signal at the receiver. This causes cancellation and superposition of the intended and interfering signals as a function of delay difference and frequency.

Ideally, the transmission channel response is real having constant magnitude across the channel bandwidth (see figure 3-2b). The corresponding time response is a $\sin(x)/x$ pulse shape which is also real and has even symmetry (see figure 3-2a). There is no out-of-phase or quadrature component in either the time or frequency domains. Alternately, there is no phase error in either the time or the frequency responses. Only the in-phase zero-time sample is non-zero. All other time samples are zero. This corresponds to reception of a single distortion-free pulse.

If the channel transfer function has linear (odd symmetry) magnitude and linear (odd symmetry) phase, then the time response is complex. If the channel transfer function has parabolic (even) magnitude and linear (odd) phase, then the time response is real.

Group delay is related to system phase by the general expression

$$\tau(f) = \frac{-1}{2\pi} \left(\frac{\partial \phi}{\partial f} \right) \quad (7-1)$$

where f is frequency and ϕ is phase.

A constant delay in the transmission path results in a linear phase in the channel, corresponding to odd symmetry in the phase component. A channel with constant magnitude and odd phase symmetry in the frequency domain corresponds to a time response which is real valued. As expected, the pulse shape is identical to the input, except that it is delayed. In this case there are non-symmetrical time samples for the in-phase vector. The out-of-phase vector samples are zero.

Linear delay in the transmission path results in parabolic phase in the channel. The resultant channel has constant magnitude and even phase symmetry in the frequency domain. The corresponding time response is complex, having even symmetry for both in-phase and out-of-phase vectors. In this case there are symmetrical time samples for both vectors.

Parabolic delay in the transmission path results in cubic phase in the channel. The resultant channel has constant magnitude and odd symmetry of phase in the frequency domain. The corresponding time response is real-valued without necessarily having any symmetry. In this case there are non-symmetrical time samples for the in-phase vector, and none for the out-of-phase vector.

A cancellation frequency at the center of the channel corresponds to even symmetry of magnitude and odd symmetry of phase. The corresponding time response is real-valued. If the cancellation frequency is not at the channel center, additional distortion results. Odd symmetry

components are added to the magnitude , and even symmetry components to the phase. The corresponding time response is complex.

7.2 Channel Reconstruction

Based on the descriptions and analyses of the chapters 4.0 and 6.0, the transmission channel may be reconstructed from the sampled time response. The accuracy of the reconstructed channel is affected by certain radio system functions that were described in chapter 6.0. Practical channel recovery requires compensation for these system limitations. In order to show channel recovery, a simulated case will be examined in detail. Measured data will then be used to reconstruct an actual transmission channel.

Communication system simulations begins with the generation of an appropriate pulse shape at a transmitter. A 40 nanosecond $\sin x/x$ pulse is shown in figure 3-2a. The transformation in the frequency domain is shown in figure 3-2b which describes the undistorted communication channel. The transmit channel shape is then multiplied by the Nyquist filter response, as is specified in equations (3-5) and is shown in figure 3-3b. A two ray distortion is selected for the simulation. A 10 dB cancellation depth cancellation frequency is placed at the channel center. The second ray delay is assumed to be 6.3 nanoseconds. The Nyquist filtered channel shape is multiplied by this multipath channel response and is shown in figure 7-1. The solid line is the magnitude component and the dashed line is the phase component. The composite channel is transformed to the time domain and is shown in figure 7-2. The pulse response is entirely real and non-symmetrical. Figure 7-3 shows the result of timing recovery, carrier recovery, and sampling on the received signal. The dotted line represents the signal after timing recovery. It has been shifted by 0.3 symbol intervals. Its peak has been aligned to zero

figure 7-1

Figure 7-1: Multipath Channel Response in the Frequency Domain
(10 dB cancellation depth, at the channel center, with 6.3 nanosecond delay)

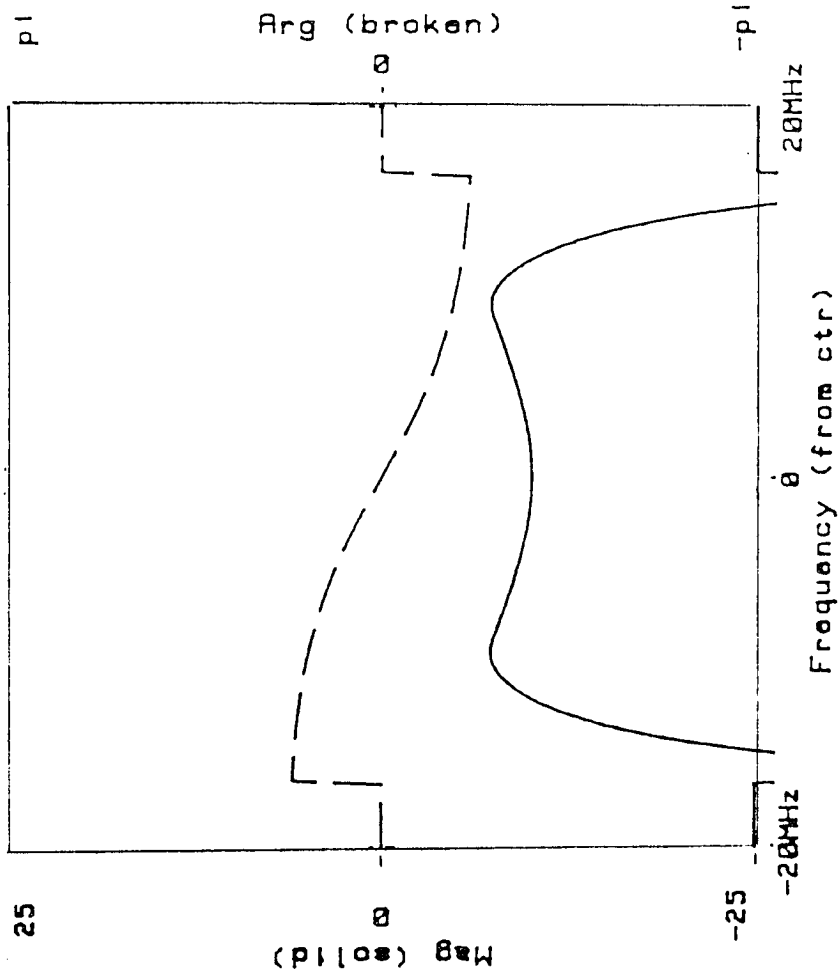


figure 7-2

Figure 7-2: Multipath Channel Response in the Time Domain
(10 dB cancellation depth, at the channel center, with 6.3 nanosecond delay)

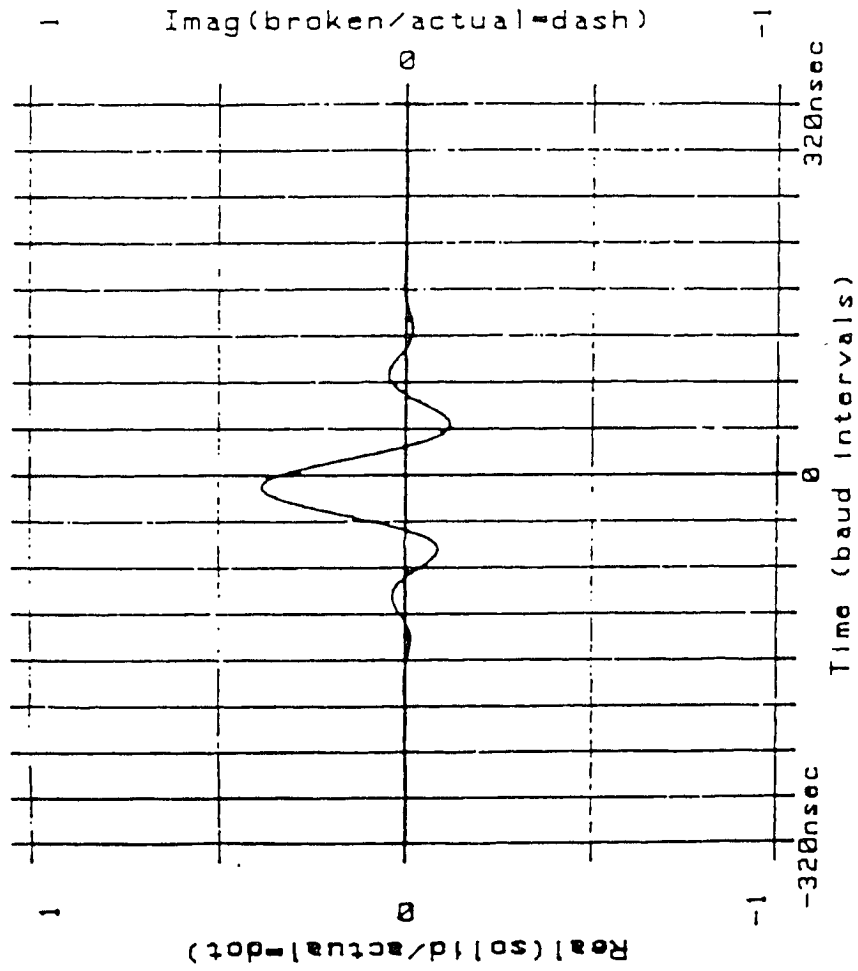
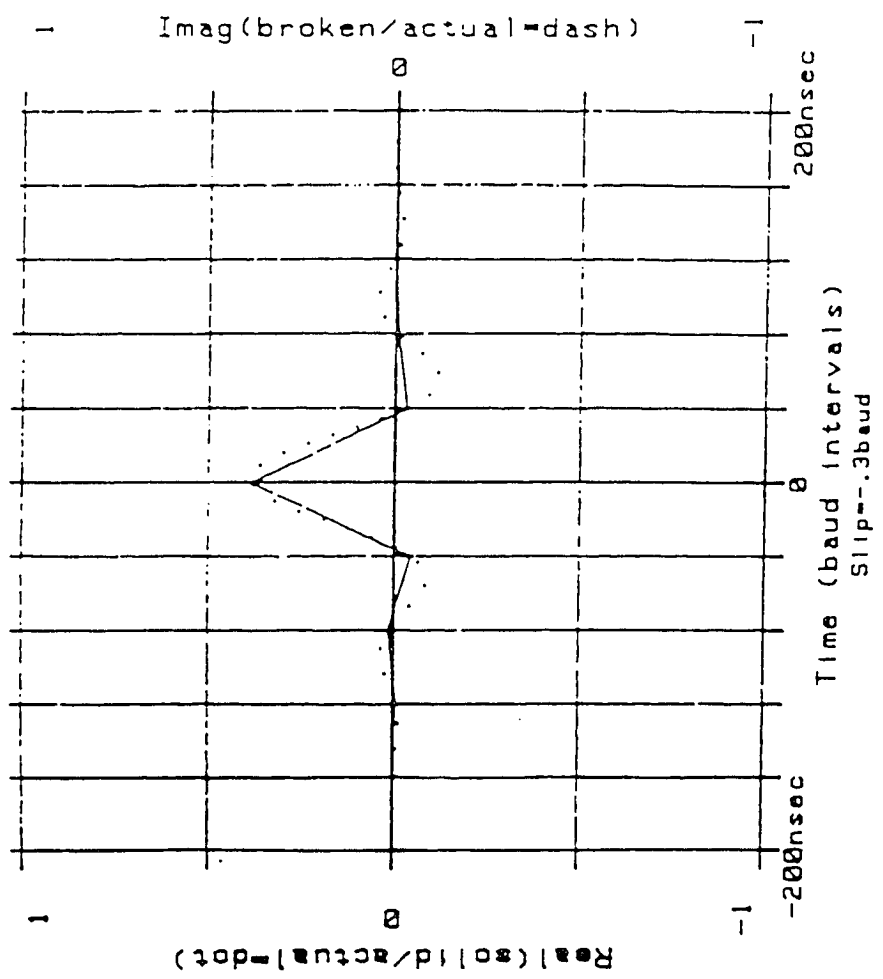


figure 7-3

Figure 7-3: Effect of Timing Recovery, Carrier Detection, and Sampling on the Multipath Channel Response (10 dB cancellation depth, at the channel center, with 6.3 nanosecond delay)



time. The solid line connects the symbol interval samples of the recovered signal. Since there is no imaginary component, there is no adjustment for carrier recovery. The symbol interval samples are related to the DTE values as shown in equation (6-8). The reconstructed channel is formed from the inverted DTE coefficients. Figure 7-4 shows a comparison of the original and reconstructed channels. The dotted line represents the original channel magnitude shape. The dashed line represents the original phase shape. The solid line represents the reconstructed channel magnitude shape. The broken line represents the reconstructed phase shape. At the channel edges there is difference between estimated and actual channel power magnitude.

The same channel was created in the laboratory using an HP 11757A Multipath Simulator as in chapter 5. It was inserted in the transmission path of an AT&T DR6-30-135 test link. The equalizer coefficients were measured and recorded in the laboratory, and were inverted as in equation (6-8). The result is the sampled time response as seen by the equalizer. This is plotted in figure 7-5. The average power in the channel was measured as -8.65 dB. The response in figure 7-5 computed from the measured data is similar to the simulated time response shown by the solid line in figure 7-3. The reconstructed channel is formed from the inverted equalizer coefficients. In the case of the actual channel, the measured channel power is used to shift the reconstructed channel magnitude to the correct average power level. Figure 7-6 shows a comparison of the original and reconstructed channels. The dotted line represents the original channel magnitude shape. The dashed line represents the original phase shape. The solid line represents the reconstructed channel magnitude shape. The broken line represents the reconstructed phase shape. As in the simulated case, there is very good

figure 7-4

Figure 7-4: Comparison of the Simulated and the Reconstructed Multipath Channel Responses in the Frequency Domain (10 dB cancellation depth, at the channel center, with 6.3 nanosecond delay)

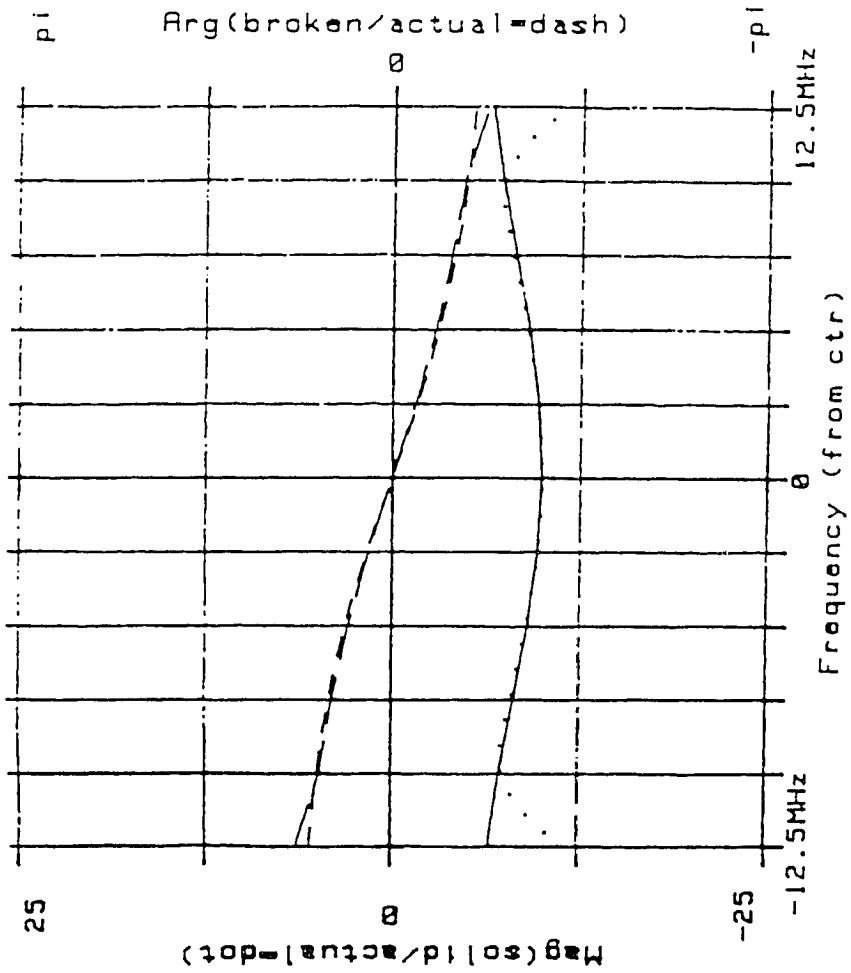


figure 7-5

Figure 7-5: Measured Multipath Channel Response in the Time Domain (10 dB cancellation depth, at the channel center, with 6.3 nanosecond delay)

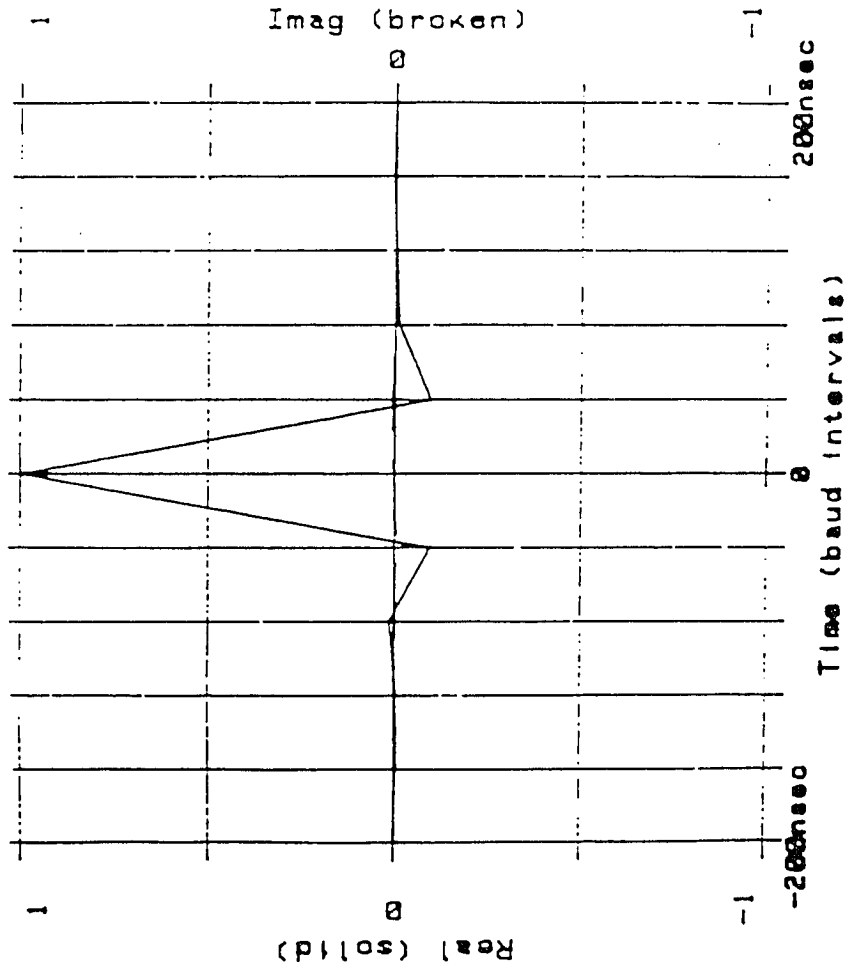
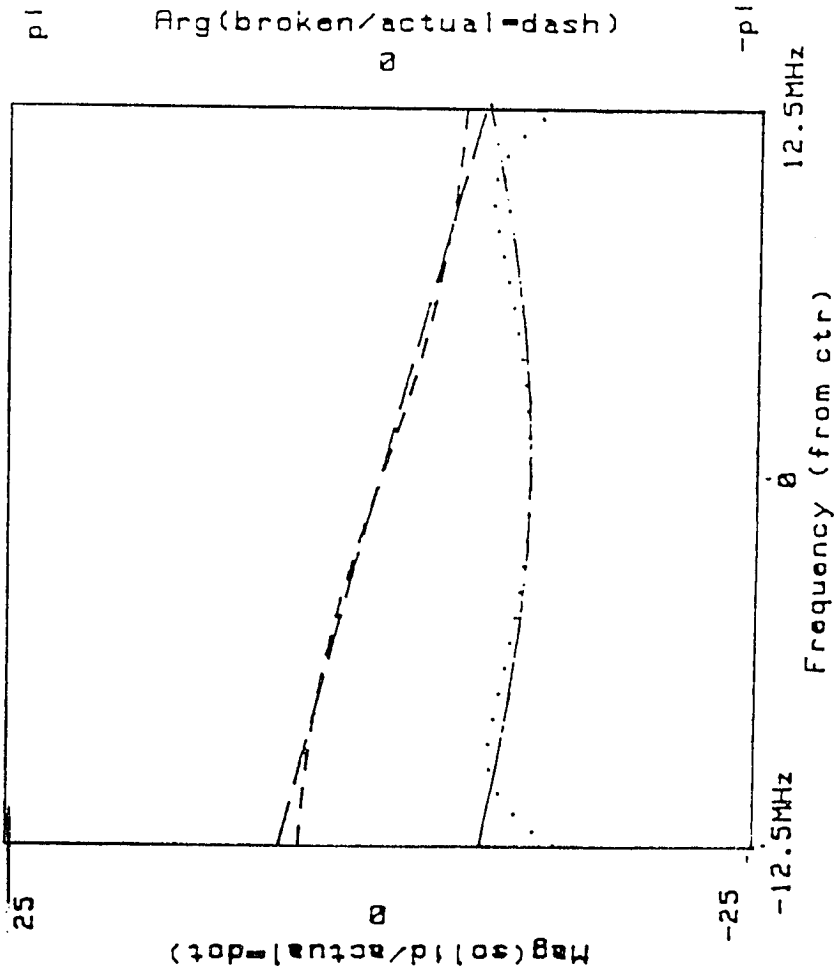


figure 7-6

Figure 7-6: Comparison of the Measured and the Reconstructed Multipath Channel Responses in the Frequency Domain (10 dB cancellation depth, at the channel center, with 6.3 nanosecond delay)



agreement between the original and reconstructed channels. The only substantial difference occurs at the channel edges.

7.3 Second Path Delay

In the multipath scenario described in chapter 4, there are, in effect, two transmission paths. This is illustrated in figure 3-4. When combining the two signals at the receiver, the system is equivalent to the two ray model described earlier. Equalization of the signals at the receiver requires knowledge of the delay difference between the two paths. If the channel is reconstructed as described chapter 6, then it is possible to estimate the delay difference.

A non-equalized channel may be reconstructed from the equalizer coefficients if the equalizer is stable and the coefficient values are converging. The AT&T DTE coefficient values will converge for BER less than 10^3 , or for regions above the 10^3 M-curve. This is composed of two ray cases where either the minimum is out-of-band (i.e. the cancellation frequency is not in the channel), or it is not sufficiently deep (i.e. the second ray is weak) as to impair the system performance.

There may be a large range of variation in delay difference, as there is a large variation in radio link geometry. As was discussed in section 6.3, the resolution of the AT&T DTE in terms of delay is from 40 to 200 nanoseconds. If the delay difference is within this range, it is identified and estimated from the magnitude component of the reconstructed channel. The frequency spacing between the minima is equal to the inverse of the delay difference.

Delay components greater than 200 nanoseconds are not resolved due to sampling limitations. However, it is possible to estimate delay differences less than 40 nanoseconds. A non-equalized channel must first be

reconstructed from the equalizer coefficients, as was described in chapter 6. The reconstructed channel magnitude may be approximated by a polynomial. The polynomial approximation is then matched to the two ray model solution. At this point, the delay difference is estimated.

A second order polynomial expansion is adequate to characterize most channel shapes having small delay. This results in a parabolic fit to the channel magnitude. The p_0 , p_1 , and p_2 represent the zero order (constant), first order (linear), and second order (parabolic) components. The normalized two ray model has the following transfer function as shown in section 4.3,

$$H(f-f_0) = 1 - b e^{j2\pi(f-f_0)\tau} \quad (7-2)$$

A solution for the two ray parameters is approximated in chapter 4. It applies to the case of a small offset notch frequency. This limits accuracy to notch positions near the channel center or within the channel.

The polynomial approximation is matched to the two ray model solution. The second ray strength is a function of the three polynomial coefficients, p_0 , p_1 , and p_2 ,

$$b = 1 - \sqrt{p_0 - \frac{1}{2} \left(\frac{p_1^2}{2p_2} \right)} \quad (7-3)$$

The delay difference is a function of second ray strength b and of the second order coefficient p_2 ,

$$\tau = \frac{2p_2}{2b} \quad (7-4)$$

A transmit pulse and Nyquist filters are simulated as before. The two ray distortion is used to create the non-equalised channel. A 10 dB cancellation depth cancellation frequency is placed at the channel center. The delay difference is 6.3 nanoseconds. The transmit and filtered channel is multiplied by the two ray model frequency response. Timing recovery and carrier recovery action are simulated on the received signal. The reconstructed channel is then formed from the inverted equalizer coefficients. Figures 7-7, -8, and -9 show comparisons of original and reconstructed channels for three combinations of parameters. In each figure, the dotted line represents the original channel magnitude shape. The dashed line represents the original phase shape. The solid line represents the reconstructed channel magnitude shape. The broken line represents the reconstructed phase shape.

For each case, the same frequency response was created in the laboratory using the HP 11757A Multipath Simulator as described in chapter 5. It was inserted in the transmission path of the AT&T DR6-30-135 test link. The average power and the equalizer coefficient values were measured and recorded in the laboratory. The reconstructed channel was formed from the inverted equalizer values. In the case of the actual channel, the measured channel power was used to shift the reconstructed channel magnitude to the correct average power level.

The test examples are listed in Table 7-1. For the first three cases where the cancellation frequency was inside the channel (figures 7-6, -7, -8) there estimated delays were relatively close to the actual values. For the fourth case where the cancellation frequency was outside the channel (figure 7-9), a solution for delay difference was not obtained.

figure 7-7

Figure 7-7: Comparison of the Measured and the Reconstructed Multipath Channel Responses in the Frequency Domain (10 dB cancellation depth, 5 MHz from the channel center, with 6.3 nanosecond delay)

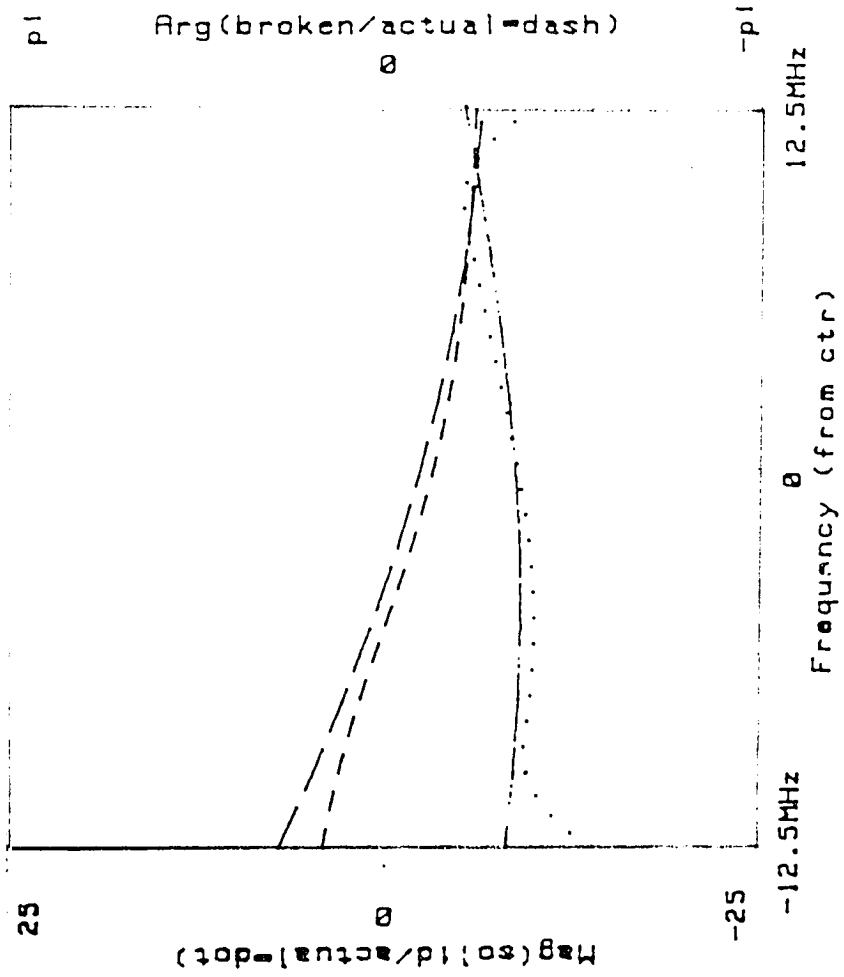


figure 7-8

Figure 7-8: Comparison of the Measured and the Reconstructed Multipath Channel Responses in the Frequency Domain (10 dB cancellation depth, at channel center, with 10 nanosecond delay)

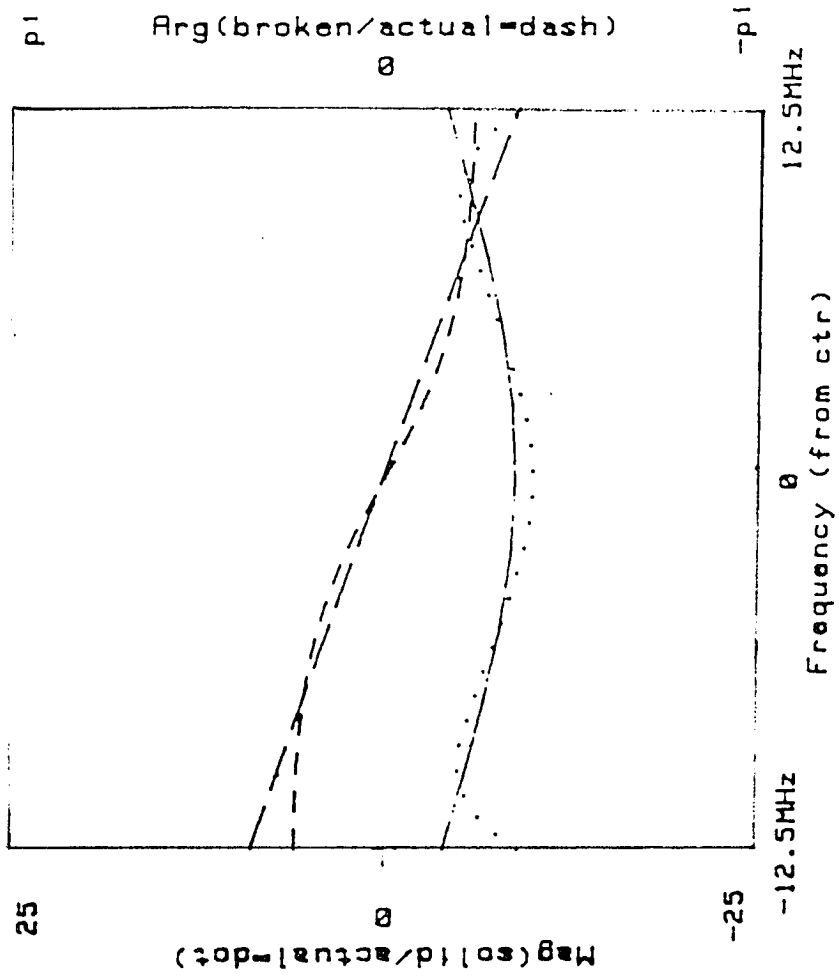
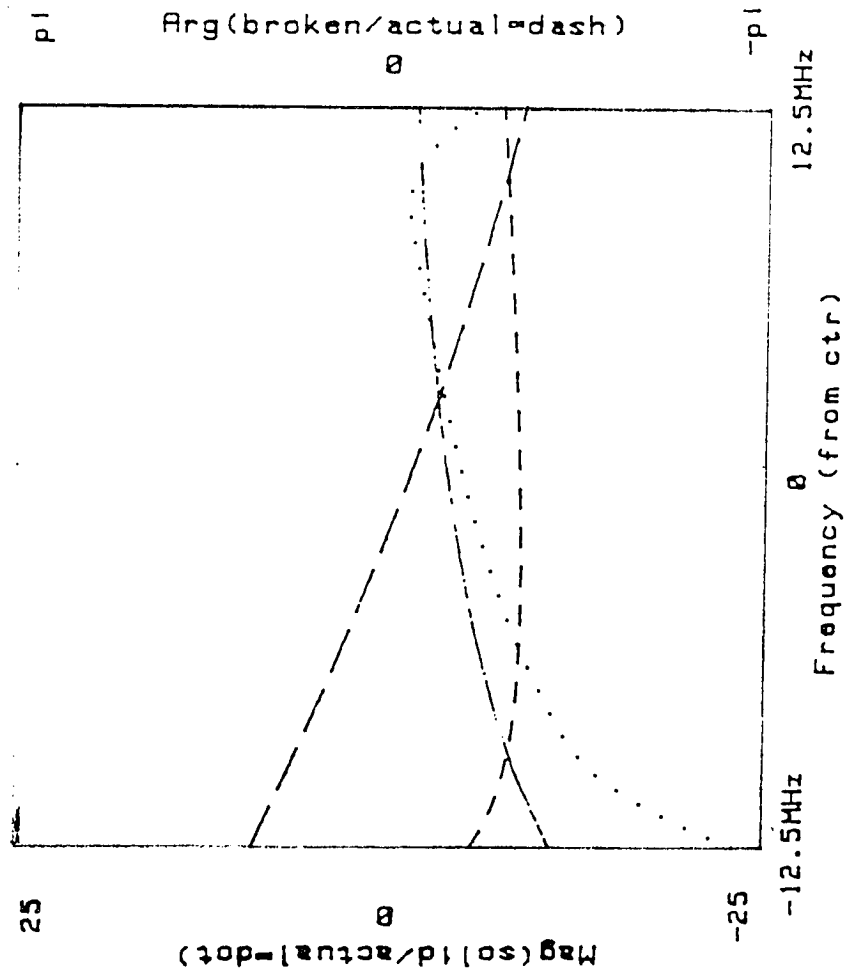


figure 7-9

Figure 7-9: Comparison of the Measured and the Reconstructed Multipath Channel Responses in the Frequency Domain (20 dB cancellation depth, 15 MHz from the channel center, with 6.3 nanosecond delay)



7.4 Signal Distortion

Channel distortion is generally characterized as intersymbol interference in the time domain. There are several mechanisms in a digital communication system which are affected by signal distortion due to multipath propagation. Timing jitter is caused by the displacement of the time of peak detection due to superposition of delayed echoes with the desired signal. Similarly, signal interference is caused at other sampling times by the presence of delayed echoes. In addition, phase deviations caused by the reception of multipath signals cause cross-talk between the signal vectors.

It is possible to measure the effect of intersymbol interference by determining the signal distortion at a given sample time. Signal distortion is expressed in the form of "eye-closure" [45]. The distortion or eye-closure is generally represented as the amount of signal level perturbation at the receiver divided by the distance to the nearest decision threshold. Peak distortion or "peak eye-closure" is a function of the peak signal deviation, and mean-square distortion or "rms eye-closure" is a function of the rms signal deviation.

Referring to equations (6-2), the complex time domain signal, $r(t)$, at the output of the QAM receiver filter is written as

$$r(t) = \sum_{k=-n}^{k=+n} s_k h(t-kT-t_0) + \eta(t) \quad (7-5)$$

where k represents an integer multiple of the symbol interval sample time T , s_k represents the k^{th} transmitted QAM symbol, $h(t)$ is the complex channel

response, t_0 represents the transit delay, and $\eta(t)$ is the additive noise. If the signal is sampled at time $t = kT + t_0$, then

$$r_n = s_n h_n + \sum_{k < n} s_k h_{n-k} + \eta_k. \quad (7-6)$$

The additive noise is not considered in this analysis of multipath interference. Examining the response for the transmitted symbol $k=0$,

$$r_0 = s_0 h_0 + \sum_{k > 0} s_k h_{(-k)} \quad (7-7)$$

where the first (product) term $s_0 h_0$ represents the desired signal, and the second (summation) term represents the total signal interference from other symbols occurring at the detection time of the desired symbol. The worst case interference will result when the symbols are similar in amplitude and phase. The resulting distortion is the ratio of the total signal interference at the detection time, to the desired signal. This ratio is expressed as,

$$\Delta = \frac{\sum_{k > 0} h_k}{h_0} \quad (7-8)$$

and is independent of the actual symbol transmitted.

7.5 Multipath Interference

The resulting distortion is the amount of signal level interference at the receiver normalized to the distance from the desired signal. Peak distortion or "peak eye-closure" is a function of the peak signal deviation. It therefore is obtained by evaluating equation (7-8) with the peak values of the sampled response h_k . The peak distortion represents worst-case decision errors due to signal distortions. The effect of multipath interference on the QAM signal can be estimated from the peak distortion for the two ray model.

The mean-square distortion or "rms eye-closure" is a function of the rms signal deviation. It therefore is obtained by evaluating equation (7-8) with the rms values of the sampled response h_k . The rms distortion may be modelled as gaussian noise, and combined with the additive noise process to determine the overall probability of decision error. However, the multipath process is not necessarily gaussian in nature. Furthermore, the scope of this thesis is to model the QAM digital radio system response to multipath interference, and not to noise in general.

In either case, the peak and the mean-square distortions are defined as measures of signal distortions at the sampling instant. A distortion exceeding 1 implies a decision error and a resulting errored bit. Hence, these measures are used to estimate the likelihood of a decision error as a function of multipath interference. Signal distortions are modelled and shown for various cases of multipath interference in figure 7-10 (a-b). The peak and mean-square distortions are computed as a function of cancellation depth and second ray delay.

The cancellation depths of 10, 15, and 20 dB are selected for the distortion experiment. These depths correspond to normalized second ray

figure 7-10a

Figure 7-10a: Peak Distortion versus Cancellation Depth and Second Path Delay Difference

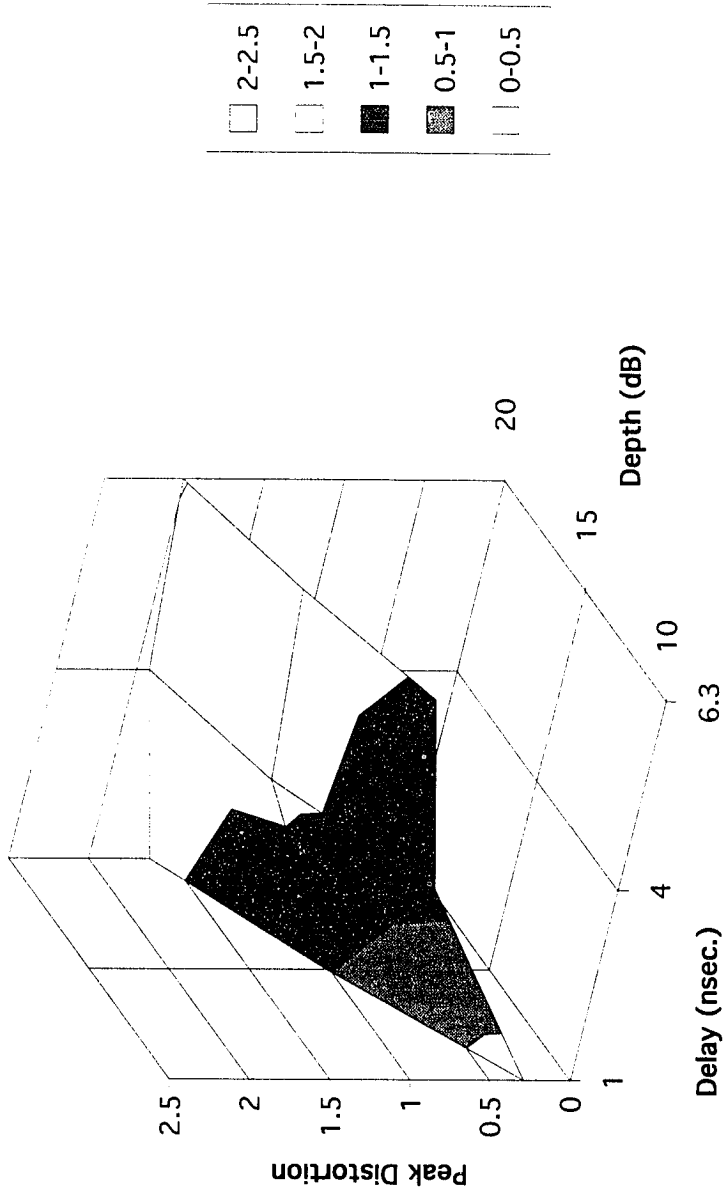
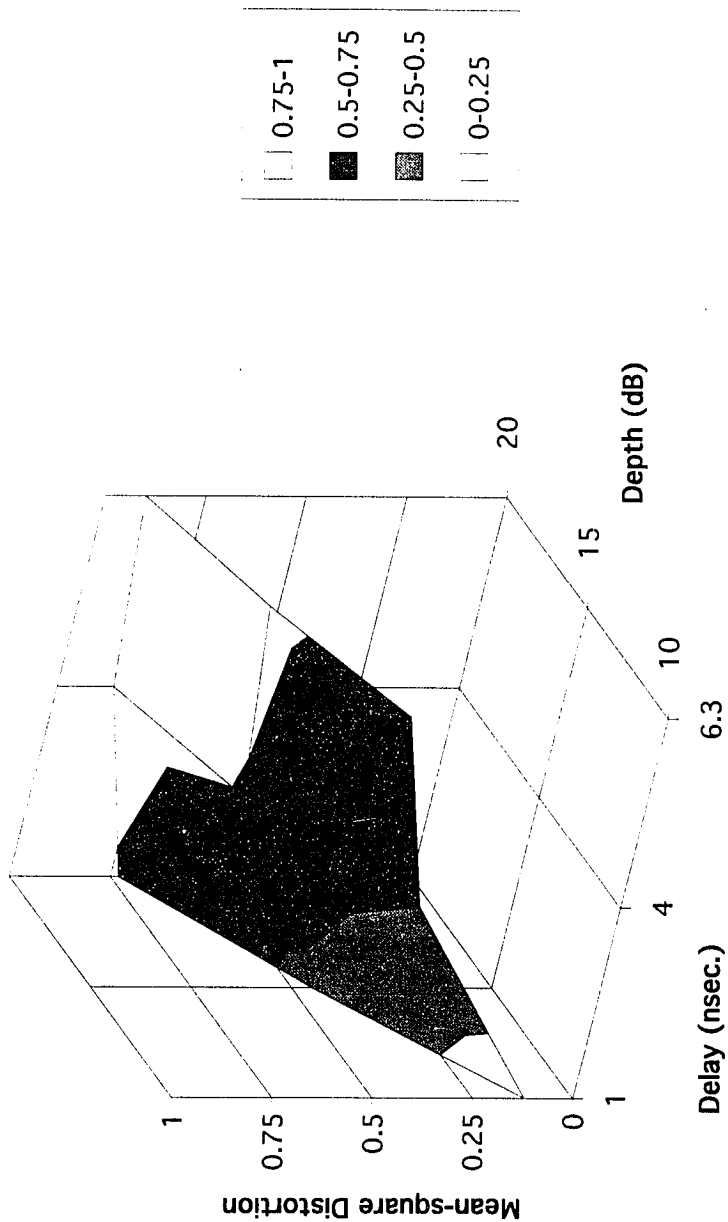


figure 7-10b

Figure 7-10b: Mean-square Distortion versus Cancellation Depth and Second Path Delay



strengths of 0.9 to 0.99. As discussed in section 4.2, the ground reflection coefficient for soil in the GHz regime approaches unity. Cancellation depths from 10 to 40 dB were measured in Brawley, as was reviewed in sections 4.4 and 4.5.

The second path delay sample set of 1, 4, and 6.3 nanoseconds was selected for the distortion experiment. As was shown in section 4.2, the second path delay for ground reflections is a function of link geometry. Second path delays were predicted in the range from 1 to 3 nanoseconds for Brawley. In sections 4.4 and 4.5 similar values were computed in the range from 1 to 3 nanoseconds. Values in the range of 1 to 10 nanoseconds have been published for several experiments. The Rummler implementation of the two ray model used a fixed 6.3 nanosecond delay.

For each pair of depth and delay, the distortion was averaged for three cases of in-band minima location: the cancellation frequency occurring at the band center, the cancellation frequency occurring at the band edge, and the cancellation frequency occurring at the midpoint between the band center and edge. As can be seen, the peak and rms distortions are functions of the values of both second ray delay difference and cancellation depth. The signal distortion increases as the delay increases. Similarly, the signal distortion increases as the cancellation deepens.

In the case of ground reflections, the second path is physically stable. It has a constant reflection coefficient, resulting in constant and deep cancellation depth (20 - 40 dB). It also has a nearly constant second path length, resulting in a stable delay with slight perturbations due to atmospheric irregularities. The small perturbations in delay cause some variation and movement of the location of the minima, but do not

significantly change the overall delay. In the common ground reflection scenario, the delay fixed by the path geometry is the dominant variable in determining the amount of signal distortion.

In the case of atmospheric multipath, the second path is very unstable. It is caused by irregularities in the gradient of the index of refraction in the lower atmosphere which give rise to re-direction and focussing of the transmitted wavefront. The effective reflection coefficient is unstable and the second path delay is variable. A strong second ray is required to create distortions of significance to current digital systems. Again, once such distortion is established, variations in strength cause some variation in signal distortion. However, the second path delay, which is a function of the path geometry, will determine the final amount of signal distortion. In the atmospheric reflection scenario, a sufficient cancellation depth is necessary to impair system performance. This is a function of highly irregular and unpredictable atmospheric conditions. However, once the appropriate conditions exist, the second path delay determines the amount of signal distortion.

As was established in chapter 4, a reflected wavefront of substantial strength and coherence is required in order to create significant interference. This requires a stable and strong reflection coefficient, and a significant reflecting area providing a constant secondary path length or delay. An accurate estimate of the delay characteristics of secondary paths on a line-of-sight microwave link was found to be necessary in order to predict the effect of multipath interference on QAM digital radio.

As the reflection path of exposed ground is stable and has a reflection coefficient of nearly unity for microwave frequencies, the majority of

interference is likely to be caused by ground reflections. The delay characteristics of multipath due to ground reflections can be estimated from an analysis of the physical link design, as was performed in section 4.2. The signal distortion due to ground reflections can then be characterized using the model of section 4.3 and the analysis of section 7.5.

For the case of multipath dominated by atmospheric reflections, a stable secondary path must be created with significant focusing of signal for significant interference to result. Prediction of the effect of this interference is subject to the prediction of unusual and unstable atmospheric phenomena.

7.6 Summary

The receiver model was verified and integrated with the channel model into an overall system model at the receiver. The receiver output was inverted to recover the second path delay of the multipath channel. Peak and mean-square signal distortions were defined and related to the principal two ray model parameters, cancellation depth and the second path delay. QAM signal distortions were computed for various multipath distortions in order to illustrate the relationship between the channel parameters and the received signal. The second path delay was shown to be the dominant parameter limiting the performance of a QAM system in the presence of multipath interference.

Table 7-1**Delay Estimation Experiments**

<u>data type</u>	<u>figure</u>	<u>notch depth</u>	<u>frequency</u>	<u>second path delay</u>	
				(simul.)	(est.)
	(dB)	(MHz)	(nsec)		
simulated	7-6	10	0	6.3	6.8
measured					6.41
simulated	7-7	10	-5	6.3	6.29
measured					5.78
simulated	7-8	10	0	10	9.42
measured					9.37
simulated	7-9	20	15	6.3	no solution
measured					no solution

VIII. CONCLUSIONS

A system model for multipath interference on terrestrial line-of-sight QAM digital radio is developed in this dissertation. A forward multipath simulation based on microwave link geometry, topography, and atmospheric refraction is used to develop a two ray multipath interference channel model. The channel model is a function of the second ray strength and delay. These parameters are estimated from measured channel data, and modelled results are compared to measured performance data. The second ray delay is shown to be a variable and to be a function of the microwave length geometry. Time variation of the delay is found to be a function of the atmospheric conditions and to be the main source of interference dynamics. The performance of the AT&T DR-6/135 radio system equipped with channel protection and adaptive equalization is measured in the field on a microwave link known to be dominated by multipath interference in the 6 GHz band. The digital radio performance is also simulated in the laboratory as a function of static and dynamic variations of the model parameters, and performance thresholds are established. The recovery of the complex transmission channel from the system time response is shown, and the limitations of recoverable channel features are identified for both simulated and measured data. In each case, successful channel reconstruction and subsequent second path delay estimation are obtained. A measure for signal distortion is established and related to the principal two ray model parameters, cancellation depth and second path delay. The second path delay is found to be the dominant multipath channel parameter for a QAM link.

IX. RECOMMENDATIONS

As was discussed earlier, there has been extensive work in the modelling of multipath channels. The early studies were limited to the effects of propagation loss and interference. Physical and statistical channel models were later developed for performance prediction and improvement design. The propagation models are physical and characterize both ground scatter and atmospheric refraction phenomena. They are site specific, requiring detailed knowledge of both terrain and atmospheric conditions. However, since they are not signal oriented, they are not well suited to performance prediction. On the other hand, the channel models are limited to the characterization of the response and the statistics of the communication channel. The channel models, both deterministic and statistic, are neither physical nor site specific. They require a priori knowledge of the channel characteristics for a specific site in order to predict performance. The above techniques are subsystem models, dealing either with the physical channel or the received channel.

As has been shown, much of the existing work has been focussed on atmospheric multipath propagation. It is evident that ground reflections play an important role in the performance of line-of-sight terrestrial microwave radio systems. A model which is based on the parameters of radio propagation, and that relates the physical geometry of a specific microwave link to the performance of line-of-sight radio, was developed in this dissertation. A channel model based on physical propagation characteristics was developed and evaluated in the field. A receiver model based on QAM

signal theory was developed and evaluated in the laboratory. The two subsystem models were integrated and used to relate channel parameters to signal distortions.

There are many applications for system modelling in the design of digital microwave links. Characterization of signal distortions allows for improvements in system design for optimum system performance, in signal design for optimum channel matching, and in countermeasure design for rugged or robust transmission. In addition, characterization of impairments allows the determination of performance objectives and limitations. Signal information is used to characterize the communication system status during both normal and stressful conditions. Identification of failures, distortions, and interfering phenomena is obtained from channel data. Intelligent tests using detection and synchronization information can reduce the manpower necessary for installation. They can also eliminate the need of test equipment (delay sets, spectrum analyzers). In general, remote diagnostic capabilities are made more effective by proper characterization of distortions and impairments.

A logical extension of this work is the modelling of the effects of multipath propagation on digital radio systems as an additive noise process. In point-to-point digital radio links, degradations are generally treated as equivalent noise sources. The noise processes are then combined to determine the operating margin for a desired system performance and to estimate the overall system performance. By modelling the characteristics of dynamic multipath interference as a noise source, the probability of error as a function of link design and atmospheric conditions could be predicted by the distortion analysis technique described above.

Another possibility for future work would be to develop a channel interference model for an undetermined number of multiple paths. This is particularly valuable for the prediction of the performance of point-to-multipoint cellular radio systems. It is also applicable to broadcast digital television systems. In either case, transmission from the source is nearly omnidirectional, subjecting the receiver to many possible signal paths. An accurate channel model can identify and characterize sources of interference. In addition, such a channel model can provide the basis for a noise process model to allow for accurate prediction of performance based on a coverage area topography.

LIST OF REFERENCES

page 231

- [1] Olsen, R. L., Martin, L., Tjelta, T., " A Review of the Role of Surface Reflection in Multipath Propagation over Terrestrial Microwave Links" Proceedings of the NATO/AGARD Conference 1986, Feb. 1987.
- [2] Rummler, W. D., "A Multipath Channel Model for Line-of-Sight Digital Radio Systems", ICC'78, p. 47.5.1, 1978.
- [3] Rummler, W. D., "A New Selective Fading Model: Application to Propagation Data", Bell System Technical Journal, p. 1037, May, 1979.
- [4] Jakes, W. C., "An Approximate Method to Estimate an Upper Bound on the Effect of Multipath Delay Distortion on Digital Communications" IEEE X-COM, Vol. 27, p. 76, January 1979.
- [5] Shafi, M. "Statistical Analysis/Simulation of a Three Ray Model for Multipath Fading with Applications to Outage Prediction" IEEE SAC-5, No. 3, April 1987.
- [6] Campbell, J. C., Coutts, R. P., Martin, A. L., Reid, R. L., "Observations and Conclusions from a Three Year Digital Radio Field Experiment in Australia" IEEE SAC-5, No. 3, April 1987.
- [7] Martin, A. L., "Dispersion Signatures, a Statistically Based, Dynamic, Digital Microwave Radio System Measurement Technique" IEEE SAC-5, No. 3, April 1987.
- [8] Lavric, A., Vagrinec, J., Petrovic, G., Tasic, J., "Computer Simulation Results of Multipath Propagation by Digital Radio" 17th IASTED, p. 21, June 1989.
- [9] Kafedziski, V., "QAM Digital Radio Outage Probability in the Presence of Multipath Fading and Additive Noise" IPCCC'92, 3.4.1.1, 1992.
- [10] Hubbard, R. W., Riley, T. J., "Summary of Propagation Conditions and Digital Radio Performance Across the English Channel" ICC'89, p. 774, 1989.
- [11] Haggman, S. G., "Microwave Line of Sight Channel Measurements, Channel Modelling, and Application of Channel Models to Digital Radio Performance Prediction" PhD., Finland, 1991.
- [12] Fechtel, S., "A Novel Approach to Modeling and Efficient Simulation of Frequency-Selective Fading Radio Channels" IEEE SAC-11, No. 3, p. 422, April 1993.

- [13] G. D. Alley, C. H. Bianchi, W. A. Robinson, "Angle Diversity and Space Diversity Experiments on the Salton/Brawley Hop", Globecom '90, August 1990.
- [14] A. Malaga and S. A. Parl, "Experimental Comparison of Angle and Space Diversity for Line-of-Sight Microwave Links", Milcom '85, paper 19.5.
- [15] R. W. Hubbard, "Angle Diversity Reception for LOS Digital Microwave Radio", Milcom '85, paper 19.6.
- [16] E. H. Lin, A. J. Giger, and G. D. Alley, "Angle Diversity on Line-of-Sight Microwave Paths Using Dual-Beam Dish Antennas", ICC '87, paper 23.5.
- [17] P. Balaban, E. A. Sweedyk, and G. S. Axeling, "Angle Diversity with Two Antennas: Model and Experimental Results", ICC '87, paper 23.7.
- [18] S. H. Lin, "Measured Relative Performance of Antenna Pattern Diversity, Antenna Angle Diversity and Vertical Space Diversity in Mississippi", Globecom '88, paper 44.1.
- [19] E. W. Allen, "Angle Diversity at 6 GHz: Methods of Alignment and Test Results", ICC '89, paper 24.1.
- [20] E. W. Allen, "The Effects of Atmospheric Conditions on Angle Diversity Performance at 6 GHz", ICC '89, paper 24.5.
- [21] E. T. Harkless and H. F. Lenzing, "Excitation of Higher-Order Antenna Modes by Multipath Propagation", IEEE Transactions on Communication Technology, August 1967.
- [22] H. F. Lenzing, "Higher-Order Mode Excitation in Large-Aperture Receiving Antennas", The Microwave Journal, December 1969.
- [23] Balaban, P., "Experimental Results for Multimoding Interference During Dispersive Fading", Globecom '89, paper 2.1.
- [24] Kenny, J. J., "Multimode Interference Generation in the Horn-Reflector Antenna System During Multipath Fading", Globecom '89, paper 2.2.
- [25] CCIR Report 784, "Effects on the Design and Operation of Line-of-Sight Radio Relay Systems," CCIR Study Group 9, ITU, Geneva, Switzerland, 1990.

- [26] Proakis, J. G., Digital Communications, McGraw-Hill, 1983, p.338.
- [27] Chamberlin, K., Luebbers, R., "Evaluating Longley-Rice and GTD Propagation Models", IEEE-AP, p.1098, November, 1982.
- [28] Giger, A. J., Low-Angle Microwave Propagation, Physics and Modelling, Artech House, 1991.
- [29] Shkarofsky, I. P., and Nickerson, S. B. "Computer Modelling of Multipath Propagation: Review of Ray-tracing Techniques" Radio Science, vol. 17, no.5, p.1133, September-October, 1982.
- [30] Lavergnat, J., Sylvain, M., "Selective Fading Radio Channels: Modelling and Prediction", IEEE-SAC, vol.5, No.3, April, 1987.
- [31] Shafi, M., "Statistical Analysis/Simulation of a Three Ray Model for Multipath Fading with Application to Outage Prediction", IEEE-SAC, vol.5, no.3, April, 1987.
- [32] Lin, E. H., Giger, A. J., "Radio Channel Characterization by Three Tones", IEEE-SAC, vol.5, no.3, April, 1987.
- [33] Lavergnat, J., Gole', P., "Statistical Behaviour of a Simulated Microwave Multipath Channel", IEEE-AP, vol.39, no.12, December, 1991.
- [34] Boithias, L., Radiowave Propagation, McGraw-Hill, 1987, p.55.
- [35] Kerr, D. E., Propagation of Short Radio Waves, Dover, 1967, p.411.
- [36] Hall, M. P. M., Effects of the Troposphere on Radio Communication, Peter Peregrinus Ltd., 1979, p.86.
- [37] Greenstein, L. J., and Shafi, M., "Outage Calculation Methods for Microwave Digital Radio", IEEE Communications Magazine, February, 1987, vol.25, no.2, p.30.
- [38] Bundrock, A. J., Murphy, J. V., "A Broad-Band 11 GHz Radio Propagation Experiment", IEEE-AP, vol. 32, no. 5, May 1984.
- [39] Martin, L. "Rates of Change of Propagation Medium Transfer Function During Selective Fading", URSI-F Symposium, June, 1983, p.31.

- [40] Rooryck, M., "Validity of Two-Path Model for Calculating Quality of Digital Radio Links; Determination of Model from Measurements on Analogue Links", *Electronics Letters*, vol. 15, no. 24, November 1979.
- [41] A.Nardoni, R.Bellani, G.Filiberti, A.Ricagni, M.Giacconi, P.Semenzato, "I.F. Signature Measurements".
- [42] IEC, Draft Publication 835 - Methods of Measurement for Digital Microwave Transmission Systems, Part 2 - Measurements on Terrestrial Radio-Relay Systems, Section Eight - Adaptive Equalizer, April 1987.
- [43] M.Emshwiller, August 1978, "Characterization of the Performance of PSK Digital Radio Transmission in the Presence of Multipath Fading", ICC'78.
- [44] G.D.Alley, C.H.Bianchi, and W.A.Robinson, April 1990, "Angle Diversity and Space Diversity Experiments on the Salton/Brawley Hop", *IEEE Transactions on Communications*, 1992.
- [45] R.W.Lucky, J.Salz, and E.J.Weldon, 1968, *Principles of Data Communications*, chapter 4.
- [46] H.C.Reeve, R.B.Ward, C.J.Lin, and G.D.Martin, 1989, "An 11 Tap 0.9μ CMOS DTE for Digital Radio", *IEEE Globecom'89*, pp. 413-417.

APPENDIX

MULTIPATH FADE SIMULATOR

The HP 11757A Multipath Fade Simulator uses an internal implementation of the Rummler model,

$$H_i(f) = a_i [1 - b_i e^{j 2 \pi \Delta f_i \tau_i}], \quad (A-1)$$

The parameters are defined as before. The delay difference τ_i is fixed to 6.3 nanoseconds. The notch frequency is specified by the user.

The channel model that is presented to the user is defined as before,

$$H(f) = a [1 - b e^{j 2 \pi \Delta f \tau}], \quad (A-2)$$

The standard two ray parameters (notch frequency, notch depth, broadband attenuation, and delay) are available to the user for selection.

To simulate a desired channel shape, the fader adjusts the internal model. The notch depth is adjusted to obtain the desired notch width. The attenuation is adjusted to obtain the required signal level. The two expressions, (A-1) and (A-2), are made equal at the notch frequency. The internal parameters a_i and b_i are then solved [i],

$$a_i = 10^{\left(\frac{A_i}{20}\right)}, \quad (\text{A-3a})$$

$$b_i = \frac{1}{2} \left(k - \sqrt{k^2 - 4} \right), \quad (\text{A-3b})$$

where

$$k = 2 + \left(\frac{1 - b}{\sqrt{b}} \frac{\tau_i}{\tau} \right)^2, \quad (\text{A-4})$$

$$A_i = B - B_i + A, \quad (\text{A-5a})$$

$$B_i = 20 \text{ Log} (1 - b_i). \quad (\text{A-5b})$$

The basic assumption that a channel with a variable delay may be fitted by a fixed delay model is not valid in the broadband frequency regime. The parameters are solved at the cancellation frequency. This is inherent to the two ray model as discussed in chapter 4. The delay τ uniquely determines the separation of minima in the frequency domain, and therefore characterizes the broadband channel.

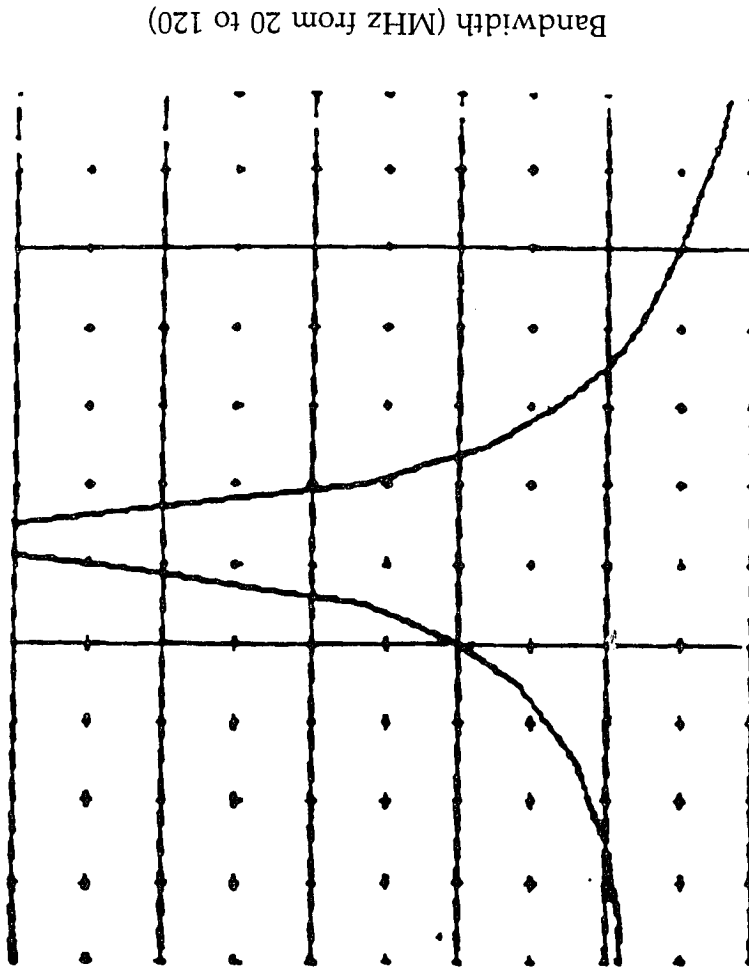
Data provided by Hewlett Packard is shown in figures A-1 and A-2. The difference in dB between two ray implementations versus offset notch frequency is shown. A two ray model with a 1 nanosecond delay is compared to an approximation of the 1 nanosecond shape with a 6.3 nanosecond fixed delay model. This is implemented for both 10 dB and 40 dB fixed notch depths across a 60 MHz band. For the 10 dB notch depth, the difference in shape does not exceed 0.5 dB. For the 40 dB notch depth the difference is

larger, but remains less than 2 dB. Further data from Hewlett Packard gives the usable bandwidth in MHz as a function of delay in nanoseconds. The criterion is signal deviation of less than 0.5 dB from the desired level. As expected, the usable bandwidth is maximum at 6.3 nanoseconds. It asymptotically decreases to approximately 20 MHz as the delay increases to 12 nanoseconds. It asymptotically decreases to approximately 30 MHz as the delay decreases to 1 nanosecond.

[i] K.Marquez, 1990, notes on the Hewlett Packard Multipath Fade Simulator.

figure A-1

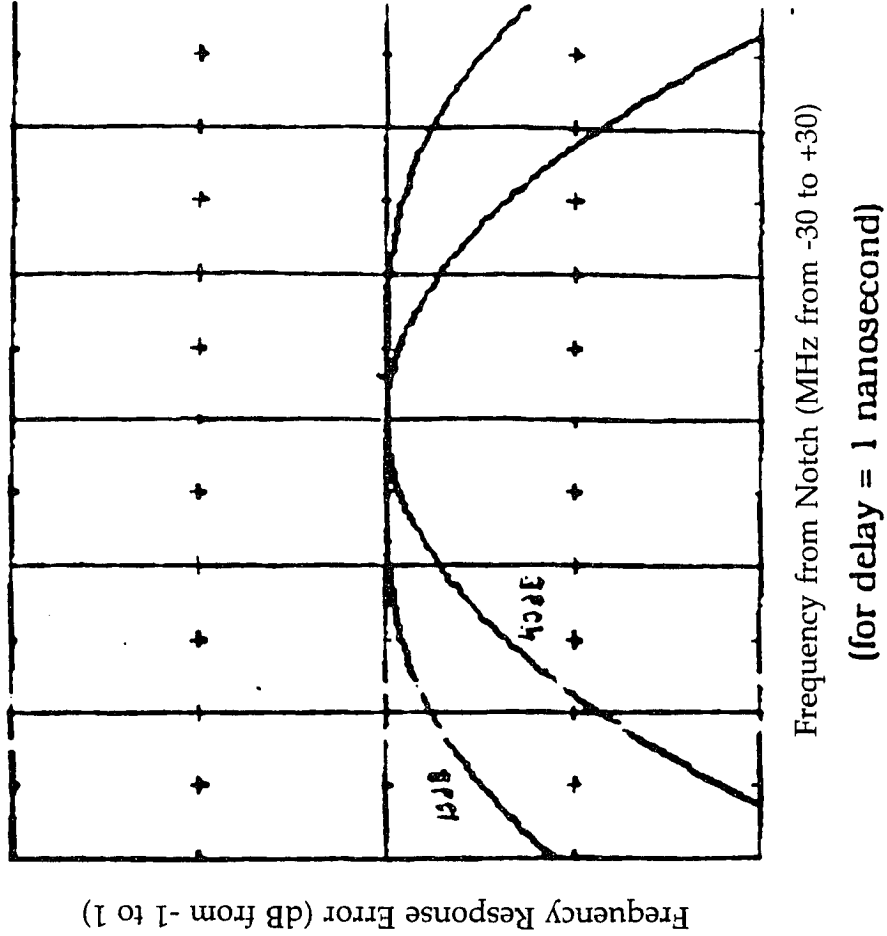
Figure A-1: Hewlett Packard Multipath Fade Simulator
Multipath Channel Response in the Frequency Domain
Usable Bandwidth



Second Ray Delay (nanoseconds from 1 to 12)

figure A-2

Figure A-2: Hewlett Packard Multipath Fade Simulator
Multipath Channel Response in the Frequency Domain
Comparison of Theoretical and Simulated



List of Abbreviations

AD:	Angle Diversity
AGC:	Automatic Gain Control
ASE:	Adaptive Slope Equalizer
A/D:	Analog to Digital Converter
BER:	Bit Error Ratio (BER)
CCITT:	International Consultative Committee for Telephony and Telegraphy ISDN: Integrated Services Digital Network
CD:	Carrier Detection
C/I:	Carrier to Interference ratio
C/N:	Carrier to Noise ratio
DEMOD:	Demodulator circuit
DM:	Degraded Minutes
DTE:	Digital Transversal Equalizer
ES:	Errored Seconds
I:	In-phase
IBPD:	In-Band Power Difference
IF:	Intermediate Frequency
ISI:	Inter-Symbol Interference
Q:	Quadrature-phase
QAM:	Quadrature amplitude modulation
RCV:	Receiver
RF:	Radio Frequency
SD:	Space Diversity
SES:	Severely Errored Seconds
SFF:	Single Frequency Fade
TBL:	Time-Below-Level
TR:	Timing Recovery
VO:	Vertical Offset
XMT:	Transmitter